Mathematical Models of Influenza A Virus Infection: From Intracellular Replication to Virus Growth in Cell Populations

Dissertation

zur Erlangung des akademischen Grades

Doktoringenieur

(Dr.-Ing.)

von: Dipl.-Ing. Frank Stefan Heldt
geboren am: 8. Mai 1985 in Magdeburg

genehmigt durch die Fakultät für Verfahrens- und Systemtechnik
der Otto-von-Guericke-Universität Magdeburg

Promotionskommission:

Jun.-Prof. Dr. Timo Frensing
Prof. Dr.-Ing. Udo Reichl
Prof. Dr. Dr. h.c. Edda Klipp
Prof. Dr. Catherine A. A. Beauchemin

eingereicht am: 3. November 2014
Promotionskolloquium am: 6. Februar 2015

Only theory can tell us what to
measure and how to interpret it.

Albert Einstein

Heldt, Frank Stefan:
Mathematical Models of Influenza A Virus Infection:
From Intracellular Replication to Virus Growth in Cell Populations
PhD Thesis, Max Planck Institute Magdeburg, 2015.

Danksagung

Diese Arbeit entstand im Rahmen meiner Tätigkeit in der Arbeitsgruppe Bioprozesstechnik am Max-Planck-Institut für Dynamik komplexer technischer Systeme in Magdeburg in der Zeit von Dezember 2009 bis Oktober 2014. Mein Dank gilt allen, die daran mitwirkten und mich während der Promotion unterstützten.

Insbesondere möchte ich mich bei Herrn Prof. Dr.-Ing. Udo Reichl bedanken, der mir ermöglichte die Promotion unter hervorragenden Bedingungen und weitgehender thematischer Freiheit zu gestalten. Die vielen inspirierenden Diskussionen und sein wertvoller akademischer Rat haben maßgeblich zum Gelingen dieser Arbeit beigetragen.

Ebenso geht mein Dank an Prof. Dr. Dr. h.c. Edda Klipp und Prof. Catherine A. A. Beauchemin für ihr Interesse an der Arbeit und deren Begutachtung.

Mein besonderer Dank gilt Jun.-Prof. Dr. Timo Frensing, der mich in den vergangenen Jahren wiederholt mit konstruktiven Ideen und kritischen Diskussionsbeiträgen in neue thematische Bahnen lenkte. Seine stete Unterstützung während dieser spannenden Phase meiner akademischen Laufbahn schätze ich sehr.

Nicht weniger dankbar bin ich meinem Kollegen und Freund Markus Rehberg. Unsere zahlreichen Gespräche über die Untiefen der Modellierung biologischer Systeme trugen einen nicht unwesentlichen Teil zur Qualität dieser Arbeit bei.

Für die wertvolle Unterstützung bei sämtlichen mathematischen Fragen danke ich Prof. Dr. Dietrich Flockerzi. Darüber hinaus möchte ich den Beitrag von Robin Gröpler zur numerischen Simulation des multiskalen Modells dankend anerkennen.

Besonders herzlich danke ich Helene Kaffka und Sebastian Dorl, die durch ihr großes Engagement im Rahmen ihrer Bachelorarbeiten den Grundstein für Teile dieser Arbeit legten.

Zusätzlich gilt mein Dank allen Kollegen in der Bioprozesstechnik-Gruppe für die schöne Zeit und das angenehme Arbeitsklima. Insbesondere die experimentellen Beobachtungen von Britta Peschel und Antje Pflugmacher halfen mir die Brücke zwischen den theoretischen Aspekten dieser Arbeit und der Wirklichkeit im Labor zu schaffen. Außerdem möchte ich mich bei Frau PD Dr. Yvonne Genzel, Mandy Bachmann, Sascha Kupke und Tanja Laske für die zahlreichen hilfreichen Diskussionen bedanken.

Der größte Dank gilt jedoch meiner Familie, ohne die diese Arbeit nicht zustande gekommen wäre.

Abstract

Influenza A viruses are human respiratory pathogens that infect 5–15% of the world's population in annual epidemics causing 3 to 5 million cases of severe illness and up to 500 000 deaths. In addition, new virus variants pose a continuous threat of sparking pandemic outbreaks like the 1918 "Spanish flu" with an estimated 50 million victims worldwide. The key to a successful fight against influenza viruses is a detailed understanding of their life cycle, which can guide the development of new antivirals and more potent vaccines.

This work aims to develop mathematical models for influenza A virus infection that can provide a quantitative description of virus replication inside an infected cell and of virus growth in a host cell population. In particular, we focus on identifying bottlenecks of virus production. These bottlenecks represent promising targets for anti-influenza drugs and limit virus yields in vaccine production.

The first part of this work covers a model for the intracellular life cycle of influenza A viruses. It comprises key steps of their replication, from virus entry to budding, with a particular emphasis on the regulation of viral RNA synthesis. We find that two control mechanisms are essential and sufficient for this model to capture the time course of viral RNAs: (i) the stabilization of replicative intermediates (cRNA) by viral polymerases and nucleoproteins (NP), which regulates the transition from viral transcription to genome replication, and (ii) the shutdown of positive-strand RNA synthesis by the viral matrix protein 1 (M1) facilitating the nuclear export of viral genome copies (vRNA). Simulations also suggest that virus production is particularly sensitive to the rate of RNA synthesis, the onset of nuclear export, and the speed of virus assembly/release. Thus, the model provides valuable insights into the mechanisms that govern virus replication inside an infected cell.

In the second part, we study the impact of molecular noise at the intracellular level. Intriguingly, simulations suggest that the replication of influenza A viruses at this level is particularly susceptible to stochastic fluctuations because of their segmented genome. More precisely, the autocatalytic mechanism of viral RNA synthesis amplifies noise, which can act independently on each segment causing large variations in the copy numbers of viral genes. These differences can span several orders of magnitude and render many cells low-productive. In addition, the random degradation of vRNAs in the beginning of infection can lead to the loss of genome segments when cells are infected by only a few

virions. Since an incomplete genome set prevents the release of infectious virus progeny, stochastic effects can, thus, result in a large number of nonproductive cells, which has also been found in experiments. Moreover, this observation provides evidence for the hypothesis that multiple virions are needed to enter the same cell in order to ensure productive infection. Taken together, noise in viral RNA synthesis may, hence, drive cell-to-cell variability during infection.

In order to identify the steps of viral replication that are most susceptible to antiviral drugs, we also developed a multiscale model of infection. It links the intracellular life cycle of the virus to its spread between different host cells. This integrative modeling approach captures a wide variety of experimental data across both levels including the time course of viral RNAs inside infected cells and the infection dynamics in a cell population. It also reveals that inhibitors of viral transcription, replication, and protein synthesis are very effective in blocking virus production because they interrupt the autocatalytic mechanism of viral RNA synthesis. Moreover, interference with nuclear export and assembly/release can readily reduce virus titers. By contrast, targeting the steps of virus entry primarily delays virus spreading but does not protect host cells from infection *in vitro* unless the drug is highly effective. Multiscale modeling, hence, provides a systems-level understanding of viral infection and therapy, and represents an ideal platform to include further levels of complexity such as the immune system and the mechanisms of viral pathogenicity.

The last part of this work discusses defective interfering (DI) viruses, which can compromise virus production at the intracellular level and in a cell population. With respect to intracellular replication, simulations suggest that DI RNAs rapidly outgrow the wild-type segments assuming that they have an advantage in replication due to their length. Moreover, the excessive production of subgenomic RNAs sequesters large amounts of viral polymerases and NP proteins that are no longer available for full-length RNA synthesis. Competition for these encapsidation factors may, hence, represent one mechanism of DI RNA–induced interference. Our simulations also indicate that the production of defective interfering particles (DIPs) heavily depends on the extend of their DI RNA's replication advantage, the initial amount of infecting virions, and the coinfection timing. Modeling may, therefore, contribute to the design of production processes for defective viruses with therapeutic potential. At the cell population level, we developed a simple mathematical model which describes the continuous production of influenza vaccines. This model shows that DIPs readily accumulate in such a system causing periodic drops in virus titers and an overall low productivity. Unfortunately, these titer oscillations are very robust against attempts to avoid them and stable virus production is only achieved in a process that is completely devoid of DIPs. Defective viruses, thus, represent a major obstacle to the continuous production of influenza A virus.

Overall, the mathematical models presented here provide valuable insights into influenza A virus replication both inside an infected cell and in a cell population. Especially the multiscale description represent a major step forward in viral kinetic modeling as it reveals how intracellular processes drive virus spreading at the tissue scale. It can, therefore, contribute to the fight against influenza by exposing the emergent properties of the viral life cycle.

Kurzfassung

Influenza-A-Viren lösen im Menschen eine akute Infektion der Atemwege aus, die als Virusgrippe bezeichnet wird. Sie verursachen jährliche Epidemien bei denen 5–15% der Weltbevölkerung infiziert werden. Dabei kommt es in drei bis fünf Millionen Fällen zu einem schweren Krankheitsverlauf, der für bis zu 500 000 Patienten mit dem Tod endet. Darüber hinaus können neue Influenzastämme zu Pandemien führen. Die sogenannte „Spanische Grippe“ aus dem Jahr 1918 war ein solcher weltweiter Ausbruch, dem circa 50 Millionen Menschen zum Opfer fielen. Um Pandemien künftig zu verhindern und das Virus wirksam zu bekämpfen, bedarf es eines umfassenden Verständnisses des viralen Lebenszyklus.

Das Ziel dieser Doktorarbeit war die Entwicklung mathematischer Modelle, die eine quantitative Beschreibung der Vermehrung von Influenza-A-Viren erlauben. Dabei sollte sowohl die Replikation des Virus innerhalb einer einzelnen Zelle als auch dessen Ausbreitung in einer Zellpopulation betrachtet werden. Insbesondere stand die Identifizierung von Faktoren, welche die Produktion von Viruspartikeln auf diesen beiden Ebenen begrenzen, im Fokus. Solche Faktoren sind nicht nur für die Optimierung der Impfstoffproduktion von Bedeutung, sondern stellen auch vielversprechende Angriffspunkte für die Entwicklung neuer antiviraler Medikamente dar.

Der erste Teil dieser Arbeit umfasst die Herleitung und Analyse eines Modells für die intrazellulären Vorgänge der Virusvermehrung. Dabei wurden alle wichtigen Schritte vom Eintritt des Virus in die Zelle bis zur Freisetzung von Tochterviren berücksichtigt. Das entstandene Modell zeigt, dass zwei Regulationsmechanismen benötigt werden, um den zeitlichen Verlauf der viralen RNA-Spezies korrekt wiedergeben zu können. Es handelt sich hierbei zum Einen um die Stabilisierung von Replikationsintermediaten (cRNA) durch virale Polymerasen und Nukleoproteine (NP), welche das Umschalten von viraler Transkription zur Genomreplikation steuern und zum Anderen um das Abschalten der Synthese positiv-strängiger RNAs durch das Matrixprotein (M1), wodurch der Export von viralen Genomkopien aus dem Zellkern ermöglicht wird. Die Simulationen offenbaren darüber hinaus eine starke Abhängigkeit der Virusproduktion von der Rate der viralen RNA-Synthese, dem Zeitpunkt des nukleären Exports und der Geschwindigkeit des Zusammenbaus und der Ausschleusung von Tochterviren. Somit kann das Modell wertvolle Einblicke in den Verlauf der intrazellulären Virusreplikation liefern, die durch Experimente allein nur schwer zu erlangen wären.

Im nächsten Schritt wurde das erstellte Modell genutzt, um den Einfluss von stochastischem Rauschen auf die intrazelluläre Replikation des Virus zu untersuchen. Dabei zeigte sich, dass Influenza-A-Viren aufgrund ihres segmentierten Erbguts besonders anfällig gegenüber zufälligen Fluktuationen sind. Insbesondere kann die Synthese viraler RNAs Schwankungen verstärken und diese Schwankungen können unabhängig auf jedes Genomsegment wirken. Dadurch kommt es zu großen Unterschieden in der Kopienzahl der einzelnen viralen Gene. Diese Unterschiede können mehrere Zehnerpotenzen betragen und dazu führen, dass ein Großteil der infizierten Zellen nur wenige Viren freisetzt. Zusätzlich können aufgrund von stochastischen Phänomenen einzelne virale RNAs abgebaut werden, bevor sie vervielfältigt wurden. Geschieht dies in der frühen Phase der Infektion in einer Zelle, die nur von wenigen Viren infiziert wurde, kann es zum unwiederbringlichen Verlust eines Genomsegments kommen. Als Folge ist die betreffende Zelle außerstande, infektiöse Tochterviren zu produzieren. Diese Modellvorhersage steht im Einklang mit Experimenten, in denen die meisten infizierten Zellen unproduktiv erscheinen. Sie legt ebenfalls nahe, dass mehrere Viruspartikel eine einzelne Zelle infizieren müssen, um eine produktive Infektion sicherzustellen. Zusammengenommen deuten die gewonnenen Erkenntnisse darauf hin, dass stochastische Fluktuationen während der viralen RNA-Replikation zu starken Unterschieden zwischen einzelnen infizierten Zellen führen können und Schwankungen innerhalb dieser Zellen die Virusproduktion kompromittieren.

Mit dem Ziel, Angriffspunkte für neue antivirale Medikamente zu identifizieren, wurde im zweiten Teil der Arbeit ein Multiskalen-Modell der Infektion entwickelt. Dieses Modell verbindet die intrazellulären Vorgänge der viralen Replikation mit der Ausbreitung des Virus in einer Population von Wirtszellen. Durch diesen integrativen Ansatz gelang es, verschiedene experimentelle Daten auf beiden Ebenen zu reproduzieren. So kann das Modell zum Beispiel die Anzahl der viralen RNA-Spezies innerhalb einer Zelle nachbilden und gleichzeitig die Infektionsdynamik des Virus in einer Zellpopulation wiedergeben. Darüber hinaus zeigt es, dass Inhibitoren der viralen Transkription, Replikation und Proteinsynthese die Produktion von Tochterviren effektiv unterbinden können. Dieser Effekt lässt sich vor allem auf eine Unterbrechung des autokatalytischen Mechanismus der viralen RNA-Synthese zurückführen. Auch eine Blockade des nukleären Exports von viralen Genomkopien sowie des Zusammenbaus und der Ausschleusung von Tochterviren kann den Virustiter verringern. Im Gegensatz hierzu führen Medikamente, welche die frühen Schritte des viralen Lebenszyklus stören, meist nur zu einer Verzögerung der Infektion, da sie die Virusproduktion durch eine Zelle nicht entscheidend stören. Das entwickelte Multiskalen-Modell vermittelt somit ein systematisches Verständnis der Replikation von Influenza-A-Viren und es offenbart vielversprechende Ansätze zu deren Bekämpfung.

Im letzten Teil der Arbeit wurde der Einfluss von defekten Viruspartikeln (DIPs) auf die intrazelluläre Replikation des Virus und dessen Produktion in einer Zellpopulation betrachtet. Dabei legen Simulationen der intrazellulären Ebene nahe, dass defekte RNA-Segmente (DI RNAs), von denen angenommen wird, dass sie aufgrund ihrer reduzierten Länge einen Replikationsvorteil besitzen, schnell ein Vielfaches der Kopienzahl von Wildtyp-RNAs erreichen. Durch diese exzessive Produktion von viralen RNAs wird die Menge an freien viralen Polymerasen und NP-Proteinen drastisch reduziert. Da diese Proteine jedoch auch zur Produktion vollständiger RNAs benötigt werden, behindern DI RNAs auf diesem Wege die Synthese des Wildtyp-Virus. Die Simulationen zeigen außerdem, dass die Produktion von DIPs zum Großteil vom Replikationsvorteil ihrer DI RNA abhängt aber auch Faktoren wie die anfänglich vorhandene Menge an defekten Partikeln und der Zeitpunkt der Koinfektion einer Zelle eine Rolle spielen. Die gezeigten Analysen können somit dabei helfen, Produktionsprozesse für DIPs mit therapeutischem Nutzen zu entwickeln. Auf der Ebene der Zellpopulation wurde außerdem ein Modell für die Beschreibung eines kontinuierlichen Prozesses für die Herstellung von Influenzaimpfstoffen entwickelt. Es zeigt, dass DIPs in einem solchen System schnell akkumulieren können und dabei periodische Schwankungen im Virustiter verursachen. Leider sind diese Produktivitätseinbrüche ungewöhnlich robust gegenüber Strategien zu deren Vermeidung und eine stabile Ausbeute wird laut Modell nur erreicht, wenn der Prozess völlig frei von DIPs betrieben wird. Defekte Viren stellen deshalb ein ernstes Hindernis für die Produktion von Influenza-A-Viren mittels kontinuierlicher Verfahren dar.

Zusammenfassend vermitteln die im Rahmen dieser Arbeit entwickelten Modelle wertvolle Einblicke in die Replikation von Influenza-A-Viren innerhalb einer einzelnen Zelle und in einer Zellpopulation. Insbesondere das Multiskalen-Modell stellt einen entscheidenden Meilenstein dar, da es Vorhersagen über den Einfluss von intrazellulären Faktoren auf die Virusausbreitung in Geweben ermöglicht. Dadurch kann es einen wichtigen Beitrag zur Entwicklung neuer Anti-Influenza-Medikamente und zur Verbesserung der Impfstoffproduktion leisten.

Contents

Abstract iv

Kurzfassung vii

List of Abbreviations xii

List of Symbols xiv

1 Introduction 1

2 Theoretical Background 4
- 2.1 Influenza A virus infection 4
  - 2.1.1 Virus structure and morphology 4
  - 2.1.2 The intracellular viral life cycle 6
  - 2.1.3 Inhibitors of viral replication 13
  - 2.1.4 Defective interfering viruses 15
- 2.2 Influenza vaccine production 18
- 2.3 Mathematical models of viral infection 20
  - 2.3.1 Classification 20
  - 2.3.2 Within-host models of infection 20
  - 2.3.3 Models of intracellular virus replication 24
  - 2.3.4 Multiscale modeling approaches 24
- 2.4 Model construction and analysis 26
  - 2.4.1 Construction of mathematical models 26
  - 2.4.2 Model analysis techniques 27

3 Models and Methods 30
- 3.1 Intracellular virus replication 30
  - 3.1.1 Deterministic model 30
  - 3.1.2 Stochastic model 37
- 3.2 Virus infection across multiple scales 40
- 3.3 Defective interfering viruses 45
  - 3.3.1 Intracellular DI RNA replication 45
  - 3.3.2 DIP growth during continuous virus infection 48

4 Results and Discussion 51
- 4.1 The intracellular life cycle of influenza A virus 51
  - 4.1.1 Dynamics of intracellular virus replication 51
  - 4.1.2 Stochastic fluctuations in viral RNA synthesis 65
  - 4.1.3 Discussion of intracellular kinetics 78

4.2 A multiscale model of influenza A virus infection . . . 90
4.2.1 From single cells to cell populations . . . 90
4.2.2 Interference by direct-acting antivirals . . . 97
4.2.3 Discussion of the multiscale model . . . 102
4.3 Replication of defective interfering viruses . . . 107
4.3.1 Interference with intracellular virus replication . . . 107
4.3.2 Oscillations in continuous influenza A virus production . . . 115
4.3.3 Discussion of defective interfering virus replication . . . 120

5 Conclusion **127**

6 Outlook **131**

List of Figures **134**

List of Tables **137**

List of Publications **139**

Bibliography **141**

Appendix A Intracellular virus replication **163**
A.1 Deterministic model . . . 163
A.2 Stochastic model . . . 168

Appendix B Multiscale model of infection **176**

Appendix C Defective interfering viruses **181**
C.1 Model for a DI RNA of segment 3 . . . 182
C.2 Model for a DI RNA of segment 4 . . . 186

List of Abbreviations

A/PR/8/34	A/Puerto Rico/8/1934
CI	confidence interval
CRM1	chromosome region maintenance 1 protein
cRNA	complementary RNA
DAA	direct-acting antiviral
DDE	delay differential equation
DI	defective interfering
DI RNA	defective interfering RNA
DIP	defective interfering particle
ER	endoplasmic reticulum
FDA	Food and Drug Administration
FISH	fluorescence in situ hybridization
HA	hemagglutinin
HAU	hemagglutination units
HBV	hepatitis B virus
HCV	hepatitis C virus
HIV	human immunodeficiency virus
hpi	hours post infection
M1	matrix protein 1
M2	matrix protein 2
MCM	minichromosome maintenance complex
MDCK	Madin-Darby Canine Kidney
MOI	multiplicity of infection
NA	neuraminidase
NEP	nuclear export protein
NES	nuclear export signal
NIVC	number of infectious viruses per cell
NLS	nuclear localization signal
NP	nucleoprotein
NS2	nonstructural protein 2
NS5A	nonstructural protein 5A of HCV
ODE	ordinary differential equation
ORF	open reading frame

PA	polymerase acidic protein
PB1	polymerase basic protein 1
PB2	polymerase basic protein 2
PFU	plaque forming unit
Pol II	cellular RNA polymerase II
RdRp	RNA-dependent RNA polymerase
RNA	ribonucleic acid
RT-PCR	reverse transcription polymerase chain reaction
RT-qPCR	quantitative reverse transcription polymerase chain reaction
SSA	stochastic simulation algorithm
SSR	sum of squared residuals
STR	stirred tank reactor
STV	standard virus
svRNA	small viral RNA
TCID_{50}	50% tissue culture infective dose
TUNEL	terminal deoxynucleotidyl transferase-mediated dUTP nick end labeling
VLP	virus-like particle
vRNA	viral genomic RNA
vRNP	viral ribonucleoprotein
VSV	vesicular stomatitis virus
WHO	World Health Organization
wt	wild-type

List of Symbols

Symbol	Unit	Description
α	–	significance level
β	$\mathrm{ml}/(\mathrm{virion}\cdot\mathrm{h})$	virus infection rate
δ	h^{-1}	death rate of infected cells
η_{ext}	–	extrinsic noise
η_{int}	–	intrinsic noise
η_{tot}	–	total noise
η_Y	–	coefficient of variation
ϵ	–	error control parameter for τ-leaping
θ	–	parameter vector
μ	h^{-1}	specific growth rate of target cells
μ_{max}	h^{-1}	maximum specific growth rate of target cells
σ_i	–	standard deviation of measurement at time point i
σ_s	–	maximum value of species s
$\sigma_{s,c}$	–	standard deviation of species s at condition c
σ_Y	–	standard deviation of quantity Y
τ	h	infection age
τ_{apo}	h	average lifespan of an infected cell
τ_{eclipse}	h	average length of the eclipse phase
χ^2	–	weighted sum of squared residuals
Ω	ml	system volume
a	cells/virion	infection efficiency
a_j	cells/h	propensity function
B_{hi}	sites or sites/ml	number of free high-affinity binding sites
B_{lo}	sites or sites/ml	number of free low-affinity binding sites
$B_{\mathrm{hi}}^{\mathrm{tot}}$	sites or sites/cell	total number of high-affinity binding sites
$B_{\mathrm{lo}}^{\mathrm{tot}}$	sites or sites/cell	total number of low-affinity binding sites
c_j	h^{-1} or $(\mathrm{virion}\cdot\mathrm{h})^{-1}$	stochastic reaction constants
c_{virus}	virions/ml	concentration of virus particles
Cp	molecules/cell	number of (nuclear) cRNPs
D	h^{-1}	dilution rate of the virus reactor
D_{Rib}	nucleotides	distance between two adjacent ribosomes on an mRNA
D^{cyt}	molecules/cell	defective complex of parental vRNPs in the cytoplasm
$D_{\mathrm{Cplx}}^{\mathrm{cyt}}$	molecules/cell	defective complex of progeny vRNPs in the cytoplasm
D^{En}	virions/cell	number of DIPs in endosomes

Symbol	**Unit**	**Description**
D^{Rel}	virions/cell	number of progeny DIPs
f	–	fraction of DIPs produced by an STV-infected cell
F_{Adv}	–	replication advantage of a DI RNA
F_{Fus}	–	fraction of fusion-competent virions
F_{Inf}	cells/virion	infection efficiency
F_{Spl_7}	–	fraction of M2-encoding mRNAs
F_{Spl_8}	–	fraction of NEP-encoding mRNAs
F_{swt}	–	switching factor
I	cells/ml	concentration of infected cells
I_{a}	cells/ml	concentration of apoptotic infected cells
I_{c}	cells/ml	concentration of coinfected cells
I_{d}	cells/ml	concentration of DIP-infected cells
I_{s}	cells/ml	concentration of STV-infected cells
K_{swt}	molecules/cell	switching constant
$K_{\mathrm{V^{Rel}}}$	virions	influence of protein concentration on virus release
k^{Apo}	h^{-1}	apoptosis rate of infected cells
$k_{\mathrm{I}}^{\mathrm{Apo}}$	h^{-1}	apoptosis rate of infected cells
$k_{\mathrm{T}}^{\mathrm{Apo}}$	h^{-1}	apoptosis rate of uninfected target cells
$k_{\mathrm{c,hi}}^{\mathrm{Att}}$	$\mathrm{ml/(site \cdot h)}$	attachment rate to high-affinity binding sites
$k_{\mathrm{c,lo}}^{\mathrm{Att}}$	$\mathrm{ml/(site \cdot h)}$	attachment rate to low-affinity binding sites
$k_{\mathrm{hi}}^{\mathrm{Att}}$	$\mathrm{(site \cdot h)^{-1}}$	attachment rate to high-affinity binding sites
$k_{\mathrm{lo}}^{\mathrm{Att}}$	$\mathrm{(site \cdot h)^{-1}}$	attachment rate to low-affinity binding sites
$k_{\mathrm{M1}}^{\mathrm{Bind}}$	$\mathrm{(molecule \cdot h)^{-1}}$	binding rate of M1 to nuclear vRNPs
$k_{\mathrm{NP}}^{\mathrm{Bind}}$	$\mathrm{(molecule \cdot h)^{-1}}$	binding rate of NP to RdRp-RNA complexes
$k_{\mathrm{RdRp}}^{\mathrm{Bind}}$	$\mathrm{(molecule \cdot h)^{-1}}$	binding rate of RdRp complexes to vRNA/cRNA
k^{Cplx}	$\mathrm{molecule^{-7} \cdot h^{-1}}$	formation rate of complexes containing eight vRNPs
$k_{\mathrm{En}}^{\mathrm{Deg}}$	h^{-1}	degradation rate of virions in lysosomes
$k_{\mathrm{M}}^{\mathrm{Deg}}$	h^{-1}	degradation rate of mRNAs
$k_{\mathrm{R}}^{\mathrm{Deg}}$	h^{-1}	degradation rate of naked cRNA/vRNA
$k_{\mathrm{Rnp}}^{\mathrm{Deg}}$	h^{-1}	degradation rate of RNPs
$k_{\mathrm{RRdRp}}^{\mathrm{Deg}}$	h^{-1}	degradation rate of RdRp-RNA complexes
$k_{\mathrm{V}}^{\mathrm{Deg}}$	h^{-1}	degradation rate of infectious virions
$k_{\mathrm{hi}}^{\mathrm{Dis}}$	h^{-1}	detachment rate from high-affinity binding sites
$k_{\mathrm{lo}}^{\mathrm{Dis}}$	h^{-1}	detachment rate from low-affinity binding sites
k^{En}	h^{-1}	endocytosis rate
$k_{\mathrm{c,hi}}^{\mathrm{Eq}}$	ml/site	equilibrium constant of high-affinity binding sites
$k_{\mathrm{c,lo}}^{\mathrm{Eq}}$	ml/site	equilibrium constant of low-affinity binding sites
$k_{\mathrm{hi}}^{\mathrm{Eq}}$	site^{-1}	equilibrium constant of high-affinity binding sites
$k_{\mathrm{lo}}^{\mathrm{Eq}}$	site^{-1}	equilibrium constant of low-affinity binding sites
k^{Exp}	$\mathrm{(molecule \cdot h)^{-1}}$	rate of NEP binding and nuclear export
k^{Fus}	h^{-1}	fusion rate

Symbol	Unit	Description
k^{Imp}	h^{-1}	nuclear import rate
k^{In}	$(\mathrm{molecule} \cdot \mathrm{h})^{-1}$	inactivation rate of nuclear vRNPs by svRNAs
k^{Inf}	$\mathrm{ml}/(\mathrm{virion} \cdot \mathrm{h})$	virus infection rate
k^{Lys}	h^{-1}	lysis rate of apoptotic cells
k^{Prod}	$\mathrm{virions}/(\mathrm{cell} \cdot \mathrm{h})$	virus production rate
k^{RdRp}	$\mathrm{molecules}^{-2} \cdot \mathrm{h}^{-1}$	formation rate of polymerase complexes
k^{Rel}	$\mathrm{virions}/(\mathrm{molecule} \cdot \mathrm{h})$	virus release rate
$k^{\mathrm{Rel}}_{\mathrm{max}}$	$\mathrm{virions}/(\mathrm{cell} \cdot \mathrm{h})$	maximum virus release rate
$k^{\mathrm{Res}}_{\mathrm{C}}$	h^{-1}	residual rate of cRNA synthesis
$k^{\mathrm{Syn}}_{\mathrm{C}}$	h^{-1}	cRNA synthesis rate
$k^{\mathrm{Syn}}_{\mathrm{M}}$	nucleotides/h	mRNA synthesis rate
$k^{\mathrm{Syn}}_{\mathrm{P}}$	nucleotides/h	protein synthesis rate
$k^{\mathrm{Syn}}_{\mathrm{S}}$	h^{-1}	synthesis rate of svRNAs
$k^{\mathrm{Syn}}_{\mathrm{V}}$	h^{-1}	vRNA synthesis rate
L_{i}	nucleotides	length of the mRNA of segment i
L^{V}	nucleotides	average length of a vRNA
$L^{\mathrm{V}}_{\mathrm{i}}$	nucleotides	length of the vRNA of segment i
$M(\gamma)$	–	characteristic of the system output γ
MOI	virions/cell	multiplicity of infection
MOI_{DIP}	virions/cell	number of DIPs per cell
MOI_{STV}	virions/cell	number of STVs per cell
n_c	–	critical reaction control parameter for τ-leaping
N_c	–	number of experimental conditions
N_j	molecules/virion	number of proteins of type j in a virus particle
N_s	–	number of measured species
N_t	–	number of measured time points
$N^{\mathrm{Nuc}}_{\mathrm{M1}}$	nucleotides	number of nucleotides bound by on M1 molecule
$N^{\mathrm{Nuc}}_{\mathrm{NEP}}$	nucleotides	number of nucleotides bound by on NEP molecule
$N^{\mathrm{Nuc}}_{\mathrm{NP}}$	nucleotides	number of nucleotides bound by on NP molecule
P_{I}	–	infection probability
P_{j}	molecules/cell	number of proteins of type j
R_j	–	stochastic reaction
R^{C}	molecules/cell	number of naked cRNAs
$R^{\mathrm{C}}_{\mathrm{i}}$	molecules/cell	number of naked cRNAs of segment i
$R^{\mathrm{C}}_{\mathrm{RdRp}}$	molecules/cell	number of RdRp-cRNA complexes
$R^{\mathrm{C}}_{\mathrm{tot}}$	molecules/cell	total number of cRNAs in a cell
r^{Inf}	h^{-1}	infection rate of target cells
r^{Lys}	h^{-1}	lysis rate of apoptotic cells
$R^{\mathrm{M}}_{\mathrm{i}}$	molecules/cell	number of mRNA of segment i
r^{Rel}	$\mathrm{virions}/(\mathrm{cell} \cdot \mathrm{h})$	virus release rate
$r^{\mathrm{Rel}}_{\mathrm{D}}$	$\mathrm{virions}/(\mathrm{cell} \cdot \mathrm{h})$	DIP release rate

Symbol	Unit	Description
$r_{\mathrm{M1}}^{\mathrm{Syn}}$	molecules/(cell · h)	synthesis rate of M1 proteins
$r_{\mathrm{mRNA7}}^{\mathrm{Syn}}$	molecules/(cell · h)	synthesis rate of mRNAs of segment 7
R^{V}	molecules/cell	number of naked vRNAs
$R_{\mathrm{RdRp}}^{\mathrm{V}}$	molecules/cell	number of RdRp-vRNA complexes
$R_{\mathrm{RdRp,i}}^{\mathrm{V}}$	molecules/cell	number of RdRp-vRNA complexes of segment i
$R_{\mathrm{tot}}^{\mathrm{V}}$	molecules/cell	total number of vRNAs in a cell
S_{θ}^{M}	–	sensitivity coefficient
t	h	time
T	cells/ml	concentration of uninfected target cells
T_0	cells/ml	initial target cell concentration
T_{a}	cells/ml	concentration of apoptotic uninfected cells
T_{in}	cells/ml	target cell concentration in the feed
T_{max}	cells/ml	maximum target cell concentration
V	virions/ml	concentration of virus particles
V_{d}	virions/ml	concentration of DIPs
V_{d0}	virions/ml	initial concentration of DIPs
v_{ij}	–	state-change matrix of a stochastic model
V_{s}	virions/ml	concentration of STVs
V_{s0}	virions/ml	initial concentration of STVs
V^{cyt}	molecules/cell	complex of eight parental vRNPs in the cytoplasm
$V_{\mathrm{Cplx}}^{\mathrm{cyt}}$	molecules/cell	complex of eight progeny vRNPs in the cytoplasm
V^{En}	virions/(cell or ml)	number of virions in endosomes
V^{Ex}	virions/cell	number of virions in the extracellular medium
V^{Rel}	virions/cell	number of progeny virions
$V_{\mathrm{tot}}^{\mathrm{Rel}}$	virions/cell	viral burst size
Vp^{cyt}	molecules/cell	number of cytoplasmic vRNPs
$Vp_{\mathrm{i}}^{\mathrm{cyt}}$	molecules/cell	number of cytoplasmic vRNPs of segment i
$Vp_{\mathrm{M1}}^{\mathrm{cyt}}$	molecules/cell	number of cytoplasmic M1-NEP-vRNP complexes
$Vp_{\mathrm{M1,i}}^{\mathrm{cyt}}$	molecules/cell	cytoplasmic M1-NEP-vRNP complexes of segment i
Vp^{nuc}	molecules/cell	number of nuclear vRNPs
$Vp_{\mathrm{i}}^{\mathrm{nuc}}$	molecules/cell	number of nuclear vRNPs of segment i
$Vp_{\mathrm{M1}}^{\mathrm{nuc}}$	molecules/cell	number of nuclear M1-vRNP complexes
$Vp_{\mathrm{M1,i}}^{\mathrm{nuc}}$	molecules/cell	nuclear M1-vRNP complexes of segment i
x	–	realization of the state vector of a stochastic model
X	–	state vector of a stochastic model
x_i	–	measurement value at time point t_i
y	–	vector of experimental observations
Y	–	stochastic variable
$y_{s,c}$	–	model output of species s at condition c
$y_{s,c}^{D}$	–	measurement of species s at condition c
Z	–	stochastic variable

Chapter 1

Introduction

Almost a century after the devastating influenza pandemic of 1918, which is considered one of the most dramatic events in medical history [1] with an estimated 50 million victims worldwide [2], influenza viruses continue to pose a serious hazard to human health [3]. According to the World Health Organization (WHO), the virus infects 5–15% of the world's population in its anual epidemics causing 3 to 5 million cases of severe illness and 250 000 to 500 000 deaths each year [4]. In addition, human influenza viruses can rapidly evolve and reassort with strains from other host organisms such that emerging virus variants have the ongoing potential of starting the next deadly pandemic.

Influenza viruses are obligate intracellular parasites that infect a broad spectrum of host species including poultry, pigs, horses, dogs, sea mammals, and humans [5]. Yet, their main reservoir are wild aquatic birds from which they can spread easily to other species. In humans, influenza viruses primarily infect the epithelial cells of the upper respiratory tract causing a highly contagious disease characterized by high fever, dry cough, myalgia, headache, sore throat, and rhinitis. Transmission occurs mainly via virus-containing droplets that are expelled during coughs and sneezes, and through contaminated surfaces. In healthy individuals infection with seasonal strains is usually mild and self-limiting with most patients recovering within one to two weeks. But increased morbidity and mortality can occur in risk groups like the young, elderly, and those with certain medical conditions or a compromised immune system.

Every year, influenza viruses cause localized disease outbreaks. In temperate climates, these seasonal epidemics typically occur during the winter months. They are caused by a variety of influenza virus species and strains, which can change from season to season with some strains dying out, while others are spreading rapidly. When seasonal influenza viruses are antigenically similar to strains from previous years, pre-acquired immunity in human hosts can reduce the severity of infection. By contrast, a pandemic outbreak originates from a new virus variant for which the human population is immunologically naïve leading to an uncontrolled worldwide spread and more severe illness. Historical data indicate that influenza pandemics occur regularly at least once every 50–60 years [1] with three major outbreaks in the last century alone claiming tens of millions of lives [6]. In

2009, the first pandemic of the 21th century occurred. It resulted in more than 22 million reported cases, the closing of schools, and the blocking of borders [7]. Recent estimates put the number of victims between 123 000 and 203 000 worldwide [8].

Because of the high burden of influenza on public health and economy major resources have been directed toward the development of treatment strategies in humans. These efforts have resulted in two classes of antiviral drugs that are currently approved in many countries [9]. However, viral resistance to these compounds occurs frequently making vaccination the most effective method for mitigating the impact of influenza and for preventing an infection. Since the virus strains in circulation change over time, the vaccine's composition is adapted annually requiring repeated vaccination to guarantee an optimal protection. This and the rapidly evolving virus calls for flexible and efficient vaccine production processes to facilitate a fast response to new strains and to accommodate large increases in the demand for vaccines during a pandemic.

The key to a successful fight against seasonal and pandemic influenza is a deep understanding of the viral life cycle. For instance, finding new targets for antiviral drugs requires information on how the virus replicates in its host cells and how it spreads throughout infected individuals. Moreover, studying the immune response to infection and the growth properties of virus strains can drive the development of better vaccines and more efficient processes for their production thereby helping to provide protection to more people. However, the inherent complexity of viral infection and of virus-host interactions represents a major obstacle to achieving these aims.

With the advent of computational biology it became possible to model and simulate complex cellular systems in order to understand their function. Such modeling approaches hold the promise of moving biology from a phenomenological to a predictive science through revealing the conserved design principles of biological processes [10]. In virology, mathematical models have contributed tremendously to our understanding of infection and the immune response over the past decades [11]. Theoretical studies of influenza have, for instance, been used to inform public health decisions by describing the transmission of the virus between infected hosts and its global spread [12, 13]. In addition, many researchers have investigated influenza virus infection within infected humans and animals or in cell culture [14, 15]. Also, viral replication inside a host cell has been the subject of theoretical studies [16, 17]. While today's models mostly focus on examining host-pathogen interactions on each of these levels in isolation, multiscale approaches may allow us to describe virus growth across different levels uncovering the emergent properties of infection that only appear when the system is considered as a whole [18].

This work aims to develop such a multiscale model in order to describe the intracellular life cycle of influenza A viruses and their growth at the cell population scale, with a particular emphasis on cell culture systems for vaccine manufacturing. With the help of this model, we seek to identify bottlenecks for virus production, i.e., mechanisms that limit the amount of virus particles an infected cell or a cell population releases. Alleviating such bottlenecks may increase the efficiency of vaccine production and reduce costs, while targeting them with specific inhibitors represents a promising approach for antiviral therapy. Including the different scales of the viral life cycle in a single coherent model is essential to finding these bottlenecks because it allows us to study which intracellular processes are most susceptible to interference and how such perturbations influence virus titers in cell culture and within a host. Therefore, three milestones were defined in this work: (i) the development of a model for intracellular viral replication, (ii) the integration of the intracellular model into a multiscale description of infection, and (iii) the *in silico* analysis of defective interfering particles (DIPs), which can compromise virus production at the intracellular and cell population level.

In the following, we first outline the basic characteristics of influenza A viruses and of their life cycle, discuss different strategies to produce vaccines, and give a short introduction to mathematical modeling (Chapter 2). We then present our models starting with a description of intracellular virus replication followed by the multiscale model of infection and an analysis of the replication of defective interfering viruses (Chapter 3). Chapter 4 covers the results of our modeling efforts beginning with the intracellular level and gradually moving toward a multiscale description. The chapter finishes with two models of DIP growth. Finally, a general conclusion of the work is given in Chapter 5 and an outlook in Chapter 6.

Chapter 2

Theoretical Background

The first section of this chapter provides an overview of influenza virus infection focusing in particular on the molecular mechanisms of viral replication. Subsequently, influenza vaccine production in mammalian cell culture and mathematical modeling approaches to the description of infectious disease are introduced. The last section outlines important theoretical aspects of model construction and analysis.

2.1. Influenza A virus infection

Influenza viruses are obligate intracellular parasites that hijack a cell's biosynthetic machinery to reproduce. They belong to the family of *Orthomyxoviridae* and comprise three different genera: the *Influenzaviruses* A, B, and C (reviewed in [19]). Among these types, only the A and B variants cause annual epidemics in humans. In the rest of this work, we solely focus on influenza A viruses because they are responsible for all pandemic outbreaks recorded thus far.

2.1.1. Virus structure and morphology

Like other members of the *Orthomyxoviridae*, influenza A viruses possess a segmented genome that comprises single-stranded RNA of negative polarity meaning that it is complementary to mRNA and cannot directly serve as a template for protein translation [19]. To distinguish different human influenza viruses, their strains are named according to the genus, location of isolation, number of the isolate, year of isolation, and subtype of the surface proteins hemagglutinin (HA) and neuraminidase (NA). The common laboratory strain A/PR/8/34 (H1N1), for instance, was the isolate number 8 in the year 1934 in Puerto Rico and harbors the surface proteins of subtype one.

Virion structure Influenza A viruses are pleomorphic [20]. Their spherical particles have a diameter of 80–120 nm, while the filamentous elongated form can reach more than 1 µm [21]. The virus particle or virion possesses a lipid envelope (Figure 2.1A), which is

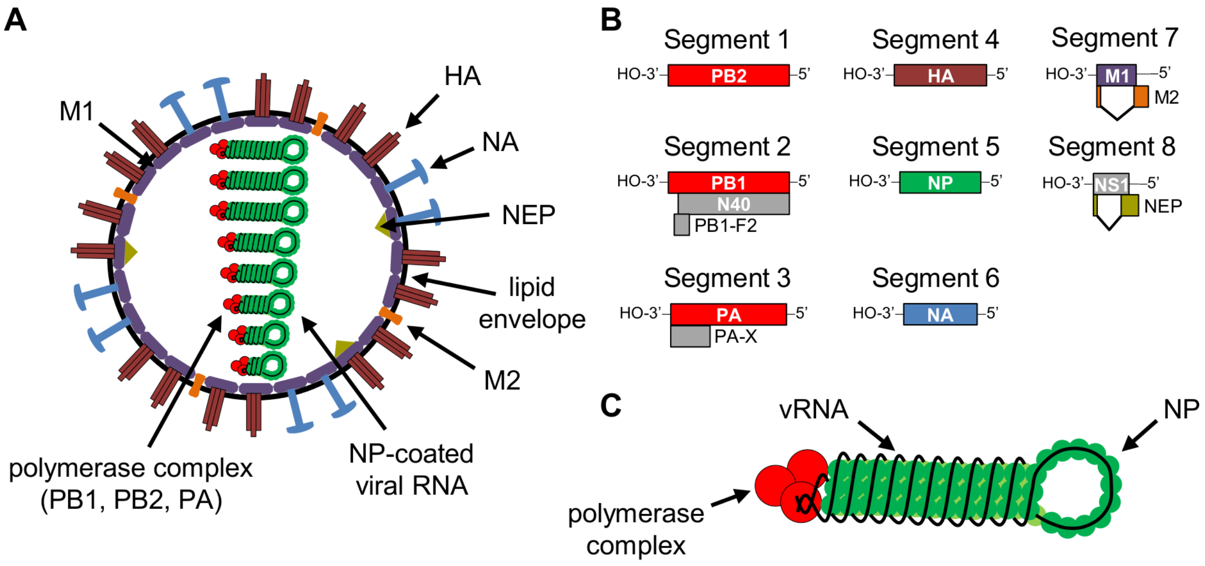
A
M1
HA
NA
NEP
lipid envelope
M2
polymerase complex (PB1, PB2, PA)
NP-coated viral RNA
B
Segment 1
HO-3'
PB2
5'
Segment 4
HA
Segment 7
M1
M2
Segment 2
PB1
N40
PB1-F2
Segment 5
NP
Segment 8
NS1
NEP
Segment 3
PA
PA-X
Segment 6
NA
C
vRNA
NP
polymerase complex

Figure 2.1.: Virus particle and genome structure. (A) Schematic diagram of a spherical influenza A virus particle. The viral proteins are: PB, polymerase basic protein; PA, polymerase acidic protein; HA, hemagglutinin; NP, nucleoprotein; NA, neuraminidase; M, matrix protein; and NEP, nuclear export protein. (B) Genome segments of the influenza A/PR/8/34 strain. Boxes represent the encoded proteins and lines at the termini symbolize the non-coding regions. Introns of the spliced mRNAs of segments 7 and 8 are indicated by V-shapes. NS 1, nonstructural protein 1. Figure adapted from [19]. (C) Scheme of an influenza viral ribonucleoprotein (vRNP).

derived from the host cell membrane, and contains three viral surface proteins: HA, NA, and matrix protein 2 (M2). Underneath the lipid membrane matrix protein 1 (M1) forms a layer, which separates the virus core from the envelope. The inside of the particle contains the nuclear export protein (NEP, previously known as the nonstructural protein 2, NS2) and eight genome segments. The genomic RNA of influenza A viruses (vRNA) does not exist as naked RNA but forms viral ribonucleoproteins (vRNPs) with the RNA-dependent RNA polymerase (RdRp) and the nucleoprotein (NP). The RdRp itself is a complex comprising the polymerase basic proteins 1 and 2 (PB1 and PB2) and the polymerase acidic protein (PA). While each vRNP contains only one copy of the RdRp, its vRNA is encapsidated by multiple copies of NP [22, 23]. Note that inside the virus particle vRNPs also interact with M1 proteins. In addition, virions contain a variety of host factors, which might be incorporated non-specifically during particle assembly or have a certain function in the viral life cycle [24].

Genome organization The genome of influenza A viruses comprises approximately 13 kb with the length of individual genome segments ranging between 890 and 2341 nucleotides (for A/PR/8/34 strain, [25]). Each of the eight segments encodes for at least one viral protein (Figure 2.1B). Segments 1 to 3 provide the three polymerase subunits, which, together with the NP protein encoded by segment 5, comprise the minimal subset of viral proteins required for genome replication [26]. The two genes for the glycoproteins HA and NA are located on segment 4 and 6, respectively, while M1 and NS1 are encoded by the two smallest genome segments 7 and 8. To increase the coding capacity of their genome, influenza viruses use alternative splicing, which facilitates the synthesis of M2 and NEP (reviewed in [27]). Furthermore, alternative open reading frames in segment 2 and ribosomal frameshifting in segment 3 give rise to additional proteins. Overall, 17 influenza A virus polypetides have been found so far and an 18^{th} was predicted to exist [27]. Some of these peptides are, however, only expressed by certain virus strains or under laboratory conditions suggesting that they are not essential for virus replication.

The genomic RNAs of influenza A viruses exist as vRNPs (Figure 2.1C), whose structure has been extensively studied in the last decades (reviewed in [28, 29]). Early works which used electron microscopy showed that vRNPs are rod-shaped with a width of 10 nm and a length between 30 and 120 nm dependent on the length of the RNA segment [22]. They adopt a double-helical arrangement with the polymerase complex at one end and a short loop of the NP-coated RNA strand folding back on itself at the other [23, 30]. The viral polymerase in a vRNP is bound to both the 5' and 3' termini of the RNA [31], which are highly conserved among influenza A viruses [32]. Inside a virus particle, the eight genome segments assume a "7+1" configuration with seven vRNPs forming a ring around a central, core segment [33]. Recent evidence suggests that this structure is built by RNA-RNA interactions of packaging signals near the polymerase end of the vRNPs [34].

2.1.2. The intracellular viral life cycle

Influenza A viruses preferentially infect epithelial cells of the respiratory tract, alveolar macrophages, and dendritic cells. Unusual for an RNA virus, they replicate inside the nucleus of their host cells and, thus, need to shuttle between different cellular compartments. Figure 2.2 provides on overview of the intracellular viral life cycle, which is discussed below.

Virus entry In order to initiate infection, influenza A viruses bind to neuraminic acids (sialic acids) on the apical surface of polarized cells via their HA protein (reviewed in [35]). Subsequently, they enter the cell by receptor-mediated endocytosis [36] using three routes of internalization: (i) via clathrin-coated pits, (ii) through non-clathrin, non-caveolae pathways, and (iii) by a dynamin-independent pathway that is characteristic of macropinocytosis [19]. Once inside the cell, the virus is trafficked through the endosomal network until the acidification in late endosomes triggers structural changes in the HA protein (reviewed in [19, 35]). These changes allow the virus envelope to fuse with the endosomal membrane. Endosomal acidification also triggers viral uncoating, i.e., the release

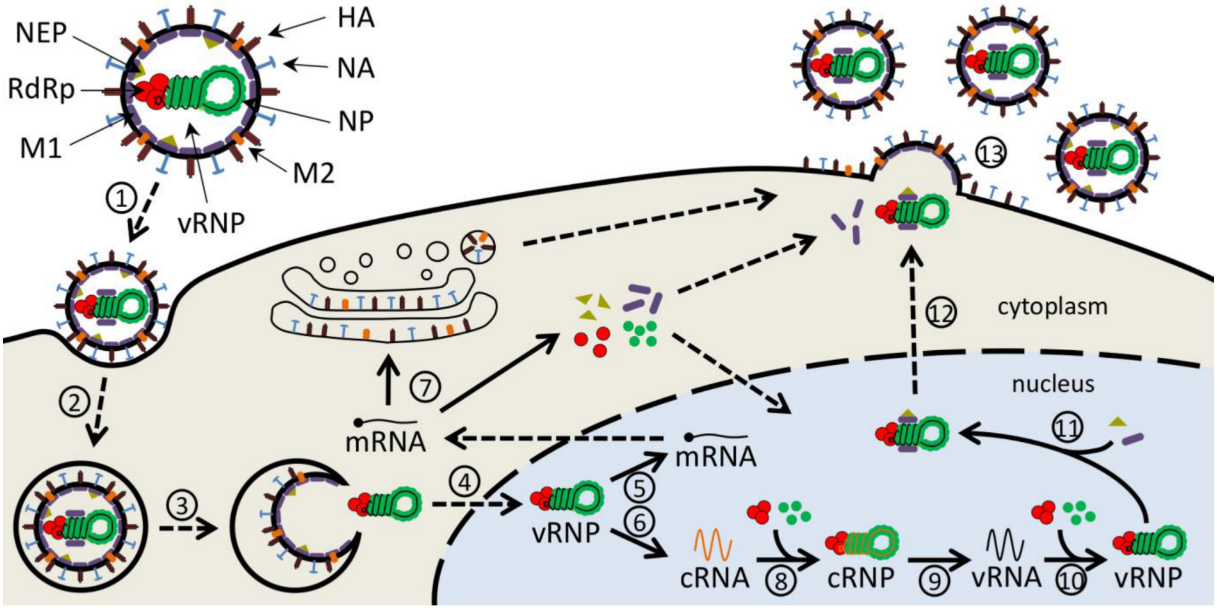

Copyright © American Society for Microbiology, [Journal of Virology, 86, 2012, 7806-7817, 10.1128/JVI.00080-12]

Figure 2.2.: Scheme of the influenza A virus life cycle. For the sake of simplicity, only one of the eight vRNPs is depicted and non-structural proteins were omitted. Solid arrows represent synthesis or protein binding, while dashed arrows indicate transport processes. Different steps are assigned by numbers (see text for details): 1, attachment; 2, endocytosis; 3, fusion in late endosomes; 4, nuclear import; 5, transcription; 6, replication (cRNA synthesis); 7, protein translation; 8, cRNA encapsidation; 9, replication (vRNA synthesis); 10, vRNA encapsidation; 11, M1 and NEP binding; 12, nuclear export; 13, virus assembly and budding.

of vRNPs from M1 proteins due to the action of protons that enter the virus interior via the M2 ion channel. As a result, parental vRNPs that are free of M1 enter the host cell's cytoplasm.

Nuclear import of vRNPs The synthesis of influenza virus RNAs and their processing depends on nuclear functions, which is why incoming vRNPs travel to the host cell's nucleus. Recent experimental evidence suggests that the eight genome segments colocalize during their cytoplasmic transport and only separate once they reach the karyoplasm [37]. The vRNP complexes are considered too large for passive diffusion across the nuclear membrane and, hence, rely on active, energy-driven transport mechanisms mediated by nuclear transport receptors, the karyopherins (reviewed in [38–41]). The interaction with these receptors requires a nuclear localization signal (NLS), which has been identified in all vRNP-associated viral proteins [40]. Yet, only the NLS in NP is both necessary and sufficient for the nuclear import of the viral genome [42, 43]. M1 proteins can mask this NLS and pre-expressed M1 has been shown to prevent the import of parental vRNPs suggesting that M1 is a crucial regulator of viral cytoplasmic-nuclear trafficking [44]. This is supported by the observation that newly assembled vRNPs, which associate with

M1 proteins in the nucleus, travel to the cytoplasm and cannot shuttle back [45, 46]. Furthermore, a mildly acidic pH that disrupts M1 binding restores the ability of these vRNPs to re-enter the nucleus [44]. Hence, the dissociation of M1 during uncoating allows the parental vRNPs to enter the nucleus, whereas association of progeny vRNPs with newly produced M1 controls their nuclear export (which is discussed later) and prevents the re-import [45, 47].

Viral mRNA synthesis After their import, parental vRNPs spread throughout the nucleus and operate as independent functional units [37, 48]. As such they, first, transcribe viral mRNA via a primer-dependent mechanism (reviewed in [31, 49]) during which the viral RdRp acts in *cis*, using the vRNA of its own vRNP as a template [50]. The primer is obtained through a process known as cap-snatching, whereby the viral polymerase binds to the cellular RNA polymerase II (Pol II, [51]) and cleaves the 5' cap-structure as well as 10–13 additional nucleotides from host cell pre-mRNAs [31]. During the elongation of the transcript, the RdRp remains associated to the 5' terminus of the vRNA while the template is threaded through in a 3'→5' direction resulting in steric hindrance at the 5' end. This causes the polymerase to slip and stutter over a stretch of five to seven uridine residues [52, 53]. As a result, viral mRNAs are polyadenylated but also terminate prematurely. Hence, the mRNAs of influenza A virus mimic cellular mRNA by having a 5' cap and a 3' poly(A) tail. However, they represent an incomplete copy of the viral genome.

Viral protein translation While transcription is a nuclear process, protein translation occurs at cytoplasmic ribosomes. Thus, viral mRNAs take advantage of the cellular mRNA trafficking machinery and shuttle out of the nucleus (reviewed in [54]). Once in the cytoplasm, they interact with cellular translation initiation factors and begin to synthesize viral proteins. At this stage, viral mRNAs have to compete with transcripts of cellular origin for resources and, hence, have evolved several mechanisms to gain preferential access to the translation machinery (reviewed in [55]). After their synthesis, the newly produced viral proteins can either enter the nucleus where they participate in vRNP assembly and other processes [39, 40], or they travel to the plasma membrane to form progeny virions [56]. For the surface proteins (HA, NA, and M2) the latter step is preceded by processing in the endoplasmic reticulum (ER) and the Golgi apparatus.

Transition from transcription to replication Genome replication requires a full-length copy of the vRNA, which prevents viral mRNAs to serve as its template. Therefore, vRNPs give rise to a second species of positive-strand RNA, the complementary

RNA (cRNA). In contrast to mRNA, cRNA is generated by a primer-independent mechanism and neither receives a 5' cap nor a 3' poly(A) tail. Yet, both RNA species are produced by vRNPs. Hence, there have to be mechanisms in place to coordinate the two different initiation and termination strategies. How exactly this is achieved has been a matter of controversial debate in the last decades (reviewed in [19, 31, 57]).

Early studies indicate that cRNA production requires an initial round of viral protein synthesis [58], which lead to the proposal that soluble NP (i.e. NP not associated to vRNPs) mediates a switch in vRNP activity from early transcription toward late replication [59] (Figure 2.3A). This switching hypothesis is supported by experiments in which the synthesis of full-length cRNA (antitermination) depends on NP [61, 62] and by temperature-sensitive NP mutants showing impaired cRNA production but normal mRNA accumulation at the non-permissive temperature [63, 64]. Yet, in another study, overexpression of NP did not promote replication [65]. More recently, Vreede *et al.* proposed a different mechanism suggesting that the binding of viral polymerases and NP proteins protects nascent cRNA from degradation by cellular nucleases [60]. In this scenario, vRNPs synthesize both positive-strand RNAs early on. However, cRNA does not accumulate unless it is encapsidated (Figure 2.3B). This is in agreement with *in vitro* experiments showing cRNA synthesis in the absence of free NP [66]. In addition to the switching and stabilization hypotheses there have been reports that NP and the cellular minichromosome maintenance complex (MCM) interact with the viral polymerase to facilitate promoter clearance thereby stimulating replication [67, 68]; that NEP exerts regulatory control over viral RNA synthesis [69–72]; and that small viral RNAs (svRNAs, 22–27 nucleotide long RNAs that correspond to the 5' end of each vRNA) can enhance

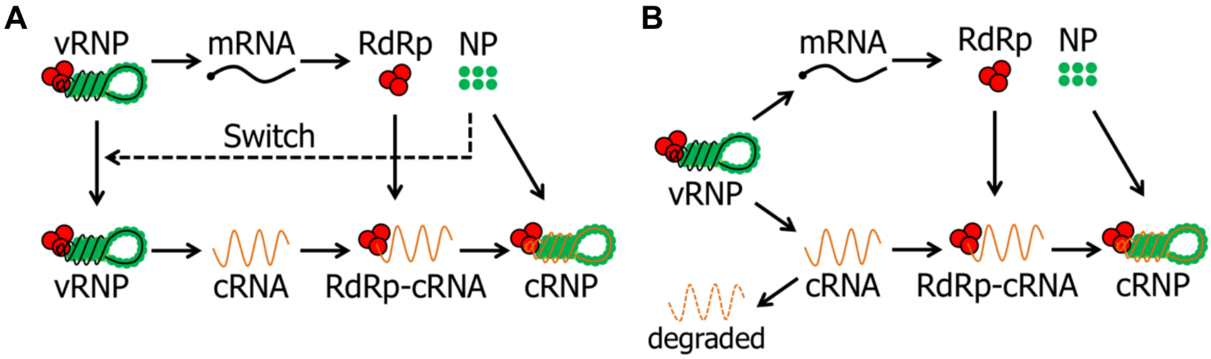

Figure 2.3.: Scheme of different hypotheses on the transition from transcription to replication. (A) Switching hypothesis suggesting that polymerases in vRNPs act as transcriptases early in infection. Accumulation of NP then switches their activity toward replication. (B) Stabilization hypothesis suggesting that vRNPs engage in both transcription and replication (cRNA synthesis) early in infection. However, cRNA is rapidly degraded by cellular nucleases unless viral polymerases and NP proteins stabilize it. Figure adapted from Vreede *et al.* [60].

vRNA synthesis [73, 74].

Another hypothesis that has gained much attention in recent years suggests that the polymerase which catalyzes transcription is physically different from the one that drives replication, i.e., that mRNA synthesis occurs in *cis*, mediated by the resident polymerase in a vRNP, while cRNAs are produced in *trans* by soluble polymerases [23, 50]. Although the latter was (so far) only described for the production of vRNA it might explain how the premature termination of cRNA is avoided. According to this model, the *trans*-acting polymerase would not stay attached to the 5' end of the vRNA template and would, thus, not encounter steric hindrance [31, 57]. However, *de novo* cRNA synthesis from vRNPs has been detected in the absence of soluble polymerases [66, 68] and pre-expression of a catalytically inactive polymerase during an infection in the presence of a protein synthesis inhibitor resulted in cRNA accumulation [60]. This indicates that vRNPs possess at least some replication activity in *cis*. Clearly, more research is needed to fully understand the regulation of viral RNA synthesis.

In the second step of replication newly produced cRNPs synthesize vRNA using a primer-independent mechanism. As mentioned above, this process can be catalyzed by soluble polymerases [50]. The resulting vRNAs are encapsidated by viral polymerases and NP such that progeny vRNPs are formed in the nucleus. Note that apart from the control of mRNA vs. cRNA synthesis there is also *temporal* regulation of viral RNA and protein levels (reviewed in [19, 49]). For instance, NP and NS1 are found early during the viral life cycle, whereas the transcription of HA and especially of M1 occurs later [75].

Nuclear export of vRNPs Following a successful round of replication the newly assembled vRNPs can either participate in mRNA and cRNA synthesis or leave the nucleus to form progeny virions. The latter occurs predominantly via a pathway involving the cellular β-importin CRM1 (chromosome region maintenance 1 protein) and is thought to be mainly directed by M1 and NEP (reviewed in [19, 38, 39, 71]).

Initial evidence for the role of M1 came from the observation that NP fluorescence, a marker for vRNP localization, is confined to the nucleus of infected cells which lack M1 expression or were treated with antibodies that retained M1 in the cytoplasm [45]. This was confirmed by a study showing that vRNP export is blocked in the presence of the protein kinase inhibitor H7, which inhibits M1 production, but can be rescued by stable expression of recombinant M1 [76]. Further support for the importance of M1 comes from a virus that carries a defect which impairs M1 SUMOylation resulting in the accumulation of vRNAs in the nucleus and a decrease in virus production [77]. In line with its function during export, M1 has also been shown to associate with vRNPs by binding to NP [78], and perhaps also to RNA [79], and may even promote vRNP formation [80]. However, interaction with the cellular export machinery requires a nuclear export signal (NES), which has only recently been identified in M1 [81]. Yet, this NES seems to trigger a CRM1-independent pathway and does not explain why vRNP export is impaired in the presence of leptomycin B, a potent inhibitor of the CRM1-mediated export [82].

In order to resolve this discrepancy it was suggested that a second viral or cellular factor may provide the interaction of M1-vRNP complexes with the cellular export machinery. The NEP protein is thought to be this factor as it can bind to both the export receptor CRM1 [83, 84] and the M1 protein [85, 86]. This observation lead to the "daisy chain" model of vRNP export whereby M1 binds to vRNPs and to NEP, while NEP recruits CRM1 (Figure 2.4) [71, 83, 85]. This model was recently challenged by the observation that NEP can associate directly with PB1 and PB2 [87] and that it enhances the binding affinity of M1 and vRNPs, which would otherwise be insufficient to establish detectable levels of M1-vRNP complexes [88]. However, due to experimental limitations the daisy chain model could not be ruled out entirely. Despite this ambiguity, NEP's role in export is further supported by experiments in which the injection of anti-NEP antibodies resulted in the nuclear retention of vRNPs [89]. Interestingly, the NEP-M1 binding interface maps to the NLS in M1 suggesting that the interaction of both proteins may override this import signal in favor of export [85]. NEP may, hence, act as a molecular timer for nuclear trafficking such that a suboptimal splicing of segment 8 ensures a late accumulation of NEP, which prevents the premature export of vRNPs [90]. Yet, nuclear export can occur without detectable levels of NEP [76] and even in its complete absence [80] arguing against such a regulatory function or at least suggesting that NEP is not required in high quantities [59]. Note that besides M1 and NEP, the NP protein may also be involved in nuclear export. It was suggested to contain an NES, can interact with CRM1, and

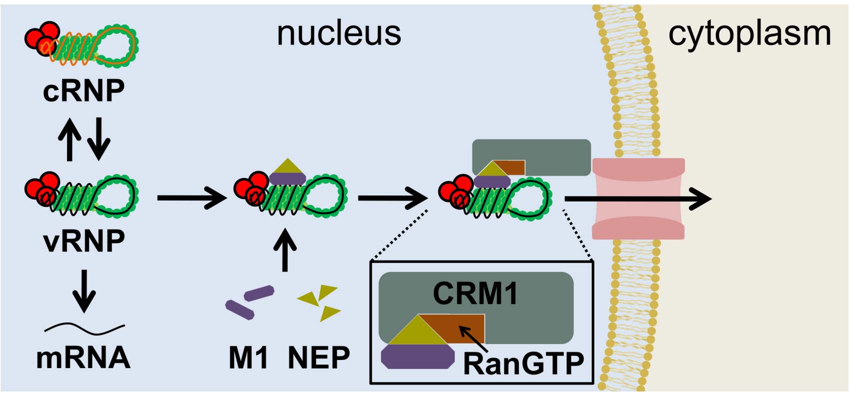

Figure 2.4.: Scheme of nuclear export. The export of vRNPs is mediated by the cellular β-importin CRM1 and its cofactor, the small GTPase Ran. NEP provides the interaction with the cellular export machinery and binds to M1, while M1 recruits the vRNP. Inset depicts magnification.

shuttles out of the nucleus in the absence of other viral proteins [59, 82, 91].

Since vRNPs direct the synthesis of mRNA and cRNA their export may have profound consequences for viral RNA production. In this context, it has been hypothesized that nuclear vRNPs comprises two distinct classes: one that actively engages in transcription and replication and is not destined to leave the nucleus, and a second, inactive class that is to be exported [92]. This would allow the vRNPs to transport across the nuclear membrane in an ordered, condensed form (with a single polymerase bound to the 3' and 5' promoter), which can be found in virus particles. M1 proteins may be the factor responsible for such an inactivation as they were shown to inhibit viral transcription and lead to impaired virus replication upon overexpression [78, 93–97].

Particle assembly and release The last step in intracellular influenza virus replication is the formation and release of progeny virions (reviewed in [56, 92, 98]). Influenza A viruses bud from the apical surface of polarized cells [99] using membrane domains known as lipid rafts, i.e., nonionic detergent-resistant microdomains with a high content of sphingolipids and cholesterol. The viral membrane proteins HA and NA are directed specifically to these domains after they have been processed in the ER and Golgi apparatus, whereas the M2 protein is excluded from lipid rafts and may instead recruit to the raft boundary [100–102]. Transport of the viral genome to the plasma membrane involves Rab11, a marker for recycling endosomes, which colocalizes with vRNPs in the perinuclear region near the microtubule organizing center after their nuclear export [103, 104]. Hence, vRNPs may associate with recycling endosomes and "hitch a ride" to the cell periphery. Furthermore, the virion structure suggests an important role of M1 during particle assembly as it bridges the membrane proteins and the viral core. In this context, M1 has been shown to bind to vRNPs, possess an intrinsic affinity to lipid membranes, and was suggested to interact with the cytoplasmic tails of HA and NA facilitating its association with lipid rafts [100, 105]. M1 may, hence, serve as a key player in the recruitment, concentration, and assembly of viral and cellular components at the budding site [56].

Once the components are present, particle assembly continues with the formation of a bud, which requires an outward curvature of the host cell membrane. This process is likely directed by several viral proteins since HA, NA, and M2 are all capable of forming virus-like particles (VLPs) when expressed alone in cells [19, 98, 106]. After budding has been initiated, the bud extends while the vRNPs are incorporated and the virus core is formed. Finally, the M2 protein completes the process by inducing membrane curvature and scission at the neck of the budding virion [107]. The release of mature particles also requires the enzymatic activity of NA, which removes sialic acids from the cell surface and the viral envelope once the protein is expressed on the cell exterior. In absence of this activity, the binding capacity of HA would retain virions at the plasma membrane and cause virus aggregation.

Genome packaging In order to induce productive infection, a single virion must contain at least one copy of each genome segment. Whether this is achieved by a random incorporation of the eight different vRNPs or by a segment-specific packaging mechanism has been disputed for many years (reviewed in [28, 108]). Combinatorial calculations suggest that in order to be compatible with measurements of infectivity, purely random packaging would require each virion to incorporate at least 10 vRNPs [108–110]. However, in electron microscopical studies most virions were found to package exactly eight vRNPs [33]. Moreover, these genome segments form an ordered "7+1" configuration in which a central, core segment is surrounded by seven other vRNPs [33, 34, 111, 112]. These results and the identification of specific packaging signals in the vRNAs (reviewed in [108]) provide strong evidence for a specific packaging mechanism. Further support for this hypothesis comes from the observation that defective interfering RNAs (DI RNAs), i.e., vRNAs with large internal deletions, compete with their full-length counterparts for packaging into virus particles in a segment-specific manner [113, 114]. In addition, recent experiments reveal RNA-RNA interactions between the influenza virus genome segments, which may facilitate the formation of the "7+1" vRNP complex [34, 111, 115]. Finally, single-molecule FISH analysis demonstrates that the majority of virus particles packages one copy of each vRNA [116]. Hence, it appears that there are mechanisms in place which enable a segment-specific packaging of the complete genome set into each virion.

2.1.3. Inhibitors of viral replication

In recent years, the discovery of new antiviral agents for influenza therapy has received much attention (reviewed in [117]). Generally, the compounds under investigation fall into either of two categories depending on their target: (i) molecules that interfere with host factors which are essential for viral infection and replication [118, 119], including pro- and antiviral signaling cascades [120], and (ii) drugs that target the viral components (i.e., proteins and RNAs) themselves [121]. In the following, we briefly introduce some examples of such inhibitors of virus growth.

Inhibition of virus entry Virus entry into the host cell is considered an excellent target for anti-influenza drugs (reviewed in [122]). M2 ion channel inhibitors like amantadine and rimantadine, for instance, were the first class of compounds approved for influenza treatment. Both these adamantane derivatives prevent the influx of protons into the virus interior and, thus, block uncoating of the viral genome [123]. In addition, amantadine may influence the pH regulation in the trans Golgi compartment, which interferes with the transport of functional HA to the plasma membrane during late infection [124]. However, in the last years almost all circulating virus strains have acquired resistance against M1 inhibitors limiting their effectiveness in clinical practice [125]. Besides targeting viral uncoating, there have been numerous efforts to prevent adsorption of the virus to the cell membrane. This can be achieved by providing decoy receptors that mimic sialic acids, peptides which bind to HA, or neutralizing monoclonal antibodies against the globular head domain of HA [117]. Moreover, the recombinant sialidase DAS181 (Fludase) can prevent influenza A virus binding in cell culture and animals by enzymatically removing sialic acids from host cells [125, 126]. Recently, it has also been tested successfully in a phase II clinical trial [127].

NA inhibitors The second class of drugs currently approved for influenza treatment are neuraminidase inhibitors. NA has two main functions during the viral life cycle. It facilitates virus penetration of mucosal secretions (most likely by removing receptors that would bind the virus [128]) and prevents the aggregation of progeny virus particles during virus release by cleaving sialic acid residues from the host cell and the virions [19, 117]. Currently, two Food and Drug Administration (FDA)-approved NA inhibitors are available (oseltamivir and zanamivir), while additional drugs are licensed in some Asian countries or are under development [117]. As with adamantanes, some circulating virus strains have already acquired resistance to NA inhibitors [129, 130].

Viral polymerase inhibitors Since its function is unique to the virus, the RNA-dependent RNA polymerase represents another promising target for anti-influenza drugs. Favipiravir (T-705), a purine analog, is one of the first compounds directed against the RdRp to reach clinical trials (reviewed in [131]). It blocks the synthesis of viral RNAs, is potent against influenza A, B and C viruses *in vitro*, and protects mice from lethal influenza infection [131–133]. Similarly, inhibitors of the endonuclease activity of PA, which interfere with viral mRNA synthesis, can impair virus replication [121, 134]. A third approach involves the disruption of polymerase assembly from its three subunits (reviewed in [135]). In particular, short peptides which correspond to the PA-binding domain of PB1 were shown to inhibit viral polymerase activity and virus growth [136, 137]. Note that virus production can also be impaired through small molecules that interfere with other viral proteins such as NP and NS1 [117].

Interference with signaling Finally, inhibition or stimulation of host cell signaling cascades can affect virus replication. Potential targets include the Raf/MEK/ERK cascade, NF-κB signaling, the PI3K/Akt/mTOR pathway, and PKC. Compounds that inhibit such essential host cell pathways are able to block influenza virus propagation [120], while the stimulation of antiviral signaling, for instance by poly(I · C), can protect mice from lethal infection [117].

2.1.4. Defective interfering viruses

Influenza virus preparations comprise a heterologous population of virus particles with different biological properties whose composition can change depending on the infection conditions [138, 139]. For instance, during successive passages in embryonated chicken eggs at high multiplicity of infection (MOI), i.e., a high initial number of infectious virions per cell, von Magnus observed a drop in the ratio of infectious to noninfectious virus particles [140]. He attributed this phenomenon, which became known as the von Magnus effect, to the production of "incomplete" viruses. Later Huang and Baltimore coined the term "defective interfering" (DI) particles for these viruses since they need a helper virus, also referred to as the standard virus (STV), to reproduce and because they replicate at the expense of this STV [141]. Defective interfering particles (DIPs) are formed by nearly all viruses (reviewed in [142–145]) and although they were initially thought to only occur under laboratory conditions, DIPs have since been identified in human infections [145, 146].

Structure of DI RNAs DI influenza viruses are deficient in one or more of the essential viral genes due to large internal deletions in their genome segments (Figure 2.5A). The defective segment retains the elements critical for replication and packaging, i.e., the 3' and 5' promoters, the adjacent non-coding regions, and parts of the coding region [108].

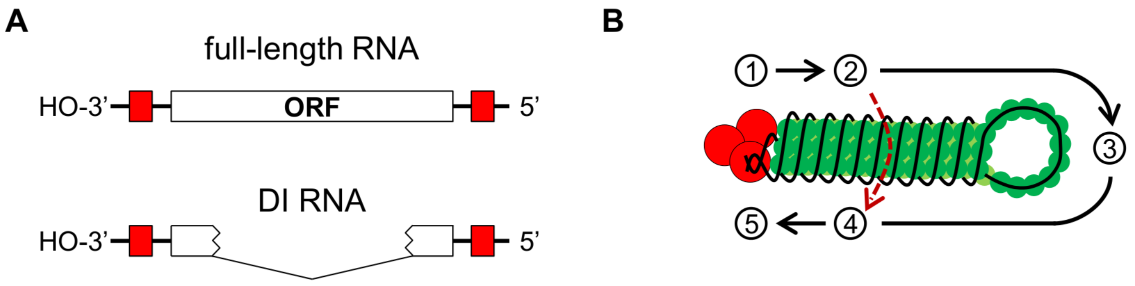

Figure 2.5.: Schematic diagram of the DI RNA structure. (A) Structure of a full-length and DI RNA. In the authentic vRNA the open reading frame (ORF) is flanked by the untranslated regions (lines) which contain the terminal promoter sequences (red boxes). DI RNAs lack the internal region (V-shape). (B) Potential mechanism for DI RNA generation. The viral polymerase reads the template along the path indicated by the numbers. Dissociation and reattachment at number 2 and 4, respectively, deletes the internal sequence (dashed arrow).

Yet, it is significantly shorter and, if at all, only encodes for a truncated form of the protein(s). The deletion can vary in size and DIP preparations usually contain multiple subgenomic RNAs that originate from different genome segments [147, 148]. However, defects in the polymerase genes on segment 1–3 are most common [147, 149]. These polymerase DI RNAs retain on average 100–300 nt of sequence from each end of the vRNA and can, thus, lack more than 80% of their original length [108, 143, 147]. The structure of influenza DI RNAs suggests that they are generated by an erroneous replication event during which the polymerase dissociates from the template and reattaches further downstream (Figure 2.5B and reference [143]). This process may be fostered by the double helical arrangement of vRNPs, which places nucleotide positions that are far apart in sequence space (such as the 3' and 5' ends) in close physical proximity [147].

Mechanism of interference Since DI RNAs contain the promoter elements of their full-length parent they are thought to be recognized by the viral polymerase and replicate in a similar fashion than the infectious genome. However, in order to form progeny virions, the DI virus needs a functional copy of the missing protein(s), which is supplied by the STV upon coinfection of a cell with both virus variants. In these coinfections, the DI RNA acts as a competitive inhibitor of the STV and interferes with its replication. In general, this interference is homotypic meaning that it acts on the parental virus from which the DIP was derived reducing its infectious virus titer [144]. However, the molecular basis of this inhibition is still not well understood (reviewed in [143]).

Northern blot analysis of high MOI infections in the presence of DIPs shows a preferential amplification of the subgenomic RNAs [113, 150] suggesting that interference occurs at the stage of RNA synthesis. In particular, the production of cRNA has been indicated as the source of the replication advantage [151]. The most likely reason for such an advantage is the reduced length of DI RNAs, which may facilitate a faster synthesis by the viral polymerase. More precisely, the polymerase may synthesize a specific, constant number of nucleotides per unit time resulting in a copy number advantage of short RNAs. Alternatively, vRNAs might contain yet unidentified regulatory elements which are impaired or completely absent in DI RNAs [143]. Evidence in favor of a simple length dependency comes from a dual reporter assay for RNA replication [152]. In this system, two luciferase-encoding influenza virus-like RNAs interfered with each other, with shorter reporter constructs showing an increased interference potential. In addition, authentic genome segments also interfered with luciferase expression showing a clear trend of stronger inhibition by short segments [152]. Considering the length dependency and the necessity for the terminal packaging signals, DI RNAs may, thus, have an optimal length where they possess an advantage over their parental segment and are still being incorporated efficiently into newly assembled virus particles. However, RNA length does not seem to be the only determinant of the interference potential since some subgenomic RNAs do not accumulate to high levels in infected cells [113] and most DI RNAs originate from the polymerase segments although smaller segments should be more likely to generate short RNAs [143]. Interference may, hence, involve additional characteristics of the DI RNA.

One mechanism that could contribute to interference is the competition for a limiting viral or cellular factor [144]. For instance, the DI and full-length RNAs of the vesicular stomatitis virus (VSV) have been found to compete for the components of the viral polymerase complex in an *in vitro*, cell-free RNA assay [153]. This has also been observed for influenza virus-like RNAs in a mini-replicon system [152]. Besides the competition for resources, peptides produced directly from the DI RNAs have been suggested to play a role since the defective segments retain both the 5' and 3' ends of the vRNA template and are, thus, able to direct mRNA transcription and translation [150, 154]. Yet, DI RNAs do not seem to maintain a specific reading frame after the deletion and DIP preparations that produce DI-specific polypeptides do not show an increased interference potential [143, 150]. Furthermore, the resulting peptides of influenza DI RNAs are short compared to the authentic proteins suggesting that these truncated forms lose their function. In addition to an advantage during replication, DI RNAs have also been shown to package more efficiently into progeny virions. In particular, it has been observed that during coinfection experiments the ratio of DI to full-length RNAs in virus particles is higher than the level in infected cells [113, 114, 155]. These studies also suggest that, due to interference by DI RNAs, coinfected cells almost exclusively release new DIPs.

In summary, the amplification of DI influenza viruses requires an inoculation with large doses of STVs such that the cells are likely to become coinfected [140]. These coinfected cells will mainly produce new DIPs reducing the infectious virus titer. This limits the replication of DIPs in subsequent undiluted serial passages and the STV may reemerge as the dominant virus species.

Therapeutic use Since DI RNAs efficiently interfere with STV growth they represent an interesting strategy for antiviral therapy (reviewed in [144, 145]). In this context, DIPs of influenza virus have been shown to impair virus growth in cell culture and can protect mice from lethal infection [145, 156, 157]. Furthermore, coinfection with wild-type and DI virus results in an activation of the immune response (including antibody production) despite reduced disease symptoms [157–159]. Therefore, treatment with DIPs would not compromise the protection against a rechallenge with the same virus. DIPs may, hence, serve as a prophylactic and therapeutic antiviral.

2.2. Influenza vaccine production

Despite the availability of antiviral drugs, vaccination is still the most effective way to prevent and control influenza (reviewed in [6, 160, 161]). Today's influenza vaccines largely use a trivalent formulation composed of two influenza A strains and one influenza B strain. They are updated annually to target the most representative virus subtypes in circulation. While new techniques enable the production of recombinant HA for vaccination (e.g. in baculovirus expression systems [6, 160]) most influenza vaccines still rely on inactivated or live-attenuated virus particles, which have to be propagated in a suitable substrate to produce the vaccine. Traditionally, this is done in embryonated hens' eggs. However, in the last decades cell culture-based processes have been established as a promising alternative. Below, we briefly introduce both methods and discuss strategies to monitor the production process.

Egg-based production Human influenza viruses were first isolated and propagated in the 1930s and soon after the first vaccine was available [160, 161]. Early on it was realized that embryonated chicken eggs provide a good substrate for most influenza strains and in the 1960s, when high growth reassortant viruses became available, egg-based influenza vaccines became a routine product. Since then production processes were constantly optimized and in 1978 the first trivalent vaccine formulation was introduced [161]. Today, more than 95% of the world's influenza vaccines are produced in eggs [162]. The advantages of egg-based production are essentially twofold: (i) as the process is established for more than half a century there are less regulatory hurdles to overcome before the product can be released and (ii) vaccine doses can be produced at relatively low costs [162]. However, the logistics of providing embryonated eggs of the required quality is complex and egg-based production alone can hardly supply sufficient quantities of a vaccine on short notice especially in case of a pandemic [162–164].

Cell culture-based production Cell culture-based production processes were developed as an alternative to traditional influenza vaccine manufacturing in the mid 1990s [163]. They distinguish themselves from egg-based systems by their higher flexibility and platform diversity (several cell lines with different growth characteristic are available), the easier scale-up, a closed sterile production chain, and the potential for shorter response times to new vaccine strains [162]. Today, several different cell lines are used or are being evaluated for influenza vaccine production (reviewed in [165]). These include conventional, continuous cell lines such as Vero, Madin-Darby Canine Kidney (MDCK), and PBS-1 cells as well as designer cell lines like PER.C6®, AGE1.CR®, and EB14®/EB66® [165]. Especially the MDCK cell line is widely used by vaccine manufactures and research institutes [162, 165]. MDCK cells are, for instance, the substrate for the first cell culture-derived human influenza vaccine, which was licensed in the Netherlands in 2001.

Typically, vaccine production is a two-stage process comprising cell-growth in large-scale cultivation systems (e.g. stirred tank reactors, STRs) up to high cell density and subsequent virus propagation using high-yield strains [165]. The actual manufacturing process can differ depending on whether it uses adherent or suspension cell lines. In case of adherent cells, the growth surface is either provided by the production vessel or by the addition of microcarriers (small spheres suspended in medium), which enable high cell concentrations and an easier scale-up [166]. Recent advances in cell culture-based influenza vaccine production include high cell density cultivations and virus propagation in designer cell lines using chemically defined media [167–169].

Process analytics In order to guarantee the vaccine's quality and facilitate process optimization various online and offline analytics are used in industry and academia. These include a close control of cultivation conditions, for example, by monitoring temperature, pH, and oxygen levels as well as the concentration of substrates for cell growth [170]. In addition, the production of the virus is usually assayed by standard dilution methods (described in [171, 172]) like the hemagglutination assay, the 50% tissue culture infective dose (TCID_{50}), and the plaque assay. Note that each of these methods quantifies a different subpopulation of virus particles. The HA assay detects all hemagglutinating particles, thus, providing a measure for the total particle count, which includes non-infectious virus [173]. By contrast, the TCID_{50} and plaque assay quantify the replication and propagation-competent viruses, respectively. For clinical samples and in virological studies northern blotting, primer extension analysis, and real-time reverse transcription polymerase chain reaction (RT-PCR) complement these standard tools as sensitive and reliable methods for the quantification of viral RNA [60, 174, 175]. The latter technique can also be adapted to analyze influenza virus replication during vaccine production [148]. Furthermore, Schulze-Horsel *et al.* developed a flow cytometric assay to investigate the dynamics of virus propagation in cell culture in greater detail [176, 177]. In particular, they stained cells for the viral NP and M1 proteins to monitor the infection status and used a TUNEL (terminal deoxynucleotidyl transferase-mediated dUTP nick end labeling) protocol to distinguish apoptotic from non-apoptotic cells. Such methods provide deep insights into infection dynamics, thereby facilitating the development of sophisticated mathematical models [177].

2.3. Mathematical models of viral infection

With the accumulation of ever larger amounts of experimental data in modern biology mathematical models play an increasingly important role for data analysis and interpretation. Modeling also holds the promise of moving biology from a phenomenological to a predictive discipline by revealing the conserved design and engineering principles of biomolecular systems [10]. In virology, mathematical models became popular in the mid 1990s when groundbreaking works on the replication of the human immunodeficiency virus (HIV) helped to develop new forms of antiviral therapy [178]. In this section, we introduce some of these works and discuss how they have established the field of viral dynamics [11] leading to the development of models for influenza virus infection.

2.3.1. Classification

Models of viral infection come in a variety of forms and use a diverse set of mathematical techniques. By far, the most common type are dynamic, deterministic models which comprise differential equations although numerous studies have also incorporated elements of randomness. In the rest of this work, we primarily consider these types of models. However, other theoretical approaches have also been proposed to describe infection. For instance, boolean frameworks in which all species are defined as binary switches that either exist in an active or inactive state can be helpful when quantitative aspects and the system's dynamics are not the main concerns [17]. In addition, cellular automaton models have proven very successful in elucidating spatial features of infection, e.g., the spread of viruses in cell culture or tissues [179–182]. Finally, agent-based models, i.e., models in which discrete entities (e.g. individual cells, molecules, or viruses) interact with each other according to a well-defined set of rules, lend themselves well to the analysis of multicellular, heterogeneous systems such as the immune response and inflammation (reviewed in [183, 184]). Besides these technical aspects infection models can also be classified according to the spatial (and temporal) scale they reflect. This includes models which focus on the simulation of molecular interactions, intracellular virus replication, the within-host kinetics of infection, and between-host virus spread. For vaccine production and antiviral drug therapy the intracellular and within-host level are of particular interest.

2.3.2. Within-host models of infection

Within-host models of infection are typically used to extract crucial infection parameters from (sparse) measurement data obtained in infected animals and humans as well as in cell culture (reviewed in [178, 185]). In addition, these simple models can also reveal causative links between experimental observations and help to compare competing hypotheses on virus replication and the immune system. The standard model of within-host viral dynamics describes the population sizes of susceptible target cells, infected cells, and virus particles (Figure 2.6 and reference [11]). These models and their successors were successfully applied to a variety of different viruses including HIV, hepatitis B and C virus (HBV and HCV), and influenza virus (introduced below).

Models of HIV infection HIV was one of the first viruses for which within-host models were established (reviewed in [186–188]). In a landmark study by Perelson *et al.* such a model was combined with experimental data from infected individuals under antiviral therapy revealing that the virus has a high turnover during infection [189, 190]. This suggested that HIV would rapidly evolve drug resistance during monotherapy. Hence, these early models contributed significantly to the development of modern day combination treatment with multiple drugs of different classes. Subsequently, the theoretical studies of HIV infection were extended to simulate further aspects of the immune system [191–193], virus evolution [187, 194], novel antiviral agents and clinical trials [194, 195], as well as viral reservoirs and virus persistence [186, 196]. Currently, modeling aims at combining these different aspects to describe the entire life cycle of HIV from the initial infection to the onset of AIDS in order to provide even more sophisticated forms of therapy [187].

Models of HBV and HCV infection Soon after the success of HIV modeling, within-host models of HBV and HCV infection were developed (reviewed in [185, 197, 198]). In particular, treatment of HBV with reverse transcriptase inhibitors and of HCV with interferon, ribavirin, and protease inhibitors was subject to theoretical studies [185]. These and other works increased our understanding of hepatitis virus infection and its interaction with the immune system during antiviral therapy. Nowadays, models of HCV

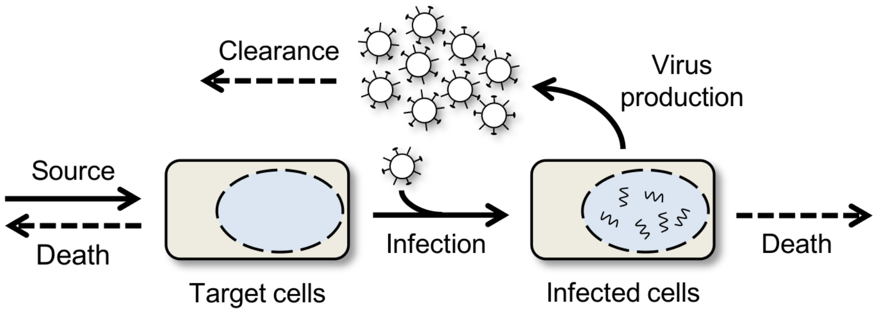

Figure 2.6.: Scheme of the standard model for within-host viral dynamics. Uninfected target cells are constantly supplied, can die, or become infected. Infected cells produce progeny virions and succumb to infection. New virus particles infect target cells or are removed/cleared from the system. Figure adapted from [14].

can also predict suitable dosing regimes for antiviral drugs and the optimal treatment duration thereby supporting decision making in clinical studies [199–201]. In addition, the traditional within-host model for HCV was recently extended by including the intracellular level of virus replication in order to elucidate the effect of direct-acting antivirals (DAAs) [202, 203]. Such works provide the basis for multiscale descriptions of viral dynamics (discussed below) which comprise both the single-cell and the multi-cell level, i.e., the kinetics of intracellular replication and within-host infection.

Models of influenza virus infection In contrast to HIV, HBV, and HCV, influenza viruses cause an acute, self-limiting infection in humans that is usually resolved within 10 days. Within-host models of influenza virus (reviewed in [14, 15]), thus, consider shorter time scales than their counterparts for other viruses, for which treatment can occur over several months or even years. Hence, they largely neglect long-term aspects such as virus evolution and the regeneration and death of target cells [14]. Due to the short duration of infection, mathematical models of influenza virus also frequently account for the eclipse phase, i.e., the delay between the infection of a cell and the release of progeny virions during which the cell amplifies the viral components [204, 205]. Usually, this is done by considering a second, latent type of infected cell. While models that do not account for the eclipse phase can capture viral titer data equally well than their more complex counterparts, the latter are considered to provide more realistic parameter estimates [205, 206].

In analogy to other viruses, early models of influenza virus kinetics focused on disease progression in infected animals and humans [206–208]. Since then, one of the central questions of influenza modeling has been the contribution of the immune system to viral clearance. Surprisingly, it was found that virus titers can be described without taking into account the innate or adaptive immune response by using models in which the availability (and death) of targets cells limits virus production [14]. Yet, destruction of the complete respiratory epithelium upon infection is not apparent *in vivo* [209] and immunocompromised patients shed virus for longer periods [210] indicating an essential role of the immune response. Hence, a rich body of literature on influenza models that incorporate aspects of the immune response like the action of interferon [206, 209, 211], the cytotoxic T-cell response [212–214], and virus-specific antibodies [211, 215, 216] exists. However, in a comparative study that reviewed many of these models, none of them was able to capture all available data making the incorporation of immune system dynamics an active area of research [210].

Another important application of models for influenza virus infection is the simulation of antiviral therapy. Modeling studies have, for instance, investigated the treatment of infection with amantadine [217] and neuraminidase inhibitors [206, 218, 219] and suggested that combination therapy with different drugs may be necessary to prevent the generation of drug-resistant viruses [220]. In addition, the emergence of resistance itself and the associated fitness costs for the virus were subject to theoretical studies [218, 221]. Although these approaches have gained much attention in recent years they are currently not as widely used as models of HIV and HCV treatment.

Besides the simulation of *in vivo* infection, modeling has also been used to describe influenza virus growth in cell culture systems and during vaccine production. Such *in vitro* experiments provide a unique view on virus replication since they take place in a tightly controlled environment, allow for extensive sampling, and can be readily perturbed. An early model of cell culture-based influenza vaccine production was developed by Möhler *et al.* [222] who showed that virus yields in this system strongly depend on the initial target cell concentration, the rate of virus production, and the lifespan of infected cells. Later, Schulze-Horsel *et al.* extended this work by considering the eclipse phase and the onset of virus-induced apoptosis via delay differential equations (DDEs) [177]. This improved model was calibrated against high quality data from flow cytometry, which allowed the authors to monitor the dynamics of infection and apoptosis in cell culture. Schulze-Horsel *et al.* found that typical vaccine strains can differ in the rate of virus production and apoptosis induction affecting their performance as vaccine producers. Flow cytometric data on the infection status of cells were also used by Sidorenko and colleagues who developed a simple stochastic model of influenza virus infection [223, 224]. Here, infected cells could either accumulate or release virus particle equivalents thereby changing the cell's degree of infection, i.e., the intracellular amount of viral proteins. This internal coordinate was compared with cytometric measurements of viral protein content and simulations were shown to reflect most aspects of the fluorescence intensity distribution observed in infected MDCK cells. A similar comparison was proposed in a study by Müller *et al.* where the authors presented a deterministic population balance model and found a transient multimodality in the degree of fluorescence in infected cell cultures [225]. The fact that cell culture experiments can also be relevant to antiviral therapy was demonstrated by Beauchemin and coworkers who estimated the efficacy of amantadine in blocking viral infection using data from a hollow-fiber bioreactor system [217]. Such an approach can be a tremendous asset to drug development as it facilitates the investigation of different dosing regimes and drug effects in a controlled environment without interference by complex features of *in vivo* systems such as the immune response. In addition, cell culture systems can provide the means to easily quantify and compare different influenza virus strains with respect to indicators of viral fitness, pathogenicity, and transmissibility without the ethical concerns associated with infections of animals or human volunteers [182, 226].

2.3.3. Models of intracellular virus replication

Although far less common than their within-host counterparts, intracellular models of viral replication have been proposed for a number of eukaryotic viruses. Typically, these models consider a single round of infection in an individual infected cell and cover the steps from virus attachment to the release of progeny virions. Dee *et al.* developed one of the first models of this type in order to estimate the kinetics of virus entry and RNA synthesis for Semliki Forest virus [227]. Later, the same group established a similar model for the trafficking of Baculovirus in insect cells [228]. This work provides a general mathematical framework for the description of acid-dependent virus entry, which can be applied to other viruses. Intracellular models of virus replication have also been proposed for bacteriophages [229], the vesicular stomatitis virus [230, 231], HIV [232], HBV [233], and HCV [234–237] with the primary aim to understand how these viruses hijack their host cells to produce viral proteins and genomic information and to reveal new drug targets.

For influenza A virus, Sidorenko *et al.* developed a description of the complete intracellular viral life cycle [16]. This model was used to estimate the viral demand for cellular resources like amino acids and nucleotides, and to identify potential targets for the optimization of virus yields in vaccine production. However, at that time much less was known about the viral life cycle and only a limited amount of data was available such that the authors based their model on qualitative observations and literature parameters only. More recently, Madrahimov *et al.* proposed a boolean model for influenza virus replication focusing on the interaction of the virus with its host cell [17]. They could show that blocking different host cell signaling pathways impairs virus replication. Yet, boolean models only provide a limited picture of infection as they neglect both quantitative and dynamic aspects. Hence, much work remains to be done in order to obtain a comprehensive mathematical description of intracellular influenza A virus replication.

2.3.4. Multiscale modeling approaches

While intracellular models only consider a single infection cycle and neglect virus spreading, cell-to-cell interactions, and the dynamics of the target cell population, within-host models treat the infected cell as a black box. The latter approach impedes an analysis of antivirals which act on intracellular processes to combat within-host infection. Hence, these forms of therapy require mathematical models that cover both scales. The theoretical foundation for this type of infection model was developed by Haseltine and coworkers who not only showed that population balance equations provide the means to combine the intracellular and the within-host (extracellular) level [238] but also proposed a strategy to reduce the computational burden associated with their computation [239]. Later, Guedj *et al.* argued that describing the viral load data in HCV-infected patients under treatment with the nonstructural 5A (NS5A) protein inhibitor daclatasvir requires such a multiscale approach [203]. In this study, the classical model of within-host viral kinetics was extended by accounting for the amplification, degradation, and secretion of viral genomic RNAs. Guedj *et al.* and a later analysis of their model by Rong and colleagues showed that the viral load dynamics upon treatment can strongly depend on these intracellular processes [203, 240, 241]. However, since their model only accounts for viral genomic RNAs it is restricted to drugs that interfere with the viral genome neglecting the complexity of intracellular HCV replication [237]. Yet, the model of Guedj *et al.* shows that coupling a description of the intracellular viral life cycle to the within-host infection dynamics can provide new insights into antiviral therapy. Note that besides linking the intracellular with the within-host level, multiscale models that connect within-host and between-host kinetics have also been developed (reviewed in [242]). Handel *et al.*, for instance, used such a model to investigate the fitness trade-offs for influenza virus persistence at high versus low temperatures [243].

2.4. Model construction and analysis

In general, mathematical models of infection can either follow deterministic rules or include elements of randomness. In this section, the construction, parameterization and analysis of both model types is briefly outlined.

2.4.1. Construction of mathematical models

Traditionally, most modeling approaches in biology assume a deterministic behavior of the system of interest meaning that it reaches the same final state given a specific set of initial conditions. By contrast, stochastic models account for the inherent randomness of biochemistry, which may affect the outcome of each individual experiment.

Deterministic models The most common type of deterministic model uses ordinary differential equations (ODEs) to describe the change of a state variable over time. For instance, the number of infected cells (I) in the standard model of viral dynamics (Figure 2.6) is given by the following equation.

$$\frac{\mathrm{d}I}{\mathrm{d}t} = \beta T V - \delta I, \tag{2.4.1}$$

where β and δ are the kinetic parameters for viral infection and cell death, respectively, T is the number of target cells and V the amount of virus particles [14]. Equation (2.4.1), thus, tracks the abundance of infected cells, which changes through the interaction of viruses with uninfected target cells and by cell death. Note that the infection rate ($\beta T V$) is described by mass action kinetics, i.e., it is proportional to the product of T and V. We will abundantly make use of this principle in our models.

Stochastic models Deterministic descriptions like the one shown above intrinsically neglect stochastic effects, which is usually justified when all state variables reach large numbers such that small fluctuations even out. However, when the reactant species are low in abundance the discrete nature of molecular populations and the randomness of reaction events can prevail. For such systems stochastic simulation techniques are the method of choice. For an excellent review on the underlying theory and the assumptions made when using different model types the reader is referred to reference [244].

Stochastic modeling approaches differ in several aspects from their deterministic counterparts. For instance, their state variables can only assume discrete numbers, whereas the deterministic states are continuous. In addition, the reaction rates are replaced by probabilities per unit time, the propensity functions $a_j(x)$ [244]. Here, $a_j(x)\mathrm{d}t$

denotes the probability that reaction R_j will occur in the time interval $[t, t+\mathrm{d}t)$ given that the state vector of the system is $X(t) = x$. The change in the number of species i caused by reaction j is provided by the state-change matrix, v_{ij}. For the number of infected cells in the standard viral dynamic model one obtains:

$$X(t) = I(t), \quad v_{ij} = [1, -1], \quad \text{and} \quad a_j = [c_1 TV, c_2 I], \tag{2.4.2}$$

where c_j are stochastic reaction constants such that any randomly chosen pair of target cell and virus particle establishes infection with probability $c_1\mathrm{d}t$ and any infected cell dies with probability $c_2\mathrm{d}t$ in the next infinitesimal time $\mathrm{d}t$. Considering the number of possible combinations of cells and viruses the overall probability that a reaction occurs in the system is $c_1 TV\mathrm{d}t$ and $c_2 I\mathrm{d}t$, respectively. It turns out that the constants c_j are related to the deterministic rate constants.

$$c_1 = \frac{\beta}{\Omega} \quad \text{and} \quad c_2 = \delta,$$

where Ω is the constant system volume [244]. Note that for a stochastic model to be an accurate representation, the system only has to be well-stirred, i.e., the positions of individual molecules in Ω must be uniformly randomized and the molecule velocities thermally randomized. The propensity functions then follow from the principles of molecular physics [244]. By contrast, the deterministic rates are only approximate consequences of these stochastic kinetics. Thus, in order for a deterministic model to be valid additional preconditions (e.g. high species concentrations) must be met.

2.4.2. Model analysis techniques

Mathematical models often comprise tens or even hundreds of free parameters whose assignment is a fundamental challenge in modeling. Typically, these parameters are either measured directly or, more often, estimated by fitting the model to experimental data. However, both methods can cause significant uncertainty in parameter values, which may lead to an ill-defined model behavior and prevent predictions on the underlying biological system. Thus, the concept of parameter identifiability is central to model construction.

Parameter sensitivity and identifiability In general, for a parameter to be identifiable from a model fit to experiments, first and foremost, it needs to cause a change in the model output of an observed state variable [245], i.e., the simulation of at least one of the measured states has to be sensitive to the parameter. This can be tested by means of a local parameter sensitivity analysis using the sensitivity coefficient,

$$S_\theta^M = \frac{\delta M(\gamma)/M(\gamma)}{\delta\theta/\theta}, \tag{2.4.3}$$

where $M(\gamma)$ and $\delta M(\gamma)$ denote a characteristic of the system output γ and the change in that characteristic, respectively, due to the change $\delta\theta$ in the parameter θ [246]. For the model response characteristic, $M(\gamma)$, aspects like the area under the curve of the output, differences in steady-state values, output after a specific amount of time, or period and amplitude of oscillations have been used [246]. However, more frequently sensitivity analysis is based on the weighted sum of squared residuals (SSR).

$$\frac{\delta M(\gamma)}{M(\gamma)} \equiv \frac{1}{N_c N_s} \sum_{s,c} \left[\frac{1}{N_t} \sum_t \left(\frac{y_{s,c}(\theta, t) - y_{s,c}(\theta^\star, t)}{\sigma_s} \right)^2 \right], \tag{2.4.4}$$

where $y_{s,c}(\theta, t)$ is the model output of the measured species s at experimental condition c and time t given the original parameter θ, and $y_{s,c}(\theta^\star, t)$ is the same output in response to a change $\delta\theta$ in that parameter [247]. Here, this change is normalized to the maximum value of species s across all conditions, σ_s. Alternatively, the standard deviation of each measurement can be used if available. Also, the SSR is normalized with respect to the number of measured time points (N_t), species (N_s), and experimental conditions (N_c). The sensitivity coefficient provides a first indication of how well the parameter is defined by the data set with low sensitivity pointing toward a poorly constrained parameter. However, even if a parameter shows a high local sensitivity, correlations with other parameters and parameter redundancies may nevertheless affect its identifiability [245]. Thus, increasing the number of free parameters by choosing a more complex model also increases the chance of encountering non-identifiable parameters. It is the quantity (and quality) of available data that should, hence, constrain model complexity. Note, however, that despite subsets of poorly constrained parameters, which seem to be a general characteristic of models in systems biology, model fits and predictions can be surprisingly well defined [247].

Parameter confidence intervals As mentioned in the last paragraph many models in systems biology suffer from poorly constrained parameters, which is why Gutenkunst *et al.* proposed to rather focus on model predictions than parameter values [247]. These predictions can be well constrained by collective parameter fits despite the fit yielding significant uncertainty in individual parameter values. If, however, the precise value of a parameter is of interest, a measure of confidence in its estimate is helpful. Such parameter confidence bounds can be derived by several different methods, e.g., from the Fisher-Information-Matrix [248] and the curvature of the likelihood function [245]. In addition, bootstrap algorithms are widely used to infer the accuracy of parameter estimates [248, 249]. As bootstrapping is an easy and reliable method to derive confidence bounds, we focus on this approach in the following.

In general, bootstrap methods use Monte Carlo sampling to obtain an estimate for the statistical properties of an unknown probability distribution from random observations of this distribution. For modeling, this means that we can sample the distribution of parameter estimates in order to derive confidence intervals for the parameters. As an example, let us consider a set of experimental observations $y = (x_1, x_2, \ldots, x_n)$, e.g., the final virus titer in n independent experiments. We can now use a Monte Carlo approach to draw a bootstrap sample, $y^\star = (x_1^\star, x_2^\star, \ldots, x_n^\star)$, i.e., a random sample of size n drawn with replacement from the original data, y, [249]. Note that for time series data we can obtain the bootstrap sample in a similar way by drawing the new value at each time point t_i from a normal distribution $\mathcal{N}\left(x_i, \sigma_i^2\right)$ (assuming that the measurement error follows a normal distribution), where x_i is the original measurement and σ_i its standard deviation. Fitting the model to the bootstrap sample then results in a parameter estimate $\theta^\star\left(y^\star\right)$. By repeating this process we obtain a distribution of parameter values from which we can calculate the confidence interval. For instance, according to the percentile method, the parameter confidence interval at significance level α is equivalent to the central interval between the $100 \cdot \alpha/2$ and $100 \cdot (1 - \alpha/2)$ percentiles of the bootstrap parameter distribution [249]. For a more detailed review on the underlying theory the reader is referred to references [248, 249].

Chapter 3

Models and Methods

In this chapter, we first describe two mathematical models of intracellular virus replication, one of which uses a deterministic approach, while the other accounts for elements of randomness. Based on the former, we then introduce a multiscale model of infection that links the intracellular and the extracellular level. Finally, two descriptions of DIP growth are presented.

3.1. Intracellular virus replication

3.1.1. Deterministic model

Our model of intracellular virus replication is loosely based on a similar description by Sidorenko *et al.* [16]. However, we modified the equations for virus entry, neglected the trafficking of viral mRNAs and proteins between the cytoplasm and the nucleus, and of envelope proteins between the ER and the budding site. Furthermore, we included a detailed description of RNP formation, the stabilization of cRNAs, and the regulation of vRNP export from the nucleus. These modifications were implemented to improve the agreement with recent insights into influenza virus biology (discussed in Section 4.1.3.1) and to facilitate an estimation of critical infection parameters using quantitative data on the intracellular viral life cycle. Our model was first published in the Journal of Virology [250] and parts of the original publication are used hereafter.

Virus entry The main features of influenza A virus replication are shown in Figure 2.2, which provides the basis for our model. First, virions bind to neuraminic acids (sialic acids) on the cell surface and enter the cell via receptor-mediated endocytosis. Based on experimental data, Nunes-Correia *et al.* proposed a kinetic model for these processes including two different types of binding sites: high-affinity and low-affinity sites, which might correspond to sialic-acid containing ligands and less-specific interactions, respectively [251]. We made minor modifications to this model to account for the infection of a single cell and added an equation for virions in early endosomes.

$$\frac{\mathrm{d}V^{\mathrm{Ex}}}{\mathrm{d}t} = k_{\mathrm{hi}}^{\mathrm{Dis}} V_{\mathrm{hi}}^{\mathrm{Att}} + k_{\mathrm{lo}}^{\mathrm{Dis}} V_{\mathrm{lo}}^{\mathrm{Att}} - \left(k_{\mathrm{hi}}^{\mathrm{Att}} B_{\mathrm{hi}} + k_{\mathrm{lo}}^{\mathrm{Att}} B_{\mathrm{lo}} \right) V^{\mathrm{Ex}}, \tag{3.1.1}$$

$$\text{with} \quad B_{\mathrm{n}} = B_{\mathrm{n}}^{\mathrm{tot}} - V_{\mathrm{n}}^{\mathrm{Att}}, \quad n \in \{\mathrm{hi}, \mathrm{lo}\}\,, \tag{3.1.2}$$

$$\frac{\mathrm{d}V_{\mathrm{n}}^{\mathrm{Att}}}{\mathrm{d}t} = k_{\mathrm{n}}^{\mathrm{Att}} B_{\mathrm{n}} V^{\mathrm{Ex}} - \left(k_{\mathrm{n}}^{\mathrm{Dis}} + k^{\mathrm{En}} \right) V_{\mathrm{n}}^{\mathrm{Att}}, \tag{3.1.3}$$

$$\frac{\mathrm{d}V^{\mathrm{En}}}{\mathrm{d}t} = k^{\mathrm{En}} \left(V_{\mathrm{hi}}^{\mathrm{Att}} + V_{\mathrm{lo}}^{\mathrm{Att}} \right) - \left(k^{\mathrm{Fus}} + k_{\mathrm{En}}^{\mathrm{Deg}} \right) V^{\mathrm{En}}, \tag{3.1.4}$$

$$\text{with} \quad k_{\mathrm{n}}^{\mathrm{Dis}} = \frac{k_{\mathrm{n}}^{\mathrm{Att}}}{k_{\mathrm{n}}^{\mathrm{Eq}}} \quad \text{and} \quad k_{\mathrm{En}}^{\mathrm{Deg}} = \frac{1 - F_{\mathrm{Fus}}}{F_{\mathrm{Fus}}} k^{\mathrm{Fus}}, \quad 0 < F_{\mathrm{Fus}} \leq 1,$$

where V^{Ex}, $V_{\mathrm{n}}^{\mathrm{Att}}$, and V^{En} are the numbers of virions in the extracellular medium, virions attached to binding sites of type n (hi, high-affinity; lo, low-affinity), and virions in early endosomes, respectively. Here, V^{Ex} corresponds to the MOI, i.e., the initial number of infectious virus particles per cell. These virions attach with rate $k_{\mathrm{n}}^{\mathrm{Att}}$ to free binding sites (B_{n}) of which there are $B_{\mathrm{n}}^{\mathrm{tot}}$ in total. By calculating B_{n} from the conservation Equation (3.1.2), we followed the formalism of Nunes-Correia and coworkers [251]. Note that this implies a fast recycling of receptors as binding sites become vacant as soon as virions enter the cell. Also, in this notation each virion occupies one binding site that may correspond to multiple receptors as virus-cell binding involves multivalent bond formation [252]. Once attached, virions can either dissociate from the cell with rate $k_{\mathrm{n}}^{\mathrm{Dis}}$, which follows directly from the equilibrium constant ($k_{\mathrm{n}}^{\mathrm{Eq}}$), or enter the cell by endocytosis with rate k^{En}. We assumed that k^{En} is the same for both binding sites, as did Nunes-Correia and colleagues. Fusion of virions in endosomes occurs with rate k^{Fus}, which includes the trafficking and acidification of early endosomes, the fusion of the viral envelope with the endosomal membrane, and viral uncoating. It has been shown that only a fraction of virions penetrate into the cytoplasm, while others presumably fail to fuse [45, 253]. We, therefore, introduced the fraction of fusion-competent virions (F_{Fus}) and calculated the degradation rate of virions in lysosomes ($k_{\mathrm{En}}^{\mathrm{Deg}}$) accordingly. For model fits to experimental data on fusion (Figure 4.2A), the total number of fused virions can be obtained by integrating $k^{\mathrm{Fus}} V^{\mathrm{En}}$ over time (equation not shown).

Viral RNA replication Following fusion, influenza viruses release parental vRNPs into the cytoplasm. These vRNPs enter the nucleus [38, 47], where they start synthesizing mRNA and, according to the stabilization hypothesis (Figure 2.3B), also cRNA [66]. However, nascent cRNA may be rapidly degraded by cellular nucleases unless it is stabilized in cRNP complexes [60]. We assumed that vRNP formation stabilizes nascent vRNA in a similar fashion. For the majority of genome segments, the vRNAs (and cRNAs) of different segments show similar levels throughout infection [174, 175]. Hence, we did not explicitly distinguish between individual segments but rather consider their total number per cell. For obtaining the abundance of an arbitrary segment, this number can be divided by eight, which we did when fitting the model to measurements of individual genome segments. Later in infection, M1 and NEP proteins enter the nucleus and trigger the nuclear export of vRNPs [39]. Since M1 binding inhibits the transcriptase activity of vRNPs [93–95], M1-vRNP complexes in our model are no longer available as templates for RNA synthesis. Thus, virus replication is described by the following equations:

$$\frac{\mathrm{d}Vp^{\text{cyt}}}{\mathrm{d}t} = 8k^{\text{Fus}}V^{\text{En}} - k^{\text{Imp}}Vp^{\text{cyt}}, \tag{3.1.5}$$

$$\frac{\mathrm{d}Vp^{\text{nuc}}}{\mathrm{d}t} = k^{\text{Imp}}Vp^{\text{cyt}} + k^{\text{Bind}}_{\text{NP}}P_{\text{NP}}R^{\text{V}}_{\text{RdRp}} - \left(k^{\text{Bind}}_{\text{M1}}P_{\text{M1}} + k^{\text{Deg}}_{\text{Rnp}}\right)Vp^{\text{nuc}}, \tag{3.1.6}$$

$$\frac{\mathrm{d}R^{\text{C}}}{\mathrm{d}t} = k^{\text{Syn}}_{\text{C}}Vp^{\text{nuc}} - k^{\text{Bind}}_{\text{RdRp}}P_{\text{RdRp}}R^{\text{C}} - k^{\text{Deg}}_{\text{R}}R^{\text{C}}, \tag{3.1.7}$$

$$\frac{\mathrm{d}R^{\text{V}}}{\mathrm{d}t} = k^{\text{Syn}}_{\text{V}}Cp - k^{\text{Bind}}_{\text{RdRp}}P_{\text{RdRp}}R^{\text{V}} - k^{\text{Deg}}_{\text{R}}R^{\text{V}}, \tag{3.1.8}$$

$$\frac{\mathrm{d}R^{\text{C}}_{\text{RdRp}}}{\mathrm{d}t} = k^{\text{Bind}}_{\text{RdRp}}P_{\text{RdRp}}R^{\text{C}} - k^{\text{Bind}}_{\text{NP}}P_{\text{NP}}R^{\text{C}}_{\text{RdRp}} - k^{\text{Deg}}_{\text{RRdRp}}R^{\text{C}}_{\text{RdRp}}, \tag{3.1.9}$$

$$\frac{\mathrm{d}R^{\text{V}}_{\text{RdRp}}}{\mathrm{d}t} = k^{\text{Bind}}_{\text{RdRp}}P_{\text{RdRp}}R^{\text{V}} - k^{\text{Bind}}_{\text{NP}}P_{\text{NP}}R^{\text{V}}_{\text{RdRp}} - k^{\text{Deg}}_{\text{RRdRp}}R^{\text{V}}_{\text{RdRp}}, \tag{3.1.10}$$

$$\frac{\mathrm{d}Cp}{\mathrm{d}t} = k^{\text{Bind}}_{\text{NP}}P_{\text{NP}}R^{\text{C}}_{\text{RdRp}} - k^{\text{Deg}}_{\text{Rnp}}Cp, \tag{3.1.11}$$

$$\frac{\mathrm{d}Vp^{\text{nuc}}_{\text{M1}}}{\mathrm{d}t} = k^{\text{Bind}}_{\text{M1}}P_{\text{M1}}Vp^{\text{nuc}} - \left(k^{\text{Exp}}P_{\text{NEP}} + k^{\text{Deg}}_{\text{Rnp}}\right)Vp^{\text{nuc}}_{\text{M1}}, \tag{3.1.12}$$

$$\frac{\mathrm{d}Vp^{\text{cyt}}_{\text{M1}}}{\mathrm{d}t} = k^{\text{Exp}}P_{\text{NEP}}Vp^{\text{nuc}}_{\text{M1}} - 8r^{\text{Rel}} - k^{\text{Deg}}_{\text{Rnp}}Vp^{\text{cyt}}_{\text{M1}}. \tag{3.1.13}$$

Upon fusion, each virion releases a complete set of eight vRNPs into the cytoplasm (Vp^{cyt}), which enter the nucleus with rate k^{Imp}. Nuclear vRNPs (Vp^{nuc}) then synthesize mRNA, which is described in the next paragraph, and cRNA (R^{C}) with rate $k^{\text{Syn}}_{\text{C}}$ (Equation (3.1.7)). Similarly, the synthesis of vRNA (R^{V}) is directed by cRNPs (Cp) with rate $k^{\text{Syn}}_{\text{V}}$ (Equation (3.1.8)). We assumed that both types of nascent RNA are degraded by nucleases with rate $k^{\text{Deg}}_{\text{R}}$ or bind to viral polymerases (P_{RdRp}) with rate $k^{\text{Bind}}_{\text{RdRp}}$. The resulting complexes of the viral polymerase with cRNA ($R^{\text{C}}_{\text{RdRp}}$) and vRNA ($R^{\text{V}}_{\text{RdRp}}$) are only partially stabilized and, thus, degraded with the rate $k^{\text{Deg}}_{\text{RRdRp}}$, which is lower than that of nascent RNA. Binding of NP (P_{NP}) with rate $k^{\text{Bind}}_{\text{NP}}$ then leads to cRNP and vRNP formation, respectively. We assumed that RNPs decay at a low rate ($k^{\mathrm{Deg}}_{\mathrm{Rnp}}$), as the RNA in vRNPs is still sensitive to digestion in the presence of an excess of RNases [254]. Note that this decay was omitted for incoming cytoplasmic vRNPs (Equation (3.1.5)) to capture the constant vRNA level observed in cells treated with the protein synthesis inhibitor cycloheximide [60]. During the late phase of infection, M1 proteins (P_{M1}) can bind to vRNPs with rate $k^{\mathrm{Bind}}_{\mathrm{M1}}$ to form M1-vRNP complexes in the nucleus ($Vp^{\mathrm{nuc}}_{\mathrm{M1}}$). Subsequent association of NEP (P_{NEP}) facilitates their nuclear export, which was combined in the rate k^{Exp} assuming that the actual transport process is fast. Cytoplasmic NEP-M1-vRNP complexes ($Vp^{\mathrm{cyt}}_{\mathrm{M1}}$) are then transported to the plasma membrane where virus budding takes place. We lumped all processes of virus assembly and budding into the virus release rate (r^{Rel}), which is described later.

When comparing the model to experimental RNA levels, we obtained the total number of vRNAs ($R^{\mathrm{V}}_{\mathrm{tot}}$) and cRNAs ($R^{\mathrm{C}}_{\mathrm{tot}}$) by summation over all viral components that contain the respective RNA species and are associated with the cell.

$$R^{\mathrm{V}}_{\mathrm{tot}} = 8\left(V^{\mathrm{Att}}_{\mathrm{hi}} + V^{\mathrm{Att}}_{\mathrm{lo}} + V^{\mathrm{En}}\right) + Vp^{\mathrm{cyt}} + Vp^{\mathrm{nuc}} + R^{\mathrm{V}} + R^{\mathrm{V}}_{\mathrm{RdRp}} + Vp^{\mathrm{nuc}}_{\mathrm{M1}} + Vp^{\mathrm{cyt}}_{\mathrm{M1}}, \tag{3.1.14}$$

$$R^{\mathrm{C}}_{\mathrm{tot}} = R^{\mathrm{C}} + R^{\mathrm{C}}_{\mathrm{RdRp}} + Cp. \tag{3.1.15}$$

The RNA level of an arbitrary genome segment (e.g. of segment 5 in Figure 4.5) was calculated by dividing these total concentrations by eight.

Viral mRNA and protein synthesis Viral transcription takes place in the nucleus, whereas translation occurs at cytoplasmic ribosomes. However, since the nuclear export of mRNAs is fast [255], we assumed that newly synthesized mRNAs are readily available for translation. In contrast to vRNA and cRNA, our model explicitly accounts for the mRNAs of different genome segments, since measurements reveal significant differences in their levels during infection [174, 175]. Protein synthesis in simulations is directly proportional to these mRNA levels, as has been found experimentally [256]. For simplicity, we only considered the net production of all structural proteins, neglecting their degradation, and assumed that protein amounts in different cellular compartments are in equilibrium. As more data become available, these assumptions can be dropped in favor of a more complex model. Equations for mRNAs and proteins are the following:

$$\frac{\mathrm{d}R^{\mathrm{M}}_{\mathrm{i}}}{\mathrm{d}t} = \frac{k^{\mathrm{Syn}}_{\mathrm{M}}}{L_{\mathrm{i}}}\frac{Vp^{\mathrm{nuc}}}{8} - k^{\mathrm{Deg}}_{\mathrm{M}} R^{\mathrm{M}}_{\mathrm{i}}, \quad i = 1, \ldots, 8, \tag{3.1.16}$$

$$\frac{\mathrm{d}P_{\mathrm{PB1}}}{\mathrm{d}t} = \frac{k^{\mathrm{Syn}}_{\mathrm{P}}}{D_{\mathrm{Rib}}} R^{\mathrm{M}}_{2} - k^{\mathrm{RdRp}} P_{\mathrm{PB1}} P_{\mathrm{PB2}} P_{\mathrm{PA}}, \tag{3.1.17}$$

$$\frac{\mathrm{d}P_{\mathrm{PB2}}}{\mathrm{d}t} = \frac{k^{\mathrm{Syn}}_{\mathrm{P}}}{D_{\mathrm{Rib}}} R^{\mathrm{M}}_{1} - k^{\mathrm{RdRp}} P_{\mathrm{PB1}} P_{\mathrm{PB2}} P_{\mathrm{PA}}, \tag{3.1.18}$$

$$\frac{\mathrm{d}P_{\mathrm{PA}}}{\mathrm{d}t} = \frac{k_{\mathrm{P}}^{\mathrm{Syn}}}{D_{\mathrm{Rib}}} R_3^{\mathrm{M}} - k^{\mathrm{RdRp}} P_{\mathrm{PB1}} P_{\mathrm{PB2}} P_{\mathrm{PA}}, \tag{3.1.19}$$

$$\frac{\mathrm{d}P_{\mathrm{RdRp}}}{\mathrm{d}t} = k^{\mathrm{RdRp}} P_{\mathrm{PB1}} P_{\mathrm{PB2}} P_{\mathrm{PA}} - k_{\mathrm{RdRp}}^{\mathrm{Bind}} P_{\mathrm{RdRp}} \left(R^{\mathrm{V}} + R^{\mathrm{C}} \right) - (N_{\mathrm{P_{RdRp}}} - 8) r^{\mathrm{Rel}}, \tag{3.1.20}$$

$$\frac{\mathrm{d}P_{\mathrm{NP}}}{\mathrm{d}t} = \frac{k_{\mathrm{P}}^{\mathrm{Syn}}}{D_{\mathrm{Rib}}} R_5^{\mathrm{M}} - \frac{L^{\mathrm{V}}}{N_{\mathrm{NP}}^{\mathrm{Nuc}}} k_{\mathrm{NP}}^{\mathrm{Bind}} P_{\mathrm{NP}} \left(R_{\mathrm{RdRp}}^{\mathrm{V}} + R_{\mathrm{RdRp}}^{\mathrm{C}} \right) - (N_{\mathrm{P_{NP}}} - 8 \frac{L^{\mathrm{V}}}{N_{\mathrm{NP}}^{\mathrm{Nuc}}}) r^{\mathrm{Rel}}, \tag{3.1.21}$$

$$\frac{\mathrm{d}P_{\mathrm{M1}}}{\mathrm{d}t} = \frac{k_{\mathrm{P}}^{\mathrm{Syn}}}{D_{\mathrm{Rib}}} \left(1 - F_{\mathrm{Spl}_7} \right) R_7^{\mathrm{M}} - \frac{L^{\mathrm{V}}}{N_{\mathrm{M1}}^{\mathrm{Nuc}}} k_{\mathrm{M1}}^{\mathrm{Bind}} P_{\mathrm{M1}} Vp^{\mathrm{nuc}} - (N_{\mathrm{P_{M1}}} - 8 \frac{L^{\mathrm{V}}}{N_{\mathrm{M1}}^{\mathrm{Nuc}}}) r^{\mathrm{Rel}}, \tag{3.1.22}$$

$$\frac{\mathrm{d}P_{\mathrm{NEP}}}{\mathrm{d}t} = \frac{k_{\mathrm{P}}^{\mathrm{Syn}}}{D_{\mathrm{Rib}}} F_{\mathrm{Spl}_8} R_8^{\mathrm{M}} - \frac{L^{\mathrm{V}}}{N_{\mathrm{NEP}}^{\mathrm{Nuc}}} k^{\mathrm{Exp}} P_{\mathrm{NEP}} Vp_{\mathrm{M1}}^{\mathrm{nuc}} - (N_{\mathrm{P_{NEP}}} - 8 \frac{L^{\mathrm{V}}}{N_{\mathrm{NEP}}^{\mathrm{Nuc}}}) r^{\mathrm{Rel}}, \tag{3.1.23}$$

$$\frac{\mathrm{d}P_{\mathrm{HA}}}{\mathrm{d}t} = \frac{k_{\mathrm{P}}^{\mathrm{Syn}}}{D_{\mathrm{Rib}}} R_4^{\mathrm{M}} - N_{\mathrm{P_{HA}}} r^{\mathrm{Rel}}, \tag{3.1.24}$$

$$\frac{\mathrm{d}P_{\mathrm{NA}}}{\mathrm{d}t} = \frac{k_{\mathrm{P}}^{\mathrm{Syn}}}{D_{\mathrm{Rib}}} R_6^{\mathrm{M}} - N_{\mathrm{P_{NA}}} r^{\mathrm{Rel}}, \tag{3.1.25}$$

$$\frac{\mathrm{d}P_{\mathrm{M2}}}{\mathrm{d}t} = \frac{k_{\mathrm{P}}^{\mathrm{Syn}}}{D_{\mathrm{Rib}}} F_{\mathrm{Spl}_7} R_7^{\mathrm{M}} - N_{\mathrm{P_{M2}}} r^{\mathrm{Rel}}, \tag{3.1.26}$$

where $R_{\mathrm{i}}^{\mathrm{M}}$ and P_{j} are the numbers of mRNAs of segment i and of proteins of type j, respectively. Experiments of Hatada *et al.* show a negative correlation between the length of an mRNA and its level, i.e., smaller mRNAs are more abundant [174]. Because we assumed that all mRNAs are degraded with the same rate ($k_{\mathrm{M}}^{\mathrm{Deg}}$), we used a length-dependent mRNA synthesis rate ($k_{\mathrm{M}}^{\mathrm{Syn}}$) and scaled it with L_{i}, denoting the length of segment i's unspliced mRNA (Equation (3.1.16)). This is in agreement with a transcription mechanism in which the resident polymerase complex in a vRNP synthesizes mRNAs in *cis* [50] and elongation is the rate-limiting step. We divided Vp^{nuc} by eight, as only this fraction of vRNPs encodes for a specific genome segment and its mRNA. To increase protein translation, multiple ribosomes can bind to a single mRNA forming polysomes. This was considered by using a length-dependent translation rate ($k_{\mathrm{P}}^{\mathrm{Syn}}$) and the average distance between two adjacent ribosomes on an mRNA (D_{Rib}). Hence, protein production is proportional to the speed with which ribosomes cover the distance D_{Rib}. New viral polymerases (P_{RdRp}) form from the three subunits with rate k^{RdRp} and bind to vRNAs and cRNAs with $k_{\mathrm{RdRp}}^{\mathrm{Bind}}$ (Equation (3.1.20)). Measurements show that the number of polymerases in one virus particle ($N_{\mathrm{P_{RdRp}}}$) is greater than the eight polymerases in a complete set of vRNPs [25]. Therefore, the remaining amount was assumed to leave the cell during budding. Similar terms were considered for NP, M1, and NEP, with $N_{P_{\mathrm{j}}}$ denoting the number of proteins of type j in one virion. To calculate the amount of NP, M1, and NEP bound in one NEP-M1-vRNP complex, we used the average length of a vRNA (L_{V}) and the number of nucleotides bound by one protein ($N^{\mathrm{Nuc}}_{\mathrm{NP}}$, $N^{\mathrm{Nuc}}_{\mathrm{M1}}$, and $N^{\mathrm{Nuc}}_{\mathrm{NEP}}$, respectively). The surface proteins HA (P_{HA}), NA (P_{NA}), and M2 (P_{M2}) only decrease due to budding. We considered the splicing of mRNAs from segment 7 and 8 by introducing the factors F_{Spl_7} and F_{Spl_8}, which represent the fractions of mRNA that encode for M2 and NEP, respectively.

Virus release When vRNPs and viral proteins reach the plasma membrane, progeny virions are assembled and released from the cell. Since the precise mechanism is still not well understood and kinetic data are lacking, we did not model budding in detail but rather used a simple description.

$$\frac{\mathrm{d}V^{\mathrm{Rel}}}{\mathrm{d}t} = r^{\mathrm{Rel}} = k^{\mathrm{Rel}} Vp^{\mathrm{cyt}}_{\mathrm{M1}} \prod_{\mathrm{j}} \frac{P_{\mathrm{j}}}{P_{\mathrm{j}} + K_{V^{\mathrm{Rel}}} N_{P_{\mathrm{j}}}}, \qquad (3.1.27)$$

$$\text{with} \quad j \in \{\mathrm{RdRp}, \mathrm{HA}, \mathrm{NP}, \mathrm{NA}, \mathrm{M1}, \mathrm{M2}, \mathrm{NEP}\},$$

where V^{Rel} is the number of progeny virions released from a cell. It has been shown that vRNPs assume a “7+1” configuration in virus particles [34], which along with other evidence supports a specific packaging mechanism of the viral genome [108]. The formation of a complex containing the eight genome segments would involve multiple inter-segment interactions [34] and may, therefore, represent a kinetic bottleneck. Hence, the overall rate of virus release (r^{Rel}) in our model is proportional to the amount of cytoplasmic vRNPs and to the virus release rate (k^{Rel}). Viral protein levels are assumed to scale this rate by multiplication of Michaelis-Menten-like terms, which depend on the abundance of each protein j in one virion ($N_{P_{\mathrm{j}}}$), i.e., enough proteins for $K_{V^{\mathrm{Rel}}}$ virions must be present to reach half the maximal release rate. Note that we neglected the reinfection of a cell by its own progeny virions. This is in agreement with the observation that neuraminidase expression on the cell surface cleaves sialic acid and limits superinfection [257].

For all steps of the virus life cycle, we assumed that cellular resources, like amino acids, nucleotides and ribosomes, as well as other host factors are abundant and do not limit replication; an assumption which has been used by several previous authors for other viruses [229, 231, 234] and which is in agreement with theoretical results for influenza [16].

Switching hypothesis The above model considers the stabilization of nascent cRNA as the cause for the transition from transcription to replication. By contrast, the switching hypothesis assumes that vRNPs solely engage in transcription during early infection and that NP changes their activity toward replication at later stages (Figure 2.3A). However, vRNPs can synthesize cRNA in the absence of NP *in vitro*, albeit at lower rates [66, 258]. When building an alternative model, we, thus, assumed that in the absence of viral proteins vRNPs not only transcribe viral mRNAs but also show residual cRNA synthesis. Accumulation of NP proteins then enhances replication at the expense of transcription. Hence, Equation (3.1.7) and (3.1.16) were modified in the following way to simulate switching:

$$\frac{\mathrm{d}R^{\mathrm{C}}}{\mathrm{d}t} = \left(k_{\mathrm{C}}^{\mathrm{Res}} + F_{\mathrm{swt}} k_{\mathrm{C}}^{\mathrm{Syn}}\right) Vp^{\mathrm{nuc}} - k_{\mathrm{RdRp}}^{\mathrm{Bind}} P_{\mathrm{RdRp}} R^{\mathrm{C}} - k_{\mathrm{R}}^{\mathrm{Deg}} R^{\mathrm{C}}, \tag{3.1.28}$$

$$\frac{\mathrm{d}R_{\mathrm{i}}^{\mathrm{M}}}{\mathrm{d}t} = (1 - F_{\mathrm{swt}}) \frac{k_{\mathrm{M}}^{\mathrm{Syn}}}{L_{\mathrm{i}}} \frac{Vp^{\mathrm{nuc}}}{8} - k_{\mathrm{M}}^{\mathrm{Deg}} R_{\mathrm{i}}^{\mathrm{M}}, \quad i = 1, \ldots, 8, \tag{3.1.29}$$

$$\text{with} \quad F_{\mathrm{swt}} = \frac{P_{\mathrm{NP}}}{P_{\mathrm{NP}} + K_{\mathrm{swt}}},$$

where $k_{\mathrm{C}}^{\mathrm{Res}}$ denotes the residual cRNA synthesis in the absence of NP and $k_{\mathrm{C}}^{\mathrm{Syn}}$ the maximum rate by which replication can be enhanced through NP. F_{swt} is the switching factor, which can vary between zero and one. At low NP levels F_{swt} is zero, mRNA synthesis occurs at its maximum rate, and cRNA production at $k_{\mathrm{C}}^{\mathrm{Res}}$. High NP concentrations cause F_{swt} to become one, mRNA production to cease, and cRNA synthesis to occur at rate $k_{\mathrm{C}}^{\mathrm{Res}} + k_{\mathrm{C}}^{\mathrm{Syn}}$. The switching constant (K_{swt}) controls how many NP proteins are required to switch the vRNP activity toward replication. Furthermore, in this scenario the encapsidation of nascent RNA by polymerases and NP does not result in stabilization. Hence, we assumed $k_{\mathrm{R}}^{\mathrm{Deg}} = k_{\mathrm{RRdRp}}^{\mathrm{Deg}} = k_{\mathrm{Rnp}}^{\mathrm{Deg}}$.

Computation We solved Equations (3.1.1)–(3.1.29) numerically using the CVODE routine from SUNDIALS [259] on a Linux-based system[1]. All model parameters and initial conditions can be found in Table A.1–A.5 in the appendix. Model files and experiments were handled in the Systems Biology Toolbox 2 [260] for MatLab (version 8.0.0.783 R2012b). We estimated parameters using the fSSm algorithm for stochastic global optimization [261] and a least-squares objective function of the form:

$$\chi^2(\theta) = \sum_{s,c} \left[\frac{1}{N_t} \sum_t \left(\frac{y_{s,c}^D(t) - y_{s,c}(\theta, t)}{\sigma_{s,c}} \right)^2 \right], \tag{3.1.30}$$

where $y_{s,c}^D(t)$ is the measurement of species s at experimental condition c and time t, and $y_{s,c}(\theta, t)$ the corresponding simulation value. The difference between both values was weighted by the standard deviation of measurements ($\sigma_{s,c}$) where available and by the number of measured time points (N_t) when multiple data sets were considered.

To assess parameter uncertainties, confidence intervals were calculated using a bootstrap method [248, 249]. For data sets where no measurement errors were available, the model's local sensitivity is provided instead. We calculated this sensitivity by quantifying the change in model output in response to parameter perturbations by 1% around the estimated value according to Equation (2.4.3) and (2.4.4). This local sensitivity shows how much a given parameter affects simulation results with respect to the available measurements indicating how accurate the parameter estimates are.

---

[1] Typical computation times are in the order of 0.02 s on a standard desktop computer (to simulate 12 h).

3.1.2. Stochastic model

Equations (3.1.1)–(3.1.27) serve as the basis for our stochastic simulation of intracellular virus replication. However, we made minor modifications to this model to reduce computational costs and to accommodate that, in a stochastic framework, molecule numbers are discrete rather than continuous. An early implementation of our stochastic model was developed by Sebastian Dorl as part of his bachelor thesis [262]. On the basis of this work, we further extended the framework by explicitly accounting for the vRNAs and cRNAs of different genome segments. In the following, we briefly outline all changes made to the original model (Section 3.1.1). Note that none of these changes significantly affects simulation dynamics in a deterministic setting (Figure A.1 in the appendix).

Model modifications In the deterministic model, the number of proteins bound in an RNP follows from the average length of an RNA and the number of nucleotides bound by one M1, NP and NEP protein, respectively (Equations (3.1.21)–(3.1.23)). For stochastic simulations, we rounded these values for M1 and NP proteins to the next smaller integer and assumed that each vRNP can only bind one NEP molecule. This yields discrete numbers for protein binding. Furthermore, we assumed that a reaction can only occur if all its substrates are available, e.g., virus release can only occur if viral proteins for at least one virus particle are present. In addition, we neglected the formation of the polymerase complex (Equation (3.1.20)) and the synthesis of its subunits (Equations (3.1.17)–(3.1.19)) in favor of a simpler description.

$$\frac{\mathrm{d}P_{\mathrm{RdRp}}}{\mathrm{d}t} = \min\left(R_1^{\mathrm{M}}, R_2^{\mathrm{M}}, R_3^{\mathrm{M}}\right)\frac{k_{\mathrm{P}}^{\mathrm{Syn}}}{D_{\mathrm{Rib}}} - k_{\mathrm{RdRp}}^{\mathrm{Bind}} P_{\mathrm{RdRp}}\left(R^{\mathrm{V}} + R^{\mathrm{C}}\right) - (N_{\mathrm{P_{RdRp}}} - 8)r^{\mathrm{Rel}}, \quad (3.1.31)$$

where the synthesis rate of the viral polymerase is proportional to the least abundant of the three mRNAs encoding its subunits. Implementing this change reduced the computational costs significantly as states with a high turnover that hover around zero, like the polymerase subunits in the original model, require a high number of iterations in stochastic algorithms. Further information on these modifications and an in-depth analysis of the resulting model are provided in reference [262]. A list of the model's reaction equations can also be found in the appendix (Section A.2.1).

Model extension In the deterministic model, we did not account for the cRNAs and vRNAs of individual genome segments separately, but rather considered their total number. This simplification does not alter the simulation results compared to a full implementation (Figure A.1 in the appendix). However, in a stochastic setting noise may affect each genome segment independently. We, thus, extended the equations for viral RNAs by including the individual segments explicitly (see Section A.2.2 for the complete set of reaction equations) and changed the virus release rate.

$$r^{\mathrm{Rel}} = 8k^{\mathrm{Rel}} \min\left(Vp^{\mathrm{cyt}}_{\mathrm{M1,i}}\right) \prod_{\mathrm{j}} \frac{P_{\mathrm{j}}}{P_{\mathrm{j}} + K_{\mathrm{V^{Rel}}} N_{\mathrm{P_j}}}, \quad i = 1, \dots, 8, \tag{3.1.32}$$

$$\text{with} \quad j \in \{\mathrm{RdRp}, \mathrm{HA}, \mathrm{NP}, \mathrm{NA}, \mathrm{M1}, \mathrm{M2}, \mathrm{NEP}\},$$

where i denotes the segment number. Hence, the release rate now depends on the least abundant of the eight NEP-M1-vRNP complexes in the cytoplasm ($Vp^{\mathrm{cyt}}_{\mathrm{M1,i}}$). We multiplied k^{Rel} by eight to obtain a rate that is comparable to the deterministic model, which used the total number of vRNPs from all eight segments instead of the level from just a single segment. In addition to these changes, we had to specify the step of virus entry in which the eight genome segments separate. A recent study shows that the vRNAs of incoming particles travel together until they reach the nucleus [37]. Thus, we modified Equations (3.1.5)–(3.1.6) and obtained:

$$\frac{\mathrm{d}V^{\mathrm{cyt}}}{\mathrm{d}t} = k^{\mathrm{Fus}} V^{\mathrm{En}} - k^{\mathrm{Imp}} V^{\mathrm{cyt}}, \tag{3.1.33}$$

$$\frac{\mathrm{d}Vp^{\mathrm{nuc}}_{\mathrm{i}}}{\mathrm{d}t} = k^{\mathrm{Imp}} V^{\mathrm{cyt}} + k^{\mathrm{Bind}}_{\mathrm{NP}} P_{\mathrm{NP}} R^{\mathrm{V}}_{\mathrm{RdRp,i}} - \left(k^{\mathrm{Bind}}_{\mathrm{M1}} P_{\mathrm{M1}} + k^{\mathrm{Deg}}_{\mathrm{Rnp}}\right) Vp^{\mathrm{nuc}}_{\mathrm{i}}, \tag{3.1.34}$$

where V^{cyt} represents the eight vRNPs traveling together through the cytoplasm. Once inside the nucleus, they separate into the individual vRNPs ($Vp^{\mathrm{nuc}}_{\mathrm{i}}$).

Computation We simulated the stochastic model as a discrete jump Markov process using the stochastic simulation algorithm (SSA), also known as the Gillespie algorithm (reviewed in [244]) and assumed that lumped reactions can also be modeled as a Markov process. Since computational performance is of critical importance we implemented an improved version of the algorithm, the sorting direct method [263]. In addition, an approximation of the SSA, the τ-leaping method with efficient step size selection [264], was used.

In order to obtain a representative sample of the system's dynamics, we performed 3 000 simulation runs for each condition[2]. A higher number of runs does not result in

---

[2] Typical computation times are in the order of one week on a Linux cluster (to simulate 3000×12 h).

a significant change of mean simulation values (Figure A.2 in the appendix). For some simulation runs, the loss of segment 7 (encoding M1 and M2) or a low number of M1 proteins prevented an efficient negative regulation of RNA synthesis. This lead to an exponential increase in RNA levels and hence computation time. We, thus, stopped simulations after 5×10^{10} iterations at the latest and disregarded such runs for all further analysis except when calculating the probability of unsuccessful infections and segment loss (Figure 4.17A, 4.18, 4.19A, and 4.22C). All model files were handled in MatLab (version 8.0.0.783 R2012b) on a Linux-based system and simulations where performed via the parallel computing toolbox on a Linux cluster.

Quantification of noise To quantify cellular noise in virus replication, we used the coefficient of variation.

$$\eta_Y \equiv \frac{\sigma_Y}{\langle y \rangle}, \tag{3.1.35}$$

where η_Y denotes the noise in quantity Y with standard deviation σ_Y and mean $\langle y \rangle$. Furthermore, the total noise (η_{tot}) in two identically regulated cellular (or viral) quantities Y and Z comprises an extrinsic component (η_{ext}), which is global to a single cell but varies from one cell to another, and an intrinsic component (η_{int}) corresponding to the inherent stochasticity in biochemical reactions [265]. These forms of noise were defined as follows:

$$\eta^2_{\text{int}} \equiv \frac{\langle (y-z)^2 \rangle}{2\langle y \rangle \langle z \rangle}, \quad \eta^2_{\text{ext}} \equiv \frac{\langle yz \rangle - \langle y \rangle \langle z \rangle}{\langle y \rangle \langle z \rangle}, \quad \eta^2_{\text{tot}} \equiv \frac{\langle y^2 + z^2 \rangle - 2\langle y \rangle \langle z \rangle}{2\langle y \rangle \langle z \rangle}, \tag{3.1.36}$$

where y and z are the realizations of the quantities Y and Z, respectively, and angled brackets denote means over these realizations [265]. As the vRNAs in stochastic simulations follow a log–normal distribution, we defined Y and Z in Equation (3.1.35) and (3.1.36) as the decadic logarithm of the vRNA level. For instance, in Figure 4.13C, Y is decadic logarithm of the mean vRNA level over all eight segments and Z the decadic logarithm of the indicated segment.

3.2. Virus infection across multiple scales

Our multiscale model of infection links the description of intracellular viral replication (see Section 3.1.1) with a model of the transmission of viruses between host cells. In the following, we first outline the extracellular part of the model before discussing the intracellular level as well as the integrated modeling approach. The complete model was first published in PLoS Computational Biology [266] and parts of the original publication are used hereafter.

Model of the extracellular level We used an age-segregated infection model for adherent cells, which follows from the general population balance [239], to describe the dynamics of uninfected target cells (T), infected cells (I), and their apoptotic counterparts (T_a and I_a, respectively).

$$\frac{\mathrm{d}T}{\mathrm{d}t} = \mu T - r^{\mathrm{Inf}} T - k_{\mathrm{T}}^{\mathrm{Apo}} T, \tag{3.2.1}$$

$$\frac{\partial I}{\partial t} + \frac{\partial I}{\partial \tau} = -\left(k_{\mathrm{T}}^{\mathrm{Apo}} + k_{\mathrm{I}}^{\mathrm{Apo}}(\tau)\right) I(t,\tau), \tag{3.2.2}$$

$$\frac{\mathrm{d}T_\mathrm{a}}{\mathrm{d}t} = k_{\mathrm{T}}^{\mathrm{Apo}} T - r^{\mathrm{Inf}} T_\mathrm{a} - k^{\mathrm{Lys}} T_\mathrm{a}, \tag{3.2.3}$$

$$\frac{\mathrm{d}I_\mathrm{a}}{\mathrm{d}t} = \int_0^\infty \left(k_{\mathrm{T}}^{\mathrm{Apo}} + k_{\mathrm{I}}^{\mathrm{Apo}}(\tau)\right) I(t,\tau)\,\mathrm{d}\tau + r^{\mathrm{Inf}} T_\mathrm{a} - k^{\mathrm{Lys}} I_\mathrm{a}, \tag{3.2.4}$$

$$\text{with} \quad \mu = \left[\frac{\mu_{\max}}{T_{\max}}\left(T_{\max} - T - \int_0^\infty I(t,\tau)\,\mathrm{d}\tau\right)\right]_+ ,$$

where uninfected cells grow with the specific rate μ or undergo apoptosis with rate $k_{\mathrm{T}}^{\mathrm{Apo}}$. Growth can occur with a maximum specific rate $\mu_{\max}$ to a maximum concentration of $T_{\max}$ cells assuming that all non-apoptotic cells occupy a finite surface area. The infection rate is denoted r^{Inf} and will be discussed at the end of this section. In Equation (3.2.2), infected cells have the age τ and undergo virus-induced apoptosis with an age-dependent rate, $k_{\mathrm{I}}^{\mathrm{Apo}}(\tau)$. Since infection creates cells with age zero, we obtained the boundary condition $I(t,\tau=0) = r^{\mathrm{Inf}} T$. Apoptotic uninfected cells in Equation (3.2.3) can either become infected or undergo cell lysis with rate k^{Lys}. The same lysis rate is used for apoptotic infected cells.

Assuming that there are no infected cells in the beginning ($I(t=0,\tau)=0$), we can rewrite Equation (3.2.2) in terms of an algebraic equation.

$$I(t,\tau) = \begin{cases} r^{\mathrm{Inf}}(t-\tau)\,T(t-\tau)\exp\left(-\int_0^\tau k_{\mathrm{T}}^{\mathrm{Apo}} + k_{\mathrm{I}}^{\mathrm{Apo}}(a)\,\mathrm{d}a\right), & t > \tau \geq 0, \\ 0, & \tau > t \geq 0, \end{cases} \tag{3.2.5}$$

where $I(t,\tau)$ can be interpreted as the infection age density such that $\int_{\tau_1}^{\tau_2} I(t,\tau)\,\mathrm{d}\tau$ gives the number of infected cells with age between τ_1 and τ_2. Equation (3.2.5) illustrates that cells which have age τ at time t were infected at time $t-\tau$. The integral term accounts for the loss of cells due to apoptosis. Using Equation (3.2.5) instead of Equation (3.2.2), thus, allows us to track the infection front precisely.

The equation for infectious virus particles (V) in the extracellular space follows as:

$$\frac{\mathrm{d}V}{\mathrm{d}t} = \int_0^\infty r^{\mathrm{Rel}}(\tau)\, I(t,\tau)\,\mathrm{d}\tau - k_{\mathrm{V}}^{\mathrm{Deg}} V + \sum_n \left[k_{\mathrm{n}}^{\mathrm{Dis}} V_{\mathrm{n}}^{\mathrm{Att}} - k_{\mathrm{c,n}}^{\mathrm{Att}} B_{\mathrm{n}} V\right], \tag{3.2.6}$$

$$\text{with} \quad B_{\mathrm{n}} = B_{\mathrm{n}}^{\mathrm{tot}}(T + T_{\mathrm{a}}) - V_{\mathrm{n}}^{\mathrm{Att}}, \quad k_{\mathrm{n}}^{\mathrm{Dis}} = \frac{k_{\mathrm{c,n}}^{\mathrm{Att}}}{k_{\mathrm{c,n}}^{\mathrm{Eq}}} \quad \text{and} \quad n \in \{\mathrm{hi}, \mathrm{lo}\},$$

where r^{Rel} denotes the age-dependent virus production rate. We assumed that virions are degraded/cleared (or lose infectivity) with rate $k_{\mathrm{V}}^{\mathrm{Deg}}$. The binding of virus particles to target cells was modeled as described before (Section 3.1.1). In brief, we considered two types of binding sites (B_{n}): high-affinity ($n = \mathrm{hi}$) and low-affinity ($n = \mathrm{lo}$) sites. The virus attaches to or dissociates from these sites with rates $k_{\mathrm{c,n}}^{\mathrm{Att}}$ and $k_{\mathrm{n}}^{\mathrm{Dis}}$, respectively, whereby the latter rate follows from the equilibrium constant, $k_{\mathrm{c,n}}^{\mathrm{Eq}}$. The concentration of free binding sites was calculated from their total number per cell ($B_{\mathrm{n}}^{\mathrm{tot}}$), the concentration of target cells, and the concentration of attached virus particles ($V_{\mathrm{n}}^{\mathrm{Att}}$). In this notation each virion occupies one binding site. Note that we did not consider binding to infected cells as neuraminidase expression on the cell surface limits superinfection [257].

In order to account for drug effects on virus entry, we defined equations for the concentration of attached virus particles ($V_{\mathrm{n}}^{\mathrm{Att}}$) on the surface of target cells (considering both apoptotic and non-apoptotic target cells) as well as for virions in the endosomes of these cells (V^{En}).

$$\frac{\mathrm{d}V_{\mathrm{n}}^{\mathrm{Att}}}{\mathrm{d}t} = k_{\mathrm{c,n}}^{\mathrm{Att}} B_{\mathrm{n}} V - \left(k_{\mathrm{n}}^{\mathrm{Dis}} + k^{\mathrm{En}}\right) V_{\mathrm{n}}^{\mathrm{Att}} - \left(r^{\mathrm{Inf}} + r^{\mathrm{Lys}}\right) V_{\mathrm{n}}^{\mathrm{Att}}, \tag{3.2.7}$$

$$\frac{\mathrm{d}V^{\mathrm{En}}}{\mathrm{d}t} = k^{\mathrm{En}} \left(V_{\mathrm{hi}}^{\mathrm{Att}} + V_{\mathrm{lo}}^{\mathrm{Att}}\right) - k^{\mathrm{Fus}} V^{\mathrm{En}} - \left(r^{\mathrm{Inf}} + r^{\mathrm{Lys}}\right) V^{\mathrm{En}}, \tag{3.2.8}$$

where k^{En} and k^{Fus} denote the endocytosis and fusion rate, respectively. The first two terms in Equation (3.2.7) account for virus binding and dissociation as well as for endocytosis. The last term quantifies the loss of virions with cells that leave the compartment of interest, i.e., with cells leaving the population of target cells by infection or cell lysis with rate r^{Inf} and r^{Lys}, respectively. Equation (3.2.8) accounts for the endocytosis of virions attached to both types of binding sites, the fusion of virions with the endosomal membrane, and again the loss of particles due to infection and lysis of target cells.

Since we considered a cell 'infected' as soon as viral genome copies enter its cytoplasm, the infection rate (r^{Inf}) follows from the fusion rate in Equation (3.2.8).

$$r^{\mathrm{Inf}} = F_{\mathrm{Inf}} k^{\mathrm{Fus}} V^{\mathrm{En}} \phi\left((T + T_{\mathrm{a}})^{-1}\right), \tag{3.2.9}$$

$$\text{with} \quad \phi\left((T + T_{\mathrm{a}})^{-1}\right) = \begin{cases} (T + T_{\mathrm{a}})^{-1}, & T + T_{\mathrm{a}} > 0, \\ 0, & T + T_{\mathrm{a}} = 0, \end{cases}$$

where F_{Inf} corresponds to the infection efficiency, i.e., the number of cells which become productively infected upon the fusion of one virion. This number cannot exceed one but may become lower if several virions are required to cause productive infection. While the first part of Equation (3.2.9) represents the number of cells that become infected per hour, the fraction serves two purposes: substituted in Equation (3.2.7) and (3.2.8) it provides the number of viruses per target cell and in Equation (3.2.1) and (3.2.3) it yields the fraction of non-apoptotic and apoptotic target cells, respectively, to total target cells. Similarly to r^{Inf}, the lysis rate of apoptotic target cells (r^{Lys}) can be derived.

$$r^{\mathrm{Lys}} = k^{\mathrm{Lys}} T_{\mathrm{a}} \cdot \phi\left((T + T_{\mathrm{a}})^{-1}\right). \tag{3.2.10}$$

Model of the intracellular level The intracellular level of infection was essentially modeled as described in Section 3.1.1. However, in contrast to the original description, we modified the equation for the virus release rate.

$$r^{\mathrm{Rel}}(\tau) = k^{\mathrm{Rel}}_{\mathrm{max}} \frac{Vp^{\mathrm{cyt}}_{\mathrm{M1}}}{Vp^{\mathrm{cyt}}_{\mathrm{M1}} + 8K_{\mathrm{V^{Rel}}}} \prod_{\mathrm{j}} \frac{P_{\mathrm{j}}}{P_{\mathrm{j}} + K_{\mathrm{V^{Rel}}} N_{\mathrm{P_j}}}, \tag{3.2.11}$$

$$\text{with} \quad j \in \{\mathrm{RdRp}, \mathrm{HA}, \mathrm{NP}, \mathrm{NA}, \mathrm{M1}, \mathrm{M2}, \mathrm{NEP}\},$$

where virus release depends on the abundance of progeny vRNPs in the cytoplasm ($Vp^{\mathrm{cyt}}_{\mathrm{M1}}$) and of structural viral proteins (P_{j}). In this context, $K_{\mathrm{V^{Rel}}}$ denotes the number of virus particles for which components must be present in order to reach half the maximum release rate. In its new form, r^{Rel} can only increase up to a maximum rate of $k^{\mathrm{Rel}}_{\mathrm{max}}$ assuming that there is only a limited number of host factors available for virus budding. This change was implemented to avoid unrealistically high virus production rates that occurred in some drug treatment regimes.

For simulations in Figures 4.23D and 4.24A, the complete intracellular model was used as described above. However, when coupling the model to the extracellular level, we neglected virus entry and initialized the model with a complete set of eight vRNPs in the cytoplasm. In these cases attachment, endocytosis, and fusion were considered at the extracellular level instead (Equation (3.2.7) and (3.2.8)).

Integrated simulation approach In order to ease the computational burden and allow for a more intuitive interpretation of simulation results, we assumed that the extracellular level has little or no influence on intracellular events, i.e., that each infected cell behaves the same independent of the time of infection and the extracellular environment. As shown by Haseltine and colleagues, this assumption permits the selective decoupling of both levels and reduces the model's complexity significantly [239]. It also allows us to first solve the intracellular level in order to obtain the virus release rate, r^{Rel}, as a function of the infection age, τ. This rate can then be used in Equation (3.2.6) to simulate the extracellular level.

The intracellular submodel was solved numerically using the CVODE routine from SUNDIALS [259] on a Linux-based system. Its parameters can be found in Table B.1 in the appendix. Model files and experiments were handled in the Systems Biology Toolbox 2 [260] for MatLab (version 8.0.0.783 R2012b). We then used Euler's method with a step size of $\Delta t = 0.05\,\mathrm{h}$ to solve the extracellular model (Equations (3.2.1) and (3.2.3)–(3.2.10)). Table B.2 provides the necessary parameters and the initial conditions are listed in Table B.3 in the appendix. The integrals in Equations (3.2.1), (3.2.4), and (3.2.6) were approximated in each step by substituting Equation (3.2.5) for $I(t, \tau)$ and using the rectangle rule with a step size of $\Delta t = 0.05\,\mathrm{h}$. To further reduce computational costs, the integral in Equation (3.2.5) was evaluated prior to simulation following the same approach[3]. The method was checked for numerical accuracy against simulations using smaller step sizes and by comparison to a discrete version of Equation (3.2.2) with a large number of age classes.

Parameter estimation Model parameters were estimated by fitting the complete intracellular submodel (including the equations for virus entry) to experimental virus titers per cell and to the levels of vRNA, cRNA and mRNA measured during single-cycle, high MOI infection (Figure 4.24A). Simultaneously, the reduced model (excluding virus entry) was coupled to the extracellular equations using the same parameters and the complete multiscale model was fitted to the time courses of uninfected and infected cells, their apoptotic counterparts, and the virus titer during multi-cycle, low MOI infection (Figure 4.24B). Estimation was performed using the fSSm algorithm for stochastic global optimization [261]. In particular, the algorithm was used to simultaneously minimize the least squares prediction error of all measured state variables (see Equation (3.1.30)), whereby the error of each variable was normalized to its respective maximum measurement value (e.g. the deviation between measured and simulated vRNA level was weighted by the maximum of the measured vRNA level). The summed errors of the intracellular and extracellular part of the model were then divided by the number of measurements, respectively, and added to attain an overall measure of fit quality. Since experiments indicated that our quantitative real-time reverse transcription polymerase chain reaction (RT-qPCR) detects free viral RNAs from the seed virus supernatant, which may adhere to cells but cannot enter them, we applied the first measurement value as an offset to all simulation values of viral RNAs. Bootstrap confidence intervals were determined as described in reference [249] considering the standard deviations in Figure 4.24A as well as a 20% error for cell counts and 0.3 log for virus titers in Figure 4.24B.

---

[3] Typical simulation times for the complete model are in the order of 0.5 s on a desktop computer (to simulate 72 h).

Simulation of drug treatment In order to simulate drug treatment with efficacy ϵ, parameters in the model which correspond to the drug's target (Table B.4 in the appendix) were perturbed by $1-\epsilon$. Treatment was assumed to occur at constant efficacy starting from 0 hours post infection (hpi). For results in Figures 4.28A and 4.29C, the reduced intracellular model was simulated first to determine the virus release rate (r^{Rel}). The total amount of virus particles produced by an average infected cell over its lifetime ($V_{\mathrm{tot}}^{\mathrm{Rel}}$), i.e., the viral burst size, was then calculated by considering cell death.

$$V_{\mathrm{tot}}^{\mathrm{Rel}} = \int_0^\infty r^{\mathrm{Rel}}\left(\tau\right) \exp\left(-\int_0^\tau k_{\mathrm{T}}^{\mathrm{Apo}} + k_{\mathrm{I}}^{\mathrm{Apo}}\left(a\right) \mathrm{d}a\right) \mathrm{d}\tau. \tag{3.2.12}$$

Cell culture and virus infection For a detailed description of the multi-cycle experiments (Figure 4.24B) the reader is referred to reference [267] from which the data were adopted. Single-cycle infections (Figure 4.24A) were carried out by our coworkers as described in reference [266]. To correctly account for the loss of intracellular viral components due to virus release, the total amount of virus particles leaving an average infected cell was determined using the hemagglutination assay as described previously by Kalbfuss *et al.* [268]. Titer measurements in $\log_{10}$ HA units (HAU) per test volume can be converted into hemagglutinating particles per ml according to the following equation.

$$c_{\mathrm{virus}} = 2 \times 10^7 \cdot 10^{(\log_{10} \mathrm{HAU}/100\,\mu\mathrm{l})}, \tag{3.2.13}$$

where we assumed that at least one virus particle per erythrocyte (present at 2×10^7 cells/ml) is required to cause agglutination [173].

3.3. Defective interfering viruses

Here, two mathematical models for the growth of DI viruses are presented. The first focuses on the replication of DI RNAs inside an infected cell, whereas the second describes the accumulation of DIPs in a continuous production system for influenza A virus.

3.3.1. Intracellular DI RNA replication

An early version of our model for DI RNA replication was developed as part of the bachelor thesis of Helene Kaffka [269]. It represents an extension of the deterministic description of intracellular virus replication (Equations (3.1.1)–(3.1.27)). We used the work of Kaffka as a basis for the model presented hereafter but explicitly accounted for the vRNAs and cRNAs of individual genome segment. This results in a more general description that can account for DI RNAs from different genome segments. In the following, we focused on a DI RNA derived from segment 3 (encoding PA). A version of the model that describes a DI RNA of segment 4 (encoding HA) can be found in the appendix (Section C.2).

Virus entry Virus entry was essentially modeled as described in Equations (3.1.1)–(3.1.4). Note that here V^{Ex}, $V_{\mathrm{n}}^{\mathrm{Att}}$ and V^{En} denote the STV only, and similar equations had to be added for DIPs (see Section C.1 in the appendix for a complete list of equations). Furthermore, we replaced Equation (3.1.5) by

$$\frac{\mathrm{d}V^{\mathrm{cyt}}}{\mathrm{d}t} = k^{\mathrm{Fus}} V^{\mathrm{En}} - k^{\mathrm{Imp}} V^{\mathrm{cyt}}, \tag{3.3.1}$$

and added

$$\frac{\mathrm{d}D^{\mathrm{cyt}}}{\mathrm{d}t} = k^{\mathrm{Fus}} D^{\mathrm{En}} - k^{\mathrm{Imp}} D^{\mathrm{cyt}}, \tag{3.3.2}$$

where V^{cyt} and D^{cyt} denote cytoplasmic complexes that contain all eight genome segments including either the full-length or the defective segment 3, respectively. These complexes were implemented based on recent experimental findings indicating that all genome segments co-localize during virus entry until they reach the nucleus [37].

Viral RNA replication Upon nuclear import, the eight genome segments separate and begin their independent replication. The equations for nuclear vRNPs are the following:

$$\frac{\mathrm{d}Vp_{\mathrm{k}}^{\mathrm{nuc}}}{\mathrm{d}t} = k^{\mathrm{Imp}} V^{\mathrm{cyt}} + k^{\mathrm{Imp}} D^{\mathrm{cyt}} + k_{\mathrm{NP}}^{\mathrm{Bind}} P_{\mathrm{NP}} R_{\mathrm{RdRp,k}}^{\mathrm{V}} - \left(k_{\mathrm{M1}}^{\mathrm{Bind}} P_{\mathrm{M1}} + k_{\mathrm{Rnp}}^{\mathrm{Deg}}\right) Vp_{\mathrm{k}}^{\mathrm{nuc}}, \tag{3.3.3}$$

$$\text{for} \quad k = 1, 2, 4, \ldots, 8 \quad \text{and}$$

$$\frac{\mathrm{d}Vp_3^{\mathrm{nuc}}}{\mathrm{d}t} = k^{\mathrm{Imp}} V^{\mathrm{cyt}} + k_{\mathrm{NP}}^{\mathrm{Bind}} P_{\mathrm{NP}} R_{\mathrm{RdRp,3}}^{\mathrm{V}} - \left(k_{\mathrm{M1}}^{\mathrm{Bind}} P_{\mathrm{M1}} + k_{\mathrm{Rnp}}^{\mathrm{Deg}} \right) Vp_3^{\mathrm{nuc}}, \tag{3.3.4}$$

$$\frac{\mathrm{d}Vp_9^{\mathrm{nuc}}}{\mathrm{d}t} = k^{\mathrm{Imp}} D^{\mathrm{cyt}} + k_{\mathrm{NP}}^{\mathrm{Bind}} P_{\mathrm{NP}} R_{\mathrm{RdRp,9}}^{\mathrm{V}} - \left(k_{\mathrm{M1}}^{\mathrm{Bind}} P_{\mathrm{M1}} + k_{\mathrm{Rnp}}^{\mathrm{Deg}} \right) Vp_9^{\mathrm{nuc}}, \tag{3.3.5}$$

where $k = 1, \ldots, 8$ are the full-length segments and $k = 9$ denotes the defective segment 3. Viral RNA synthesis and encapsidation were modeled as described in Equations (3.1.7)–(3.1.12). However, we assumed that DI RNAs have a replication advantage over wild-type (wt) segments during cRNA synthesis due to their reduced length.

$$\frac{\mathrm{d}R_9^{\mathrm{C}}}{\mathrm{d}t} = (F_{\mathrm{Adv}} + 1)\, k_{\mathrm{C}}^{\mathrm{Syn}} Vp_9^{\mathrm{nuc}} - k_{\mathrm{RdRp}}^{\mathrm{Bind}} P_{\mathrm{RdRp}} R_9^{\mathrm{C}} - k_{\mathrm{R}}^{\mathrm{Deg}} R_9^{\mathrm{C}}, \tag{3.3.6}$$

where F_{Adv} denotes the factor with which the synthesis of the DI cRNA exceeds the production of its full-length counterpart. Note that whether this advantage occurs in cRNA or vRNA synthesis does not affect simulation result [269]. As a first approximation we chose the following.

$$F_{\mathrm{Adv}} = \left(\frac{L_3^{\mathrm{V}}}{L_9^{\mathrm{V}}} - 1 \right), \tag{3.3.7}$$

where L_3^{V} and L_9^{V} are the length of the full-length and defective segment 3 vRNA, respectively. By using Equation (3.3.7), we assumed that a DI RNA replicates twice as fast as its cognate full-length RNA if it comprises half the length.

Viral mRNA and protein synthesis Similar to the original model, viral mRNAs are produced by vRNPs in the nucleus.

$$\frac{\mathrm{d}R_{\mathrm{i}}^{\mathrm{M}}}{\mathrm{d}t} = \frac{k_{\mathrm{M}}^{\mathrm{Syn}}}{L_{\mathrm{i}}} Vp_{\mathrm{i}}^{\mathrm{nuc}} - k_{\mathrm{M}}^{\mathrm{Deg}} R_{\mathrm{i}}^{\mathrm{M}}, \quad i = 1, \ldots, 8, \tag{3.3.8}$$

where vRNPs of segment i synthesize their corresponding mRNA. Note that we neglected mRNA synthesis by the defective segment as such mRNAs would most likely not encode for functional proteins. The kinetics of viral protein dynamics were modeled as described in Equations (3.1.17)–(3.1.26) with two exceptions: (i) the release of both, STVs and DIPs drains the pool of M1, HA, NA and M2 proteins, and (ii) following the model of Kaffka, virus budding does not require additional RdRp, NP and NEP proteins, i.e., proteins that are not bound in vRNPs [269]. The latter change was implemented as DI RNA synthesis can deplete the pool of NP and RdRps. We assumed that virus release can still occur in this regime and that *free* viral polymerases, NP, and NEP proteins are not essential for budding.

Virus release To account for a proposed competition between full-length and DI RNAs during virus assembly, we included a segment-specific packaging mechanism based on experimental work by Fournier *et al.* [34] and the model of Kaffka [269]. In particular, we assumed that cytoplasmic vRNPs ($Vp^{\text{cyt}}_{\text{M1}}$) form complexes that comprise all eight genome segments including either the full-length or defective segment 3 ($V^{\text{cyt}}_{\text{Cplx}}$ and $D^{\text{cyt}}_{\text{Cplx}}$, respectively).

$$\begin{aligned}\frac{\mathrm{d}Vp^{\text{cyt}}_{\text{M1,k}}}{\mathrm{d}t} &= k^{\text{Exp}} P_{\text{NEP}} Vp^{\text{nuc}}_{\text{M1,k}} - k^{\text{Cplx}} Vp^{\text{cyt}}_{\text{M1,3}} \prod_k Vp^{\text{cyt}}_{\text{M1,k}} \\ &\quad - k^{\text{Cplx}} Vp^{\text{cyt}}_{\text{M1,9}} \prod_k Vp^{\text{cyt}}_{\text{M1,k}} - k^{\text{Deg}}_{\text{Rnp}} Vp^{\text{cyt}}_{\text{M1,k}}, \qquad (3.3.9)\\ &\text{for} \quad k = 1, 2, 4, \ldots, 8 \quad \text{and}\end{aligned}$$

$$\frac{\mathrm{d}Vp^{\text{cyt}}_{\text{M1,3}}}{\mathrm{d}t} = k^{\text{Exp}} P_{\text{NEP}} Vp^{\text{nuc}}_{\text{M1,3}} - k^{\text{Cplx}} Vp^{\text{cyt}}_{\text{M1,3}} \prod_k Vp^{\text{cyt}}_{\text{M1,k}} - k^{\text{Deg}}_{\text{Rnp}} Vp^{\text{cyt}}_{\text{M1,3}}, \qquad (3.3.10)$$

$$\frac{\mathrm{d}Vp^{\text{cyt}}_{\text{M1,9}}}{\mathrm{d}t} = k^{\text{Exp}} P_{\text{NEP}} Vp^{\text{nuc}}_{\text{M1,9}} - k^{\text{Cplx}} Vp^{\text{cyt}}_{\text{M1,9}} \prod_k Vp^{\text{cyt}}_{\text{M1,k}} - k^{\text{Deg}}_{\text{Rnp}} Vp^{\text{cyt}}_{\text{M1,9}}, \qquad (3.3.11)$$

$$\frac{\mathrm{d}V^{\text{cyt}}_{\text{Cplx}}}{\mathrm{d}t} = k^{\text{Cplx}} Vp^{\text{cyt}}_{\text{M1,3}} \prod_k Vp^{\text{cyt}}_{\text{M1,k}} - r^{\text{Rel}} - k^{\text{Deg}}_{\text{Rnp}} V^{\text{cyt}}_{\text{Cplx}}, \qquad (3.3.12)$$

$$\frac{\mathrm{d}D^{\text{cyt}}_{\text{Cplx}}}{\mathrm{d}t} = k^{\text{Cplx}} Vp^{\text{cyt}}_{\text{M1,9}} \prod_k Vp^{\text{cyt}}_{\text{M1,k}} - r^{\text{Rel}}_{\text{D}} - k^{\text{Deg}}_{\text{Rnp}} D^{\text{cyt}}_{\text{Cplx}}, \qquad (3.3.13)$$

where k^{Cplx} is the complex formation rate and r^{Rel} and $r^{\text{Rel}}_{\text{D}}$ denote the release rates of STVs and DIPs, respectively. The amount of released virus particles is described by the following equations.

$$\frac{\mathrm{d}V^{\text{Rel}}}{\mathrm{d}t} = r^{\text{Rel}} = 8k^{\text{Rel}} V^{\text{cyt}}_{\text{Cplx}} \prod_{\text{j}} \frac{P_{\text{j}}}{P_{\text{j}} + K_{V^{\text{Rel}}} N_{P_{\text{j}}}}, \qquad (3.3.14)$$

$$\frac{\mathrm{d}D^{\text{Rel}}}{\mathrm{d}t} = r^{\text{Rel}}_{\text{D}} = 8k^{\text{Rel}} D^{\text{cyt}}_{\text{Cplx}} \prod_{\text{j}} \frac{P_{\text{j}}}{P_{\text{j}} + K_{V^{\text{Rel}}} N_{P_{\text{j}}}}, \qquad (3.3.15)$$

$$\text{with} \quad j \in \{\text{HA}, \text{NA}, \text{M1}, \text{M2}\},$$

where V^{Rel} and D^{Rel} are progeny STVs and DIPs, respectively. We multiplied k^{Rel} by eight to obtain a similar release rate than in the original model that used the total amount of cytoplasmic vRNPs instead of a complex containing all eight genome segments (see Equation (3.1.27)).

Coinfection probability Assuming that the infection of a cell by a virus particle is a random process, the infection probability (P_{I}) follows a Poisson distribution.

$$P_{\mathrm{I}} = 1 - e^{-aMOI}, \tag{3.3.16}$$

where MOI denotes the multiplicity of infection, i.e., the average number of infectious virus particles per cell, and a is a constant defining the infection efficiency [270]. Since the MOI considers infectious particles only, we obtain $a = 1$. The probability of coinfecting a cell with an STV and a DIP (P_{CI}) follows as the joint probability.

$$P_{\mathrm{CI}} = \left(1 - e^{-MOI_{\mathrm{STV}}}\right)\left(1 - e^{-MOI_{\mathrm{DIP}}}\right), \tag{3.3.17}$$

where MOI_{STV} and MOI_{DIP} are the numbers of infectious STVs and DIPs per cell, respectively.

Computation Parameter values and initial conditions for the model can be found in Table C.1 and C.2 in the appendix. The model files were handled in the Systems Biology Toolbox 2 [260] for MatLab (version 8.0.0.783 R2012b) and simulation were conducted using the CVODE routine from SUNDIALS [259] on a Linux-based system[4].

3.3.2. DIP growth during continuous virus infection

In order to analyze oscillations in virus titers which were observed in a continuous system for influenza A virus production, we developed a segregated mathematical model for the replication of DIPs and STVs in a cell population. This model is based on an existing description of a batch process proposed by Kirkwood and Bangham [271] and was first published in PLoS One [148]. Parts of the original publication are used hereafter.

Model in the presence of DIPs Our model for DIP replication focuses on three key components: the number of uninfected cells, infected cells, and virus particles. The concentration of uninfected target cells (T) is given by the following equation.

$$\frac{\mathrm{d}T}{\mathrm{d}t} = \mu T - k^{\mathrm{Inf}}\left(V_{\mathrm{s}} + V_{\mathrm{d}}\right)T + D\left(T_{\mathrm{in}} - T\right), \tag{3.3.18}$$

where V_{s} and V_{d} denote the concentrations of STVs and DIPs, respectively. We assumed that cells grow exponentially with rate constant μ and become infected by virus particles with rate k^{Inf}, which is the same for both virus types. The last term in Equation (3.3.18) accounts for the continuous feed of cells with concentration T_{in} and their harvest with D

---

[4] Typical simulation times are in the order of 0.6 s on a standard desktop computer (to simulate 12 h).

denoting the virus reactor's dilution rate. Here, ideal mixing is assumed. With respect to the roughly constant concentration of cells observed in the cell reactor, we chose T_{in} to be independent of time. In general, T_{in} may vary in the initial phase of cultivation to a certain degree until the cell reactor reaches steady state.

The population of infected cells was subdivided into cells infected with STVs (I_{s}) and DIPs (I_{d}) as well as into coinfected cells (I_{c}).

$$\frac{\mathrm{d}I_{\text{d}}}{\mathrm{d}t} = k^{\text{Inf}} V_{\text{d}} T - \left(k^{\text{Inf}} V_{\text{s}} - \mu\right) I_{\text{d}} - D I_{\text{d}}, \tag{3.3.19}$$

$$\frac{\mathrm{d}I_{\text{s}}}{\mathrm{d}t} = k^{\text{Inf}} V_{\text{s}} T - \left(k^{\text{Inf}} V_{\text{d}} + k^{\text{Apo}}\right) I_{\text{s}} - D I_{\text{s}}, \tag{3.3.20}$$

$$\frac{\mathrm{d}I_{\text{c}}}{\mathrm{d}t} = k^{\text{Inf}} \left(V_{\text{s}} I_{\text{d}} + V_{\text{d}} I_{\text{s}}\right) - k^{\text{Apo}} I_{\text{c}} - D I_{\text{c}}. \tag{3.3.21}$$

The first term in Equation (3.3.19) and (3.3.20) accounts for the infection of target cells by both viruses. Similarly, infection of I_{s} and I_{d} by DIPs and STVs, respectively, yields coinfected cells in Equation (3.3.21). Since DIPs do not replicate in the absence of an STV, we assumed that DIP infection alone does not interfere with normal cellular processes. Hence, DIP-infected cells may continue to grow giving rise to infected daughter cells, an assumption already used by Kirkwood and Bangham [271]. Furthermore, I_{d} cannot revert back to the uninfected state by virus degradation. In cells infected with the STV or coinfected with both types of particles replication takes place resulting in virus-induced apoptosis with rate k^{Apo}. Again, the last term in Equations (3.3.19)–(3.3.21) accounts for the dilution of the reactor content. To keep the model simple, we neglected that DIPs may not interfere with STV replication after it is well advanced. Kirkwood and Bangham accounted for this by introducing further subclasses of cells which track the infection age, i.e., the time that has elapsed since the cell was infected [271]. However, such subclasses severely increase the dimensionality of the model and impair a mathematical analysis.

Finally, the concentration of STVs (V_{s}) and DIPs (V_{d}) is the following.

$$\frac{\mathrm{d}V_{\text{s}}}{\mathrm{d}t} = k^{\text{Prod}} I_{\text{s}} - \left(\frac{k^{\text{Inf}}}{F_{\text{Inf}}} \left(T + I_{\text{d}} + I_{\text{s}} + I_{\text{c}}\right) + k_{\text{V}}^{\text{Deg}} + D\right) V_{\text{s}}, \tag{3.3.22}$$

$$\frac{\mathrm{d}V_{\text{d}}}{\mathrm{d}t} = k^{\text{Prod}} I_{\text{c}} + f k^{\text{Prod}} I_{\text{s}} - \left(\frac{k^{\text{Inf}}}{F_{\text{Inf}}} \left(T + I_{\text{d}} + I_{\text{s}} + I_{\text{c}}\right) + k_{\text{V}}^{\text{Deg}} + D\right) V_{\text{d}}, \tag{3.3.23}$$

where STV-infected cells produce primarily STVs with rate k^{Prod} and a small fraction of DIPs (f). By contrast, coinfected cells exclusively release DIPs. Furthermore, free virus particles are taken up by all four cell types or degrade with rate $k_{\text{V}}^{\text{Deg}}$. For the sake of simplicity, we assume that the uptake of one virion is sufficient to cause productive infection such that the infection efficiency is $F_{\text{Inf}} = 1$.

Model in the absence of DIPs As was proven in reference [148], the system in Equations (3.3.18)–(3.3.23) reduces to a three dimensional model of virus growth if the seed virus is free of DIPs ($V_{\mathrm{d}}\left(t=0\right)=0$), no DIP-infected or coinfected cells are present in the beginning ($I_{\mathrm{d}}\left(t=0\right)=I_{c}\left(t=0\right)=0$), and cells infected by STVs do not generate DIPs *de novo* ($f=0$):

$$\begin{aligned}\frac{\mathrm{d}T}{\mathrm{d}t} &=\mu T-k^{\mathrm{Inf}}V_{\mathrm{s}}T+D\left(T_{\mathrm{in}}-T\right), && (3.3.24)\\ \frac{\mathrm{d}I_{\mathrm{s}}}{\mathrm{d}t} &=k^{\mathrm{Inf}}V_{\mathrm{s}}T-\left(k^{\mathrm{Apo}}+D\right)I_{\mathrm{s}}, && (3.3.25)\\ \frac{\mathrm{d}V_{\mathrm{s}}}{\mathrm{d}t} &=k^{\mathrm{Prod}}I_{\mathrm{s}}-\left(k^{\mathrm{Inf}}\left(T+I_{\mathrm{s}}\right)+k_{\mathrm{V}}^{\mathrm{Deg}}+D\right)V_{\mathrm{s}}. && (3.3.26)\end{aligned}$$

Computation For both the full model and the reduced version, we chose parameters and initial conditions according to Table 4.5 (and Table C.3 in the appendix). We solved the models numerically using the CVODE routine from SUNDIALS [259] on a Linux-based system[5]. Model files were handled in the Systems Biology Toolbox 2 [260] for MatLab (version 8.0.0.783 R2012b).

---

[5] Typical simulation times are in the order of 0.01 s on a standard desktop computer (to simulate 18 days).

Chapter 4

Results and Discussion

With respect to the hierarchical nature of influenza virus infection the following chapter was divided into three parts starting with the intracellular level and gradually moving toward virus growth in cell culture. In the first section, we use deterministic and stochastic modeling approaches to elucidate the intracellular life cycle of influenza A viruses. We then build on these models to develop a multiscale description of infection which links intracellular replication with the dynamics of the host cell population. The last section is devoted to the synthesis of DI RNAs inside an infected cell and DIP production in continuous cell culture.

4.1. The intracellular life cycle of influenza A virus

The analysis of intracellular virus replication is key to a systems-level understanding of viral infection because it is the level where the virus synthesizes its genome and proteins to assemble the smallest carrier of infection, the virion, and where it most intimately interacts with its host. It is also the level where state-of-the-art antiviral agents counteract the disease. Thus, we developed a model of the intracellular life cycle of influenza A viruses as a first step toward a more comprehensive description of infection. Traditionally, such models follow a deterministic formalism, which we also use in the first part of this section. In the second part, we then turn toward stochastic simulation techniques to account for the inherent randomness of biochemical reactions.

4.1.1. Dynamics of intracellular virus replication

For the development of our model, we followed a top-down approach such that we only included the key steps of intracellular influenza A virus replication and neglected details where data are lacking. In this way, the resulting model becomes less complex, easier to interpret and, most importantly, has fewer unknown parameters, whose estimation would be difficult in the absence of measurements. The main features of the final model are depicted in Figure 2.2 on page 7. In the following, we discuss in detail the simulation of virus entry, the transition from transcription to genome replication, nuclear export, and virus release. Note that in the rest of this section parts of the original research article on our intracellular model were used [250]. Copyright of these passages lies with the Journal of Virology (Copyright © American Society for Microbiology, [Journal of Virology, 86, 2012, 7806-7817, 10.1128/JVI.00080-12]).

Virus entry Intracellular virus replication starts with the binding of virus particles to the cell surface. We modeled this process based on the work of Nunes-Correia *et al.* who performed experiments and theoretical studies on the adsorption of influenza A virus to MDCK cells [251]. In agreement with their findings, our model considers two types of binding sites, high-affinity and low-affinity sites, which, according to Nunes-Correia *et al.*, might correspond to sialic acid-containing ligands and less specific interactions, respectively. In their study, Nunes-Correia and colleagues calculated the rates of virus attachment to these sites. However, they did so for binding at 4 and 20°C only. To obtain the binding rates at 37°C, we tuned our model to experiments showing that the equilibrium of binding is reached after 20 min (Figure 4.1A and reference [251]). Note that viruses which attach to high-affinity sites reach the equilibrium faster than their counterparts that interact with low-affinity sites. The resulting parameter estimates for virus adsorption can be found in Table 4.1. Despite adjusting the binding rates, our description of virus adsorption still yields the steady state binding characteristics determined by Nunes-Correia *et al.* and is in good agreement with their experiments (Figure 4.1B).

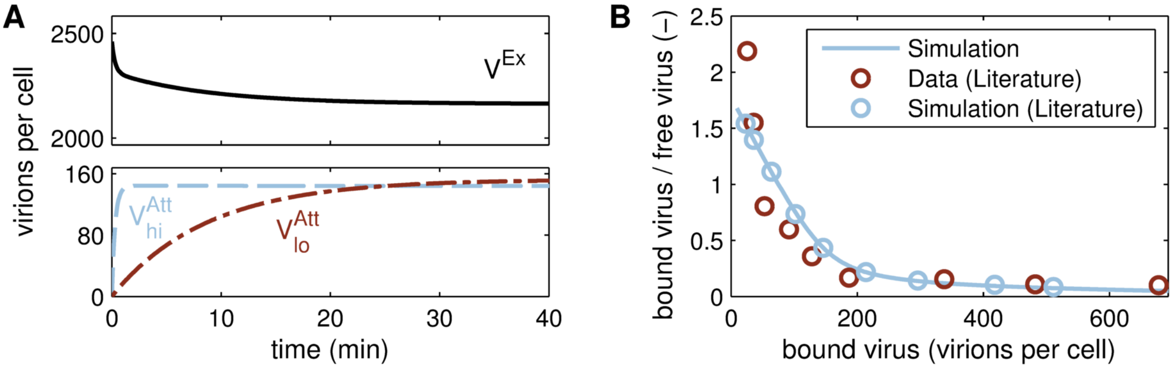

Figure 4.1.: Virus attachment to the cell surface. Virus binding was simulated according to the experimental setup of Nunes-Correia *et al.* and compared to their measurement data and simulation results [251]. In brief, R18-labeled influenza virus (A/PR/8/34 (H1N1)) was added to MDCK cells at various concentrations in the presence of endocytosis inhibitors and incubated at 37°C. Virus-cell binding was determined by dequenching of the label. (A) Simulated amount of extracellular virus (V^{Ex}), virus bound to high-affinity sites ($V_{\mathrm{hi}}^{\mathrm{Att}}$), and virus bound to low-affinity sites ($V_{\mathrm{lo}}^{\mathrm{Att}}$) for an infection at an MOI of 2460. Binding was assumed to be in equilibrium when V^{Ex} reaches 95% of its steady state level. (B) The amount of free virions in the medium and virus bound to both types of binding sites in steady-state for different MOIs.

Table 4.1.: Parameter estimates for virus entry.

Parameter		Value	Local sensitivity[a] (%)
F_{Fus}	(–)	0.51	0.44
$k_{\mathrm{hi}}^{\mathrm{Att}}$	$(\mathrm{sites}\cdot\mathrm{h})^{-1}$	8.09×10^{-2}	3.06×10^{-4}
$k_{\mathrm{lo}}^{\mathrm{Att}}$	$(\mathrm{sites}\cdot\mathrm{h})^{-1}$	4.55×10^{-4}	4.35×10^{-6}
k^{En}	(h^{-1})	4.80	4.46×10^{-2}
k^{Fus}	(h^{-1})	3.21	1.32×10^{-2}

[a] Normalized change in model output in response to parameter perturbations by 1% (see Equation (2.4.3) and (2.4.4)).

Once bound to the plasma membrane, virions can enter the cell via receptor-mediated endocytosis where they migrate through the cytoplasm within endosomes. The acidification in late endosomes then triggers viral fusion with the endosomal membrane. We used R18-labeling data obtained by Stegmann *et al.* [272] to calibrate these steps in our model (Figure 4.2A). Based on these experiments, the first fusion events occur within 5 min after adsorption with most of the fusion-competent viruses escaping from endosomes within 80 min. Yet, half of the adsorbed virus particles fail to fuse and are degraded in lysosomes. We considered this in our model by defining the fraction of fusion-competent viruses, F_{Fus}. Note that the high sensitivity of F_{Fus} indicates an accurate estimation of this parameter from R18-labeling experiments (Table 4.1). By linking the binding and fusion experiments, we were able to infer the dynamics of virus entry (Figure 4.2B). At

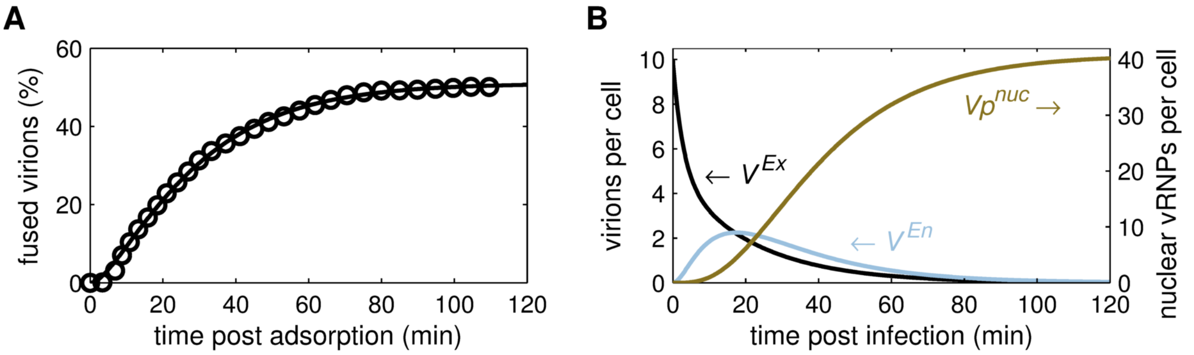

Copyright © American Society for Microbiology, [Journal of Virology, 86, 2012, 7806-7817, 10.1128/JVI.00080-12]

Figure 4.2.: Fusion with endosomes and virus entry dynamics. (A) Model fit (lines) to data (circles) for the fusion of R18-labeled influenza virus (strain NIB26) with endosomes in MDCK cells adopted from Stegmann *et al.* [272]. In brief, virus was added to MDCK cells at 0°C for 1 h to allow for virus adsorption, cells were washed, and warm buffer (37°C) was added. The percentage of fused to total cell-associated virus is shown. (B) Simulated amount of extracellular virions in the medium (V^{Ex}), virions in endosomes (V^{En}), and vRNPs in the nucleus (Vp^{nuc}) for an infection at an MOI of 10 in the absence of viral protein synthesis and vRNP degradation.

an MOI of 10 most extracellular virions enter the cell within 1 h. During this process, the number of available binding sites is not a limiting factor. Subsequently, a peak in endosomal virus particles occurs around 20 min post infection. After approximately 90 min, half of the parental vRNPs have reached the nucleus, while the rest was degraded within fusion-incompetent viruses.

Stabilization hypothesis Once in the nucleus, vRNPs first transcribe viral mRNAs whereas cRNA accumulation is only observed after an initial round of viral protein synthesis [58]. Vreede *et al.* proposed that this transition to genome replication results from the stabilization of nascent cRNA by viral polymerases and NP proteins, which prevents the degradation by cellular nucleases (see Figure 2.3B). We included this mechanism into our model and tested whether it can capture published data from two experimental studies [60, 66]. In these works, Vreede *et al.* obtained the time course of mRNA, cRNA, and vRNA under various experimental conditions by semi-quantitative NA gene-specific primer extension analysis. To use the data for modeling, we performed a densitometric analysis[1] and normalized each data point to the vRNA signal (at the same time point), which Vreede and coworkers assumed to be constant in their experiments. This provided us with the level of mRNA and cRNA relative to vRNA.

One key observation in favor of cRNA stabilization is the synthesis of both mRNA and cRNA by virion-derived vRNPs *in vitro*, i.e., in the absence of *de novo* synthesized viral proteins and cellular nucleases [66]. Our model can reproduce this observation (Figure 4.3A) and allows us to estimate the kinetic parameters of the processes involved. As expected in the absence of nucleases, simulations yield a low degradation rate of cRNA ($k_{\mathrm{R}}^{\mathrm{Deg}}$ in Table 4.2) indicating its stability under *in vitro* conditions. By contrast, degradation of viral mRNAs ($k_{\mathrm{M}}^{\mathrm{Deg}}$) occurs more rapidly, which results from the observation that mRNAs reach steady state after 12 h (Figure 4.3A). However, estimation of this rate might be biased by the assumption that mRNA synthesis occurs at a constant rate throughout the experiment. This might not be the case due to the loss of enzymatic activity or the depletion of precursors, such as cap sources, which would also yield a constant mRNA level but at a much lower degradation rate.

To resemble the *in vivo* situation more closely, we next analyzed infection experiments in 293T cells from literature [60]. Vreede *et al.* conducted these experiments in the presence of cycloheximide, which inhibits *de novo* viral protein synthesis and, hence, prevents cRNA stabilization. To rescue cRNA accumulation, four viral proteins were expressed in different combinations prior to infection: wild-type NP, PA, and PB2 as well as a catalytically inactive PB1 (PB1a, containing the PB1-D445A/D446A mutation). A trimeric poly-

---

[1] Quantification of band intensities against background was performed using the ImageJ software.

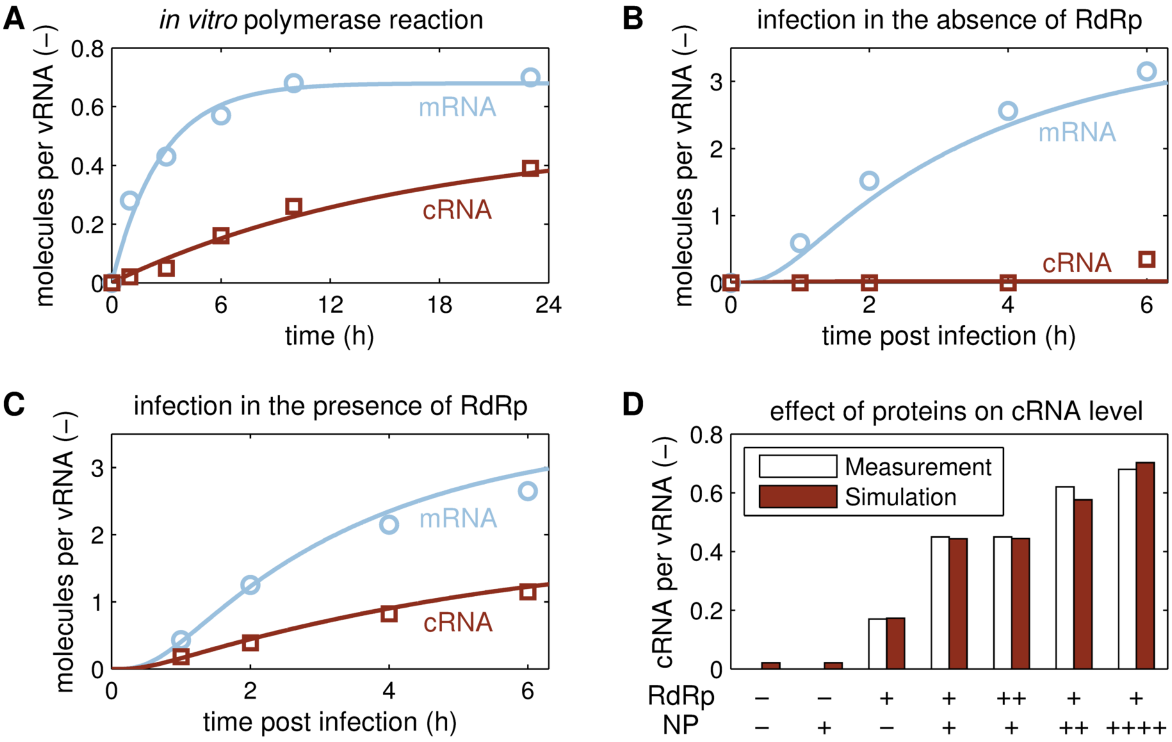

Copyright © American Society for Microbiology, [Journal of Virology, 86, 2012, 7806-7817, 10.1128/JVI.00080-12]

Figure 4.3.: Simulation of the cRNA stabilization hypothesis. Experiments yielding NA gene-specific mRNA (○) and cRNA levels (□ and open bars) were conducted by Vreede *et al.* using primer extension analysis [60, 66]. (A) Model fit to data of an *in vitro* polymerase assay using virion-derived vRNPs [66]. (B,C) Model fit to infections of 293T cells with influenza A/WSN/33 at an MOI of 5 [66]. In brief, protein synthesis during infection was inhibited and plasmids expressing NP, PA and PB2 (B), or NP, PA, PB2 and PB1a (C) were transfected prior to infection. (D) Same as in C except that various amounts of plasmids expressing PA, PB2 and PB1a (RdRp), NP, and empty vector (–) were transfected prior to infection. Bars represent the cRNA level at 2 hpi. PB1a, catalytically inactive mutant PB1-D445A/D446A.

merase complex with PB1a does not synthesize viral RNAs yet still stabilizes cRNA [60]. For model calibration, we fitted all available infection experiments simultaneously using the same parameter set, and we only changed the initial conditions according to the experimental setup (see Table A.2 in the appendix). Figure 4.3B shows the time course of cRNA and mRNA in the presence of NP proteins but absence of complete viral polymerases (the PB1 subunit was omitted in the experiment). While mRNAs accumulate within a few hours, cRNAs are rapidly degraded in the simulation, which agrees well with the experimental observation. According to Vreede *et al.* the increase in cRNA at 6 hours post infection (hpi) is due to a minor breakthrough of cycloheximide inhibition and is, thus, not reflected in the model [60]. In support of a degradation by cellular nucleases, parameter estimation yields a much higher cRNA degradation rate in infection experiments than in the *in vitro* assay ($k_{\mathrm{R}}^{\mathrm{Deg}}$ in Table 4.2). By contrast, the rate

Table 4.2.: Parameter estimates for the transition from transcription to genome replication based on a model that accounts for the stabilization hypothesis.

Parameter		**Value**		**Local sensitivity**	
		in vitro[a]	**cell culture**[b]	***in vitro***[a]	**cell culture**[b]
$k_{\mathrm{NP}}^{\mathrm{Bind}}$	$(\mathrm{molecule} \cdot \mathrm{h})^{-1}$	–	3.01×10^{-4}	–	7.16×10^{-3}
$k_{\mathrm{RdRp}}^{\mathrm{Bind}}$	$(\mathrm{molecule} \cdot \mathrm{h})^{-1}$	–	1[c]	–	6.62×10^{-7}
$k_{\mathrm{M}}^{\mathrm{Deg}}$	(h^{-1})	0.37	0.33	0.13	1.37×10^{-2}
$k_{\mathrm{R}}^{\mathrm{Deg}}$	(h^{-1})	0.06	36.36	1.76×10^{-2}	1.21×10^{-5}
$k_{\mathrm{RRdRp}}^{\mathrm{Deg}}$	(h^{-1})	–	4.25	–	1.16×10^{-2}
$k_{\mathrm{C}}^{\mathrm{Syn}}$	(h^{-1})	0.03	0.76	8.78×10^{-2}	5.31×10^{-2}
$k_{\mathrm{M}}^{\mathrm{Syn}}$	(h^{-1})	0.21[d]	0.96[d]	0.18	8.01×10^{-2}

[a] Model fit presented in Figure 4.3A.
[b] Model fit presented in Figure 4.3B–D.
[c] We can only estimate the lower bound of this rate since polymerase binding is in saturation in experiments.
[d] For better comparison the synthesis rate of an mRNA of average length is shown. In the model, transcription is proportional to the actual mRNA length of each segment and a length specific synthesis rate (here 350 and 1630 nucleotides $\cdot$ h^{-1}, respectively).

of mRNA degradation ($k_{\mathrm{M}}^{\mathrm{Deg}}$) hardly changes between both setups. Note, however, that for high values of cRNA degradation, which are required to compensate for the ongoing replication activity of vRNPs, $k_{\mathrm{R}}^{\mathrm{Deg}}$ becomes increasingly insensitive. Hence, an accurate estimation of this rate requires separate experiments. In the presence of NP proteins and complete viral polymerases stabilization takes place resulting in an accumulation of cRNA in the model and the experiment (Figure 4.3C). As the expression of a catalytically inactive polymerase complex should not affect transcription, the simulated mRNA levels in Figure 4.3B and C are the same and correspond well to the averages from these two independent experiments. Figure 4.3D shows the cRNA level in response to different combinations of pre-expressed viral proteins. In the absence of the viral RdRp, the model yields only low levels of cRNA regardless of the expression of NP proteins (Figure 4.3D, columns 1 and 2). These residual amounts are due to the ongoing synthesis of cRNA by vRNPs, which is in equilibrium with cRNA degradation. However, such low levels may be below the detection limit of the primer extension assay and may, therefore, not appear in experiments. The expression of polymerases in the absence of NP results in an accumulation of cRNA to intermediate levels (Figure 4.3D, column 3). Note that the model requires the formation of an RdRp-cRNA complex that is more stable than nascent cRNA (compare $k_{\mathrm{R}}^{\mathrm{Deg}}$ and $k_{\mathrm{RRdRp}}^{\mathrm{Deg}}$ in Table 4.2) to correctly reproduce this scenario. Finally, in the presence of both RdRp and NP, cRNPs are formed providing an even higher protection from degradation (Figure 4.3D, column 4). Furthermore, simulation results and measurements agree in that an increased concentration of viral polymerases does not yield higher cRNA levels, whereas an increase in NP protein concentration does (Figure 4.3D, columns 4 to 7). Hence, in these experiments, polymerase binding is in saturation indicating a high affinity of the RdRp to nascent cRNA. By contrast, binding of NP is the rate-limiting step of cRNA stabilization given the experimental conditions. In summary, our model can capture the time course of cRNA and mRNA under various experimental conditions as well as the qualitative response of cRNA levels to different combinations and amounts of pre-expressed viral proteins.

Switching hypothesis An alternative hypothesis on the transition to genome replication proposes that NP proteins facilitate a switch from early translation to late replication by regulating vRNP activity directly (see Figure 2.3A, reviewed in [59]). We implemented a simple version of this mechanism into our model such that NP enhances cRNA synthesis at the expense of mRNA production. In addition, viral protein binding no longer affects RNA stability in these simulations. A key argument against the switching hypothesis is the synthesis of cRNA by virion-derived vRNPs *in vitro* in the absence of non-vRNP-associated NP proteins [66]. However, our estimation yields a very low rate of cRNA synthesis in this *in vitro* experiment ($k_{\mathrm{C}}^{\mathrm{Syn}}$ in Table 4.2). We, therefore, hypothesized that vRNPs might posses a residual replication activity, i.e., that they can synthesize small amounts of cRNA in absence of NP, and that the expression of NP merely increases this activity. With such a leaky cRNA production our switching model can reproduce the *in vitro* data (Figure 4.4A). We then turned toward the infection experiments and fitted the model simultaneously to all available data sets (parameters can be found in Table A.4 in the appendix). In the presence of NP proteins, simulations show similar cRNA dynamics regardless of whether the viral polymerase is expressed (Figure 4.4B and C). This results from the assumption that NP proteins are the sole regulator of vRNP activity. Because NP is present in both experiments at similar concentrations cRNA synthesis is equivalent and simulations attempt to match the averages from these two data sets. However, this model prediction stands in sharp contrast to the experiments in which cRNA accumulates upon polymerase expression. A similar observation can be made from the response of cRNA levels to different combinations of pre-expressed viral proteins (Figure 4.4D). Although the model qualitatively agrees with the measurements with respect to changes in NP concentration, e.g., expression of NP in the presence of RdRp increases cRNA levels (compare column 3 and 4) and an increased NP level results in stronger cRNA accumulation (compare columns 5 to 7), it cannot reproduce the response to RdRp expression. For instance, simulations predict the same cRNA concentration in the absence of NP proteins whether the polymerase is present or not (compare column 1 and 3). These levels result from the

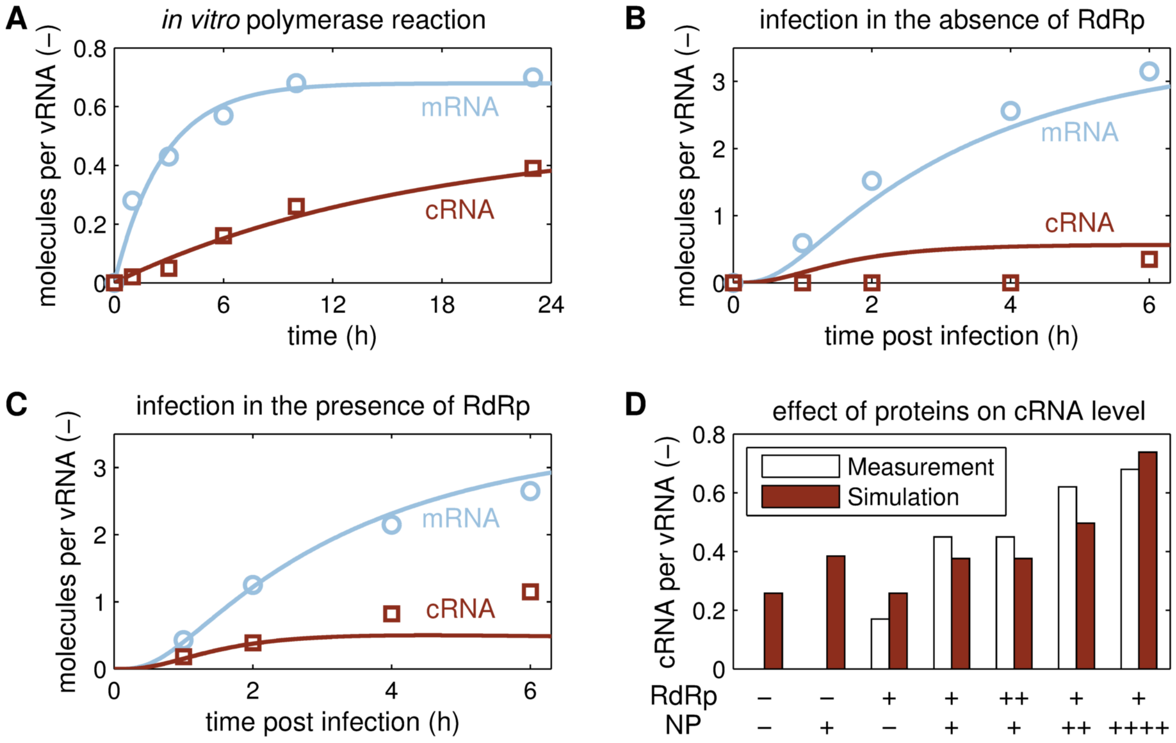

Figure 4.4.: Simulation of the switching hypothesis. Same as in Figure 4.3 except that the switching hypothesis was simulated. (A) *In vitro* polymerase assay using virion-derived vRNPs [66]. (B,C) Infections of 293T cells with influenza A/WSN/33 at an MOI of 5 [66] in the absence (B) and presence (C) of a catalytically inactive viral polymerase complex. (D) Same as in C except that various amounts of plasmids expressing the viral RdRp, NP protein, and empty vector (–) were transfected prior to infection.

residual replication activity we implemented to fit Figure 4.4A. However, cRNA was not detected in experiments where the viral polymerase is absent. Similarly, polymerase expression increases cRNA accumulation in the experiments but not in the model (compare column 2 and 4). Overall, our simple implementation of the switching hypothesis, thus, captures the effect of differential NP expression on cRNA levels, albeit only qualitatively, but it cannot correctly reproduce the response to changes in RdRp concentration. We, hence, use a model of the stabilization hypothesis in the following.

Nuclear export and shutdown of RNA(+) synthesis As the infection advances, newly produced vRNPs leave the nucleus to travel to the plasma membrane where they are packaged into progeny virions. In our model, two viral proteins are the main regulators of this process, M1 and NEP. While M1 was shown to bind directly to vRNPs through interaction with NP and possibly also with RNA, NEP links the complex to the cellular exportin CRM1 in a “daisy chain” by binding to an NLS on M1 (see Figure 2.4 on page 11 and reference [71]). Somewhere along this process, vRNPs have to stop transcription and replication in order to enter the cytoplasm (and later the virus particles) in an inactive form [92]. We assumed that M1 binding is the step that inactivates vRNPs because M1 proteins are known to inhibit viral transcription [93–95, 97]. Once bound to the M1-vRNP complex, NEP can then facilitate the export of vRNPs from the nucleus in our simulations. Using this mechanism as well as cRNA stabilization and the virus entry dynamics described in the beginning allowed us to recover the dynamics of all three viral RNA species during infection (Figure 4.5A and B). Simulation results show an early increase in mRNA levels within the first hour post infection when vRNPs reach the nucleus. In the following, viral protein synthesis facilitates the transition to genome

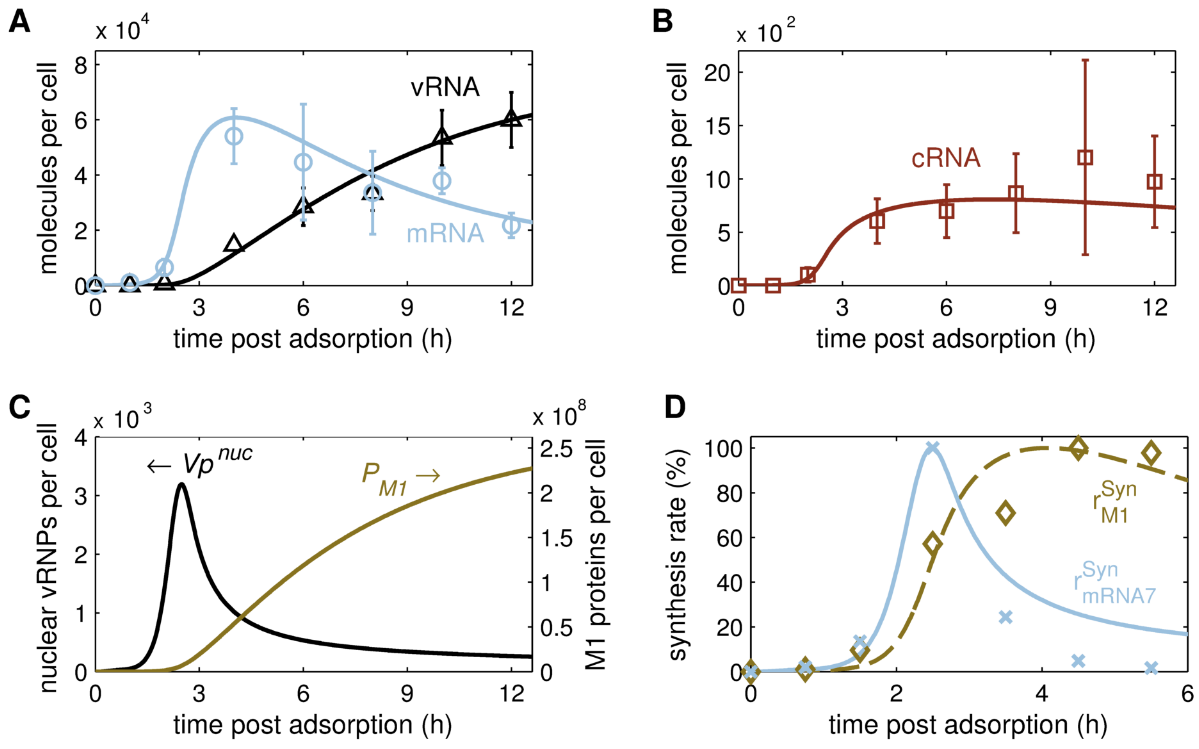

Copyright © American Society for Microbiology, [Journal of Virology, 86, 2012, 7806-7817, 10.1128/JVI.00080-12]

Figure 4.5.: Viral RNA dynamics during infection. (A,B) Model fit (lines) to the vRNA (△), mRNA (○), and cRNA (□) levels of segment 5 (encoding NP) during three independent infections of MDCK cells with influenza A/WSN/33 at an MOI of 10 after 1 h of virus adsorption at 4°C. Data were determined by Kawakami *et al.* using strand-specific real-time RT-qPCR [175]. (C) Model prediction for the accumulation of unbound M1 proteins (P_{M1}) and vRNPs engaged in RNA synthesis (Vp^{nuc}). (D) Comparison of model predictions to data of Shapiro *et al.* for the synthesis rates of M1 (◊) and mRNAs (×) of segment 7 (encoding the M proteins) [75]. In brief, BHK-21 cells were infected with influenza A virus (WSN strain) at an MOI of 10 to 20 and virus was allowed to adsorb for 1 h at 4°C. Protein and mRNA levels were determined by pulse chase experiments. In simulations, $r^{\mathrm{Syn}}_{\mathrm{M1}}$ and $r^{\mathrm{Syn}}_{\mathrm{mRNA7}}$ correspond to the synthesis rates of M1 proteins (first term in Equation (3.1.22)) and mRNAs of segment 7 (first term in Equation (3.1.16) with i=7), respectively. Data points and simulations are given in percent of their maximum.

replication around 1.5 hpi marked by an accumulation of both cRNA and vRNA in the model and in experiments. At approximately 3.5 to 4 hpi, the mRNA level shows a distinct peak (Figure 4.5A) caused by the inactivation and subsequent nuclear export of progeny vRNPs, which can no longer serve as templates for positive-strand RNAs. For the same reason, cRNA production slows down during late infection (Figure 4.5B). Finally, the level of viral genome copies increases throughout infection as their template, the cRNA, remains in the nucleus at nearly constant levels. These dynamics are in general agreement with experiments using different influenza A virus strains, cell lines, and experimental assays [75, 174, 255, 273].

Our model proposes that the RNA dynamics during late infection are mainly governed by a shutdown of positive-strand RNA synthesis due to the inactivation of vRNPs in preparation for nuclear export. In particular, M1 proteins accumulate to high levels starting around 2 hpi (Figure 4.5C). Subsequently, they bind to vRNPs causing a reduction in the number of active vRNPs from 2.5 hpi onward, which impairs the synthesis of cRNA and mRNA. Yet, in our model, some vRNPs remain active, even at late times, and produce low amounts of RNAs. Since cRNAs are stabilized in cRNPs this residual vRNP activity suffices to keep the cRNA level roughly constant. By contrast, the higher rate of mRNA degradation causes a decline in mRNA levels during late infection. To provide further evidence that the inactivation of vRNPs by M1 proteins determines late RNA dynamics, we compared our simulation results to measurement data not used for model construction. Figure 4.5D illustrates the simulated synthesis rates of M1 proteins and mRNAs of segment 7 along with experimental data obtained by Shapiro and colleagues [75]. Although these experiments were conducted in BHK-21 cells our model correctly predicts the synthesis kinetics. In particular, mRNA synthesis peaks at 2.5 hpi (preceding the peak in mRNA levels shown in Figure 4.5A) and its decrease coincides with a strong increase in M1 protein production. However, the experiments show a complete shutdown of mRNA synthesis, while transcription barely falls below 20% in our simulations. This might be related to the depletion of host factors not accounted for in the model or the sensitivity of the experimental procedure. In summary, the proposed model is in good agreement with quantitative data on viral RNA levels during infection and qualitative features of RNA and protein synthesis. Furthermore, simulations suggest a prominent role of nuclear export in the shutdown of positive-strand RNA synthesis, which shapes late RNA dynamics.

Table 4.3 summarizes all parameter estimates we obtained from the data in Figure 4.5A and B. Note that we re-estimated the rates of mRNA and cRNA synthesis, which are also provided in Table 4.2 for the experiments in Figure 4.3. We found an increase in both these rates after re-estimation that was especially pronounced for mRNA production (compare $k_{\mathrm{M}}^{\mathrm{Syn}}$ in Table 4.2 and 4.3). This difference might be cell line-dependent (experiments

Table 4.3.: Parameter estimates for viral RNA synthesis during late infection.

Parameter		Value	95% CI[a]
$k_{\mathrm{M1}}^{\mathrm{Bind}}$	$(\mathrm{molecule}\cdot\mathrm{h})^{-1}$	1.39×10^{-6}	$(0.57-2.63)\times10^{-6}$
$k_{\mathrm{Rnp}}^{\mathrm{Deg}}$	(h^{-1})	0.09	$0^{\mathrm{b}}-0.16$
$k_{\mathrm{C}}^{\mathrm{Syn}}$	(h^{-1})	1.38	0.65-2.76
$k_{\mathrm{M}}^{\mathrm{Syn}}$	(h^{-1})	147^{c}	54-225
$k_{\mathrm{V}}^{\mathrm{Syn}}$	(h^{-1})	13.86	6.39-20

[a] 95% confidence intervals provided by 3 000 bootstrap replicates [249].
[b] Estimates reached the lower parameter bound of $9\times10^{-4}\,\mathrm{h}^{-1}$.
[c] Synthesis rate of an mRNA of average length using a length specific rate of $2.5\cdot10^{5}$ nucleotides $\cdot\,\mathrm{h}^{-1}$.

for Table 4.2 are from 293T cells whereas parameters in Table 4.3 are for infections of MDCK cells), or it may be caused by the data quality. While 293T experiments were assayed by semi-quantitative primer extension analysis, the real-time RT-qPCR method used for MDCK cell infections facilitates an exact quantification of RNA levels. The latter data set should, hence, yield more accurate parameter estimates. For these data, we also find a tenfold higher rate of vRNA synthesis compared to cRNA production (compare $k_{\mathrm{V}}^{\mathrm{Syn}}$ and $k_{\mathrm{C}}^{\mathrm{Syn}}$ in Table 4.3).

RNA dynamics in the switching model The RNA measurements obtained by Kawakami *et al.* provide an opportunity to revisit our implementation of the switching hypothesis and compare it against a second, independent data set, i.e., against experiments that were not used to develop the stabilization hypothesis. When fitting the model to RNA levels, we again observe significant deviations from the data especially for cRNA (Figure 4.6). More specifically, the cRNA level in the simulation is much lower than in experiments. However, the model can capture the dynamics of vRNA and mRNA for most data points. Surprisingly, parameter estimation yields a very insensitive switch for the model fit in Figure 4.6 such that the transition to genome replication did not occur (data not shown and Table A.5 in the appendix). This results in an insufficient cRNA synthesis which is balanced by a higher rate of vRNA production. Upon closer inspection, we find that a sensitive switch cannot reproduce the simultaneous accumulation of mRNA and cRNA between 2 and 4 hpi that was observed in experiments (data not shown). This is due to our implementation of switching, which permits an increase in replication only at the expense of transcription. Because of the poor agreement with data, we use a model of the stabilization hypothesis in the rest of this manuscript.

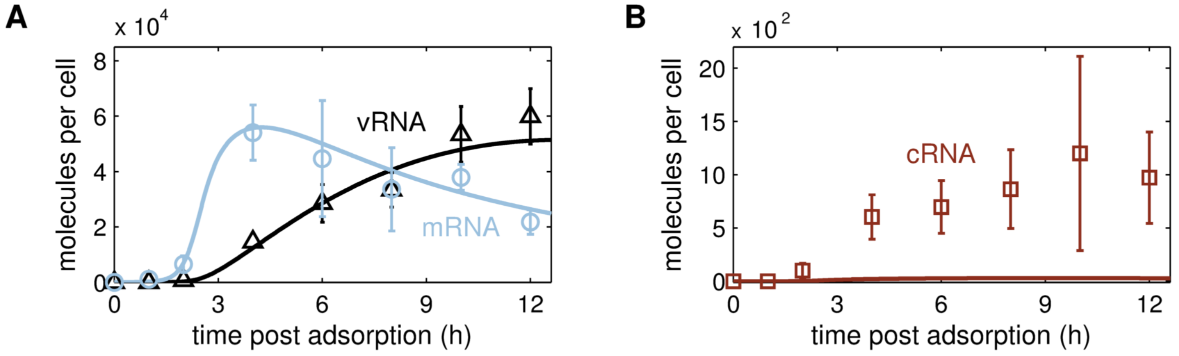

Figure 4.6.: Viral RNA dynamics in the switching model. Same as in Figure 4.5A and B except that the switching hypothesis was simulated. (A,B) Model fit (lines) to the vRNA (△), mRNA (○), and cRNA (□) levels of segment 5 (encoding NP) during three independent infections measured by Kawakami *et al.* [175]. Note that, for the fit, the residual vRNP activity (k_C^{Res}) was fixed to the value determined from data in Figure 4.4 and the increase in cRNA synthesis by NP was limited to $k_C^{\mathrm{Syn}} < 10^3\,\mathrm{h}^{-1}$. The cRNA level in B never exceeds 30 molecules/cell.

Virus release and the bottlenecks for virus production After having developed a model of intracellular influenza A virus replication, we were interested in what viral or cellular factor(s) limits the production of progeny virions, i.e., whether there is a bottleneck for virus replication. In infection experiments with influenza A/WSN/33 each MDCK cell releases up to 10^4 progeny virions based on HA titers (data not shown). We tuned our model such that it reflects this cell-specific yield (Figure 4.7A). In simulations, the first virus particles leave the cell after 3 to 4 hpi when progeny vRNPs enter the cytoplasm. Thereafter, virus release increases due to the accumulation of vRNPs and viral proteins (Figure 4.7B). The differences in protein concentration in Figure 4.7B arise due to two reasons: (i) budding viruses require different amounts of each protein, and

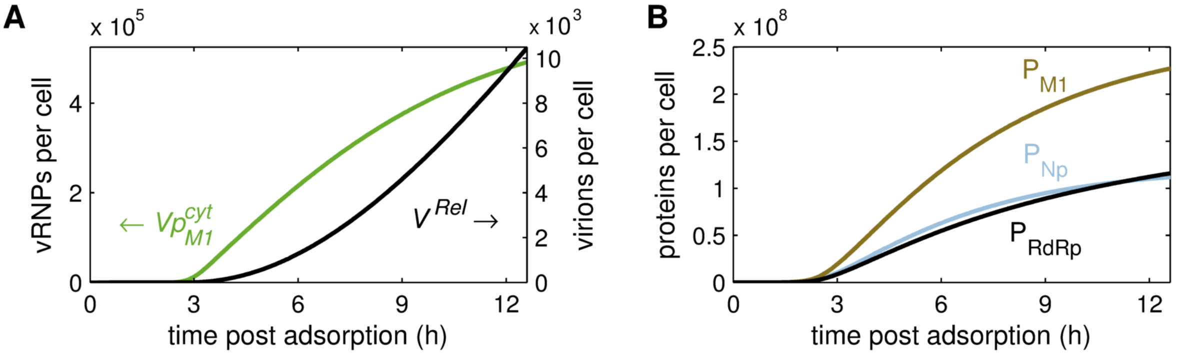

Copyright © American Society for Microbiology, [Journal of Virology, 86, 2012, 7806-7817, 10.1128/JVI.00080-12]

Figure 4.7.: Dynamics of virus release and viral protein accumulation. (A) Model prediction for the level of cytoplasmic vRNPs (Vp^{cyt}) and the cumulative number of released progeny virions (V^{Rel}) based on the model fit in Figure 4.5. (B) Level of unbound M1 (P_{M1}), NP (P_{NP}), and viral polymerase complexes (P_{RdRp}) for the simulation presented in Figure 4.5.

(ii) mRNAs of small genome segments accumulate to higher levels in our model based on data obtained by Hatada *et al.* [174]. Similar differences in protein abundance have been observed experimentally by quantitative proteomics [274]. Interestingly, neither the pool of cytoplasmic vRNPs (Figure 4.7A) nor of viral proteins (Figure 4.7B) becomes depleted by virus release. Hence, cells might be able to release even more virus particles. To elucidate which intracellular process would be the most promising target to achieve higher cell-specific virus yields with respect to cell culture-based vaccine production, we performed a local sensitivity analysis. To this end, each model parameter was perturbed by 15% around its estimated value and virus production was monitored (Figure 4.8A)[2]. In simulations, an increase in the rate of cRNA or vRNA synthesis enhances virus production by up to 35%. This results from an increase in viral RNA and protein levels (Figure 4.8B, number 1). In particular, the increase in the number of cytoplasmic vRNPs drives virus production in our model as we assumed that virus release is proportional to vRNP abundance (see Equation (3.1.27)). In this context, targeting RNA synthesis is especially promising because viral RNAs engage in an autocatalytic reaction where vRNAs produces cRNAs, which in turn provide the template for new vRNAs. A small increase in the RNA synthesis rate can, thus, cause a large increase in RNA levels. Another target for process optimization is the negative regulation of vRNP activity during nuclear export. In our simulations, delaying this negative feedback by impairing M1 protein binding, the synthesis of mRNAs, or viral protein prodution increases virus yields. Again, this results primarily from an enhanced production of cRNA and vRNA (Figure 4.8B, number 2). Note, however, that impairing viral mRNA and protein synthesis beyond a certain threshold will eventually prevent virus release when proteins become a limiting factor (data not shown). Finally, enhancing virus assembly/release can also increase cell-specific virus yields (Figure 4.8B, number 3). In summary, the model suggests that, based on the abundance of viral components alone, cells have the potential to produce more virus paricles. In additon, viral RNA replication, the inactivation of vRNPs during nuclear export, and virus assembly/release are promising targets for the optimization of vaccine production in cell culture.

---

[2] Table A.6 in the appendix shows which parameters correspond to the mechanisms listed in Figure 4.8

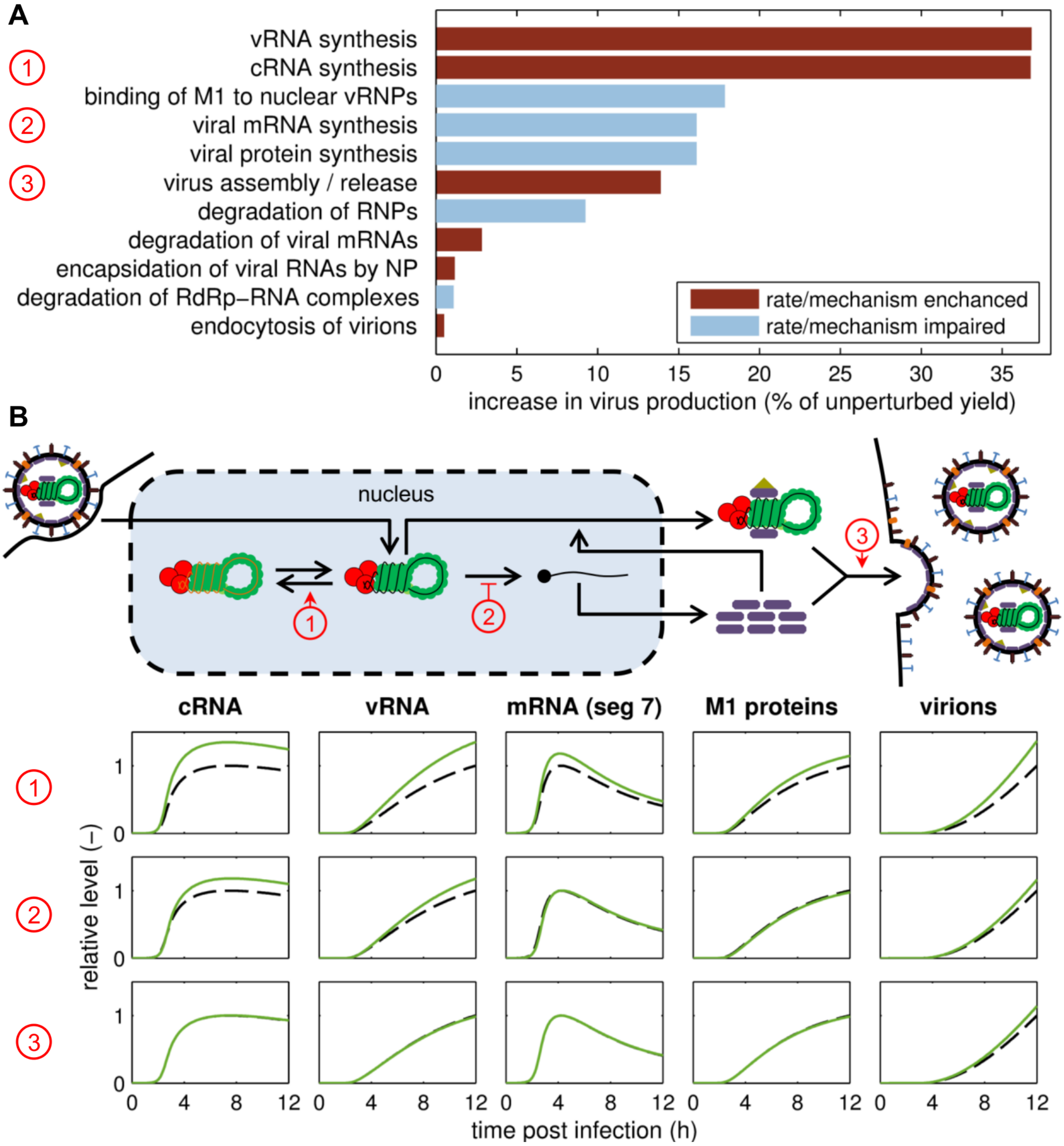

Figure 4.8.: Increase in cell-specific virus yield through intracellular perturbations. (A) Predicted increase in the cumulative number of progeny virions 12 hpi given a perturbation of the indicated mechanisms by 15%. Colors indicated whether the rate/mechanism was enhanced or impaired. Numbers in circles correspond to the examples shown in B. (B) Time courses of selected viral components in response to perturbations. Columns correspond to components depicted in the scheme. Dashed and solid lines are time courses in the unperturbed and perturbed model, respectively. All components were normalized to their maximum in the unperturbed model.

4.1.2. Stochastic fluctuations in viral RNA synthesis

In contrast to deterministic models, like the description of intracellular virus replication presented in the previous section, stochastic simulation techniques take into account that molecules come in whole numbers and that biochemical reactions exhibit some degree of randomness (reviewed in [244]). Such stochastic effects can play a role especially when molecule counts are low, e.g., when a single virus particle initiates infection by delivering a single copy of its genome into a host cell. To elucidate whether noise can lead to deviations from the deterministic kinetics of intracellular virus replication, we developed a stochastic version of our model, whose analysis is provided in the following section.

Model structure The stochastic model accounts for the same reactions and mechanisms that were included in its deterministic counterpart (see Figure 2.2 on page 7). However, it considers the discreteness and stochasticity of these processes. More precisely, in stochastic simulations reactions are discrete, random events whose average occurrence is equivalent to the deterministic reaction rate; yet, each individual event is probabilistic and leads to a discrete change in species concentrations (Figure 4.9). Hence, the model considers the inherent randomness of molecular dynamics at the microscopic scale. In the following, we restrict our analysis to stochastic simulations of the first 12 h of infection. This was done for two reasons. Namely, because the parameter values of the deterministic model (on which the stochastic reaction constants are based) were estimated from data that only covered 12 h, and because the model does not account for cell death, which would terminate intracellular virus replication in an experimental setting.

The effect of genome segmentation The results of a deterministic model can be considered as the behavior of an infected cell averaged over a large population, whereas a stochastic simulation represents a single random walk through the possible system states,

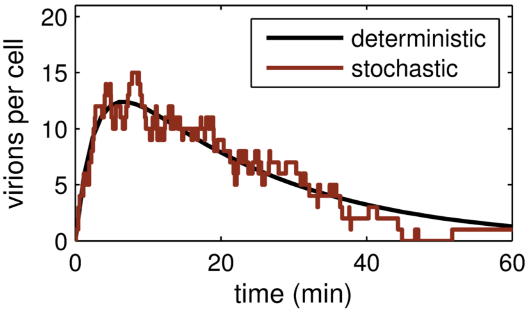

Figure 4.9.: Example of a stochastic simulation run. The number of virus particles attached to the cell surface was simulated using either a deterministic or a stochastic model.

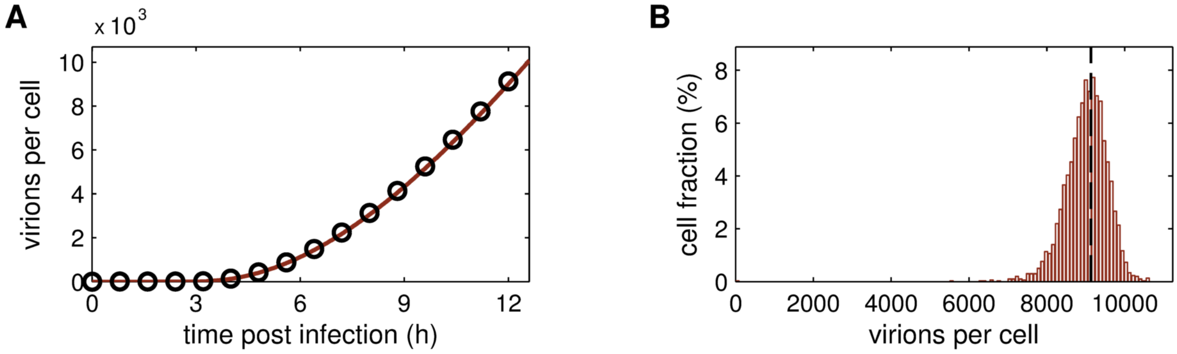

Figure 4.10.: Comparison of the deterministic and stochastic simulation. An infection at an NIVC of 10 was simulated using either the deterministic model of intracellular virus replication or its stochastic implementation. (A) Cumulative number of released virus particles in the deterministic model (circles) and the mean of stochastic simulations (line). (B) Histogram of the cumulative number of released virus particles in stochastic simulations at 12 hpi. The dashed line indicates the deterministic result.

i.e., the response of a specific single cell to infection. We can, hence, compare the average of multiple stochastic runs to the deterministic model. If we find that both are similar and that the individual stochastic trajectories do not deviate significantly from one another, we can conclude that microscale randomness does not influence viral replication [244]. Stochastic simulations of an infection at a high initial number of infectious viruses per cell (NIVC)[3], where the effect of noise should be small, do indeed match the deterministic result (Figure 4.10A and Figure A.3 in the appendix). However, the number of released virus particles shows substantial variation (with an average infected cell yielding 9013 ± 555 virions/cell) indicating that stochastic effects do play a role (Figure 4.10B). These variations are mainly caused by noise in virus entry [262]. For an in-depth analysis of the results, the reader is referred to a bachelor thesis which was supervised as part of this work [262].

Although Figure 4.10 provides some initial evidence for the influence of stochastic effects the underlying model (Section A.2.1 in the appendix) oversimplifies the synthesis of viral genome segments. In particular, it assumes that all eight genome segments maintain similar vRNA (and cRNA) levels throughout infection. While this was found for the cell population average in experiments [174, 175], and may hence be justified for deterministic simulations, segment levels in individual cells may very well differ. We, therefore, dropped the assumption of equimolar segment levels during viral replication in subsequent stochas-

---

[3] In the following, we use the NIVC instead of the MOI because the MOI typically refers to cell population experiments where it describes the overall ratio of infectious viruses per target cell. In such experiments, the actual number of viruses that infect a cell is a statistical property with some cells absorbing more viruses than others. By contrast, the NIVC should emphasize that in stochastic simulations each cell receives the same number of extracellular virions, which carry a full complement of eight functional vRNPs. Hence, the NIVC also corresponds to the number of infecting genomes.

tic simulations. Note that in the beginning of infection segment levels are still equimolar since infecting virions contain one copy of each segment in our simulations. Intriguingly, once the model accounts for an independent synthesis of genome segments, cells produce on average significantly lower numbers of virus particles (Figure 4.11A). In addition, we observe a much wider distribution of cell-specific virus yields and a bias toward lower productivity with an average cell producing 3064 ± 2914 virions/cell (Figure 4.11B). In the model, virus release primarily depends on the number of cytoplasmic vRNPs available for packaging. Since the vRNP level can vary between different genome segments but virions require one copy of each segment, the level of the least abundant cytoplasmic vRNP restricts virus production in our simulations (see Equation (3.1.32)). Hence, cell-specific virus yields correlate strongly with the level of the least abundant vRNA in each

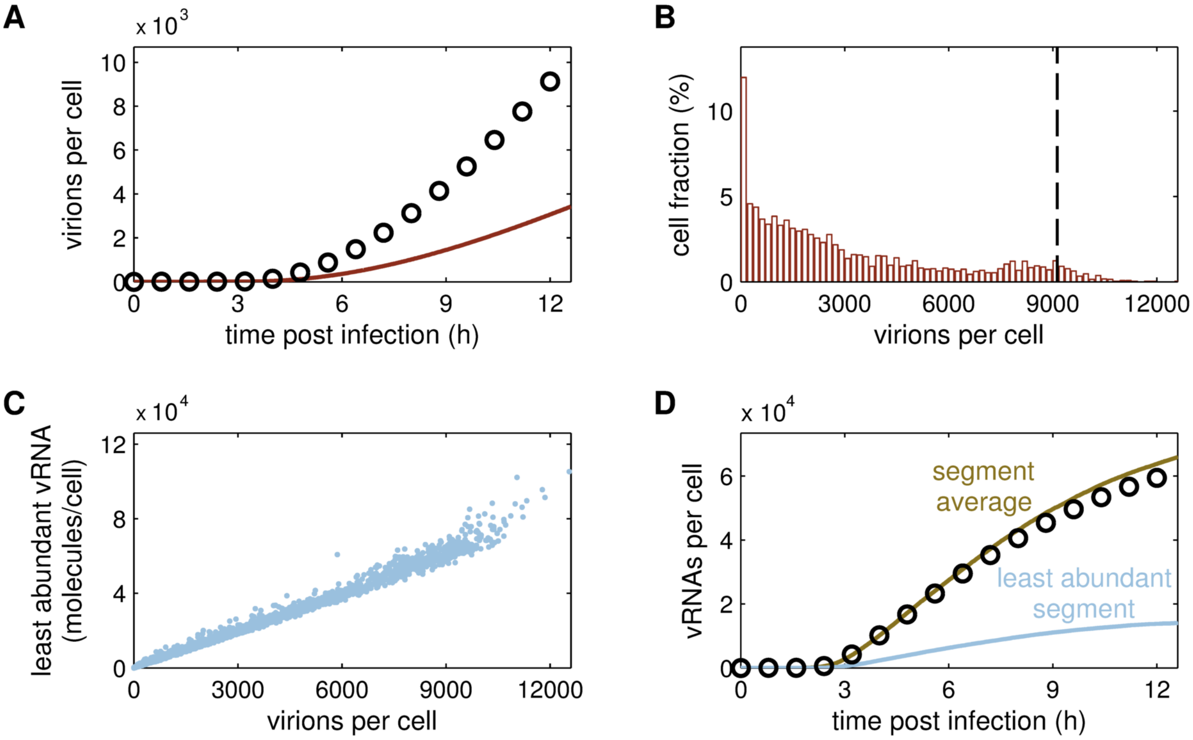

Figure 4.11.: Virus production in a stochastic model that accounts for an independent genome segment synthesis. An infection at an NIVC of 10 was simulated using a stochastic model in which genome segments replicate independently, i.e., the vRNAs (and cRNAs) of different genome segments are not constrained to the same level. (A) Cumulative number of released virus particles in the deterministic model (circles) and the mean of stochastic simulations (line). (B) Histogram of the cumulative number of released virus particles in stochastic simulations at 12 hpi. The dashed line indicates the deterministic result. (C) Correlation between the cumulative number of released virus particles and the level of the least abundant genome segment in stochastic simulations at 12 hpi. (D) vRNA level of an arbitrary genome segment in the deterministic model (circles) and the median of stochastic simulations (lines) considering the average over all genome segments and the level of the least abundant segment in a cell.

cell (Figure 4.11C). On average this level is much lower than the vRNA level in the deterministic simulation, which is why we observe an impaired virus release (Figure 4.11D). Yet, the total vRNA level, averaged over all eight genome segments, is slightly higher in the stochastic model due to the reduced depletion by virus release. Overall, the simulations reveal significant deviations from the deterministic model and a strong influence of noise due to the independent synthesis of genome segments. Furthermore, stochastic fluctuations reduce cell-specific virus yields compared to a model that constrains the vRNAs (and cRNAs) of different genome segments to the same level.

Stochastic fluctuations in genome segment levels Having identified the independent synthesis of viral genome segments as a major source of noise, we next analyzed how stochastic effects influence vRNA levels. In our simulations, the vRNA of segment 1 follows a log-normal distribution around the deterministic result (Figure 4.12A). Interestingly, segment 1 levels differ by up to four orders of magnitude in individual cells. We observe similar fluctuations for all eight genome segments except for segment 7 (Figure 4.12B). In our model, segment 7 is the only segment that exerts negative control over RNA synthesis. It encodes for the M1 protein, which inactivates vRNPs during nuclear export. This negative feedback loop reduces noise by shutting down the synthesis of RNAs when segment 7 levels (and thus M1) reach a certain threshold.

According to Elowitz *et al.*, the noise that causes cell-to-cell variability (which we observe for the vRNA levels in infected cells) can be divided into two components [265]: (i) extrinsic factors such as cell cycle stage, cell size, or protein content, which are global

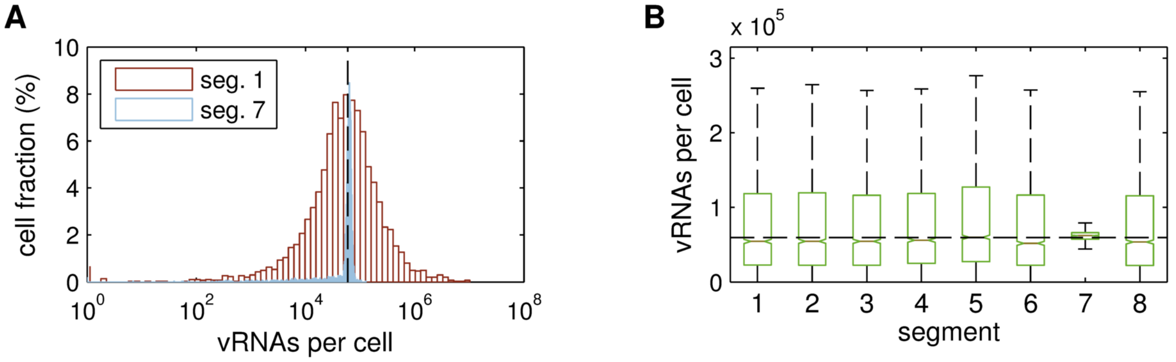

Figure 4.12.: Fluctuations in genome segment levels. The stochastic model of virus replication was used to simulate an infection at an NIVC of 10. (A) Distribution of vRNA levels of segment 1 and 7 (encoding PB2 and the M proteins, respectively) at 12 hpi. The dashed line indicates the deterministic result. (B) Fluctuations in the vRNA levels of all eight genome segments at 12 hpi. On each box, horizontal edges are the lower and upper quartile, the central line is the median and the whiskers cover all vRNA levels within 1.5 inner quartile range of the lower and upper quartile, respectively. The horizontal dashed line indicates the deterministic result.

to a single cell but vary between different cells and (ii) intrinsic factors, i.e., the inherent randomness of biochemistry, that can cause variations in identically regulated genes within a cell even though global factors are the same. Although we do not explicitly accounted for extrinsic factors, viral proteins such as NP and M1, or the timing of virus entry would affect all genome segments in a cell equally and may, hence, appear to cause extrinsic noise. By contrast, the independent synthesis of genome segments can cause differences between the segments inside a cell and, thus, constitutes an intrinsic factor. For the vRNA level of segment 1 and 2 (encoding PB2 and PB1, respectively) we find both, differences within cells and differences between them (Figure 4.13A). If extrinsic factors were the primary source of genome segment variations, vRNA levels would be strongly

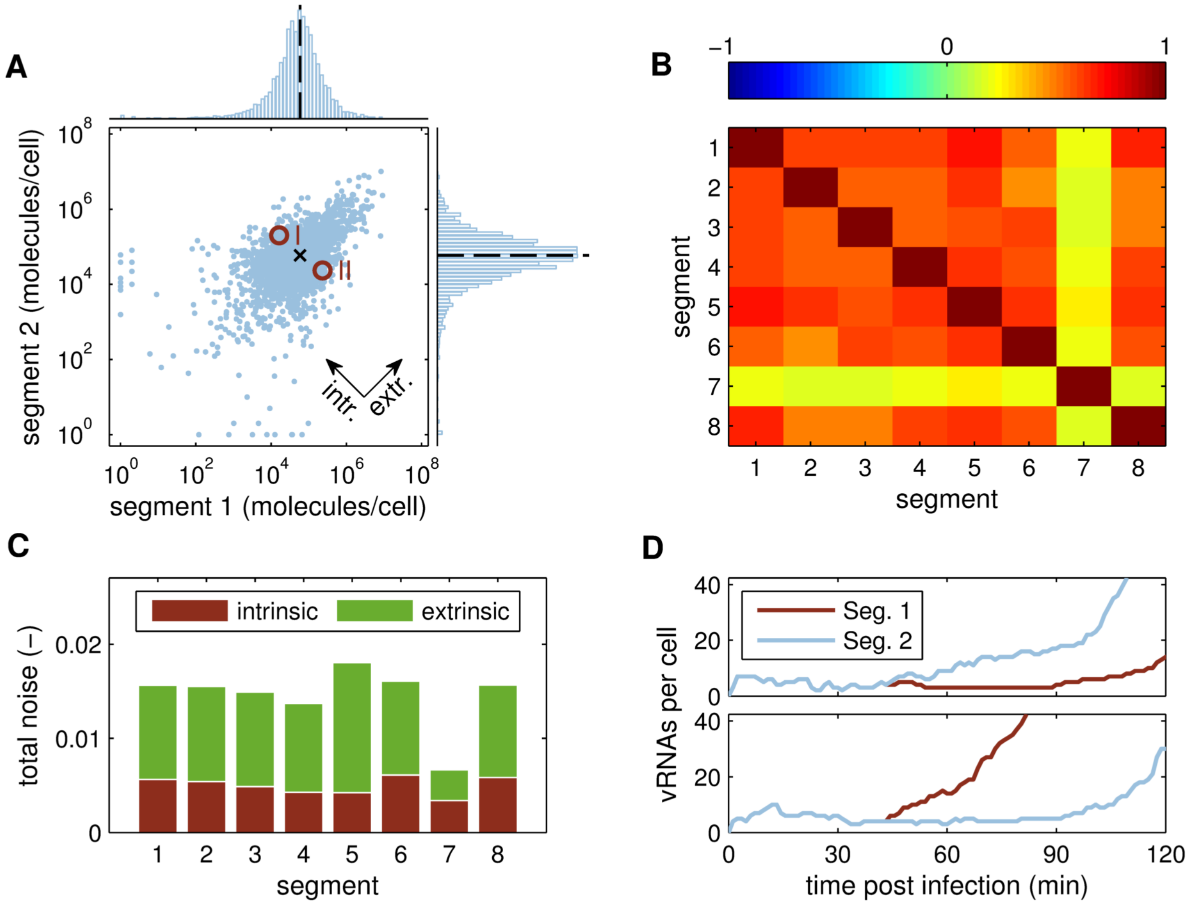

Figure 4.13.: Noise in genome segment levels. The stochastic model of virus replication was used to simulate an infection at an NIVC of 10. If not otherwise indicated, the amount of viral components at 12 hpi is shown. (A) Total number of vRNAs of segment 1 and 2. The black X represents the vRNA level in the deterministic model. Circles mark the two examples shown in D. Arrows indicate the contribution of extrinsic noise and intrinsic noise. (B) Pearson's linear correlation coefficient between the vRNA levels of different segments. (C) Noise in the vRNA levels of the indicated segments with respect to the mean vRNA level in a cell (see Equation (3.1.36)). (D) Early vRNA dynamics of segment 1 and 2 for the two cells indicated in A (I, upper panel; II, lower panel).

correlated, whereas strong intrinsic noise would result in the absence of correlation. We observe a weak correlation between the vRNAs of segment 1 and 2 as well as between the other segments, again indicating the presence of extrinsic as well as intrinsic noise sources (Figure 4.13B). Note that segment 7 shows an even weaker correlation to the other vRNAs because of its overall low variability and the negative regulation of RNA synthesis via M1. Elowitz *et al.* proposed a method to quantify the noise in two genes and to discriminate its extrinsic and intrinsic components ([265]). Applied to our results, this method confirms the presence of both types of noise (Figure 4.13C). Hence, factors like viral protein content and virus entry timing can cause extrinsic noise in stochastic simulations although classical extrinsic factors such as the cell cycle are not accounted for. Also note that the noise in segment 7 levels is again reduced, whereas the other vRNAs show only marginal differences.

Next, we analyzed at which moment during infection the levels of individual genome segments start to differ. Based on experimental evidence [37], the vRNPs of incoming virions in our model travel together through the cytoplasm until they reach the nucleus. After nuclear import, they start to replicate independently and we begin to see differences in their abundance (Figure 4.13D). While small in the beginning, these differences grow rapidly over the course of the next hours. In fact, noise is almost exclusively generated in the early phase of infection where viral transcription and replication take place (Figure 4.14). Later in infection, when nuclear export impairs the synthesis of positive-strand RNAs, noise levels start to decrease again.

Finally, we investigated whether viral proteins are also subject to stochastic fluctuations. Indeed, similar to viral genome copies, HA and NP protein levels differ by up to four orders of magnitude between individual cells (Figure 4.15A). By contrast, M1 shows a much narrower distribution due to its regulatory role. Furthermore, we observe a strong corre-

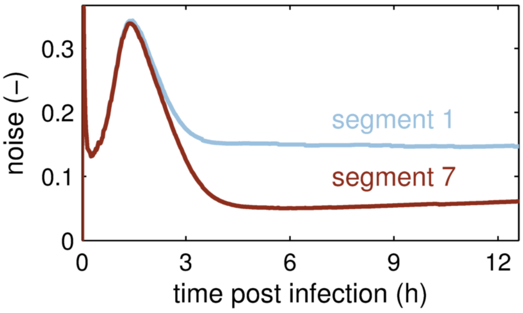

Figure 4.14.: Amplification of noise during virus replication. The noise in vRNA levels of different genome segments was calculated over the course of an infection at an NIVC of 10 through dividing the standard deviation of $\log_{10}$ vRNA levels by their mean (see Equation (3.1.35)).

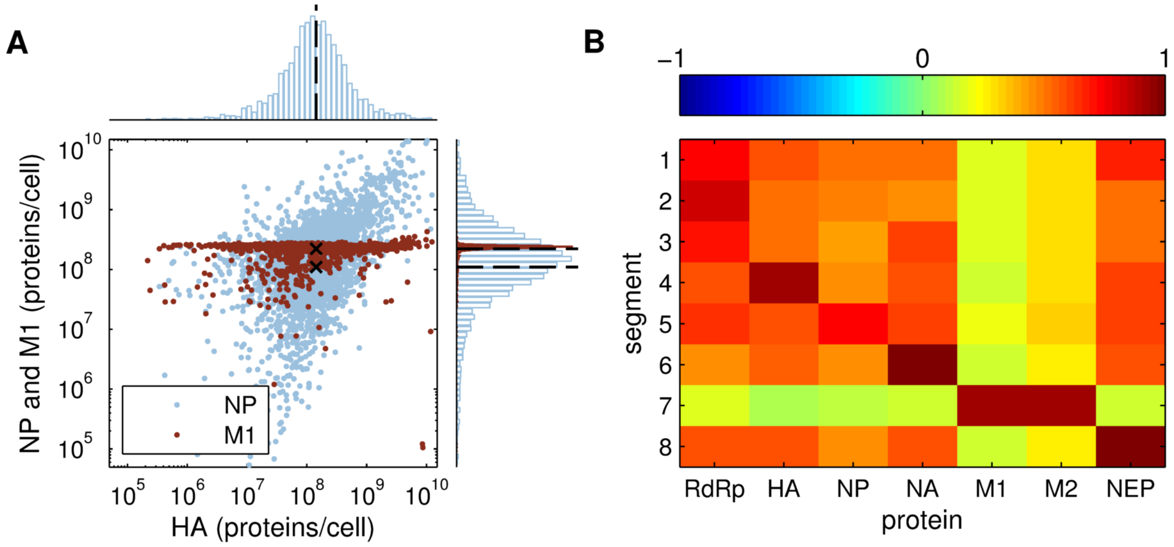

Figure 4.15.: Fluctuations in viral protein levels. The stochastic model of virus replication was used to simulate an infection at an NIVC of 10. (A) Total number of NP and M1 proteins against unpackaged HA at 12 hpi. Black Xs mark the protein levels in the deterministic model. (B) Pearson's linear correlation coefficient between viral proteins and vRNA levels at 12 hpi.

lation between viral proteins and their encoding genome segments suggesting that most of the noise in protein levels results from fluctuations in vRNA abundance (Figure 4.15B). Note that the inhibitory effect of M1 causes a negative correlation to all genome segments, i.e., higher M1 levels impair RNA synthesis, which is superimposed onto the positive correlation between vRNA and protein levels observed in general. Taken together, these results suggest that infected cells differ in their content of viral genome segments due to the inherent noise of biochemical reactions. This noise is amplified by the autocatalytic mechanism of viral RNA replication, propagates to viral protein levels, and impairs virus release.

Nonproductive infections at low initial virus numbers So far, we have only considered infections at a high NIVC where stochastic effects should be weak. Nevertheless, we observed a strong influence of noise and significant differences between the deterministic model and the stochastic simulations. For low concentrations of infecting virions these differences are even more pronounced (Figure 4.16A). Note that one virus particle per cell is the lowest feasible initial condition in a stochastic model since it accounts for whole numbers of viruses only. In our simulations, such low numbers of infecting virions result in a 35-fold reduction in the number of virus particles an average infected cell releases (comparing stochastic results for an NIVC of 10 and 1, respectively). By contrast, the deterministic results barely change. Interestingly, this reduction is not primarily due to an impaired virus release from productively infected cells, which only accounts for a 2.6-fold decrease

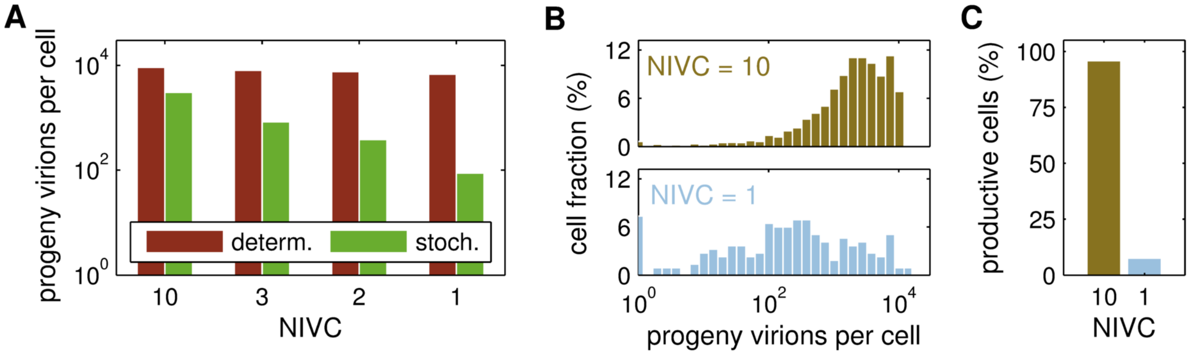

Figure 4.16.: Increasing differences in virus production at low NIVCs. (A) Cumulative number of released virus particles at 12 hpi in the deterministic model and the mean of stochastic simulations at different NIVCs. (B) Histogram of the cumulative number of released virus particles at 12 hpi in stochastic simulations at an NIVC of 10 (upper panel) and 1 (lower panel). The fraction of all productive cells is shown. (C) Fraction of productive cells at an NIVC of 1 and 10.

with some cells producing as much virus as observed at a high NIVC (Figure 4.16B). Instead a significant proportion of cells becomes nonproductive (Figure 4.16C). In particular, at an NIVC of 10, most of the cells release progeny virions, whereas less than 10% of the cells are productively infected when only one virion is added initially. These nonproductive infections only occur in the stochastic model. In deterministic simulations the average infected cell produces virus progeny.

Further analysis points to virus entry as a major source of abortive infections. From the experiment in Figure 4.2 on page 53, we estimated that 49% of all virus particles fail to fuse with endosomes. Hence, adding only one virion per cell leaves half of the cells with virues that do not reach the cytoplasm (Figure 4.17A). Note that a higher number of parental virions can increase the chance of successful virus entry. Currently, viral fusion is the only step of entry that can fail in our model. If other mechanisms are also error prone, these would add to the overall probability of an abortion during virus entry, which decreases the number of productive infections at low NIVCs according to the corresponding binomial distribution function. For instance, if the chance of a virion to enter successfully is only 25% and 5 virions per cell are added, the probability of an abortion during entry is $F\left(k=0;n=5,p=0.25\right)=\left(1-0.25\right)^5\approx 24\%$.

Although abortive virus entry is a key reason for nonproductive infections in our model it only accounts for roughly half of the observed failures to produce virus progeny. In most of the rest of nonproductive cells one (or more) of the viral genome segments is absent at 12 hpi. In particular, there are cells in which incoming vRNPs are degraded before they can replicate (Figure 4.17B). In the model, the probability of losing a particular genome segment follows from the ratio of vRNP replication and degradation, which was estimated

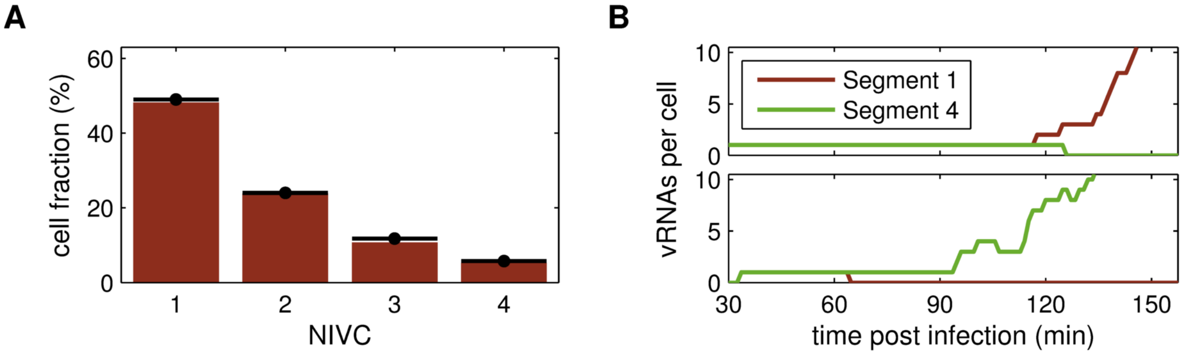

Figure 4.17.: Failed fusion and segment loss cause nonproductive infections. (A) Fraction of cells in which virus entry failed (bars) for different NIVCs. The black dots and lines correspond to the binomial cumulative distribution function $F(k; n, p)$, where $k = 0$ is the number of particles entering successfully, n the number of trials, i.e., the indicated NIVC, and $p = 0.51$ the percentage of entry success for one virion. (B) Early vRNA dynamics in two cells (upper and lower panel, respectively) that were infected at an NIVC of 1 and did not produce virus progeny in the first 12 hpi although virus entry was successful.

from data in Figure 4.5 on page 59. With one genome set entering the nucleus this probability is between 15 and 18% (with a mean of 16%) in our simulations (Figure 4.18A). In addition, the conditional probabilities for genome segment loss are largely independent from one another, e.g., the loss of segment 5 (encoding NP) does not significantly increase the chance of losing another segment. This suggests an important role of primary transcription (the synthesis of mRNA from parental vRNPs) in our model since the loss of segments essential for replication, like those encoding for the viral polymerase

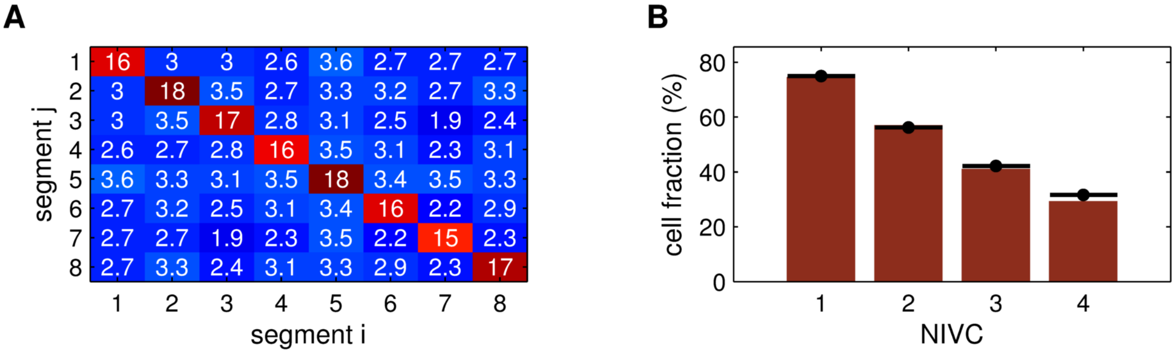

	1	2	3	4	5	6	7	8
1	16	3	3	2.6	3.6	2.7	2.7	2.7
2	3	18	3.5	2.7	3.3	3.2	2.7	3.3
3	3	3.5	17	2.8	3.1	2.5	1.9	2.4
4	2.6	2.7	2.8	16	3.5	3.1	2.3	3.1
5	3.6	3.3	3.1	3.5	18	3.4	3.5	3.3
6	2.7	3.2	2.5	3.1	3.4	16	2.2	2.9
7	2.7	2.7	1.9	2.3	3.5	2.2	15	2.3
8	2.7	3.3	2.4	3.1	3.3	2.9	2.3	17

Figure 4.18.: Probability of genome segment loss. (A) Probability of segment loss for an infection at an NIVC of 1. Colors and numbers correspond to the probability that the indicated segment is absent in a cell at 12 hpi although virus entry was successful. Diagonal elements show the probability that segment $i = j$ is missing, whereas off-diagonal elements correspond to the conditional probability that segment j is absent given the loss of segment i. (B) Fraction of cells which are nonproductive because one or more viral genome segments are absent at 12 hpi although virus entry was successful. Black dots and lines correspond to the binomial cumulative distribution function $F(k = 0; n, 25\%)$.

and NP protein, would otherwise impair genome replication. Reduced genome synthesis would then tip the balance toward segment degradation increasing the chance of losing another segment. Intriguingly, genome segment loss is a major challenge for the virus at low NIVCs although any given segment replicates successfully with a probability above 80%. This is due to the fact that all eight segments are required for the cell to produce infectious virus progeny. Hence, even among cells that successfully underwent fusion a large proportion is rendered nonproductive (Figure 4.18B). More presicely, given an average chance of segment replication of $1 - 0.16 = 84\%$, production of all eight segments occurs in only $0.84^8 \approx 25\%$ of the cases. Again, increasing the number of infecting virions per cell can mitigate this problem.

In summary, at low NIVCs the production of infectious virus progeny by individual cells is unreliable due to the abortion of virus entry and the loss of genome segments (Figure 4.19A). The latter also results in distinct cell populations with respect to viral protein content (Figure 4.19B). Cells that lose a specific genome segment show a reduction in the expression level of the corresponding protein(s) by three orders of magnitude whereby the residual protein level mainly results from primary transcription. Hence, stochastic effects can cause significant variation in single cell trajectories and substantial deviations from the observed cell population average especially at low NIVCs.

Noise reduction by segment-specific regulation In the previous paragraphs, we observed that viral RNA replication amplifies stochastic fluctuations but also that negative feedback regulation can suppress noise. In our model, M1 proteins provide such a negative

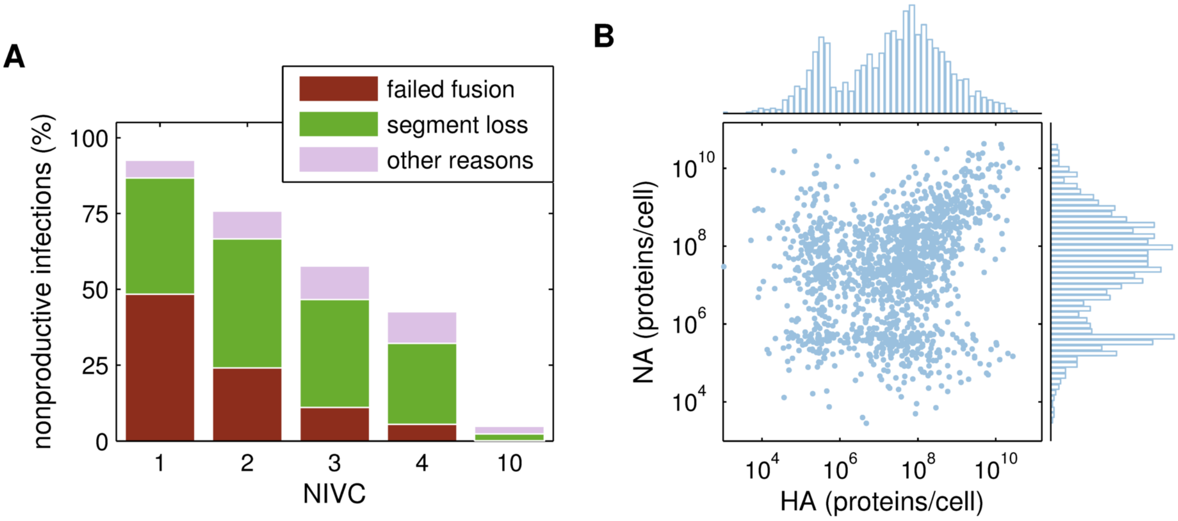

Figure 4.19.: Success of infection. (A) Probability that an infected cell does not release infectious virus progeny until 12 hpi for different NIVCs. Cells were divided into infections where virus fusion failed and where one or more viral genome segments are absent. (B) Number of unpackaged NA against HA proteins at 12 hpi for an infection at an NIVC of 1.

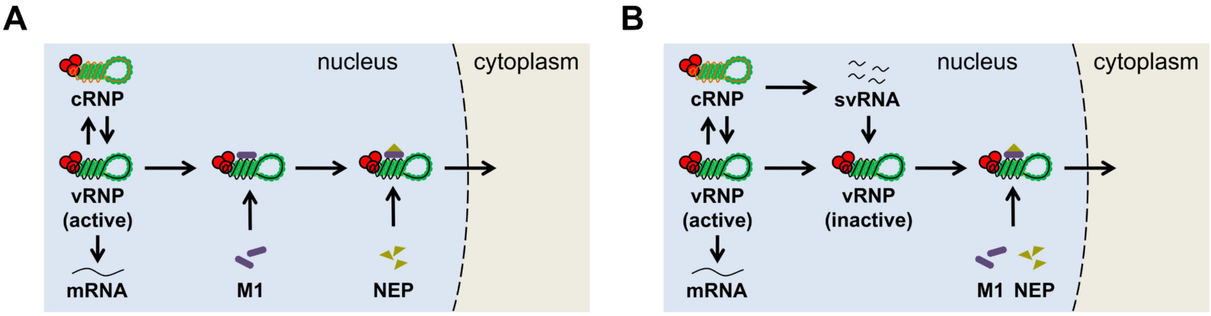

Figure 4.20.: Different models for the regulation of viral RNA synthesis. (A) Nuclear export in the original model where M1 proteins unspecifically inhibit the activity of all vRNPs. (B) Model of segment-specific regulation. Each cRNP produces svRNAs, which specifically inactivate vRNPs of the segment they originate from.

feedback (Figure 4.20A). However, this mechanism primarily reduces noise in segment 7 levels as this segment encodes for the regulator. We were wondering whether a segment-specific regulation would be able to decrease stochastic fluctuations in all eight genome segments. In a recent study, Perez *et al.* described a mechanism by which svRNAs (22 to 27 nt long RNAs synthesized from cRNA) may regulate viral RNA synthesis in such a manner [74]. These svRNAs were shown to interact with the viral RdRp in order to promote genome replication of the segment they originate from. However, such a positive regulation would not be able to maintain the balance between segments as suggested by Perez and colleagues. On the contrary, an increase in the vRNA synthesis rate of a segment that already shows a high cRNA level (and thus a high svRNA concentration) would increase noise. We, thus, developed a model in which svRNAs instead engage in a segment-specific negative regulation, i.e., they inactivate the synthesis of positive-strand RNAs of the segment they originate from (Figure 4.20B and Section A.2.3). Intriguingly, this mechanism can reduce the fluctuations in vRNA levels of segment 1 below one order of magnitude (Figure 4.21A). This noise reducing effect extends to all eight genome segments and leads to an improved agreement with the deterministic solution (Figure 4.21B). Hence, segment-specific negative regulation can drastically reduce the influence of stochastic effects. In addition, the differences between genome segments within infected cells span a much narrow range making the cell population more homogeneous with respect to viral genome content (Figure 4.22A). This results in a substantial increase in cell-specific virus yields (Figure 4.22B). Yet, due to the differences in segment levels that remain, mean virus yields in the stochastic model are still lower than in the deterministic simulation. Moreover, negative regulation does not decrease the amount of cells that fail to produce virus progeny due to an abortion of virus entry or genome segment loss when there is only one infecting virion (Figure 4.22C). However, it does prevent the depletion of viral polymerases and NP proteins by excessive viral RNA replication and the shut-

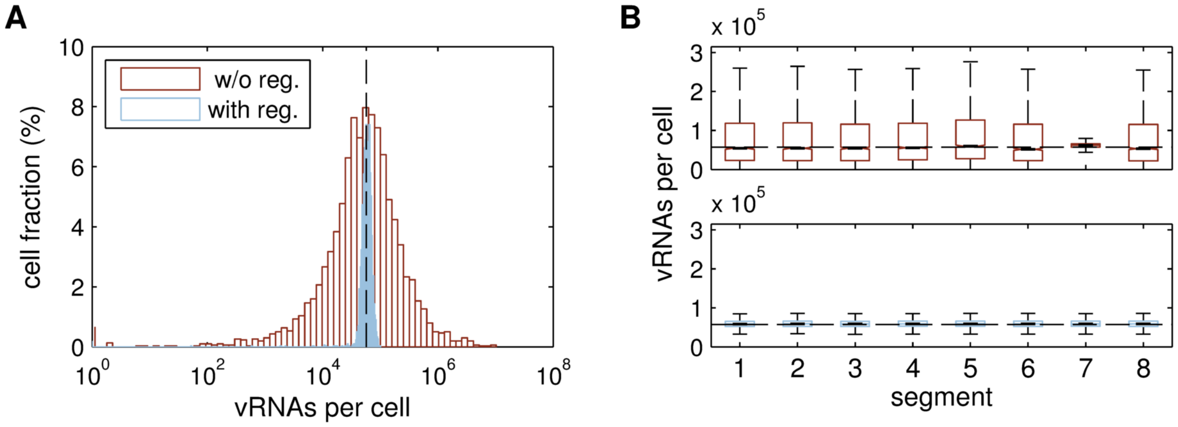

Figure 4.21.: Noise reduction by segment-specific regulation. Stochastic models with and without segment-specific regulation of viral RNA synthesis were used to simulate an infection at an NIVC of 10. (A) Distribution of vRNAs of segment 1 (encoding PB2) at 12 hpi. The dashed line indicates the deterministic result. (B) Fluctuations in the vRNA level of all eight genome segments at 12 hpi in the absence (upper panel) and presence (lower panel) of segment-specific regulation. Boxes were drawn as described in Figure 4.12B.

down of RNA synthesis before a segment was sufficiently amplified, which were other reasons for nonproductive infections in the original model (compare Figure 4.19A and Figure 4.22C). In summary, segment-specific negative regulation represents a mechanism that would allow the virus to counteract noise amplification during viral RNA synthesis. Furthermore, it would lead to an increase in virus production at high concentrations of infecting virions but cannot prevent nonproductive infections at low NIVCs.

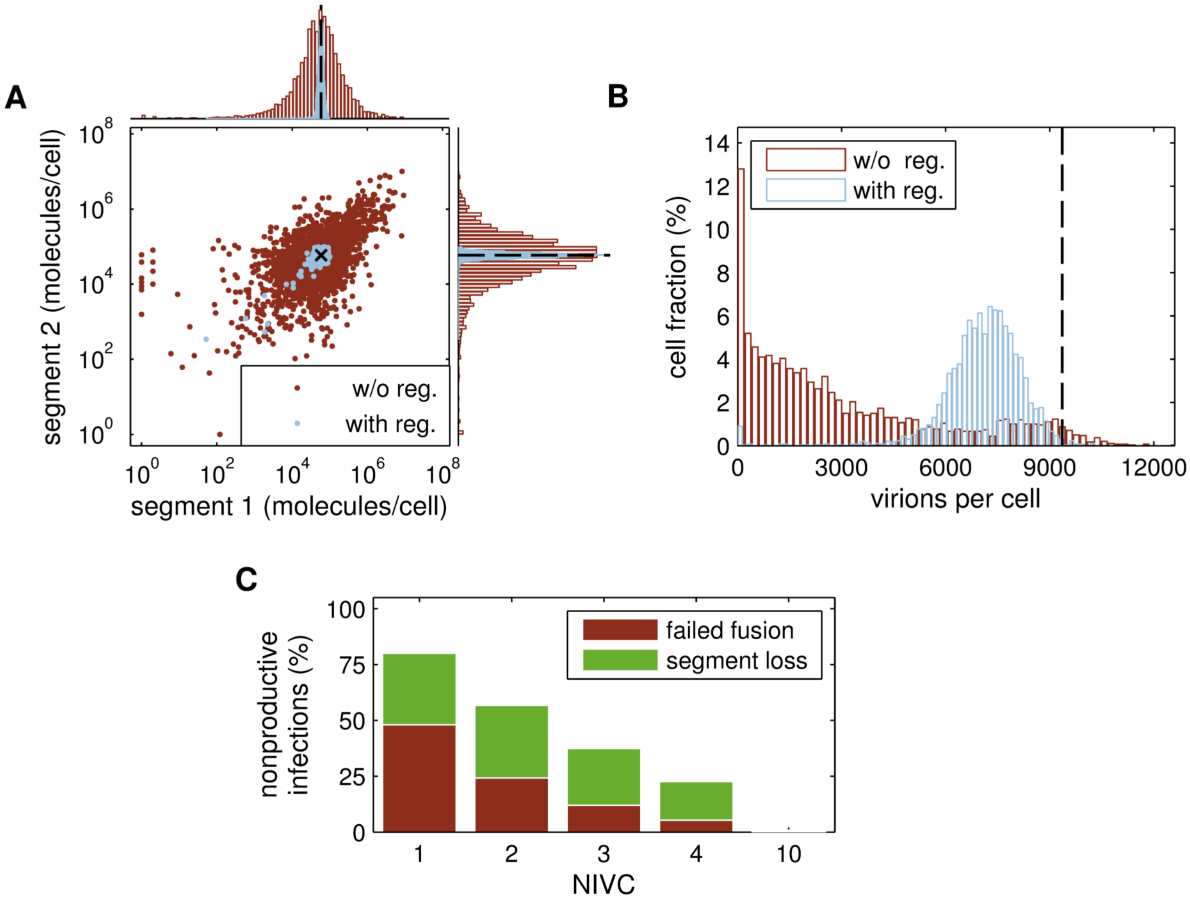

Figure 4.22.: Reliability of infection in the presence of segment-specific regulation. Stochastic simulations in the presence and absence of segment-specific regulation were performed at different NIVCs. (A) Total number of vRNAs of segment 1 and 2 (encoding PB2 and PB1, respectively) at 12 hpi for an infection at an NIVC of 10. The black X represents the vRNA level in the deterministic model. (B) Cumulative number of released virus particles at 12 hpi for an infection at an NIVC of 10. The dashed line indicates the deterministic result. (C) Probability that an infected cell does not release virus progeny until 12 hpi in the presence of segment-specific regulation. Cells were divided into infections where virus fusion failed and where one or more viral genome segments are missing.

4.1.3. Discussion of intracellular kinetics

In the previous two sections, we first derived a deterministic model for the intracellular life cycle of influenza A viruses and then extended this description by considering the inherent randomness of biochemistry. In the following, the merits and weaknesses of both approaches are discussed.

4.1.3.1. Deterministic model of virus replication

Our deterministic model of influenza A virus replication integrates key experimental results published by various research groups over the last two decades. In doing so it allows us to capture both qualitative and quantitative features of virus entry, the transition from mRNA transcription to genome replication, and the dynamics of viral RNA synthesis in a single coherent framework. Using these data, the model facilitates a systematic analysis of the regulatory mechanisms involved in virus replication and of potential targets for the optimization of vaccine production.

Improvement compared to other models To our knowledge, there are only two models for the complete intracellular life cycle of influenza A viruses in literature. One has been proposed by Madrahimov *et al.*, who do however only account for the qualitative aspects of infection since they use a Boolean approach in which the modeled entities can only assume an active or inactive state [17]. Hence, the model can neither reproduce the dynamics of viral replication nor the quantity of the viral components involved. However, it does provide insights into viral interactions with selected host cell pathways, like PKC and ERK signaling, which our description lacks so far. The second model was developed by our group [16]. It comprises ODEs to describe the time courses of major viral components, but does only use literature parameters and general information on influenza virus infection for model calibration. Compared to this model, we tailored our framework to a variety of published data sets and neglected aspects like the cytoplasmic-nuclear trafficking of viral mRNAs and proteins, and the transport of envelope proteins between the ER and the budding site, which reduces model complexity. Furthermore, we included a detailed description of RNP formation, cRNA stabilization, and the regulation of nuclear export. Taken together these features result in a multitude of differences between the outputs of both models. Most prominently, the model of Sidorenko *et al.* predicts a monotonic increase in all three viral RNA species until 12 hpi (at which point the simulation was stopped) [275]. Experimental results do, however, typically show an almost stable cRNA level and a decreasing mRNA concentration during late infection clearly contradicting these predictions (see for instance references [175, 273]). Since our model reproduces these measurements (Figure 4.5), we consider it to more closely resemble influenza A virus infection. For the same reason, the new model is better suited to validate or invalidate hypotheses on the regulation of viral RNA synthesis.

Virus entry As a first step toward an intracellular model of influenza A virus replication we simulated virus entry. In the model, binding to the cell surface occurs fast and the virus can rapidly enter the host cell via endocytosis (Figure 4.2). This agrees well with experimental studies in which virion-containing endosomes have been found as early as 5 min after adsorption [36, 276], while fusion and uncoating typically occur between 5 and 90 min with a half time of approximately 25 min [47, 253, 272]. In our simulations, vRNPs accumulate in the nucleus until 90 min post infection, which is in good agreement with the staining pattern of NP in experiments [47]. Intriguingly, virus uptake seem to stop thereafter. Modeling suggests that this is caused by the depletion of extracellular virions. However, in cell culture infections complete depletion of free viruses is typically not observed [36, 177]. Thus, we speculate that only the virus particles in the vicinity of an infected cell become depleted, while diffusion limits the transport of virions from the bulk of medium. In this case, the number of extracellular viruses in our model would reflect the infectious particles in close proximity to a cell. Alternatively, or additionally, the internalization or removal of sialic acid-containing receptors could restrict virus entry during late infection [257]. This scenario is not captured by the current model since we adopted a binding mechanism that implies fast receptor recycling. But it could be readily incorporated in future studies. In summary, virus entry requires on average 25 min, after which the first vRNPs enter the nucleus [47]. This delay is in agreement with the onset of mRNA synthesis in our model, indicating that vRNPs start to transcribe viral mRNAs immediately after reaching the nucleus.

Stabilization hypothesis In order to account for the transition from mRNA transcription to genome replication, our model considers the stabilization of nascent cRNA by viral polymerases and NP proteins. This allows us to quantitatively analyze the experiments that have led to this hypothesis. The model can capture these measurements successfully but requires several key features to do so. In particular, it predicts a high degradation rate of naked cRNA in the absence of viral proteins, which compensates for the continuous synthesis of cRNA by vRNPs, a core assumption of the stabilization hypothesis (Figure 4.3B). Interestingly, this degradation rate is significantly higher in cell culture infections than the rate inferred from cell-free experiments suggesting that cRNA is stable under *in vitro* conditions (in the absence of nucleases), whereas efficient degradation takes place in infected cells. It would be interesting to determine whether cellular nucleases can cause such high degradation rates.

In addition to the rapid degradation of naked cRNA, the model also requires the existence of an encapsidation intermediate with enhanced stability, the RdRp-cRNA complex. This mechanism facilitates the accumulation of cRNA to intermediate levels in the presence of replication-incompetent viral polymerases (Figure 4.3D). Moreover, such an obligate intermediate state would explain why cRNA levels do not increase in the exclusive presence of free NP. Confirming the two-step process of cRNP formation would, thus, provide further evidence for the stabilization hypothesis. Note, however, that NP has been found to bind RNA with high affinity in an unspecific manner in the absence of viral polymerases (reviewed in [59]). To be consistent with the stabilization model, the resulting NP-cRNA complexes should still be susceptible to nuclease digestion. Studying whether this is the case and, if so, why polymerases are required for stabilization may provide further insights into the transition to genome replication.

With respect to the kinetics of encapsidation, modeling suggests a high affinity of polymerases to cRNA based on the observed saturation of polymerase binding in experiments (Figure 4.3D). By contrast, NP binding is the rate-limiting step of encapsidation in our model such that an increase in NP expression can result in higher cRNA levels. Whether this is a general feature or only holds true for the experimental conditions used for model calibration remains to be determined. But evidence for the latter comes from a study by Mullin *et al.*, who showed that pre-expression of increasing amounts of NP does not alter RNA levels in infected cells [65].

Switching hypothesis In addition to cRNA stabilization, we also derived a simple mathematical model for the switching hypothesis in which NP directly promotes replication at the expense of transcription. Furthermore, the vRNPs in this model were assumed to posses a residual replication activity in the absence of NP proteins. It is this feature that allows us to capture the experimentally observed synthesis of cRNA by virion-derived vRNPs in a cell-free assay (Figure 4.4A), which is a key argument against switching [66]. Modeling, however, shows that the cRNA synthesis rate in this *in vitro* system is approximately 25-fold lower than the rate found in cell culture infections indicating the absence of important cofactors for replication, suboptimal assay conditions, or the presence of only the proposed residual vRNP activity. Surprisingly, the comparison of our switching model to cRNA levels in response to differential NP expression reveals a qualitative agreement, despite major quantitative dissimilarities (Figure 4.4D). Hence, experiments which alter NP levels may not provide sufficient information to confirm or dismiss switching (or stabilization). By contrast, the model was unable to reproduce cRNA abundances in response to changing polymerase expression. Once again, unraveling the role of viral polymerases in the transition to genome replication may, therefore, be key to resolve this mechanism.

Shutdown of RNA(+) synthesis The inhibition of viral mRNA synthesis during late infection constitutes the second important regulatory feature of influenza A virus replication. This step was proposed to be part of the switch to genome replication (reviewed in [59]), such that NP proteins change the activity of vRNPs from transcription toward replication. By contrast, our simulations suggest that there is no immediate shutdown of transcription but rather a sustained period of time in which both mRNA and cRNA are synthesized simultaneously (Figure 4.5A and B). This facilitates the accumulation of transcriptionally active progeny vRNPs, which support the rapid increase in mRNA levels between 1 and 3.5 hpi. In the model, parental vRNPs alone could not sustain such an increase and yield the high mRNA levels observed experimentally. In addition, our simulation results also predict an essential role of progeny vRNPs in cRNA synthesis arguing against the hypothesis that most cRNA production originates from parental vRNPs [57].

If the decrease in transcription is not the result of the switch to replication, what does cause the reduction in mRNA levels after 4 hpi? Our simulations suggest that mRNA synthesis shuts down because its template, the vRNA, leaves the nucleus (Figure 4.5C and D). More precisely, M1 and NEP proteins start to accumulate around 3 hpi at which point they direct vRNPs toward the cytoplasm. This is in good agreement with NP staining in experiments, which is localized almost exclusively to the nucleus during the first 2.5 hpi before becoming more and more cytoplasmic [45]. Once vRNPs have left the nucleus, they no longer engage in transcription and mRNA levels begin to decrease due to mRNA degradation. In our model, the lack of templates also impairs cRNA synthesis, which agrees well with the observed reduction in their accumulation during late infection. Thus, it seems that nuclear export itself or the processes regulating it impair positive-strand RNA synthesis.

In our model, M1 proteins are the sole regulator of vRNP activity during export; they impair RNA(+) synthesis. This is based on three lines of evidence. First, several independent studies have shown that M1 is a potent inhibitor of viral transcription [93–95, 97]. Second, in RNP-reconstitution assays (where cells are transfected with the polymerase subunits, NP, and a vRNA) M1 expression causes a general reduction in all three viral RNA species [70]; and third, infection of cells with a virus that carries a mutant M1 protein (impaired in its binding to vRNPs) results in an increase in intracellular vRNA levels by 250% [77], indicating a lack of negative regulation. Moreover, it has been speculated that M1 binding to NEP might abrogate NEP's polymerase enhancing function [88]. Considering M1 as the main regulator allows our model to not only reproduce the time courses of the viral RNAs but also to predict the mRNA and M1 synthesis rate observed in experiments not used for model calibration (Figure 4.5D). However, we can not exclude that other model variants would work equally well. In particular, an inactivation by NEP or the export process itself may be able to produce similar results. That these processes can at least contribute to the shutdown of RNA synthesis is suggested by two observations: (i) Robb *et al.* found that in an RNP-reconstitution assay mRNAs continue to increase up to high levels and that these high levels are not reached in the presence of NEP [70]; and (ii) the treatment of infected cells with inhibitors of nuclear export increases cRNA levels [277, 278] and reduces the inhibition of viral polymerase activity [88]. Also, a recent study indicates that in order to exert negative control over RNA synthesis, M1 requires the presence of NEP [88], a mechanism not yet implemented in the model. We, thus, propose that the accumulation of M1 and NEP during late infection signals a sufficient supply with viral proteins for particle assembly and diverts vRNPs from transcription and replication toward budding. The M1 level would be a particularly well-suited signal because M1 proteins are the most abundant viral component in a virus particle and may, hence, be the first protein that limits particle formation. From a systems perspective, M1 may hence act as a negative feedback regulator during late infection that, perhaps together with NEP, prevents an excessive RNA production by vRNPs in favor of virus assembly.

Viral RNA dynamics Taken together our results suggest that after the transition to genome replication, influenza A viruses synthesize all three viral RNA species until nuclear export reduces the number of vRNAs that are available as templates for RNA(+) synthesis (Figure 4.5A and B). Afterward, viral mRNA levels decrease due to degradation, whereas cRNA levels stay roughly constant as cRNPs are more resistant to digestion. Since cRNPs remain available as templates, the vRNA level continues to increase throughout infection. These dynamics have been observed for several different influenza A strains in various cell lines [75, 174, 255, 273] supporting the notion that they are an emergent property of the system common to most (if not all) influenza A viruses.

Fitting the model to quantitative data on vRNA and cRNA levels also reveals that the vRNA synthesis rate is ten times higher than that of cRNA. Previous experimental studies have suggested that vRNA production occurs in *trans* by soluble polymerases [50], whereas cRNAs are synthesized in *cis* by the resident polymerase in a vRNP (indicated by the ability of virion-derived vRNPs to produce cRNA [66, 68]). It is, thus, tempting to speculate that on average ten soluble polymerases simultaneously produce vRNA from one cRNP. Alternatively, structural differences in the promoter region of vRNPs and cRNPs may affect their efficiency to initiate synthesis [57].

Host cell factors In order to keep the model simple, we solely focused on the action of viral components and assumed that host factors exert a constant or an insignificant influence (in which case they can be omitted from the model). In fact, we demonstrated that by considering virus entry, cRNA stabilization, and nuclear export alone, simulations are able to reproduce the principle dynamics of intracellular replication. Nevertheless, interactions with host cell factors play a crucial role in influenza virus infection (reviewed in [279]). For instance, the activity of the cellular RNA polymerase II (Pol II) is essential for viral mRNA synthesis and Pol II degradation was suggested to contribute to the shutdown of viral transcription [280]. In our model, the export of vRNPs accounts for most of the decrease in mRNA synthesis (Figure 4.5D). Yet, at late time points simulations overestimate viral transcription. A lack of Pol II in experiments may explain this overestimation, in which case Pol II degradation would contribute approximately 20% to the overall shutdown of viral mRNA synthesis. Furthermore, the association of Pol II with viral polymerases was found to peak at 3 hpi and to decline thereafter [280], similar to the amount of transcriptionally active nuclear vRNPs in our model. Hence, M1 and NEP binding may disrupt the interaction of vRNPs and Pol II starting around 3 hpi, whereas Pol II degradation later on further impairs viral transcription. Incorporating this and other host factors explicitely in our model would facilitate a quantitative analysis of virus–host cell interactions. But it would also increase the model's complexity thereby requiring additional data to identify the new parameters.

Bottlenecks of virus production In line with experimental observations, our model shows a continuous increase in viral genome copies throughout infection. In addition, it predicts an accumulation of all viral proteins until at least 12 hpi (Figure 4.7). In support of this, protein synthesis in infected cells proceeds unhindered even at late times post infection [256], and M1 protein levels continue to increase up to 24 hpi despite significant virus release [77], which requires large amounts of M1. Similarly, strong M1 and NP fluorescence can be detected by flow cytometry until at least 18 hpi [176]. Hence, it seems that none of the essential viral components is depleted by virus assembly and release. But what constrains the amount of virus particles a cell can produce? Prime candidates for such bottlenecks are host factors and transport processes. vRNPs, for instance, were shown to accumulate in the perinuclear region around the microtubule-organizing centers at intermediate times post infection and at the plasma membrane at late time points [103, 104], indicating that the transport to the budding zone or budding itself may constitute a limiting step. Indeed, in our model an increase in the rate of assembly and release can result in higher virus titers (Figure 4.8). Optimizing these processes by cell-line engineering may, hence, help to obtain higher virus yields in vaccine production.

Besides virus assembly and release, perturbations in viral RNA replication can strongly affect virus production in our simulations. Since viral genome copies engage in an autocatalytic process to produce all three viral RNA species and the viral proteins, small changes to the replication rate have large consequences. By contrast, processes upstream of RNA replication, like virus entry, have only a limited impact on yields. Therefore, vaccine production may benefit from increasing the rate of viral RNA synthesis, delaying the onset of nuclear export and the shutdown of RNA(+) synthesis, and enhancing the transport of viral components and their assembly into virus particles. This could be achieved by modifying production cell lines in order to provide more of the required host factors or by adding specific beneficial genome segments to high growth reassortant viruses, e.g. a faster polymerase and an M1 (and NEP) protein that causes a delay in nuclear export.

Summary We have developed a quantitative mathematical model for the intracellular replication of influenza A viruses. It explicitly accounts for the stabilization of viral RNAs via their encapsidation by polymerases and NP proteins, and for the role of M1 and NEP during nuclear export. Together these mechanism can capture a wide variety of experimental data sets in a consistent way. However, the fact that the model reproduces these measurements does not necessarily prove its correctness. Because of this we have outlined several model features that are required to obtain the observed behavior. These features can be probed experimentally to validate or invalidate the underlying hypotheses leading to a deeper understanding of influenza A virus replication. The model can guide such experiments to increase their information content. It can also provide the means to exchange knowledge on influenza A virus replication and to check new theories against existing data.

4.1.3.2. Stochastic model of virus replication

Based on our deterministic description of influenza A virus replication, we developed a stochastic model that accounts for the discrete nature of molecular populations and the randomness of biochemical reactions. This model reveals a significant influence of stochastic effects on viral replication at the single-cell level. In particular, our simulations show that genome segmentation poses a serious challenge to influenza A viruses as molecular noise can act independently on each segment. Together with the autocatalytic mechanism of viral replication, which amplifies noise, large fluctuations in viral RNA and protein levels are the consequence. These fluctuations can impair progeny virus production.

Differences to the deterministic model Stochastic models can show significant differences to their deterministic counterparts thereby revealing how the system responds to the inherently random nature of biology [281]. To explore whether noise has any effect on influenza A virus replication, we compared our deterministic description of the intracellular viral life cycle with a stochastic implementation. Intriguingly, mean stochastic results differ significantly from the deterministic kinetics, even at a high number of infecting viruses where noise should be weak (Figure 4.11). Most prominently, there is a substantial decrease in virus production and large variations in virus yields between individual cells. Similar observations have been made experimentally for VSV infection where virus yields from single cells span over 150-fold [282, 283] and for cells infected by poliovirus whose production capacity varies at least between 269 and 4,225 PFU/cell [284]. In addition, the yield distributions in these studies are skewed to the left displaying many low-productive cells. This agrees well with our predictions for influenza A virus. Since individual stochastic trajectories show significant variations in our model and even mean stochastic results differ from the deterministic solution, we conclude that microscale randomness does play a role in intracellular influenza A virus replication. This supports earlier modeling work on VSV infection showing that low-abundant species can affect viral replication [231] and the general notion that viral infections are particularly prone to noise [282, 284, 285]. Hence, stochastic effects in virus replication may drive cell-to-cell variability (e.g. in virus production) during influenza A virus infection.

Noise in viral RNA synthesis By comparing two variants of our model, we found that influenza A virus replication is particularly susceptible to stochastic effects because the eight genome segments can show variations in vRNA (and cRNA) levels that are independent from one another. Hence, the copy number ratio of different genes is not intrinsically fixed, like during the replication of single-stranded viruses, but rather varies substantially causing large cell-to-cell differences in our simulations. Specifically, genome segment levels differ by up to four orders of magnitude between individual cells (Figure 4.12). Such large variations have been observed experimentally for influenza A viruses (Kupke, unpublished data) suggesting that their RNA synthesis is indeed vulnerable to noise. The stochastic model also predicts that vRNA levels follow a log-normal distribution around the deterministic result. This type of distribution is common to biology and known to result from noise propagation in cascades of catalytic reactions [286]. Since viral genome synthesis forms such a cascade, we expect this distribution to be a general feature of the genome copy numbers in influenza A virus infection.

Surprisingly, segment 7 levels show lower fluctuations than the other vRNAs in our model (Figure 4.12B). This is caused by the regulatory role of M1, which is encoded by this segment. As discussed in the context of the deterministic model, we assumed that M1 proteins control viral RNA synthesis including the production of their own template. Such negative feedback loops are known to suppress noise [287, 288]. However, since we cannot exclude that other viral or cellular factors contribute to the shutdown of RNA production this result should be taken with caution until the exact mechanism is clarified. Nevertheless, it suggests that negative–feedback regulation can suppress fluctuations in viral RNA synthesis to a certain extend.

A closer investigation of the origin of noise in our model reveals that most fluctuations arise early in infection when viral RNAs are synthesized (Figure 4.14). This agrees well with the theory that autocatalytic reactions, which underlie intracellular virus growth, can account for large amounts of noise [285, 289]. Thus, we propose that the randomness of reaction events causes small fluctuations in vRNA numbers during early infection, i.e., chance determines whether and when a particular RNA is synthesized or degraded, and that these small fluctuations are amplified by the exponential growth of viral RNAs. Because each vRNP can replicate independently, this leads to large differences between different genome segments and to substantial variations in viral protein levels.

Stochastic effects in virus entry Stochastic simulations that were started with low amounts of infecting viruses reveal additional differences to the deterministic description. In particular, the model predicts that more than 90% of the cells fail to produce infectious virus progeny when infection is initiated by a single virion (Figure 4.16C). One reason for these nonproductive infections is an abortion of virus entry by fusion-incompetent viruses, which accounts for roughly half of the observed cases. In the deterministic model, failure to produce virus progeny upon infection is not observed since state variables are continuous: instead of some cells undergoing successful fusion and others aborting virus entry, the deterministic model simulates an average infected cell in which a fraction of the virus particles enters the cytoplasm causing productive virus replication. By contrast, stochastic simulations segregate the intracellular species (e.g. the viral genome copies) into individual cells and they can “jump” to the unstable, virus free equilibrium, which the deterministic model can not reach once left [281]. The latter is caused by two features of stochastic simulations: they account for the discrete nature of molecular populations allowing the state variables to actually reach zero, and for the randomness of reaction events such that the degradation of a virus particle can occur before its fusion.

Burden of genome segmentation The second major reason for nonproductive infections in our model is the loss of one or more viral genome segments during replication. Again, this is only observed in stochastic simulations because vRNA degradation can occur before replication and the molecular populations can become zero. Our model predicts that, once in the nucleus, each vRNP has a chance of 84% to replicate successfully (Figure 4.18A). Considering a cell in which fusion was successful and only a single viral genome set reaches the nucleus, the probability to replicate all eight vRNPs, which is required to release propagation-competent viruses, is only $0.84^8 \approx 25\%$. This is in good agreement with the small number of productive cells observed in low MOI infections [290] revealing the disadvantages of genome segmentation: it not only poses a serious challenge to packaging (reviewed in [108]), but also requires that RNA synthesis is successful in eight independent instances. Note that the latter may also restrict the total number of genome segments an influenza virus (or other viruses with segmented genomes) can posses as each additional segment would decrease the chance of successful virus production at low MOI further.

These results are particularly interesting in the context of a recent study by Brooke *et al.*, who measured the expression of four viral proteins during low MOI infection with influenza A virus and found that most infected cells fail to express at least one of these proteins [290]. More precisely, the average expression frequency of a particular protein in an infected cell was 78.1% and the chance to express the products of all eight genome segments 13.8%. This is comparable to our results predicting a probability of 84% and 25% for the successful amplification of a specific genome segment and the complete genome set, respectively[4]. We, therefore, propose that stochastic effects during early infection at low MOI can cause the loss of genome segments contributing to the observed failure to express viral proteins. The remaining cases of missing protein expression, i.e., the differences between our estimation of 84% and the experimental result of 78.1%, may be caused by internal deletions in genome segments (e.g. DI RNAs), non-sense and lethal mutations, or parental virions that lack a vRNA (as suggested by Brooke and coworkers [290]). Our estimation would, hence, represent an upper limit for successful protein expression and virion release at low MOI because we assumed that all infecting viruses contain a full set of functional vRNPs. This also implies that even if all parental viruses were propagation-competent many infections would not produce infectious virus progeny. Hence, the term "semi-infectious virions" [291] may be misleading in that it could also be the replication process itself that fails and not only the virus.

Note that although a genome segment can get degraded in our simulations, primary transcription (i.e. the synthesis of mRNAs from parental vRNPs) results in the presence of its encoded protein(s), albeit at much reduced levels (Figure 4.19B). More precisely, early segment degradation causes a drop in the protein level by approximately three orders of magnitude. In order to be consistent with the data of Brooke *et al.* [290], these residual protein levels must be below the detection limit of flow cytometry such that cells in which only primary transcription occurs appear to lack the protein entirely. Hence, investigating whether primary transcription results in detectable protein levels can help to validate or

---

[4] Note that both, the experimental and simulation results are given in percent of infected cells, i.e., of cells where fusion was successful, which make up only 50% of all cells.

invalidate our hypothesis that segment degradation leads to a failure in detectable protein expression.

Success of low MOI infections Taken together, our stochastic results suggest that low MOI infections can lead to a significant proportion of cells that do not release infectious virus progeny (Figure 4.19A). Consequently, stochastic effects would be particularly important in the early phase of infection where the virus establishes itself in a host or cell population. During later stages, progeny virions that were released by the few productively infected cells would increase the MOI and (super-)infect cells that may have been left with a fusion-incompetent virus or suffered from genome segment loss in an earlier infection wave. Thereby, multiple virus particles would complement one another to cause virus production in subsequent waves. Previously, it has been suggested that complementation dependency might constitute an evolutionary advantage for the virus during late infection by imposing a step that mandates the mixing of segments from different strains [290, 291]. Hence, it may be selected for. Our results put forward an alternative hypothesis in which the requirement for complementation is simply a consequence of random vRNA degradation and of the segmented genome of influenza A viruses. Nevertheless, the virus may exploit it to enhance genetic shift.

Infections at a low MOI are often part of virus quantification assays where the sample is diluted until the readout cannot be observed anymore. According to our model, these techniques would particularly suffer from stochastic effects. More precisely, assuming that all virus particles are replication-competent and can undergo fusion only 25% of them would be detected as infectious particles in a plaque assay at maximum dilution because of random genome segment loss. If the expression of a viral protein is the readout (e.g. in some forms of the TCID_{50} assay [170]), at most 84% of the infections would be observed, assuming that the loss of the genome segment which encodes for the marker protein prevents detection. If other segments, like those encoding the viral polymerase subunits or the NP protein, would also be required to cause detectable protein expression, this percentage would decrease even further. Hence, noise in virus replication may bias infectivity assays and explain part of the difference between TCID_{50} and plaque titers, i.e, the difference between the probability to loose a particular segment (encoding the marker protein) and any one of the eigth segments, which prevents infectious virus production and plaque formation.

Segment-specific regulation Given the large fluctuations in vRNA levels, we wondered whether there is a way for the virus to suppress noise. Based on a previously proposed mechanism [74], we, thus, developed a model in which each genome segment controls its own level by means of negative–feedback regulation. Note that the experimental results instead suggested a positive feedforward where cRNAs produce small viral RNAs (svRNAs), which then promote vRNA replication in a segment-specific manner [74]. However, such a mechanism would most likely increase noise since svRNAs would enhance their own production (by increasing the level of vRNAs which then synthesize more cRNAs). This resembles an autocatalytic reaction cascade known to facilitate the accumulation of noise [289]. By contrast, segment-specific negative regulation can, indeed, efficiently suppress noise in our simulations, resulting in more homogeneous vRNA levels and higher virus yields (Figure 4.22). Further experiments are required to determine whether influenza A viruses have evolved such a mechanism to control noise.

Summary We have developed a stochastic model of intracellular influenza A virus replication and could show that it significantly differs from the deterministic kinetics. In particular, simulations suggest that the abortion of virus entry, the loss of genome segments, and the autocatalytic mechanism of RNA synthesis cause noise in virus replication at the single-cell level. These processes may, hence, drive cell-to-cell variability during infection. From a modeling perspective, the results argue for using stochastic models to study intracellular viral growth. Yet, their computational inefficiency for systems with large numbers of reactants (like the vRNAs and proteins in influenza A virus-infected cells) still prevents a broad application. Hybrid simulation algorithms (reviewed in [292]) may be able to address this issue and facilitate an estimation of infection parameters from stochastic models in future studies.

4.2. A multiscale model of influenza A virus infection

In the previous sections, we considered the intracellular life cycle of influenza A viruses and, thus, focused on single-cycle infections. Yet, *in vivo* the virus spreads from one target cell to the next such that multiple infection rounds can occur. To understand the interplay between intracellular replication and extracellular transmission we developed a multiscale model of virus growth that integrates these two processes. In the first part of this section, we show that such a model can capture measurement data on both levels thereby providing a systems-level understanding of infection. Subsequently, the model is used to study direct-acting antivirals *in silico* and to provide a ranking of the most promising targets for antiviral therapy. In the following, parts of the original publication of the model in PLoS Computational Biology are used [266].

4.2.1. From single cells to cell populations

In order to simulate the extracellular level of infection, we followed the classical model of viral kinetics within a host or cell population, which considers uninfected target cells, infected cells, and free virus particles (reviewed in [14] and [15]). We augmented this framework by including the number of apoptotic cells and by modeling virus entry in more detail (Figure 4.23A). The simulation of virus entry is based on the structure and kinetics of the intracellular model (see Section 4.1.1). Once inside the cell, the virus starts to replicate and produce viral RNA and proteins. To account for these intracellular changes, we segregated the infected cell population according to the infection age, i.e., the time that has elapsed since the virus entered the cell (Figure 4.23B). Hence, the extracellular model tracks the number of infected cells, their lifespan, and how they progress through the stages of infection, while the intracellular model provides the amount of viral components in an infected cell over its age (Figure 4.23C). The two submodels were coupled by assigning the age-dependent state of a cell to the age-segregated cell population (Figure 4.23D). In simulations, intracellular virus replication primarily affects the extracellular level via the age-dependent virus release rate, which depends on the abundance of viral RNAs and proteins inside a cell and determines the number of virions released into the extracellular medium.

Kinetics of viral infection For an accurate calibration of the model, we followed a two-way strategy. At the intracellular level, we considered high MOI experiments, which result in a single, synchronized infection round (Figure 4.24A). The RNA levels and virus titer in these experiments can be interpreted as the average response of an individual cell to infection. By contrast, the extracellular level was compared to flow cytometric data of

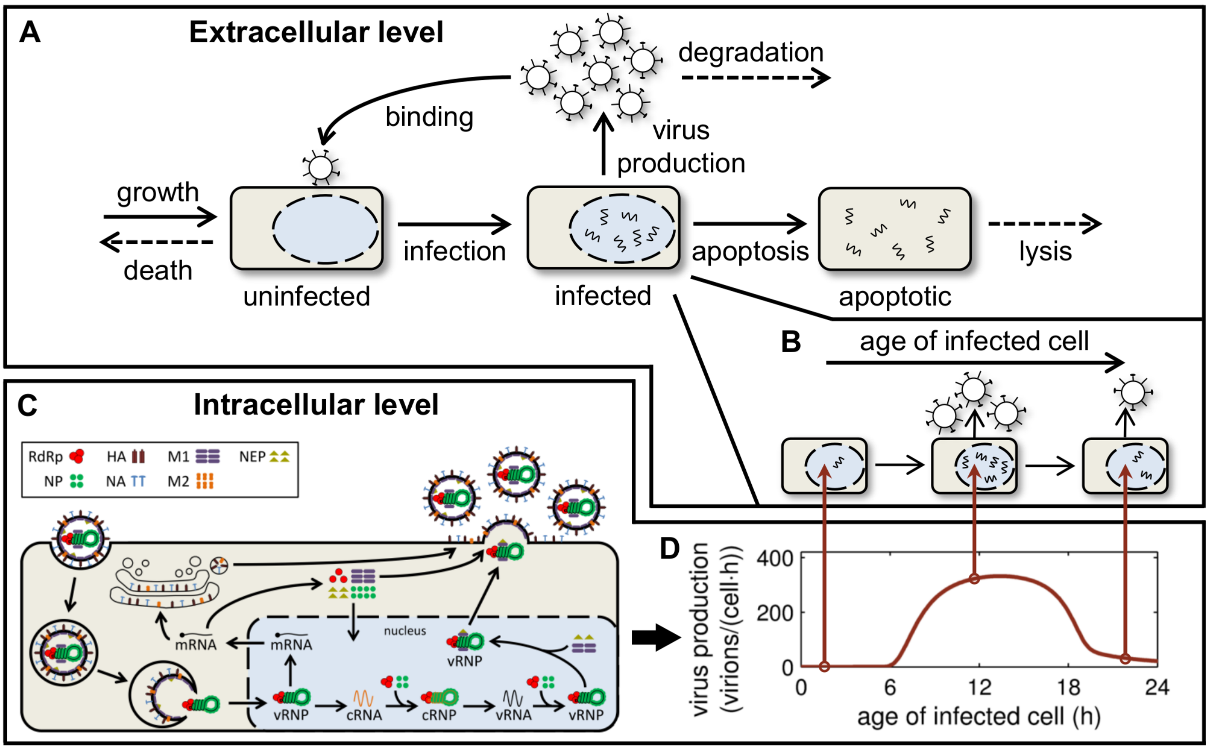
A
Extracellular level
degradation
binding
virus production
growth
death
uninfected
infection
infected
apoptosis
apoptotic
lysis
B
age of infected cell
C
Intracellular level
RdRp
HA
M1
NEP
NP
NA
M2
mRNA
mRNA
nucleus
vRNP
vRNP
cRNA
cRNP
vRNA
vRNP
D
virus production (virions/(cell·h))
400
200
0
0
6
12
18
24
age of infected cell (h)

Figure 4.23.: Schematic depiction of the multiscale model. (A) The extracellular level of infection comprises the growth and death of uninfected cells, their infection by free virions, the production of virus by infected cells, viral degradation/clearance, virus-induced apoptosis, and the lysis of apoptotic cells. (B) Infected cells are further segregated according to the infection age. (C) The intracellular state of an infected cell is simulated using the deterministic model of influenza A virus replication (see Section 4.1.1 for details). (D) Both levels are coupled via the age-dependent virus production rate. Figure taken from Heldt *et al.* [266].

low MOI experiments to assess the dynamics of virus transmission in a cell population during multiple cycles of infection (Figure 4.24B). For parameter estimation, the complete multiscale model was fitted simultaneously to both data sets using the same parameters. Hence, in the final simulation, each infected cell behaves according to the time courses shown in Figure 4.24A, while a population of such cells infected at low MOI exhibits the dynamics in Figure 4.24B.

On both levels, simulations are in good agreement with the experimental results, which allows us to analyze the infection kinetics in more detail. We find that viral mRNAs rapidly accumulate upon infection (Figure 4.24A). By contrast, cRNA and vRNA synthesis does not start until 3 to 4 hpi since viral proteins are required for genome replication. Note that in comparison to the original intracellular model, which is based on data by Kawakami *et al.* [175], measurements in Figure 4.24A suggest that, for these experiments, genome replication starts roughly 2 h later (compared to Figure 4.5A and B). Also, the shutdown of positive-strand RNA synthesis is delayed with vRNPs leaving the nucleus around 5 to 6 hpi. At the same time, cells release the first virus particles such that the

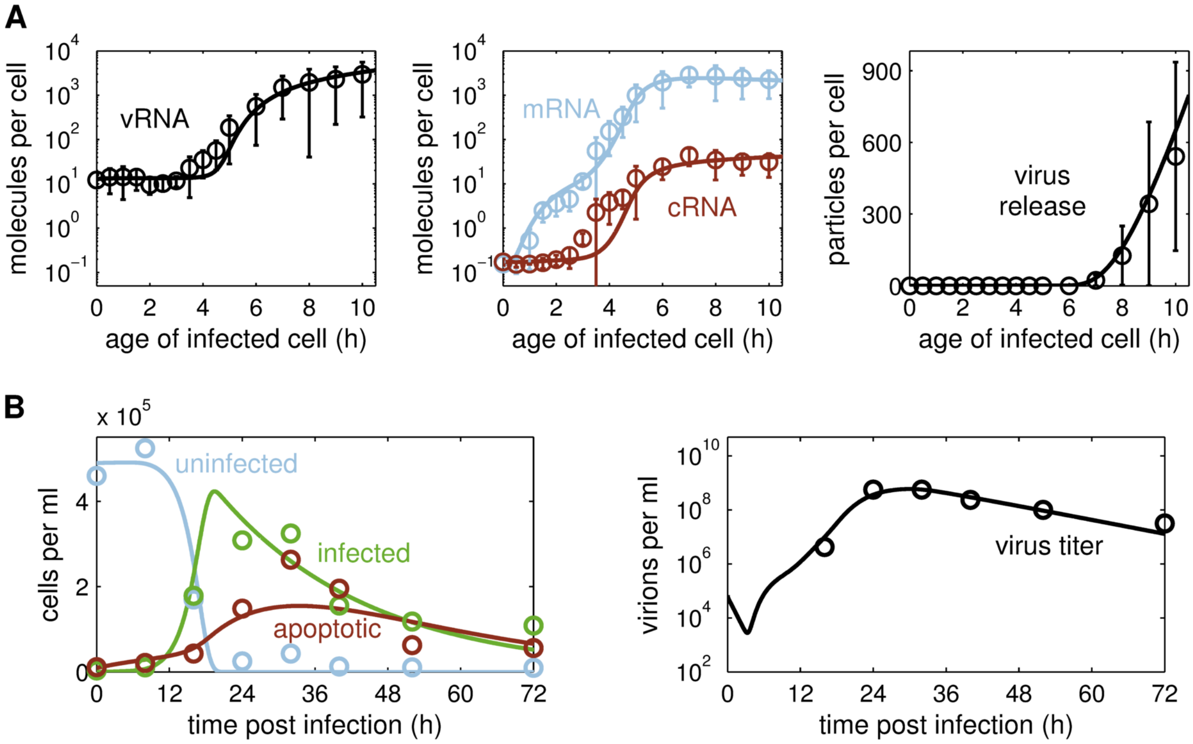

Figure 4.24.: Model fit to measurements of intracellular and extracellular infection dynamics. Curves represent model fits to experimental infections of MDCK cells with influenza A/PR/8/34 (H1N1) depicted by circles. (A) Levels of intracellular vRNA, cRNA and mRNA of segment 5 (encoding NP), and the amount of virus particles produced by an average infected cell in a synchronous, single-cycle infection experiment (MOI = 6). Particle numbers correspond to the amount of hemagglutinating virus particles and were calculated from virus titer measurements by HA assay (Equation (3.2.13)). Bars indicate the standard deviation of three independent experiments (two for the 9 and 10 hpi measurements). (B) Concentration of uninfected, infected and apoptotic cells, and infectious virus titer in a multi-cycle infection (MOI = 0.1). Measurements were adopted from Isken *et al.* and are representative of three independent experiments [267]. Figure adapted from Heldt *et al.* [266].

eclipse phase, i.e., the time from infection to virus release, is approximately 6 h (τ_{eclipse} in Table 4.4). Thereafter, virus production increases as vRNPs and viral proteins accumulate inside the cell (data not shown), whereas the depletion of these factors at very late time points impairs virus release from 14 h onward (Figure 4.23D). These intracellular dynamics are in good agreement with the course of infection at the extracellular level (Figure 4.24B) considering that typical errors in adherent cell counts are in the range of 10–20% due to variations introduced by the measurement technique, handling, and trypsinization. In particular, at an MOI of 0.1 most of the cells become infected between 12 and 19 hpi in the second and third round of infection. Simultaneously to the decrease in uninfected cells, simulations show a corresponding increase in infected cells, which, later, gradually succumb to virus-induced apoptosis. At 32 hpi, we observe a large

Table 4.4.: Parameter estimates for the multiscale model fit in Figure 4.24.

Parameter		Value	95% CI[a]
F_{Inf}	(cells/virion)	1[b]	$0.47 - 1$
$k_{\text{I}}^{\text{Apo}}$	(h^{-1})	3.28×10^{-2}	$(2.26 - 5.90) \times 10^{-2}$
$k_{\text{T}}^{\text{Apo}}$	(h^{-1})	7.35×10^{-3}	$(4.89 - 11.09) \times 10^{-3}$
$k_{\text{M1}}^{\text{Bind}}$	$(\text{molecule} \cdot \text{h})^{-1}$	2.43×10^{-4}	$(0.59 - 4.35) \times 10^{-4}$
k^{Fus}	(h^{-1})	9.56×10^{-3}	$(3.95 - 21.31) \times 10^{-3}$
k^{Lys}	(h^{-1})	6.39×10^{-2}	$(4.64 - 8.83) \times 10^{-2}$
$k_{\text{max}}^{\text{Rel}}$	$(\text{virions}/(\text{cell} \cdot \text{h}))$	586	$170 - 2650$[c]
$k_{\text{C}}^{\text{Syn}}$	(h^{-1})	5.29	$1.97 - 9.33$
$k_{\text{M}}^{\text{Syn}}$	(h^{-1})[d]	502	$245 - 814$
$k_{\text{V}}^{\text{Syn}}$	(h^{-1})	32.18	$13.90 - 61.96$
τ_{apo}	(h)[e]	24.9	$14.3 - 36.3$
τ_{eclipse}	(h)[f]	5.7	$5.1 - 6.5$

[a] 95% confidence intervals provided by 2 000 bootstrap replicates [249].
[b] One is the upper bound of F_{Inf} as no more cells can become infected than virions fuse with endosomes.
[c] Estimates reached the lower and upper parameter bounds.
[d] Synthesis rate of an mRNA of average length. In the model, transcription is length dependent with a rate of 8.53×10^5 nucleotides/h (see Section 3.1.1 for details).
[e] The average lifespan of an infected cell was calculated as $\left(k_{\text{T}}^{\text{Apo}} + k_{\text{I}}^{\text{Apo}}\right)^{-1}$, which includes the eclipse phase.
[f] The end of the eclipse phase was defined as the time when $r^{\text{Rel}}(\tau) > 1\,\text{virion}/(\text{cell} \cdot \text{h})$. Note that this includes the steps of virus entry. The delay between fusion and virus release is only 2 h.

deviation between the model and the experimental results. However, this single data point can be regarded as an outlier because the measured total cell number at 32 hpi increased by 30% compared to the 24 hpi sample. Such a large increase is unlikely to occur during late infection when cell growth is already impaired. Furthermore, simulations of the infectious virus titer (Figure 4.24B), which directly depend on the number of infected cells, are in good agreement with the data providing additonal evidence for the model's accuracy. Due to virus binding, entry, and degradation, the virus titer decreases in the first hours after addition of the inoculum. At approximately 30 hpi, the virus concentration peaks when production and degradation are in equilibrium. Thereafter, the virus titer decreases due to the decreasing number of infected cells and the rate constant of virus degradation.

Effect of seed virus concentration To test the predictive capabilities of the model, we next simulated infections at different MOIs and compared the results to measurement data not used for model construction. In these scenarios, the model correctly predicts the shift in infection dynamics for very low and high amounts of infectious virus particles

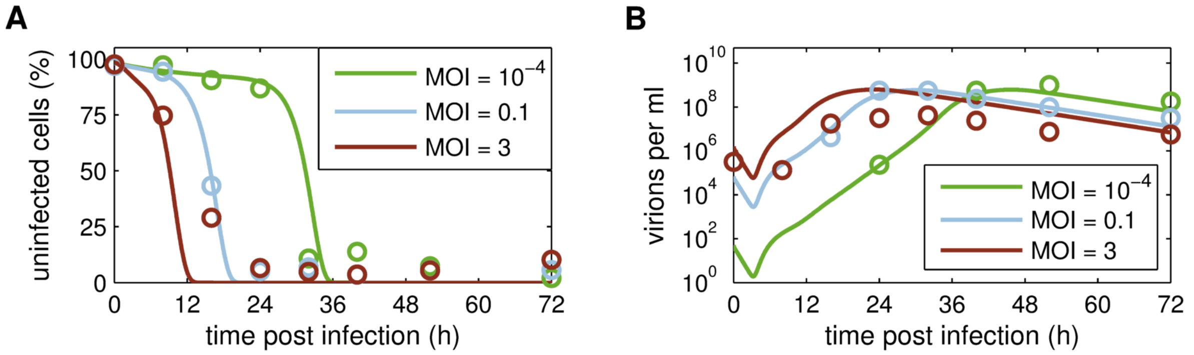

Figure 4.25.: Model predictions for different infection conditions. The model fit from Figure 4.24 was used to predict the percentage of uninfected cells (A) and the infectious virus titer (B) for infections at an MOI of 10^{-4} and 3, respectively. These predictions were compared to data sets not used for model construction. Measurements were adopted from Isken *et al.* and are representative of three independent experiments [267]. Figure adapted from Heldt *et al.* [266].

in the inoculum (Figure 4.25A). Furthermore, it can reproduce the delay in peak virus titers observed at low MOI (Figure 4.25B). However, the simulation overestimates virus production at a high seed virus concentration. Overall, the model can, thus, be of predictive value especially for low MOI regimes where multiple infection rounds occur, which resembles the *in vivo* situation more closely than single-cycle, high MOI experiments.

Connection of intracellular replication and extracellular infection A major advantage of the proposed multiscale description is the integration of virus replication inside infected cells with infection dynamics in cell populations. Through this link, the model can infer the time course of key viral components in multi-cycle infections based on the kinetics of RNA synthesis at the intracellular level. For instance, it can predict the distribution of NP proteins in a cell population during infection, which is a valuable experimental readout for monitoring vaccine production [176]. For this purpose, the model uses the number of uninfected and infected cells (Figure 4.26A) to estimate the infection age density (Figure 4.26B). This density shows very low numbers of cells in the early phase of infection at 8 hpi, whereas at 20 hpi cells form a distribution with an age between 0 h (very recently infected) and 12 h (intracellular replication is already advanced). In the following, infected cells grow older and the distribution moves to the right. The spread of the age density depends on the slope of the increase in infected cells between 12 and 20 hpi in Figure 4.26A. Furthermore, the apoptosis rate determines how fast the density's integral, the total number of infected cells, decreases. In addition to this information, the intracellular model provides the number of NP proteins over the age of an infected cell based on the viral RNA levels (Figure 4.26C). More specifically, it predicts an increase in NP up to an age of 18 h after which protein levels decrease due to the shutdown of mRNA synthesis.

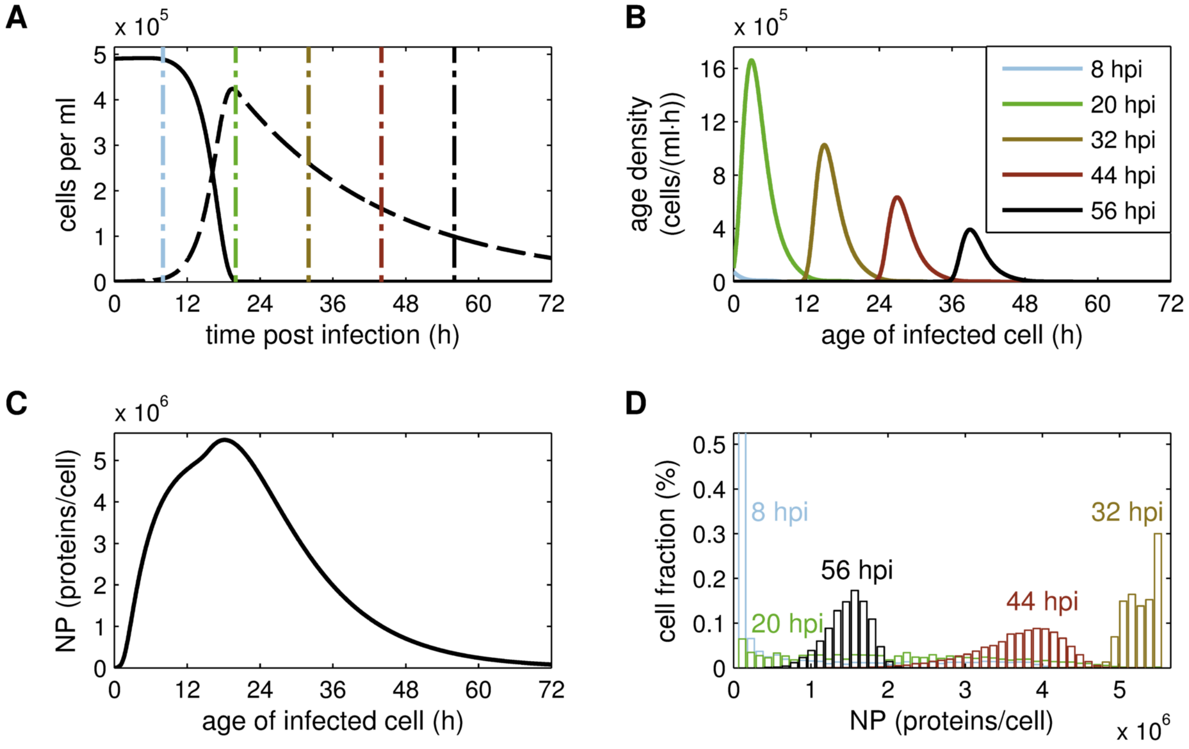

Figure 4.26.: Dynamics of cellular NP content during multi-cycle infection. An infection at MOI 0.1 was analyzed for the amount of NP proteins in the host cell population. (A) Concentration of uninfected (solid) and infected cells (dashed). Vertical dash-dotted lines indicate the time points post infection that were used as examples in B and D. (B) Infection age density (see Equation (3.2.5)) over the age of an infected cell illustrating how many infected cells have the indicated age at different times post infection. (C) Abundance of NP proteins (including free and RNP-bound NP) in an average infected cell over its age. (D) Distribution of NP expression in the cell population for different times post infection.

The combination of the age distribution and the age-dependent intracellular state yields the distribution of NP proteins in the cell population over time (Figure 4.26D). At early times, where most of the cells are uninfected, NP expression levels are low. Subsequently, the protein level increases in individual cells and in the cell population (compare distribution at 8, 20, and 32 hpi). At late time points, the decrease in intracellular NP concentration causes a characteristic shift of the NP distribution to the left (compare distribution at 32, 44, and 56 hpi). For an MOI of 1, we even observe bimodal protein distributions (see Figure B.1 in the appendix). Thus, the time course of viral components inside an infected cell directly translates into protein expression levels in a cell population. Cell population measurements can, hence, be used to infer the dynamics of the intracellular viral life cycle even if the experiment features multi-cycle infection (i.e. if it was performed at low MOI).

Lifespan of infected cells The multiscale model also facilitates an estimation of the lifespan of infected cells from experimental data allowing us to combine this estimate with the virus release kinetics at the intracellular level. We can, hence, assess whether cell death limits virus production. Based on the measurements in Figure 4.24B an infected cells survives on average 25 h (τ_{apo} in Table 4.4). At this age, virus production is already impaired due to the depletion of cytoplasmic vRNPs and viral proteins (Figure 4.27, solid line). However, similar to the standard model of viral infection [11], our simulation assumes that the probability of cell death is independent of time such that cell survival times follow an exponential distribution around the average (for a detailed discussion and alternatives see reference [204]). Therefore, many cells die before the end of the productive phase with more than one quarter succumbing to apoptosis before they reach the peak in virus release. Cell death can, hence, affect the viral burst size, i.e., the number of virus particles an infected cell releases (Figure 4.27, dashed line), and may, thus, limit virus yields in vaccine production.

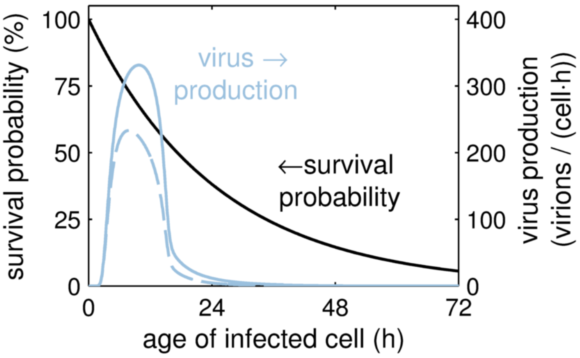

Figure 4.27.: The impact of cell death on virus production. Survival probability of an infected cell and its virus production rate over the infection age neglecting cell death (solid) and considering cell death (dashed). Figure adapted from Heldt *et al.* [266].

4.2.2. Interference by direct-acting antivirals

Mathematical models of viral infection are often used to identify and design treatment strategies. Thus, previous studies have extended the classical model of viral kinetics by considering drug interference with the infection of cells and with virus production at the within-host scale [14, 206, 217]. In addition to these general effects, our multiscale model can also predict the impact of DAAs, which directly target specific steps of the intracellular virus life cycle to impair viral replication and spread.

Interference with virus production In order to find promising targets for antiviral drugs, we analyzed our model for the most susceptible steps of intracellular replication with respect to virus production (Figure 4.28A). In theory, each tested mechanism may correspond to a specific class of DAA, whereby the drug efficacy depends on factors like the chosen compound, dosing regime, or virus strain. In simulations, most of the targets eventually lead to reduced virus production with increasing efficacy. Yet, in some cases a weak interference can already suffice to cause an effect. For instance, targeting viral mRNA and protein synthesis or virus assembly/release is highly effective in our model even at low efficacies. Note that drugs which are currently in use for influenza treatment typically show a maximum efficacy of 90% and above [206, 218, 293]. At this interference potential, compounds that affect viral mRNA splicing, cRNA and vRNA synthesis, or nuclear export also impair virus production. Interestingly, simulations at low drug efficacies show an increase in virus yield when viral genome synthesis or RNA encapsidation are targeted. Such an increase is also observed for inhibitors of M1 protein binding.

The multiscale model predicts drug effects based on how a compound interferes with intracellular virus replication. Inhibitors of viral mRNA synthesis, for instance, reduce mRNA and protein levels and, thereby also impair the accumulation of viral genome copies (Figure 4.28B, upper panel). Especially the later leads to a significant decrease in virus production. The minor increase in cRNA and vRNA during early infection in these simulations results from a decrease in M1 protein levels causing a weaker inhibition of positive-strand RNA synthesis. Besides this regulatory function, M1 proteins are also the most abundant viral component in progeny virions. Therefore, a reduction in virus assembly/release leads to a higher abundance of M1, which decreases RNA levels slightly (Figure 4.28B, middle panel). However, most of this drug's effect results from the retention of viral components in the cell. Note that targeting assembly/release with 50% efficacy reduces the viral burst size to roughly half its pretreatment value, whereas the inhibition of transcription with similar efficacy causes a drop by approximately 90%. Hence, release inhibitors exert a linear influence on virus production in contrast to the nonlinear response to blocking of mRNA and protein synthesis. For the inhibition of cRNA synthe-

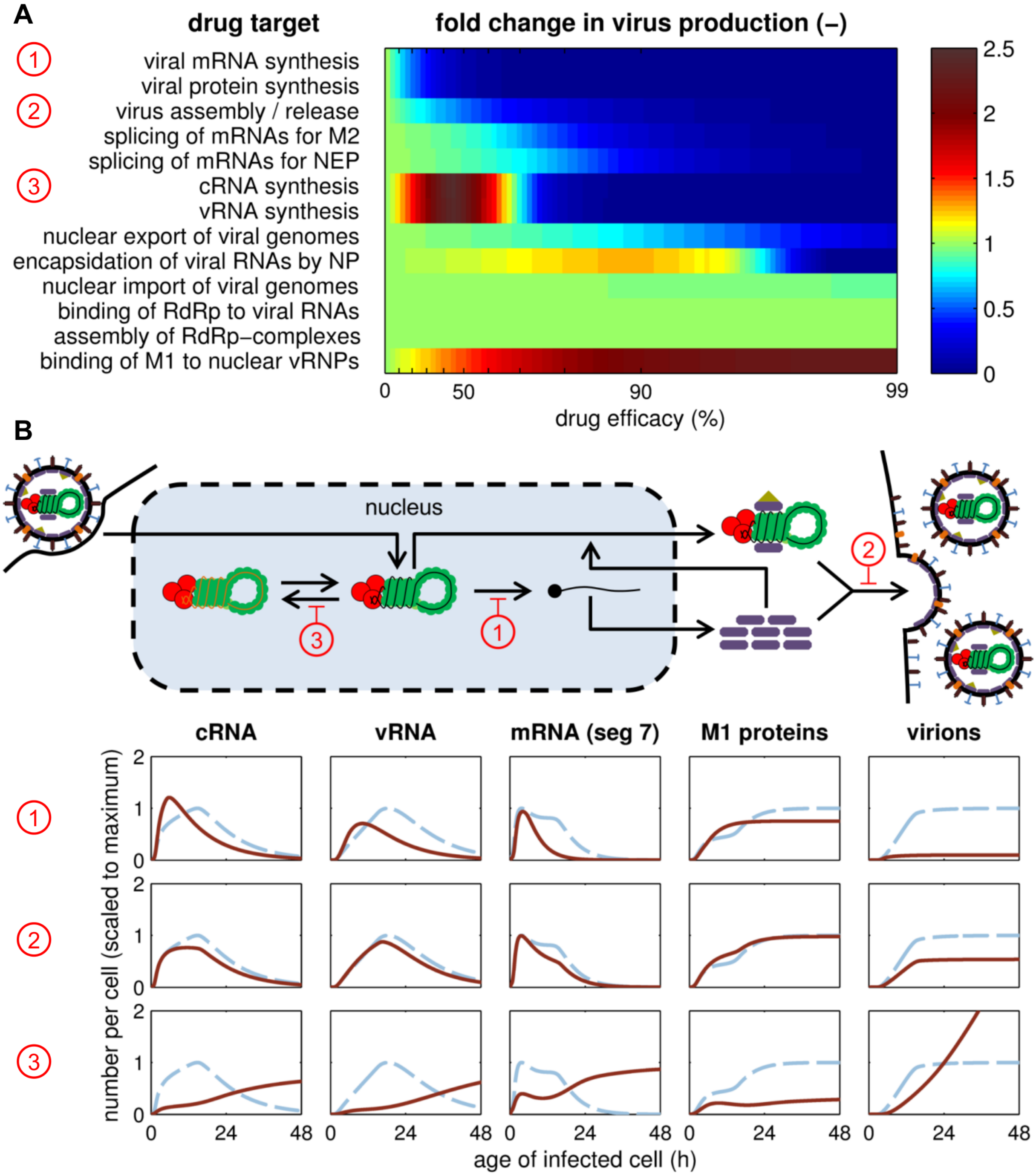

Figure 4.28.: Impact of DAAs on intracellular virus replication. (A) Simulated effect of drugs that target the indicated steps of intracellular virus replication with varying efficacy. Colors indicate the fold change in the total number of virus particles an average infected cell produces over its lifetime compared to the drug-free regime. Numbers in circles correspond to the examples shown in B. (B) Time courses of selected viral components during drug treatment with 50% efficacy. Columns correspond to components depicted in the scheme. Dashed and solid lines are time courses in the absence and presence of drugs, respectively. All components were normalized to their maximum in the drug-free regime. Figure taken from Heldt *et al.* [266].

sis, we observe a reduction in cRNA levels up to 27 hpi, which is accompanied by a lower abundance of vRNAs and mRNAs (Figure 4.28B, lower panel). Surprisingly, however, the RNA levels under treatment catch up with the concentrations in the drug-free regime at late time points. Again, this is caused by the lack of M1 proteins, which prevents an efficient shutdown of positive-strand RNA synthesis in the model. Since the release of virus particles further drains the pool of M1, inhibition of cRNA production at low drug efficacy results in a later but more sustained release of virions. In summary, viral polymerases are promising targets for DAAs as interfernce at the stage of RNA synthesis interrupts the autocatalytic mechanism of viral replication causing a large effect on virus production. By contrast, the viral burst size scales only linearly with drug efficacy when processes downstream of nuclear export (e.g. virus assembly and release) are impaired.

Effect of cell death In the previous paragraph, we observed that some drugs can change the replication dynamics such that they increase virus production at the expense of an early virus release (Figure 4.29A). Whether these drugs result in treatment success depends primarily on the lifespan of an infected cell; more precisely, on whether the cells reach the phase of higher productivity. In our *in vitro* experiments, infected cells survive

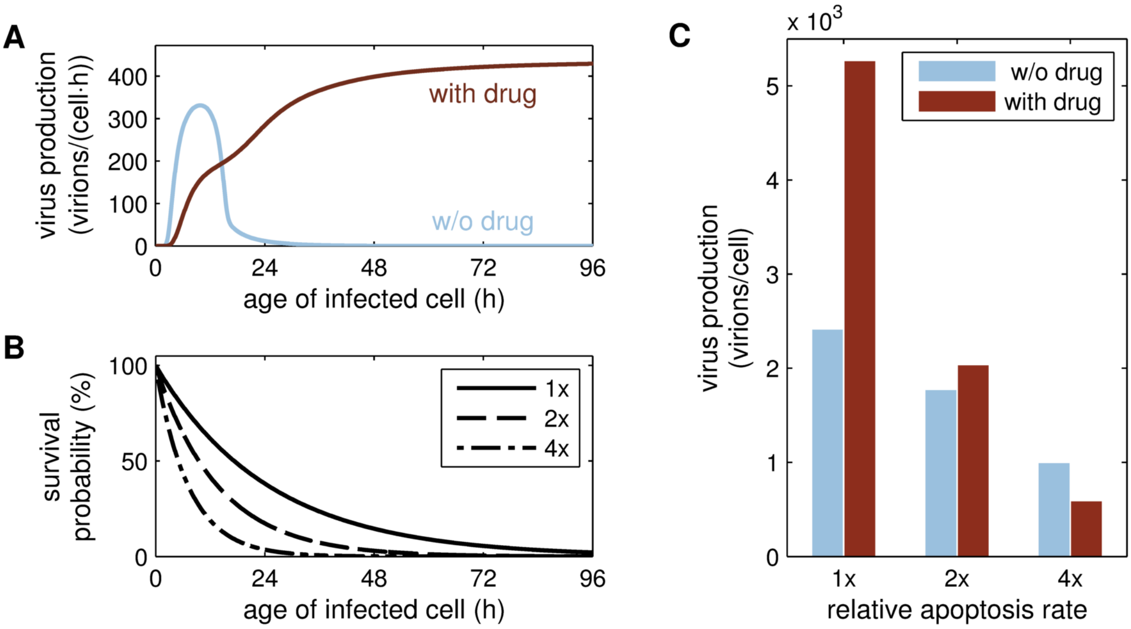

Figure 4.29.: The effect of cell death dynamics on virus production. (A) Virus production rate over the age of an infected cell in the absence of drugs and during inhibition of cRNA synthesis with 50% efficacy. (B) Different survival probabilities for an infected cell assuming that virus-induced apoptosis occurs with the rate estimated from data in Figure 4.24 (1x) or at twofold (2x) and fourfold (4x) this rate. (C) Total number of virus particles released by an infected cell considering the combination of different production rates and survival probabilities shown in A and B, respectively. Figure taken from Heldt *et al.* [266].

on average 25 h (Figure 4.29B). However, *in vivo* the immune response might decrease the productive lifespan of a cell, e.g., by the action of cytotoxic T lymphocytes. These shorter survival times may result in treatment success despite the drug having no significant effect on virus production *in vitro* or even causing an increase in titers (Figure 4.29C). Hence, the treatment potential of a drug should be judged with respect to cell death dynamics.

Delay in infection dynamics Besides impairing virus particle production, drugs can also delay virus spreading thereby providing the immune system with time to counteract the infection. Figure 4.30A illustrates the time course of the infectious virus titers in our model during antiviral treatment at high efficacy. Again, inhibitors of viral RNA and protein synthesis are most effective in reducing virus titers. They even protect a large percentage of cells from infection (Figure 4.30B, number 3). By contrast, inhibition of viral fusion with endosomes delays virus infection by approximately two days but neither decreases the peak titer significantly nor protects the cells (Figure 4.30B, number 2). A similar response can be observed when the other steps of virus entry are targeted (e.g. when attachment to the cell surface or endocytosis are inhibited; see Figure B.2 in the appendix). Note that in the presence of these drugs, virus titers are mainly constrained by the number of available host cells. When these cells are depleted, virus production stops and the titer decreases according to the rate of virus degradation. Hence, targets upstream of viral RNA synthesis merely delay infection in the absence of an immune response unless the drug is highly effective.

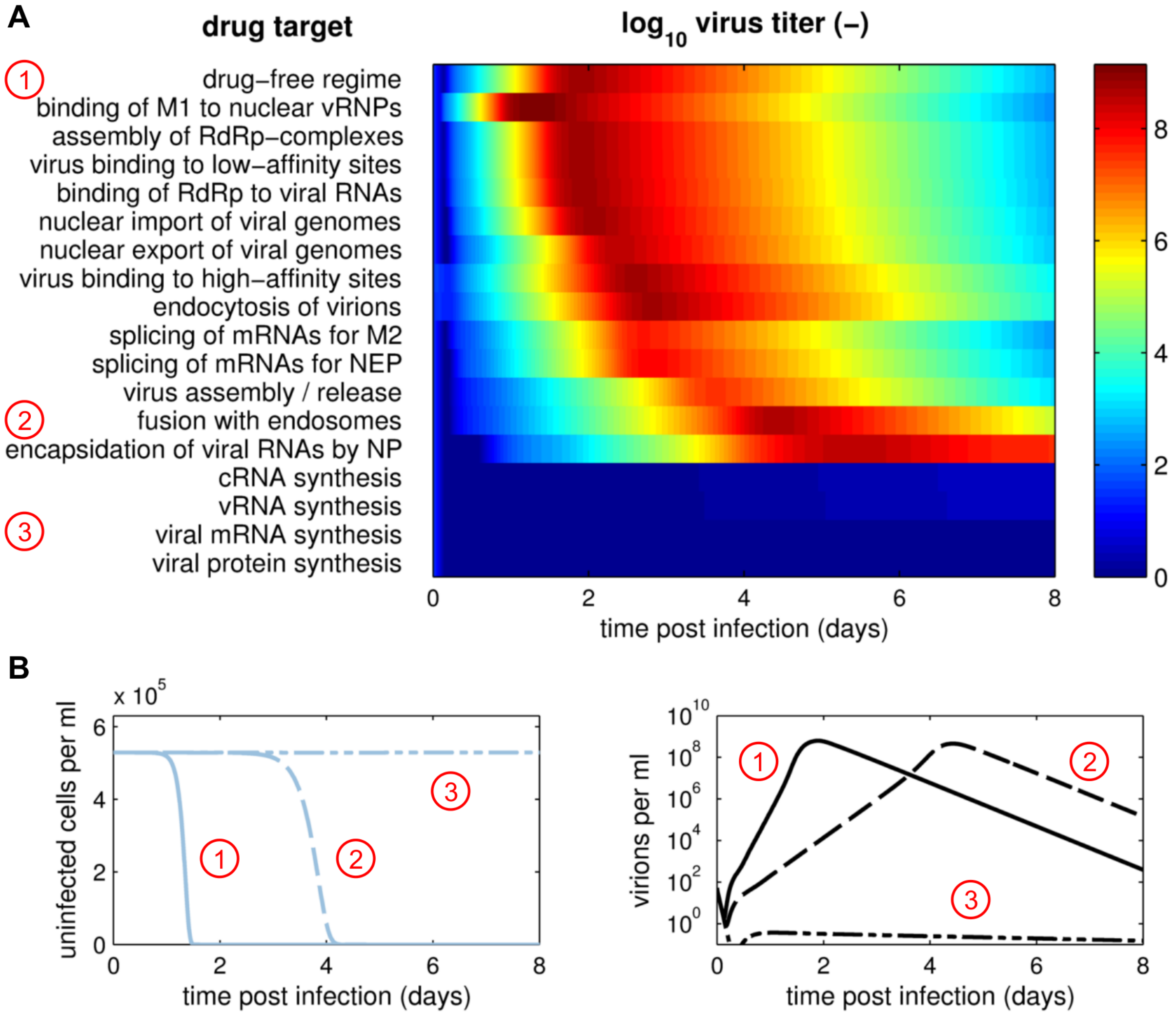

Figure 4.30.: Impact of DAAs on viral infection dynamics. Model predictions for an infection at an MOI of 10^{-4} are shown. (A) Simulated effect of drugs that target the indicated steps of virus infection with an efficacy of 95%. Colors indicate the $\log_{10}$ infectious virus titer over time. Numbers in circles correspond to the examples shown in B. (B) Concentration of uninfected target cells and infectious virus titer in the absence of drugs (solid line) and during treatment with inhibitors of virus fusion (dashed) and mRNA synthesis (dash-dotted) at 95% efficacy. Figure modified from Heldt *et al.* [266].

4.2.3. Discussion of the multiscale model

Viral infections inherently cover several spatial and temporal scales, which is of particular importance for antiviral therapy since state-of-the-art drugs typically target intracellular virus replication in order to induce changes at the within-host scale. To elucidate the effects of such drugs, we developed a multiscale model of influenza A virus infection that integrates a description of the intracellular viral life cycle into a model of cell-to-cell transmission and target cell dynamics. This approach accurately captures a wide variety of *in vitro* experiments on both scales, including the quantity of all three viral RNA species inside an infected cell as well as the infection dynamics and virus titers in a cell population. An analysis of the model suggests that drug interference with viral RNA synthesis, the nuclear export of viral genomes, and the assembly/release of virus particles is most effective in suppressing virus production. By contrast, blocking the steps of virus entry primarily delays *in vitro* infection but does not reduce peak virus titers significantly unless the inhibition occurs with very high efficacy. The model also demonstrates that cell death dynamics can strongly affect treatment success thereby providing valuable insights into the multiscale nature of viral infection.

An integrated modeling approach The limited availability and diversity of experimental data still represents a serious challenge to the construction and calibration of within-host models for viral kinetics [15]. Most *in vivo* descriptions, for instance, exclusively rely on virus titer data since such measurements are easily attainable from infected individuals and animals (reviewed in [14]). However, only four independent parameters can be reliably extracted from such virus titer curves, severely limiting the level of detail one can incorporate into a mathematical model [204]. A promising approach to address this issue is to include data on the intracellular viral life cycle from *in vitro* experiments (Figure 4.23). Hence, we used our deterministic model of influenza A virus replication, which reproduces the dynamics of virus entry, the regulation of viral RNA synthesis, and the levels of the three viral RNA species (see Section 4.1.1), to obtain a detailed picture of intracellular events. This information was then linked to the within-host (cell population) scale. Based on RNA data, the model, for instance, predicts a delay between the infection of a cell and virus release of approximately 6 h, after which virus production increases for another 7 h as viral components accumulate. The length of the eclipse phase is in good agreement with estimates from other studies (7 h for MDCK cell infection in bioreactors [177], 0.2–6 h for cultivations in a hollow-fiber system [217], and 6 h for human infection [206]). However, previous within-host models have assumed that virus production proceeds at a constant rate in the productive phase. By contrast, our model suggests a bell-shaped production rate over the age of an infected cell. Since simulations are very sensitive to such assumptions [204, 205], multiscale modeling can lead to more realistic estimates of key infection parameters [203], which can greatly support the design of antiviral therapy.

Based on flow cytometric data our model also provides the average *in vitro* lifespan of an infected cell. With 25 h (including the eclipse phase) it is similar to previous theoretical estimates and direct experimental measurements (reviewed in [15]). Due to the depletion of viral components (caused by the shutdown of RNA(+) synthesis) virus release from an infected cell would cease around the same time. Nevertheless, most of the cells in our model die before becoming nonproductive, which reduces overall virus yields, because survival times vary significantly around the mean. More precisely, cell death in our model, like in the majority of other studies, follows an exponential distribution such that a significant proportion of cells dies at an early age (Figure 4.27). Note that a study by Holder and Beauchemin suggests that other distributions might be more appropriate to describe cell survival [204]. In principle, our model can easily accommodate such assumptions since the apoptosis rate can be an arbitrary function of the infection age. Yet, our simulations and data on apoptosis induction during single-cycle infections [267] do not justify more complex approaches at the moment. If more data become available the apoptosis rate could, however, be related to the abundance of intracellular viral factors like vRNAs or pro- and anti-apoptotic viral proteins.

The proposed multiscale model also allowed us to couple the time courses of intracellular viral components to the infection dynamics in a cell population. For instance, the model predicts that the NP expression level in cells increases during the first day of a low MOI infection before showing a characteristic decrease (Figure 4.26). Intriguingly, such a shift of the cell population to low NP levels during late infection was observed experimentally [176, 223]. While most previous models were unable to capture this shift [223, 224], with the exception of a population balance model by Müller *et al.* who assumed that apoptosis causes the reversal in propagation direction [225], our multiscale approach provides a mechanistic explanation for the phenomenon. At late times post infection, the shutdown of viral mRNA synthesis and the demand for NP proteins by encapsidation and virus release cause a decrease in intracellular NP levels. Therefore, older infected cells show lower NP fluorescence. Multiscale models are ideal to reveal such functional connections between intracellular replication and the infection dynamics in a cell population.

Predictive capabilities of the model When testing our model against data not used for model construction we found that it can correctly predict the time course of uninfected target cells and the virus titer for low MOI infection but overestimates virus production at high MOI (Figure 4.25). In our model, peak virus titers depend on the initial number of target cells, which was comparable in the experiments, and the viral burst size, i.e., the number of virions produced per infected cell. The burst size follows from the virus production rate and the life span of an infected cell. Hence, the experimentally observed decrease in virus production at high MOI may have two reasons. On the one hand, the virus inoculum may contain factors, such as DI viruses (see Section 4.3), which impair intracellular replication and reduce the rate of virus production; and on the other hand, substances in the inoculum, like interferon, may cause an increase in cell death [267]. Additional measurements are required to distinguish between these two possibilities.

Limitations of *in vitro* models Due to the limited availability of *in vivo* data, we primarily relied on cell culture experiments for the construction and calibration of our model. In contrast to infections in animals and humans, which are mostly monitored by means of viral titers, such *in vitro* systems provide access to a variety of information, like the number of available target cells, their infection status, and the intracellular levels of viral RNAs. These high quality data were a prerequisite for the development of a multiscale model. However, the focus on cell culture experiments necessitates some adjustments if the model should be applied to animal or human infections in the future. In particular, the growth and death of uninfected target cells is typically neglected by *in vivo* models as both processes are assumed to be slow compared to infection [14]. Furthermore, virus clearance in the lung may occur faster as it is caused by active processes such as phagocytosis and mucociliary transport as opposed to thermal or enzymatic degradation in cell culture. However, the most prominent feature of an authentic infection that our model currently lacks is an immune response. In the past, a number of different strategies were suggested to incorporate the innate and adaptive immune response into within-host models of influenza A virus infection. However, none of them agreed completely with the experimental data available [210]. Including an adequate representation of the immune system, thus, remains a key challenge of current modeling efforts. Multiscale approaches could support these efforts as they allow for the integration of antiviral mechanism at the intracellular level (like the interferon-induced antiviral response) and of extracellular factors (such as natural killer cells and neutralizing antibodies).

Effects of DAAs Accounting for the intracellular replication of influenza A viruses allowed us to investigate which steps of the viral life cycle are most susceptible to drug interference. At efficacies above 90%, which are usually found for antivirals in clinical use, inhibitors of viral transcription, RNA replication, protein synthesis, nuclear export, and virus assembly/release are very successful in blocking virus production in our simlations (Figure 4.28). In agreement with the latter prediction, neuraminidase inhibitors, which target the release of progeny virions, are widely used for influenza therapy today. Yet, the emergence of drug-resistance in circulating virus strains urges the need for new antivirals [121]. Judging from our model, inhibitors of the viral polymerase are the most promising alternative. During viral replication polymerases engage in an autocatalytic reaction where they synthesize cRNA from vRNA and vice versa. Disrupting this mechanism has detrimental consequences for all major viral components in our model. In agreement with this, compounds that specifically inhibit viral transcription efficiently impair influenza A virus growth in cell culture and in mice [294]. Moreover, favipiravir (T-705), an inhibitor of the viral RdRp [133], is potent against influenza viruses *in vitro* and *in vivo* [132, 295], and has entered clinical trials recently [131] demonstrating the potential of polymerases inhibitors as antiviral drugs. Multiscale models could support such clinical trials by predicting the effect of different dosing regimes and drug concentrations.

In addition to a direct inhibition of polymerase activity, experimental studies have also identified 25-amino-acid peptides [136] and small molecule inhibitors [296] that can impair the growth of influenza viruses by preventing viral polymerase assembly. By contrast, a blockage of RdRp formation has hardly any influence on virus production in our model unless drug efficacy well exceeds 99%. This discrepancy most likely originates from the kinetics of polymerase assembly in our model. Due to a lack of experimental data, we assumed that polymerases form rapidly from their three subunits according to mass action kinetics (see Section 3.1.1). Thus, the availability of the subunits limits polymerase formation rather than the formation rate of the complex. In light of the above mentioned experimental results, future studies may want to revise this assumption. Note that reconciling model predictions that are initially inconsistent with the data provides an ideal opportunity to refine our understanding of the underlying biological mechanisms. However, it also requires an experimental setup specifically designed to resolve the discrepancy.

Inhibition of virus entry Instead of reducing peak virus titers, inhibitors of virus entry merely delay infection in our simulations unless they are highly effective (Figure 4.30). This is in good agreement with theoretical studies showing that peak viral loads do not change with viral infectivity [216] and with *in vitro* experiments in which the infection of MDCK cells with influenza A virus was delayed by up to two days in the presence of amantadine, an inhibitor of viral uncoating [217]. In our model, the delay of infection results from the ability of entry inhibitors to protect uninfected target cells from the virus. However, since interference is not perfect, a few viruses will overcome the block. Once this occurs, the infected cells will produce the same amount of virus particles than they would have in the absence of the drug because entry inhibitors do not impair the production of viral components. Thus, the treatment success that has been observed *in vivo* with these drugs most likely depends on mechanisms that take advantage of the delay to clear infection (e.g. the immune response).

Another aspect that may contribute to the success of antivirals which act on the early steps of intracellular virus replication are stochastic effects. As we have demonstrated in Section 4.1.2, low MOI situations, which occur primarily when the virus establishes itself in a host, feature a high percentage of nonproductive cells. The first infection wave may, hence, depend on only a few cells that release progeny virions. At this early stage, the inhibition potential (i.e. the drug's efficiency) needed to stop virus spreading may be comparatively low making entry inhibitors an effective prophylactic drug. Further insights into how molecular noise affects the susceptibility of virus entry to antivirals could be provided by a stochastic multiscale model of infection.

Lifespan of infected cells affects treatment Surprisingly, our simulations show that a weak inhibition of viral RNA replication can lead to an increase in virus production at the expense of early virus release. While this result should be taken with caution until experimentally validated, it demonstrates that some interventions may change the release phenotype of a cell from an early production toward a later but more sustained one. From an evolutionary perspective such a change may be detrimental for the virus since faster growing strains would outcompete slower variants. However, during treatment it may nevertheless occur. In these cases, the drug's ability to prevent virus production (and spreading) heavily depends on the lifespan of infected cells (Figure 4.29). In particular, an antiviral compound which was rejected based on *in vitro* cell survival times may result in lower virus titers when lifespans are shorter. *In vivo*, the latter is indeed very likely as the immune response increases cell death rates [214, 297]. Also, virus strain-dependent factors such as the expression of the PB1-F2 protein can lead to faster cell death [298]. Screening approaches for novel antiviral drugs may, hence, benefit from using conditions that mimic *in vivo* cell survival times.

Summary Our multiscale model combines the intracellular events of viral replication with infection dynamics at the cell population level. In doing so, it allows us to estimate crucial infection parameters from a broader set of experimental data, and to simulate the effects of DAAs on virus production. In the future, such approaches may help to elucidate how viruses overcome antiviral drug treatment, and why acquiring drug resistance can change critical features of intracellular replication like the length of the eclipse phase and the viral burst size [226]. Our description could also be integrated into a model for between-host viral kinetics in order to understand how drugs affect the epidemic scale and how molecular characteristics determine viral fitness and persistence across different levels. Including an immune response in the multiscale model represent an important step toward these goals.

4.3. Replication of defective interfering viruses

Defective interfering particles (DIPs) are incomplete viruses that require coinfection with an STV to propagate. However, they also interfere with STV replication at the intracellular level such that coinfected cells mainly produce progeny DIPs. To elucidate the mechanism of interference, we developed a model of intracellular DI RNA replication, which is described in the first part of this section. Subsequently, we introduce a second model for the continuous production of influenza A virus in cell culture where DIPs can cause oscillations in virus titers that decrease the process' productivity.

4.3.1. Interference with intracellular virus replication

In order to simulate how DIPs interfere with the intracellular life cycle of influenza A virus, we extended our deterministic model of virus replication to include a DI RNA. Due to their reduced length, these RNAs were suggested to have an advantage in replication over full-length segments [143]. In addition, the preferential amplification of DI RNAs in coinfected cells suggests that this advantage occurs during viral genome production at the step of cRNA synthesis [113, 150, 151]. Note that whether the advantage occurs in cRNA or vRNA synthesis (or is a mixture of both) does not influence model outputs [269]. For the sake of simplicity, we chose a linear dependency of the synthesis rate on DI vRNA length, i.e., defective segments that are half as long as their wild-type (wt) RNA produce cRNA twice as fast (Figure 4.31A). Most of the experimentally observed DI RNAs originate from one of the three polymerase segments [147, 149]. The model, thus, considers a

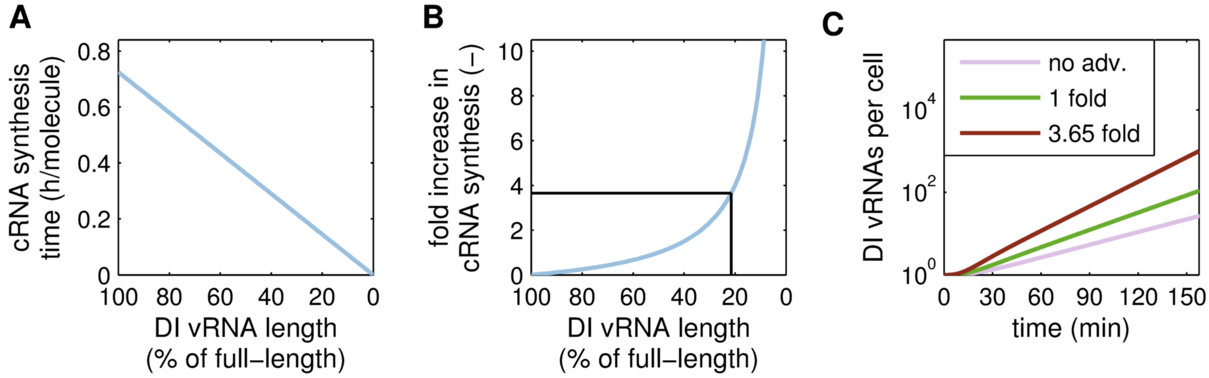

Figure 4.31.: Assumed effect of DI RNA length on synthesis kinetics. (A) Simulation of the time that is required to synthesize one cRNA molecule from a segment 3 DI vRNA with the indicated length. (B) Estimated replication advantage, i.e., increase in cRNA synthesis rate (see Equation (3.3.7)) of DI vRNAs with the indicated length over the full-length segment 3 (encoding PA). Black lines indicate the advantage of a DI vRNA that comprises 480 nt. (C) Time course of DI vRNAs with the indicated replication advantage over the wt segment assuming a constant supply with viral polymerases and NP proteins.

DI vRNA of segment 3, which comprises 480 nt (the average length of sequenced DI RNAs of segment 3 [108]). This length corresponds to a synthesis advantage of approximately 3.65-fold over the wt vRNA in our simulations (Figure 4.31B). Note that due to the autocatalytic mechanism of viral replication, RNA levels in the model scale exponentially with synthesis rates such that small increases in these rates result in substantial differences in vRNA abundance (Figure 4.31C).

Competition for viral resources To understand DI vRNA synthesis, we compared the intracellular replication of an STV to coinfections by an STV and a DIP. In these simulations, coinfected cells show a significant reduction in overall vRNA levels including the segments for which there is no DI RNA present (Figure 4.32A). In particular, coinfection with our model DI RNA reduces the vRNA level of segment 5 by two orders of magnitude with coinfected cells starting to differ significantly from their STV-infected counterparts from 3 hpi onward. In the model, interference with wt segment synthesis was primarily caused by an excessive amplification of DI RNAs, which reached levels approximately

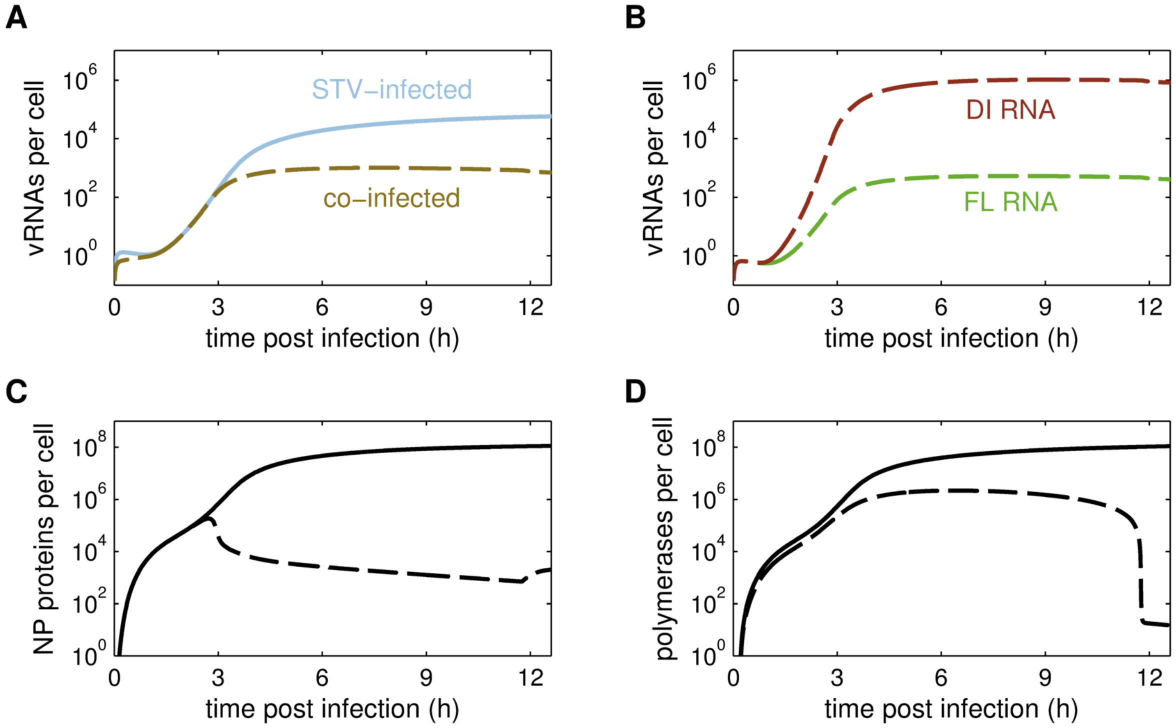

Figure 4.32.: Interference of DI RNA synthesis with viral replication. Simulated infection of a cell by two STVs (solid) and coinfection by one STV and one DIP with a defective segment 3 (dashed). The DI RNA comprises 480 nt and has a 3.65-fold advantage over its full-length counterpart. (A) Intracellular level of vRNAs of segment 5 (encoding NP). (B) Level of the full-length vRNA (FL RNA) and DI vRNA of segment 3 in coinfected cells. (C,D) Level of unbound NP proteins (C) and viral polymerases (D) during STV infection and coinfection.

three orders of magnitude higher than the corresponding full-length RNA (Figure 4.32B). Again, a modest advantage in RNA synthesis results in large differences in viral genome levels. Like wt segments, the newly produced DI RNAs require viral polymerases and NP proteins for encapsidation. Hence, excessive RNA synthesis can deplete the pool of both proteins (Figure 4.32C and D). Surprisingly, however, NP is the first protein that becomes exhausted although one might think that a defect in segment 3, which encodes for the PA subunit, mainly affects viral polymerases. Yet, the coinfecting STV provides a copy of the PA gene, which is sufficient to meet the demand for polymerases during early infection since each RNA requires only one RdRp. By contrast, a DI RNA of 480 nt binds 24 NP proteins (considering an estimated stoichiometry of one NP molecule per 24 nt [59]). Hence, encapsidation quickly drains the pool of NP starting around 3 hpi from which moment on coinfected cells contain significantly less of this protein. In our simulations, the depletion of viral proteins causes an accumulation of encapsidation intermediates in coinfected cells (compare Figure 4.33A and B). In STV–infected cells, most vRNAs are fully encapsidated, especially during late infection. By contrast, coinfected cells show an increase in the relative level of RdRp-vRNA (and RdRp-cRNA) complexes. Since these partially protected RNAs are subject to rapid degradation and only complete RNPs engage in replication, the insufficient supply of NP and RdRp impairs the accumulation of cRNA and vRNA. This also affects viral transcription and reduces viral protein levels even further. Hence, in our simple model, a modest replication advantage causes the depletion of NP proteins and RdRps due to an excess of DI RNAs. Thereby, defective

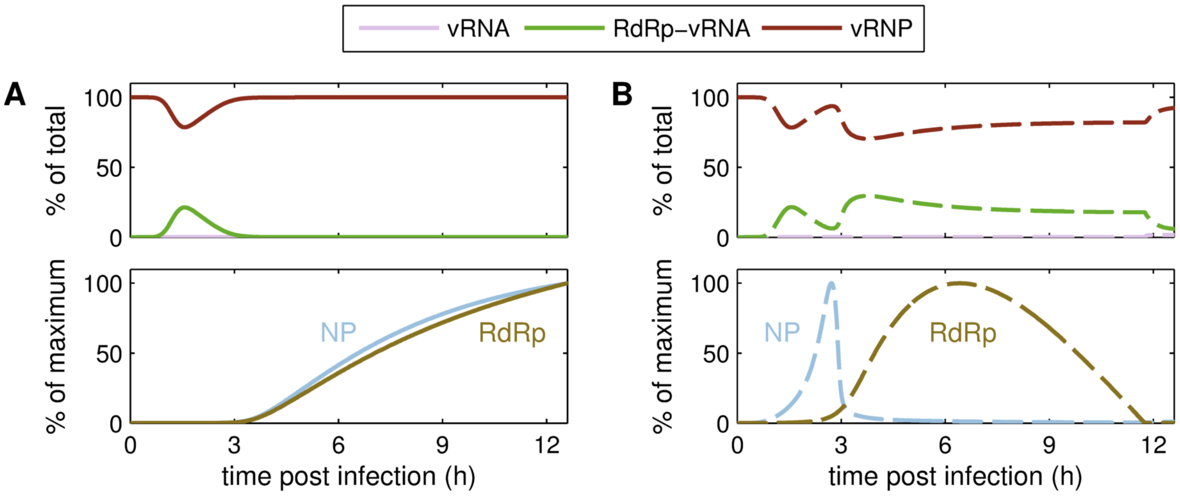

Figure 4.33.: Accumulation of replication intermediates during coinfection. STV infection (A) and coinfection (B) were simulated as described in Figure 4.32. Upper panels show the levels of naked vRNAs, RdRp-vRNA complexes, and vRNPs of segment 5 as the fraction of total vRNA of segment 5. Lower panels depict the abundance of unbound NP proteins and viral polymerases (RdRp) normalized to their maximum.

RNAs interfere unspecifically with the synthesis of all full-length genome segments.

In experiments, coinfected cells mainly produced progeny DIPs [113, 114, 155]. We investigated whether our model can reproduce this observation based on the predicted excess in DI RNA synthesis. As described before, an STV-infected cell releases up to 10^4 virus particles (Figure 4.34). A simulation of DIP infection in the absence of STVs yields no progeny virions since no complete viral polymerases are formed. Interestingly, upon coinfection, the model predicts almost exclusive DIP production in good agreement with experimental results [113, 114, 155]. This is due to the exponential scaling of RNA levels with synthesis rates (i.e. with the replication advantage). When the DI RNA has no advantage in replication, infected cells release the same amount of DIPs and STVs demonstrating that the replication advantage and not the RNA length (i.e. the binding of fewer NP molecules) is the key factor for interference in our simulations. However, although these effects can be separated in a mathematical model they are most likely tightly linked in reality.

The effect of initial virus concentration and replication advantage A central influence factor in DIP infection is the number of infecting viruses. For instance, DIPs require a high MOI for replication where coinfection is likely (Figure 4.35). Therefore, we used our model to predict how differences in the initial STV and DIP concentration affect virus production (Figure 4.36). Note that for each condition, we simulated an average cell that is infected by the indicated amount of virus particles. In infection experiments, stochastic effects and limitations in virus diffusion can lead to a mixture of cells including subpopulations that are infected by STVs or DIPs alone. Most measurement techniques

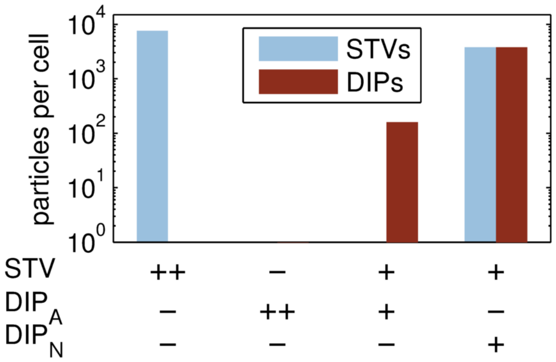

Figure 4.34.: Reduced virus production in coinfected cells. Cumulative number of progeny virus particles at 12 hpi considering a cell that was either infected by two STVs, two DIPs, or one STV and one DIP. The DI RNA originates from segment 3, comprises 480 nt, and has either a 3.65-fold replication advantage over its full-length RNA (DIP$_A$) or no advantage (DIP$_N$).

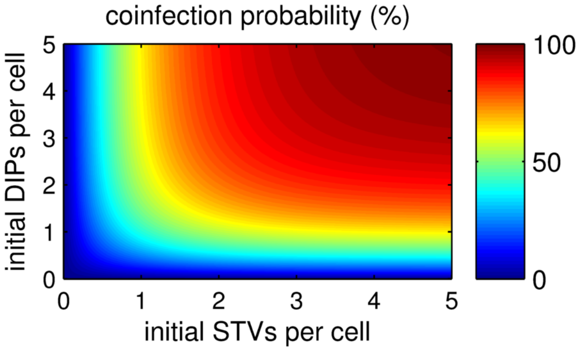

Figure 4.35.: Coinfection probability. Probability that a cell is coinfected by an STV and a DIP according to the Poisson distribution (Equation (3.3.17)) given different initial amounts of both virus types.

can only provide an average of this heterogeneous cell population. As observed before, the presence of a single DIP is enough to prevent the release of STVs from coinfected cells in our model (Figure 4.36A). In addition, increasing the STV concentration in the absence DIPs increases cell-specific virus yields slightly. This is caused by a higher initial level of wt segments and, thus, a faster synthesis of full-length RNAs and viral proteins (data not shown). For the same reason, an increase in the initial amount of STVs increases the number of progeny DIPs produced by a coinfected cell (Figure 4.36B). By contrast, higher initial amounts of DIPs impair virus production since they interfere with RNA replication and compete for viral proteins.

So far, we have only considered a well-defined DIP with a specific length and replication advantage. However, virus preparations can contain a variety of DI RNAs comprising different lengths [148]. Hence, the influence of the length-dependent replication advantage in our model was analyzed next. As described before, with no difference in length and,

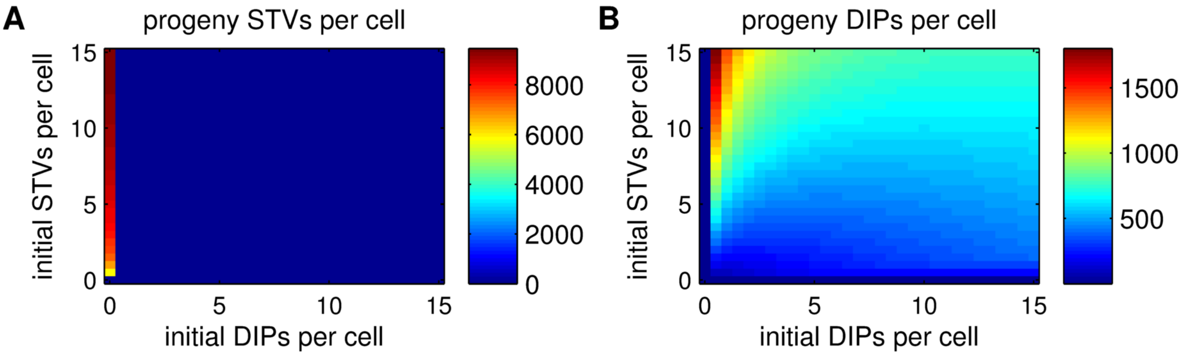

Figure 4.36.: Influence of initial virus concentration on virus production. Cumulative number of progeny STVs (A) and DIPs (B) at 12 hpi considering infections at different initial amounts of both virus types. The DI RNA originates from segment 3, comprises 480 nt, and has a 3.65-fold replication advantage.

thus, no replication advantage at the level of RNA synthesis, cells produce the same amount of STVs and DIPs (compare Figure 4.37A and B). For an increasing replication advantage there are two distinct regimes. First, STV production decreases and DIP levels show a corresponding increase such that the overall virus yield remains roughly constant. Then, when the replication advantage exceeds 0.8, i.e., the synthesis rate of the DI RNA is 1.8 times that of the full-length segment (corresponding to a length of 1240 nt in the model), DIP yields decrease as well. In the first regime, NP proteins and RdRps are available in sufficient quantities (Figure 4.37C). Hence, the replication advantage of DI RNAs leads directly to an increase in their vRNP level and there is no interference with wt segment synthesis (Figure 4.37D). The small increase in segment 3 vRNPs in this regime is caused by the reduced production of STVs. By contrast, vRNPs of segment 5 remain constant because they are required for both, the formation of STVs and DIPs. Despite these initial differences segment 3 and 5 show similar levels for the rest of tested parameter range. In the second regime, excess DI RNA synthesis depletes the pool of

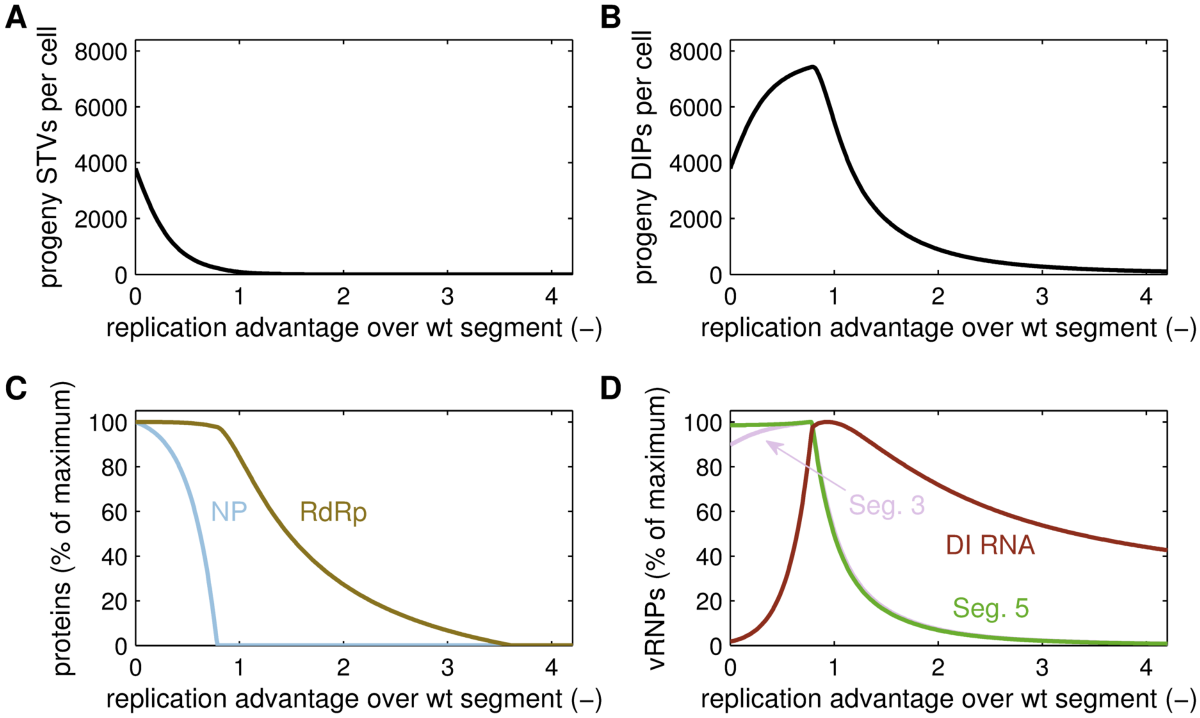

Figure 4.37.: Effect of the replication advantage on virus production. Simulated infection of a cell with one STV and one DIP. The DI RNA originates from segment 3, has the indicated replication advantage, and comprises the corresponding length. All components are shown at 12 hpi. (A,B) Cumulative number of progeny STVs (A) and DIPs (B) that are released from the cell. (C) Levels of the unbound viral RdRp and NP protein normalized to their maximum. (D) Levels of vRNPs formed from segment 3, 5, and the DI RNA normalized to their maximum.

NP proteins (and later also of RdRps) and impairs the production of full-length and DI vRNPs. Hence, modeling suggests that there is an optimal replication advantage at which DI RNAs can outcompete the wt segments without interfering with viral protein synthesis such that DIP production is maximized.

Coinfection timing The above simulations assume that STVs and DIPs enter the cell at the same time. However, in a realistic infection scenario both events can occur successively, which might change the outcome of coinfection. Indeed, our model shows a dependency of virus production on coinfection timing (Figure 4.38A). When STV infection occurs first, wt segments can replicate without interference and viral proteins accumulate. A DIP which infects the cell later can benefit from these proteins and produce more virus progeny. However, when the DIP enters the cell after nuclear export has been initiated and positive-strand RNA synthesis was shut down, the DI RNA can no longer replicate and the cell will release mostly STVs. In a situation where the DIP infects first, progeny DIP yields decrease with an increasing delay in STV infection (Figure 4.38B). Here, primary transcription causes an accumulation of M1 proteins, albeit to low levels. The higher these levels are at the time of STV infection, the faster M1 accumulates to a concentration where it inhibits RNA replication, which reduces wt segment production and DIP release.

DI RNAs from different segments Considering that most experimentally observed DI RNAs originate from the polymerase segments, we were wondering whether defects in other segments might hinder successful replication or DIP production such that these DI RNAs die out. Hence, we simulated the amount of virus progeny produced by DIPs of

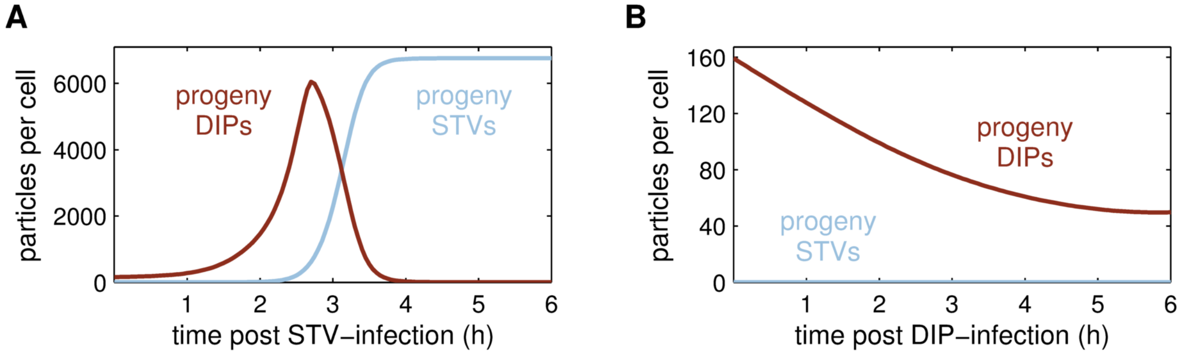

Figure 4.38.: Influence of coinfection timing. Cumulative number of progeny virus particles that are released by a coinfected cell until 12 h post STV infection. The DI RNA originates from segment 3, comprises 480 nt and has a 3.65-fold replication advantage. (A) STV infection occurs at 0 h and DIP infection with the indicated delay. (B) DIP infection occurs at 0 h and STV infection with the indicated delay.

segment 3 and 4 (encoding PA and HA, respectively) with respect to coinfection timing and replication advantage (Figure 4.39A and B), which were the main influence factors in previous simulations. As observed before, there is an optimal replication advantage for both DI RNAs, which, if exceeded, leads to lower virus yields. Intriguingly, however, defects in segment 3 and 4 differ significantly in their response to delayed STV infection. With a defect in a polymerase segment, DIP production remains fairly constant even at large delays. By contrast, the segment 4 DI RNA produces no virus progeny for delays larger than 2 h. Again, this results from a differential accumulation of M1 proteins and the inactivation of vRNPs during nuclear export (Figure 4.39C and D). In cells infected with a segment 3 DI RNA there is only primary transcription since no complete viral polymerases are formed, whereas a defect in segment 4 allows the production of all viral proteins except HA. Hence, viral RNAs are synthesized in the latter case and nuclear export occurs just like it does in STV-infected cells. Therefore, full-length RNAs which are introduced by an infecting STV after 2 h do not replicate and are unable to complement for the defective segment. Taken together these results suggest that in a scenario where coinfection times vary, segment 3 DI RNAs may produce more virus progeny than their segment 4 counterparts and might, thus, outgrow them.

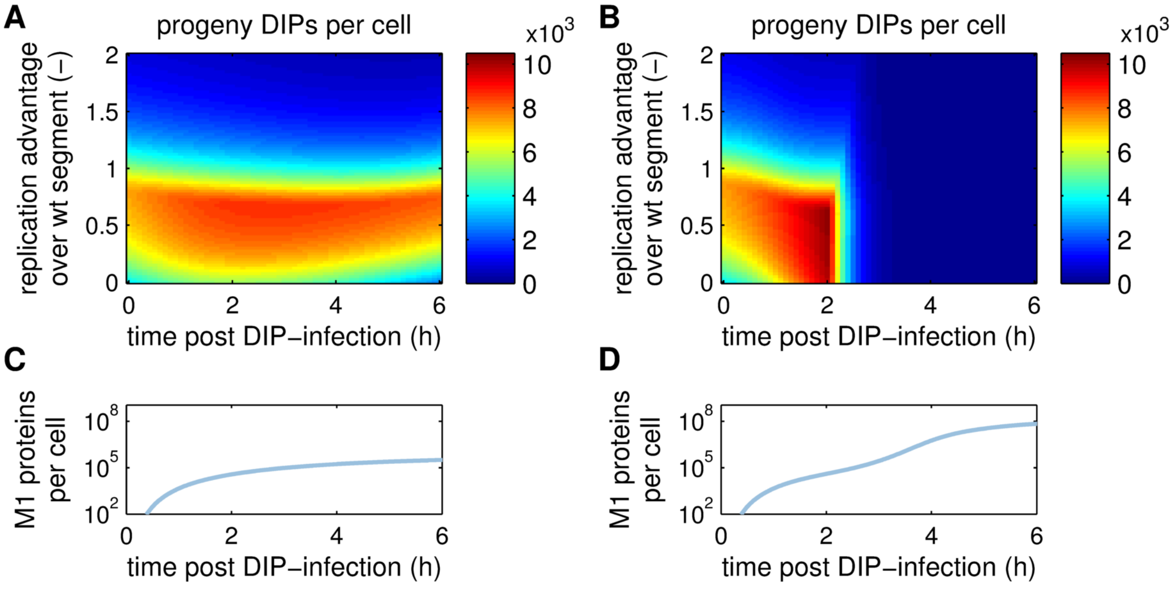

Figure 4.39.: Virus production for DI RNAs from different segments. Simulated infection of a cell by one STV and one DIP. The DI RNA either originates from segment 3 (A,C) or from segment 4 (B,D). (A,B) Cumulative number of progeny DIPs at 12 h post STV infection considering that the DI RNAs have the indicated replication advantage over their wt segments (and comprise the corresponding length) and that STV infection occurs with the indicated delay. (C,D) Number of unbound M1 proteins in a DIP-infected cell in the absence of STVs. The DI RNAs exert a 0.5-fold replication advantage (and comprises the corresponding length).

4.3.2. Oscillations in continuous influenza A virus production

Due to their interference potential, DIPs can compromise influenza virus infection whenever high MOI situation arise. Here, we present a mathematical model for the production of influenza A virus in a continuous cultivation system. The model demonstrates that DIPs readily accumulate in such a process and that they can cause oscillations in virus titers. Note that we use parts of the original publication of the model in PLoS ONE in the following [148].

Continuous infection system In contrast to batch cultivations, continuous systems have a number of advantages. They reduce down times for equipment cleaning, can achieve higher space-time yields, and provide products at constant quality to name only a few. Therefore, Frensing *et al.* established a continuous system for influenza A virus production [148]. This system comprises two stirred tank reactors with a working volume of 1 L each (Figure 4.40). The process was started by cultivating avian AGE1.CR suspension cells in both reactors in batch mode prior to infection. At the time of infection, the virus reactor was inoculated with influenza A/PR/8/34 (H1N1) at an MOI of 0.025. Both reactors were then switched into continuous cultivation mode and connected. Subsequently, cells were constantly transfered from the cell to the virus reactor where virus propagation took place. Excess medium from the virus reactor, which contained the

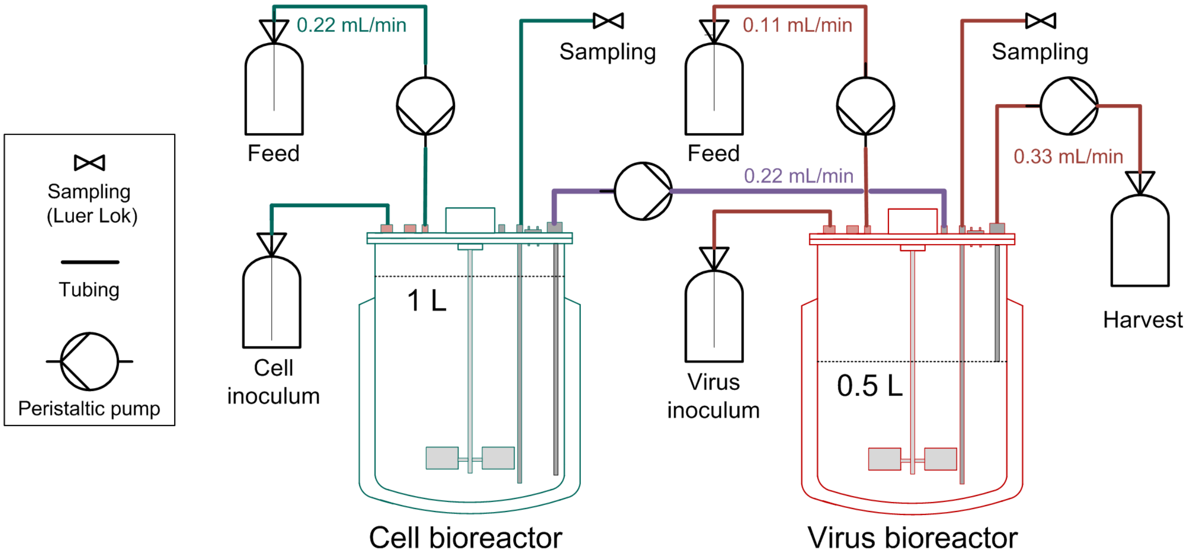

Figure 4.40.: Reactor setup for continuous influenza A virus infection. The setup comprises two stirred tank reactors in which AGE1.CR suspension cells were cultivated in continuous mode. Both reactors were connected via the purple tubing such that cells were constantly fed into the virus reactor where infection took place. Green components belong to the cell reactor and red components to the virus reactor. Figure taken from Frensing and Heldt *et al.* [148].

produced virus and the cells, was harvested at a constant rate.

Frensing *et al.* monitored the cell concentration as well as the virus titers in both reactors during two independent cultivations (Figure 4.41). Surprisingly, virus titers in both cultivations showed periodic fluctuations. At the same time, cell numbers stayed constant in the cell reactor and changed apparently at random in the virus reactor. The oscillations in virus titers spanned six orders of magnitude in $TCID_{50}$ measurements and one order of magnitude in HA data. Note that while the $TCID_{50}$ method detects infectious virus only, the HA assay accounts for all hemagglutinating virus particles including DIPs and other noninfectious viruses.

Virus titers in the absence of DIPs Since the declines in virus titers were preceded by a high MOI situation, Frensing *et al.* hypothesized that DIPs might be involved in the observed oscillations [148]. This was supported by the detection of subgenomic RNAs via segment-specific PCR. In particular, Frensing *et al.* found 500 to 700 nt long RNAs of segment 1 to 3 in the virus stock and showed that both the subgenomic and the full-length RNAs oscillated during continuous infection. Yet, it was not clear whether DIPs were the cause of these oscillations or the continuous cultivation mode had introduced periodic fluctuations which were affecting virus titers. We, therefore, developed a simple mathematical model for the infection kinetics in the virus reactor, which initially neglected the influence of DIPs (Figure 4.42A). This model considers a population of uninfected cells, which increases through intake from the cell reactor and through cell growth in the virus reactor itself. Extracellular virions can infect these cells causing them to produce infectious virus progeny. Infected cells can die due to virus-induced apoptosis and infectious particles degrade over time. Furthermore, cells and virus particles are constantly removed from the reactor. An analysis of this model by our coworkers, indeed, revealed parameter

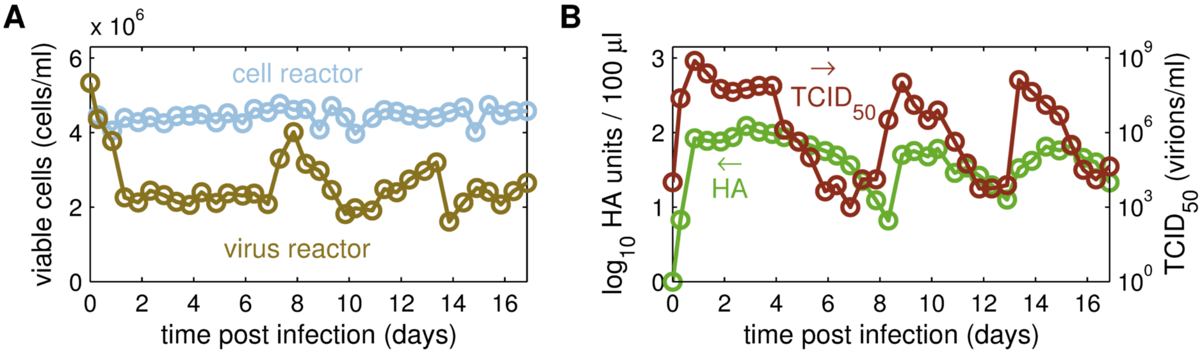

Figure 4.41.: Measurements of continuous influenza virus infection. (A) Viable cell concentrations in both reactors for the second of two independent cultivations in reference [148]. (B) Virus titer determined by HA and $TCID_{50}$ assay for the same cultivation. Figure modified from Frensing and Heldt *et al.* [148].

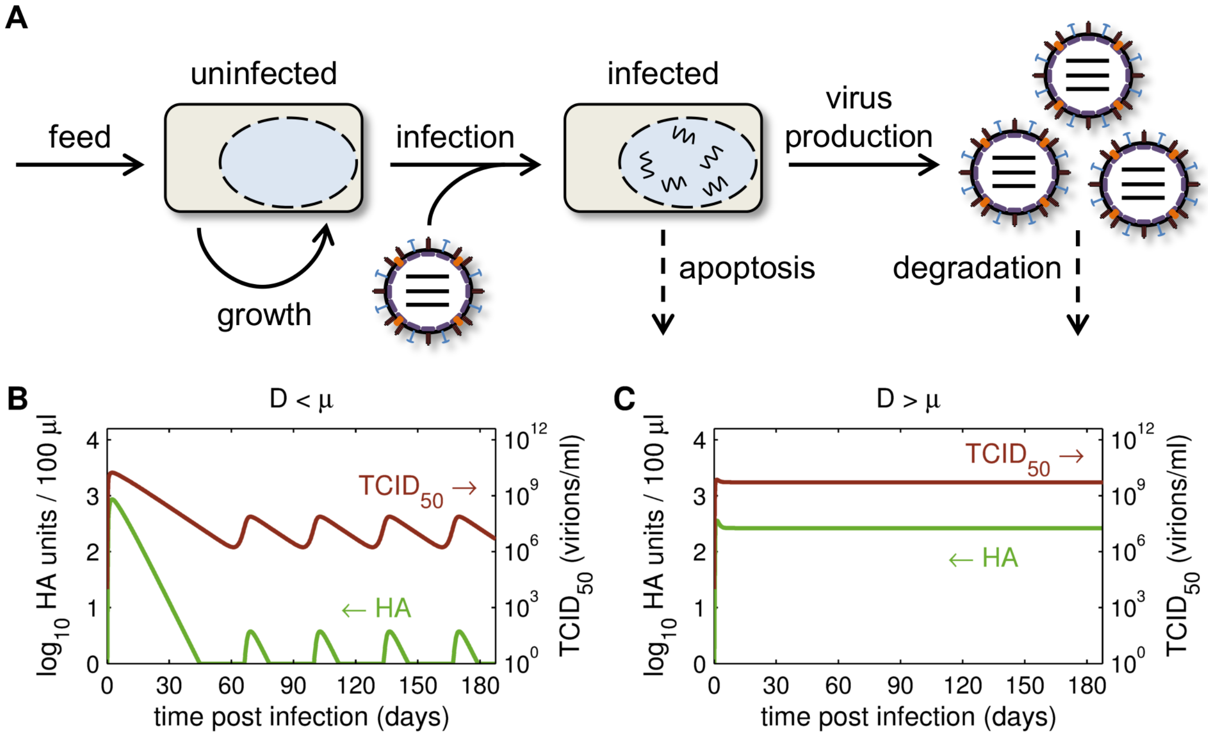

Figure 4.42.: Simulation of continuous infection in the absence of DIPs. (A) Schematic representation of the model for continuous influenza A virus infection in the absence of DIPs. The continuous harvest of cells and viruses was omitted for illustrative reasons. (B,C) Simulated virus titers for a dilution rate of the virus reactor, D, which is lower than the specific growth rate, μ (B), or higher than μ (C). Parameters were chosen according to Table 4.5 except that the dilution rate in B was reduced to $D = 10^{-8}$ 1/h. Figure adapted from Frensing and Heldt *et al.* [148].

regions where a Hopf bifurcation gives rise to periodic solutions that are independent of DIPs [148]. Specifically, oscillations can occur if and only if the dilution rate of the virus reactor (D) is lower than the specific growth rate of the cells (μ), which is confirmed by our numerical simulations (Figure 4.42B). However, these fluctuations do not occur on the same time scale as those observed in experiments. More importantly, in the experimental setup, the dilution rate was higher than the growth rate (Table 4.5). Hence, virus titers should remain constant if DIPs do not influence the system (Figure 4.42C).

Virus titers in the presence of DIPs Next, we extended the model by including the DI virus population (Figure 4.43A). In these simulations, DIP-infected cells do not produce virus progeny in the absence of STVs. However, once coinfection occurs, virus replication proceeds and DIPs are released. Furthermore, the model accounts for the *de novo* generation of DIPs by STV-infected cells, which, in addition to producing large quantities of STVs, release a small amount of DIPs. For the sake of simplicity, we did not consider the influence of coinfection timing and the identity of the defective segment here. Instead

Table 4.5.: Parameters and non-zero initial conditions for the simulation of continuous influenza virus infection.

Parameter		Description	Value
μ	(h^{-1})	specific growth rate	0.027
D	(h^{-1})	dilution rate of virus reactor	0.0396
f	(–)	*de novo* DIP production	10^{-3}
F_{Inf}	(cells/virion)	infection efficiency	1
k^{Apo}	(h^{-1})	apoptosis rate of infected cells	7.13×10^{-3}
$k_{\mathrm{V}}^{\mathrm{Deg}}$	(h^{-1})	virus degradation rate	0.035
k^{Inf}	(ml/(virion · h))	virus infection rate	2.12×10^{-9}
k^{Prod}	(virions/(cell · h))	virus production rate	168
T_0	(cells/ml)	initial target cell concentration	5.33×10^{6}
T_{in}	(cells/ml)	cell concentration in feed	2.96×10^{6}
V_{s0}	(virions/ml)	initial STV concentration	1×10^{4}

the model focuses on the key features of DIP infection, i.e., that they only replicate in coinfected cells and suppress STV production. Intriguingly, this simple implementation readily shows oscillations in virus titers (even for $D > \mu$) in agreement with the experimental observations (Figure 4.43B). In particular, the model captures the frequency of titer fluctuations, the extended first peak, and the phase shift between infectious and total virus titers. Yet, it does not correctly reproduce the amplitude of TCID_{50} and HA measurements. Nevertheless, the simulations confirm that DIPs can cause oscillations during continuous virus production.

Since the observed fluctuations in virus titers reduce virus yields and, thus, represent a challenge to vaccine production, we investigated two strategies to avoid DIP accumulation: (i) the use of seed viruses which contain a low amount of DIPs (Figure 4.43C) and (ii) a reduction of *de novo* DIP generation through the optimization of virus strains or cell lines (Figure 4.43D). In both scenarios, virus titer oscillations continued to emerge even with a very pure seed virus or low *de novo* DIP generation. In fact, constant virus titers were only found when DIPs were completely absent from the system (i.e. in the absence of both, DIPs in the inoculum and DIP production by STV-infected cells). This was confirmed by our coworkers via an analysis of the model equations showing that the DIP-free regime is unstable upon introduction of defective interfering viruses [148]. Hence, the two investigated strategies of process optimization are unlikely to prevent virus titer fluctuations. However, a reduction in the *de novo* generation of DIPs can slightly delay the first decrease in virus titers, whereas the fluctuations are surprisingly robust to differences

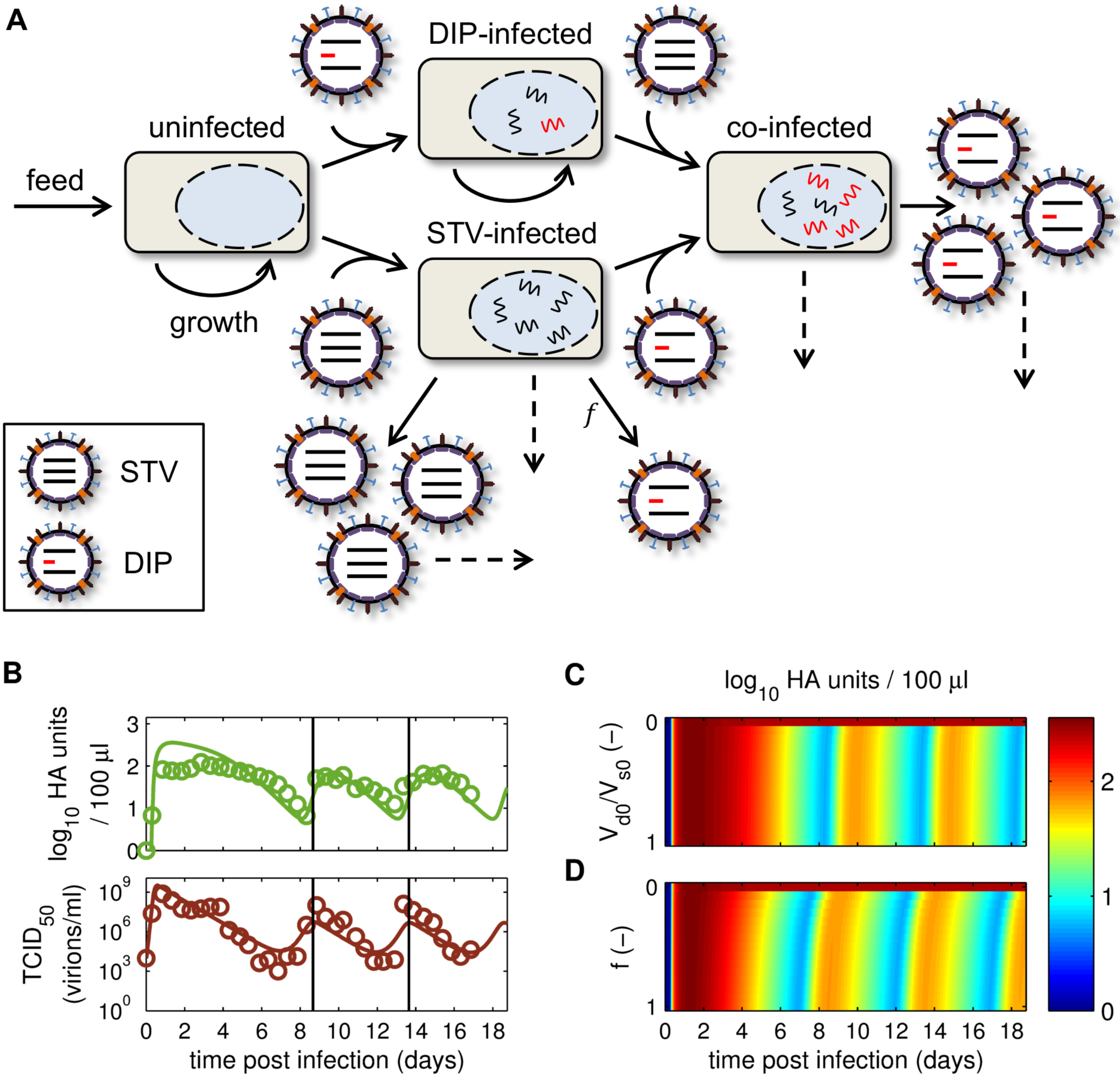

Figure 4.43.: Simulation of continuous infection in the presence of DIPs. (A) Schematic representation of the model for continuous influenza A virus infection in the presence of DIPs. Dashed arrows indicate apoptosis and virus degradation. The continuous harvest of cells and viruses was omitted for illustrative reasons. (B) Simulated virus titers for the parameters used in Table 4.5. Vertical lines mark the peaks in TCID$_{50}$. (C,D) Log$_{10}$ HA units / 100 μl over process time for various ratios of DIPs (V_{d0}) to STVs (V_{s0}) in the seed virus neglecting *de novo* DIP generation (C) and for different rates of *de novo* DIP generation by STV-infected cells, f (denoting the fraction of DIP to STV production), without DIPs being present in the seed virus (D). Figure adapted from Frensing and Heldt *et al.* [148].

in seed virus composition (compare Figure 4.43C and D). In summary, DIPs can readily accumulate in a continuous infection system which features high MOI situations posing a serious challenge to the production of influenza vaccines in such a process.

4.3.3. Discussion of defective interfering virus replication

We derived two mathematical models to study the effect of DIPs on influenza A virus infection. The first considers the replication of a defective RNA at the intracellular level, while the second accounts for DIP growth in bioreactor experiments. In the following, the results of both approaches are discussed.

4.3.3.1. Intracellular DI RNA replication

Despite half a century of research, the molecular basis for DI RNA interference with the intracellular life cycle of influenza A viruses is still not well understood. To elucidate this process we developed a quantitative mathematical model which describes the replication of defective RNAs inside an infected cell. We assumed that these DI RNAs posses an advantage in replication causing them to accumulate to high levels and to sequester large amounts of NP proteins and viral polymerases. The lack of these factors impairs the synthesis of full-length RNAs in our model representing one mechanism of interference. We also observe that cells which are coinfected by an STV and a DIP mainly produce defective viruses and that DIP production strongly depends on the extend of the replication advantage and the coinfection timing. Hence, the model sheds light on the replication of subgenomic RNAs of influenza A virus but also shows where current hypotheses struggle to explain the available data.

Advantage of DI RNAs Although numerous studies have found a preferential amplification of DI RNAs over their full-length counterparts [113, 114, 150], it is still unclear how they gain this competitive advantage. The most common hypothesis suggests a length dependency of RNA synthesis such that viral polymerases produce more copies of a short viral RNA per unit time (reviewed in [143, 144]). We incorporated this mechanism into our model. However, the model may also be used to investigate other hypotheses since the replication advantage and RNA length can be studied independently from one another.

Simulations of an example DI RNA revealed that even a modest advantage in replication can lead to large differences in copy numbers due to the exponential growth of viral RNAs (Figure 4.32). Hence, DI RNAs rapidly outnumber the wild-type segments as suggested on theoretical grounds [144] and found experimentally [113, 114, 150]. In particular, our model DI RNA exceeds the level of its full-length counterpart by three orders of magnitude at 3–4 hpi. Note that the same should be true for short wild-type RNAs if replication is strictly length dependent, i.e., segment 8 should replicate significantly faster than segment 1 leading to substantial difference in vRNA levels. Yet, such differences have not been observed in cell culture infections [174] suggesting that the replication advantage is limited to DI RNAs and that other factors than mere RNA length play a role. A mechanism that could explain this restriction is the presence of yet unknown regulatory elements in full-length RNAs that are impaired or lost upon deletion [143].

In agreement with experimental data [113, 114, 155], our simulations show that co-infected cells almost exclusively release progeny DIPs (Figure 4.34). In the model, this results from the preferential amplification of DI RNAs, which outnumber their corresponding full-length segment by far. However, infection studies have also found an advantage in DI RNA packaging such that released virus particles display an increased ratio of DI to full-length RNAs compared to the level in infected cells [113, 114, 155]. We have not incorporated this advantage in our model since enhanced replication already suffices for exclusive DIP release. However, future studies may want to address this mechanism.

Competition for viral resources Given the preferential amplification of DI RNAs and their similarity to full-length segments, both species may compete for a common viral or cellular resource [144]. Modeling suggests that, among the viral factors, polymerases and NP proteins are most likely to become such bottlenecks for replication since both components participate in the encapsidation of viral RNAs. NP, in particular, is rapidly depleted in our model although the DI RNA originates from a polymerase-encoding segment (Figure 4.32). This is because the encapsidation of an RNA molecule requires only one polymerase complex but multiple copies of NP. Thus, the full-length segment, introduced by the STV, can provide sufficient copies of the intact polymerase subunit. However, after the consumption of NP, the pool of viral polymerases is also drained. The competition for viral proteins has also been observed in experiments where two vRNA-like fluorescent reporters interfered with each other and this interference was mitigated by an increase in polymerase expression [152]. That no dependency on NP was found may be caused by the artificial nature of the system, i.e., a minireplicon approach was used to drive replication instead of an authentic infection. Alternatively, our model might overestimate the number of available polymerases in an infected cell. In this case, polymerases would be depleted first and no limitation in NP would occur because we assumed that encapsidation is a two-step mechanism which requires the formation of an RdRp-RNA complex before NP can bind. Whatever the exact mechanism, both the model and the experiments [152] suggest that encapsidation factors are the most likely candidates for viral resources that become limiting during DI RNA replication.

In our simulations, the competition for viral resources causes a reduction in all full-length viral RNAs. Some experiments show such a reduction upon coinfection of cells by STVs and DIPs [150]. Yet, in other studies, wild-type RNA levels remain unaffected by DI RNA replication [113, 114]. Hence, this effect might depend on the characteristics of the DI RNA such as its initial concentration and its advantage in replication (discussed below). Besides a global effect on viral RNA levels, some DI RNAs have also been shown to cause a reduction in only the level of their corresponding full-length segment, while other full-length vRNAs were produced normally [113]. This observation would argue for a segment-specific effect of DI-RNAs mediated by factors other than NP proteins and viral polymerases. However, the current model cannot capture such a mechanism. Also note that our simulations do not account for limitations in host factors, which are the subject of ongoing investigations.

Influence factors of DIP production Considering the heterogeneity of DIPs and the different infection conditions they encounter, we used our model to predict how changes in the replication advantage and the initial virus concentration affect DIP production at the single-cell level. With respect to changing MOI, we observed that DIP yields from coinfected cells increase with higher initial concentrations of STVs (Figure 4.36). In experiments, increasing the MOI of the STV indeed results in higher virus titers [299]. We propose that this is caused by an increase in the availability of polymerases and NP proteins due to a higher copy number of the full-length vRNAs. Yet, in the above mentioned study, the authors also found an increase in infectious virus progeny [299], which is not present in our model since coinfected cells almost exclusively produce DIPs. This discrepancy may be related to the replication advantage of the DI RNA (discussed below) or to cell population effects, i.e., the fact that the number of STVs and DIPs absorbed by each cell is a statistical property leading to a heterogeneous cell population with respect to the degree of coinfection. By contrast, our model simulates an average infected cell.

Previously, it has been proposed that DI RNAs may have an optimal length because larger deletions are assumed to increase replication speed but would also eventually disrupt the terminal packaging signals [144]. Our results suggest that there may be another constrain. As the replication advantage increases, DI RNAs sequester more and more viral (and perhaps also cellular) proteins, which eventually impairs full-length RNA synthesis (Figure 4.37). Since the full-length RNAs and their products are required for virus release, too much of an advantage may hurt DIP production. Hence, at its optimal length, the defective RNA would outcompete the full-length segments but not deplete the pool of viral resources. Such an optimal DI RNA may replicate efficiently without altering the wild-type RNA levels similar to what has been observed in some experiments [113, 114].

Finally, the time point at which a DIP and an STV coinfect a cell has an impact on virus production in our simulations. In particular, the potential to interfere with STV release decreases markedly when DIP infection occurs after the shutdown of viral RNA synthesis around 3 hpi (Figure 4.38). This is in excellent agreement with experiments showing that interference is most effective when the DI virus is added within the first 3 h after STV infection [300]. Hence, cells in the late infection phase may be resistant to DI RNA replication because the DI RNA is no longer able to enter the nucleus due to high concentrations of M1 and NEP.

DI RNAs of different origin The observation that DI RNAs mostly originate from the polymerases segments [147, 149] raises the question of whether such defects are more likely to occur in the first place or cause a more efficient replication such that they emerge as the dominant species after several rounds of infection. Surprisingly, we find that a defect in segment 3 does indeed have an advantage in DIP production over a DI RNA of segment 4 when STV coinfection is delayed (Figure 4.39). More precisely, a defect in segment 4, which encodes HA, allows viral RNA synthesis to proceed unhindered such that replication shuts down normally at which point an infecting STV can no longer rescue virus release. Eventually, the cell dies under the burden of infection without producing progeny viruses. By contrast, failure to encode a functional polymerase subunit stalls virus replication and the DI RNA can persist at low levels in the cell; it can wait for an STV to infect. Thus, we hypothesize that defects in segments which are essential for viral RNA synthesis (e.g. segment 1–3 and 5) can result in an advantage in DIP growth when STV infection is delayed. Such DIPs may, hence, outgrow others over subsequent passages and emerge as the dominant species.

Summary By incorporating a defective RNA into our model of intracellular influenza A virus replication, we were able to reproduce many qualitative features of DI RNA synthesis but also found some discrepancies to measurement data. Especially the length-dependent replication advantage, which leads to large differences in vRNA levels even at low rates, requires further studies as simulations indicate that, if present, it has to be restricted to DI RNAs and should not affect short wild-type segments. The cause of such a restriction remains elusive. Furthermore, modeling suggests that the growth properties of a DIP depend on the replication advantage of its DI RNA, the initial number of infecting viruses, the coinfection timing, and the segment carrying the defect. In a heterogeneous DIP population, DI RNAs that originate from segments essential for viral RNA synthesis and DI RNAs that do not drain the pool of viral proteins may, hence, have a growth advantage. Taken together, these results contribute to our understanding of DI RNA replication and may also help to design production processes for DIPs with therapeutic potential (reviewed in [144, 145]).

4.3.3.2. DIP growth during continuous infection

Continuous production processes for influenza virus hold the promise of increasing virus yields and avoiding batch-to-batch variations. Yet, they suffer from oscillations in virus titers, which cause periods of low productivity [148]. Using a simple mathematical model we inferred that such oscillations can have two reasons: the continuous cultivation mode itself and the growth of DIPs. However, for the experimental system considered here only the latter can explain why cyclic variations occur.

Oscillations due to process mode The most surprising observation in the continuous infection experiments conducted by Frensing *et al.* are the oscillations in HA and TCID_{50} titers [148]. Our mathematical model indicates that, in principle, such oscillations can arise in the absence of DIPs due to the continuous cultivation mode (Figure 4.42). More precisely, the continuous feed from the cell growth reactor prevents the depletion of host cells by infection, which is typically observed in batch cultivations [177]. At low dilution rates, these cells can spawn a new cycle of virus production after the previous infection wave has subsided. The existence of periodic solutions in the absence of DIPs was confirmed by an analysis of our model by Frensing and coworkers [148], which also revealed that such oscillations can only occur if the dilution rate of the virus reactor is lower than the cell growth rate. Since this was not the case in the experiments, other factors than the process mode are causing the periodic decrease in virus titers. Also note that oscillations are not unusual in continuous cultivation systems and it has been suggested that they can arise from cell growth due to feedback interactions between cell metabolism and the environment, and from interactions among linked intracellular reactions [301, 302]. However, we do not expect that such oscillations play a role here since cell concentrations in the cell bioreactor were approximately constant.

Oscillations due to DIPs When we introduced DIPs into our model it readily showed oscillations in virus titers that match the experimental observations (Figure 4.43). In the past, models of DIP growth have also displayed cyclic variations [271, 303, 304]. However, these studies considered serial passage infections and the titer fluctuations exerted features of deterministic chaos, i.e., virus titers were intrinsically unpredictable after a short amount of time, which is supported by serial passage experiments [304, 305]. By contrast, the oscillations in our continuous system are much more regular. A similar observation has been made in a model for continuous baculovirus infection although the authors did not check whether these fluctuations could have also originated from the process mode [306]. Yet, such regular patterns correspond well to the measurements of Frensing *et al.* [148] and our simulations suggesting that regular oscillations are a general feature of continuous infection processes in the presence of DIPs. Hence, this type of process lends itself well to the analysis of DIP replication under controlled conditions.

Although our model reproduces the frequency of virus titer oscillations, it fails to capture their amplitude. In particular, it underestimates the fluctuations in TCID_{50}. This is most likely caused by the relatively simple structure of the model we chose to enable an analysis of the equation system for bifurcations. These simplifications include the assumption that coinfection by DIPs can interfere with virus production even if STV infection is already well advanced. By contrast, our intracellular model of DI RNA replication (Section 4.3.1) and experimental results [300] suggest that DIPs need to enter the cell within 3 h after STV infection. Moreover, we adopted a single-hit mechanism of DIP interference from previous models [271, 303], i.e., infection by a single DIP suffices to convert an STV-infected cells to a cell that exclusively releases DIPs. While this is supported by our intracellular model, experimental studies on VSV infection suggest a multi-hit inhibition with at least four types of productively infected cells whose virus production depends on the amount of infecting DIPs [307]. Taken together, these features may allow a more detailed model to reproduce the measurements more faithfully.

Features of DIP-induced oscillations Our simulations and the measurements display a delay between the peak in TCID_{50} and HA titer. Such a delay was also found for infections by VSV in the presence of its DIPs [308]. It results from the observation that DIPs need a high MOI to replicate but also interfere with the production of infectious virus. Hence, large amounts of STVs, which increase the TCID_{50}, favor the accumulation of DIPs resulting in high HA titers but also causing a drop in infectious viruses. In a continuous production process, high MOIs could, thus, serve as an indicator for an imminent drop in HA titer. Yet, assays for the quantification of infectious virus are usually time consuming, preventing an online control of this parameter. Hence, a mathematical model, like the one presented here, could be used to predict titer dynamics facilitating interventions to control the process.

Our simulations also indicate that the DIP-free regime is unstable such that the introduction of DIPs (either by their presence in the inoculum or *de novo* generation) causes the rapid accumulation of defective viruses and a decrease in virus titers. This is confirmed by our colleagues who analyzed the equation system [148]. Hence, DIPs readily grow under the chosen experimental conditions and impair virus production unless the inoculum is completely free of DIPs and they are not produced by STV-infected cells. A similar observation has been made in a model for VSV infection, in which DIPs dominate subsequent coinfections once they are available [309]. Hence, counteracting DIP amplification in continuous influenza virus infection is not an easy task. Nevertheless, decreasing the *de novo* generation of DIPs by STV-infected cells can delay DIP accumulation, whereas oscillations are surprisingly robust to changes in seed virus purity. The latter was also observed in a model for serial passaging of VSV, where the initial DIP concentration had no effect on steady state virus titers [309].

Summary Our simple mathematical model shows that DIPs can cause periodic oscillations and low productivity in a continuous infection system for influenza A virus. It also indicates that the DIP-free regime is unstable such that DIPs readily grow once introduced. Hence, DIP accumulation is a general obstacle in continuous infection systems in agreement with previous observations of reduced productivity in a two-stage bioreactor setup for baculovirus infection [310–312]. Different reactor configurations, like a fed-batch-operated growth reactor coupled to an infection reactor run in batch mode [306], may be able to address this problem facilitating the production of influenza viruses in a semi-continuous manner.

Chapter 5

Conclusion

The general aim of this study was to build mathematical models for influenza A virus infection at the intracellular and cell population level that can identify bottlenecks of virus production. Discovering such bottlenecks is a key step toward a better understanding of virus-host cell interactions. It can also help to increase virus yields in vaccine production and to develop new, more potent antiviral drugs. Based on our models we proposed various strategies to meet these goals. In addition, we developed a multiscale model of influenza A virus infection that links the intracellular processes of viral replication to the extracellular cell-to-cell transmission and the dynamics of the host cell population. This model represents a major milestone of the present work allowing us to elucidate how both levels interact and to uncover emergent properties of infection that only appear when the system is considered as a whole.

Intracellular virus replication In the first part of this work, we used experimental results from various sources in literature to derive a kinetic model of influenza A virus infection at the intracellular level. This model describes the crucial steps of viral replication from virus entry to the release of progeny virions with a particular focus on the synthesis of viral RNAs and its regulation. Since the latter is still a matter of controversial debate we analyzed two model variants that represent different hypotheses on the transition from viral transcription to genome replication: the switching and stabilization hypothesis, respectively. While our switching model agrees qualitatively with part of the data, it fails to correctly account for the influence of viral polymerases on cRNA levels in experiments. By contrast, simulations that incorporate the stabilization of nascent cRNA by viral proteins reproduce the measurements well allowing us to capture the time course of the three viral RNA species during early infection. To also describe later stages of the viral life cycle a second regulatory mechanism was required. This mechanism controls the fate of vRNPs, which can either act as templates for viral mRNA and cRNA synthesis while inside the nucleus or form progeny virions after nuclear export. Our results suggests that balancing these two roles is key to the successful production of influenza A viruses. In particular, the nuclear export of vRNPs, which is triggered by M1 and NEP, facilitates virus assembly but also causes a shutdown of positive-strand RNA synthesis. Hence, leaving the nucleus too early may result in an insufficient production of mRNA and cRNA, whereas a late export can delay progeny virus release. The latter can be detrimental for the virus as apoptosis may kill the cell before virions can be released and because virus variants which leave cells faster may have an evolutionary advantage. However, during vaccine production, where competition between strains is not an issue, the timing of nuclear export could be tuned to increase virus yields. In addition, increasing the rate of viral RNA synthesis can boost virus production significantly in our simulations. In fact, virus yields are particularly sensitive to this process as viral RNAs engage in an autocatalytic reaction where vRNA produces cRNA and vice versa. Hence, vaccine strains could benefit from a fast viral polymerase and a slow nuclear export. Moreover, the fine tuning of host factors required for these processes may improve production cell lines. In summary, our model captures a wide variety of experimental data and provides a detailed picture of virus replication at the intracellular level.

Stochastic fluctuations in viral RNA synthesis At the intracellular level viral infections are often considered noisy because they involve reactions with small molecule numbers (e.g. when a single virus particle releases a single copy of the viral genome into the cytoplasm). In our simulations such stochastic effects do indeed strongly affect influenza A virus replication decreasing mean virus yields and causing large numbers of low-productive cells even if each cell is infected by multiple viruses. When infection is initiated by a single virion noise can have an even more dramatic effect with most cells failing to produce infectious virus progeny. Our simulations suggest that both phenomena are favored by the segmented genome of influenza viruses. Since genome segmentation allows each vRNP to act as an independent replication unit, stochastic effects, which are amplified by the autocatalytic mechanism of viral RNA synthesis, can cause large fluctuations in the copy number of viral genes. These differences between the vRNAs in an infected cell can impair virus production. Also, stochastic effects can lead to the random degradation of vRNPs, which has profound consequences when it occurs in the beginning of infection and in cells where only one copy of the parental viral genome enters the nucleus. In these cases, the loss of a genome segment prevents the release of replication-competent virions. Especially at low MOI this effect may contribute to the large number of nonproductive infections observed experimentally. Taken together, the model shows how stochastic effects can drive cell-to-cell variability during infection and it provides additional evidence for the hypothesis that influenza virus particles need to complement each other in order to ensure a productive infection. Moreover, modeling reveals that, despite its advantages for genetic diversity, genome segmentation may increase the susceptibility of virus replication to noise and may, hence, require regulatory mechanisms that can suppress molecular fluctuations.

Multiscale model of infection In order to study how the intracellular viral life cycle interacts with infection dynamics at the cell population level we integrated our deterministic model of virus replication into a description of target cell dynamics and virus transmission from one target cell to the next. Coupling these two scales allows the model to reproduce intracellular data (e.g. the levels of the three viral RNA species) and, at the same time, the number of uninfected, infected, and apoptotic cells as well as the virus titer in cell culture. Furthermore, it facilitates a systematic analysis of the intracellular processes that are most susceptible to antiviral therapy. We found that the inhibition of viral RNA and protein synthesis, nuclear export, and assembly/release can efficiently suppress virus production. Especially inhibitors of the viral polymerase are highly promising compounds as they interfere with the exponential growth of viral RNAs. By contrast, targeting the steps of virus entry (e.g. attachment, endocytosis, and fusion/uncoating) primarily delays infection but does not reduce peak virus titers *in vitro* unless the drug is highly effective. Our simulations also demonstrate that the extend of virus-induced cell death strongly affects therapy success especially for antivirals that change the time course of virus release at the intracellular level. These drugs may benefit from the active killing of infected cells by the immune system *in vivo*. Overall, multiscale modeling can link experimental results on the intracellular and cell population level, and provide a systems-level understanding of virus infection across these different scales. Our model, therefore, represents a promising platform to incorporate further levels of detail like the immune response and viral pathogenesis.

Replication of defective interfering viruses The last part of this work focuses on the growth of DIPs, which can compromise virus production at the intracellular and cell population level. For the replication inside an infected cell simulations show that DI RNAs rapidly outgrow the full-length vRNAs competing with them for viral encapsidation factors. Depletion of NP proteins and viral polymerases may, hence, represent one mechanism of DI RNA–induced interference. We also find that, due to the autocatalytic mechanism of viral replication, a modest advantage in replication suffices to induce large differences between the full-length and DI RNAs causing coinfected cells to almost exclusively release progeny DIPs. Since such differences have not been observed between wild-type segments of different length, the replication advantage does not seem to be strictly length dependent but may rather apply to DI RNAs only. This favors the hypothesis that wild-type segments contain regulatory elements that are impaired or completely lost upon deletion of large internal stretches of the vRNA. The model also provides insights into the features that determine whether a subgenomic RNA replicates successfully. In order to produce large amounts of DIPs in our simulations a DI RNA requires an intermediate replication advantage allowing it to accumulate rapidly without draining the pool of viral proteins. Moreover, it needs to coinfect a cell no later than 3 h after STV infection to be able to cause interference. Finally, we found that DI RNAs which originate from segments essential for viral RNA synthesis may have an additional growth advantage as they can persist in DIP-infected cells at low levels allowing them to wait for STV coinfection. Taken together, these result shed light on the replication of DI RNAs inside infected cells and suggest further experiments to better characterize their growth.

In order to study a continuous production process for influenza vaccines we also developed a simple mathematical model of DIP replication at the cell population level. This model suggests that DIPs can readily accumulate in such a system causing regular oscillations in virus titers, which show remarkable resemblance to the measurement data. Since these oscillations lead to periods of low productivity, the model was used to test different strategies to avoid DIP accumulation. Neither of these strategies succeeded in eliminating the oscillations although reducing *de novo* DIP generation was able to delay the first decrease in virus titers. The persistence of oscillations agrees well with the observation that the DIP-free model regime is unstable such that constant virus titers can only exist in the absence of *de novo* DIP generation and of DIPs in the inoculum. Overall, DIPs thus represent a significant challenge to the continuous production of influenza A virus, which calls for different process modes and/or reactor configurations.

Summary We have developed several quantitative mathematical models of influenza A virus infection at the intracellular and cell population level. These models suggest novel targets for antiviral therapy and strategies to increase virus yields in vaccine production. They also allowed us to integrate some of the current knowledge on influenza A virus infection into a systematic framework and to test competing hypotheses on the viral life cycle against data from different experimental sources. In contrast to previous modeling approaches, which mainly studied the different levels of infection in isolation, we also built a multiscale model that links intracellular virus replication with infection dynamics at the within-host scale. While such an approach facilitates an investigation of the system's emergent properties today, it may become even more important in the future by allowing us to predict the pathogenicity and pandemic potential of new virus variants from their molecular traits and perhaps also from their genome sequence.

Chapter 6

Outlook

The mathematical models presented in this work capture a wide variety of *in vitro* data and provide a detailed picture of viral kinetics in cell culture. Applying these findings to *in vivo* infections and in particular to influenza in humans holds great promise for future studies. Especially the multiscale model lends itself well to such an investigation as it could link the molecular traits of a virus, which govern its intracellular replication, to viral pathogenesis at the tissue scale and organ level. Multiscale models may, hence, contribute to clinical drug trials and to the development of more potent vaccines. In order to be compatible with *in vivo* data the model does, however, need an adequate representation of the immune response. This could include both, antiviral mechanisms within a cell, like the interferon response and other antiviral signaling cascades, as well as processes at the extracellular level, such as virus-specific antibodies and cell-mediated immunity. Due to its integrative nature, multiscale modeling could use existing descriptions of these processes allowing future studies to benefit from the large pool of models already available in systems immunology [184].

Accounting for the transmission of viruses between hosts (i.e. the epidemic scale) would represent another promising step toward a more detailed multiscale description of influenza virus infection. This approach may reveal how differences between virus strains at the molecular level affect their fitness across various scales, e.g., whether a fast polymerase, which increases the number of virions an infected cell can release, also leads to higher lung titers in infected patients and provides an advantage with respect to virus spreading in the human population. Such models may eventually allow us to predict the virulence and pandemic potential of new virus variants from their sequence data (i.e. the phenotype from the genotype) by revealing the molecular events that lead to disease at the organism level and epidemic scale.

At the intracellular level, future studies may benefit from extending the scope of modeling to host cell factors that are essential for influenza virus replication. Incorporating these factors could support cell line engineering for vaccine production, e.g., the identification of cellular proteins whose knockdown or overexpression can increase virus production. In addition, it would facilitate an *in silico* analysis of host factors for their potential as antiviral drug targets [118]. However, extending the intracellular model in such a way is currently limited by the available data. Cell culture experiments in which a specific cellular factor is perturbed and intracellular viral kinetics are measured could provide such data. In addition, modeling could be guided by the results of large-scale siRNA screens although these screens typically produce only limited insights into the kinetics of intracellular infection. More sophisticated models may provide such information thereby contributing to a quantitative understanding of virus-host cell interactions.

Another aspect that deserves further attention is the regulation of viral RNA synthesis. Although a model of the stabilization hypothesis can reproduce many of the experimental observations it does not rule out other regulatory interactions proposed in literature. Building alternative model variants from these hypotheses and using model discrimination techniques may reveal which mechanisms are strictly necessary to explain the data. Moreover, model-based experimental design can suggest what components to measure and when to measure them in order to validate or invalidate these hypotheses. Such theoretical studies could be supported by experiments that use specific inhibitors of virus replication or by monitoring the replication of DI RNAs. Hence, applying the iterative cycle of mathematical modeling and experimental validation may help to gain a comprehensive picture of the factors that control the intracellular viral life cycle.

With respect to the noise observed in virus replication it would be highly desirable to use stochastic models for the estimation of intracellular parameters. However, two circumstances prevent their application at the moment. On the one hand, data on virus replication in individual cells are required to accurately calibrate stochastic intracellular models but such measurements are currently lacking. Recent advances in experimental techniques do, however, allow to probe single cell infection. On the other hand, computational efficiency is a major bottleneck for the simulation of stochastic models. One way to improve the performance are hybrid algorithms that combine deterministic and stochastic simulation techniques. If these algorithms can reduce computation time significantly, stochastic models may replace their deterministic counterparts in the analysis of intracellular viral kinetics in the future.

The development of multiscale models that account for molecular noise represents another interesting avenue of research. In particular, stochastic effects could influence the cell population level in low MOI scenarios (e.g. shortly after inoculation) and during an infection with DIPs, where the number of viruses that infect a particular cell is a statistical property. Noise in the initial phase of infection could, for instance, cause large fluctuations in the onset of virus production (i.e. the delay until the virus titer increases), which are typically observed between low MOI experiments. Modeling could reveal what part of this inter-experiment variation is caused by the inherent randomness of biochemical reactions.

Moreover, our stochastic model at the intracellular level suggests that low MOI situations result in a large percentage of nonproductive infections. Hence, a relatively small number of virus-producing cells may determine whether the virus is able to establish itself in a host. Entry inhibitors which further reduce this number, may, therefore, be particularly suitable to act as prophylactic antivirals.

Overall, the combination of mathematical modeling with state-of-the-art experimental techniques holds great promise for influenza virus research. Especially multiscale models and stochastic approaches provide the means of moving virology from a descriptive to a predictive science. In the future, mathematical models may, thus, gain a more prominent role in the fight against influenza.

List of Figures

Figure 2.1: Virus particle and genome structure 5
Figure 2.2: Scheme of the influenza A virus life cycle 7
Figure 2.3: Scheme of different hypotheses on the transition from transcription to replication 9
Figure 2.4: Scheme of nuclear export 11
Figure 2.5: Schematic diagram of the DI RNA structure 15
Figure 2.6: Scheme of the standard model for within-host viral dynamics . . . 21

Figure 4.1: Virus attachment to the cell surface 52
Figure 4.2: Fusion with endosomes and virus entry dynamics 53
Figure 4.3: Simulation of the cRNA stabilization hypothesis 55
Figure 4.4: Simulation of the switching hypothesis 58
Figure 4.5: Viral RNA dynamics during infection 59
Figure 4.6: Viral RNA dynamics in the switching model 62
Figure 4.7: Dynamics of virus release and viral protein accumulation 62
Figure 4.8: Increase in cell-specific virus yield through intracellular perturbation. 64
Figure 4.9: Example of a stochastic simulation run 65
Figure 4.10: Comparison of the deterministic and stochastic simulation 66
Figure 4.11: Virus production in a stochastic model that accounts for an independent genome segment synthesis 67
Figure 4.12: Fluctuations in genome segment levels 68
Figure 4.13: Noise in genome segment levels 69
Figure 4.14: Amplification of noise during virus replication 70
Figure 4.15: Fluctuations in viral protein levels 71

Figure 4.16: Increasing differences in virus production at low NIVCs 72
Figure 4.17: Failed fusion and segment loss cause nonproductive infections . . . 73
Figure 4.18: Probability of genome segment loss 73
Figure 4.19: Success of infection 74
Figure 4.20: Different models for the regulation of viral RNA synthesis 75
Figure 4.21: Noise reduction by segment-specific regulation 76
Figure 4.22: Success of infection in the presence of segment-specific regulation . 77
Figure 4.23: Schematic depiction of the multiscale model 91
Figure 4.24: Model fit to measurements of intracellular and extracellular infection dynamics 92
Figure 4.25: Model predictions for different infection conditions 94
Figure 4.26: Dynamics of cellular NP content during multi-cycle infection . . . 95
Figure 4.27: The impact of cell death on virus production 96
Figure 4.28: Impact of DAAs on intracellular virus replication 98
Figure 4.29: The effect of cell death dynamics on virus production 99
Figure 4.30: Impact of DAAs on viral infection dynamics 101
Figure 4.31: Assumed effect of DI RNA length on synthesis kinetics 107
Figure 4.32: Interference of DI RNA synthesis with viral replication 108
Figure 4.33: Accumulation of replication intermediates during coinfection 109
Figure 4.34: Reduced virus production in coinfected cells 110
Figure 4.35: Coinfection probability 111
Figure 4.36: Influence of initial virus concentration on virus production 111
Figure 4.37: Effect of the replication advantage on virus production 112
Figure 4.38: Influence of coinfection timing 113
Figure 4.39: Virus production for DI RNAs from different segments 114
Figure 4.40: Reactor setup for continuous influenza A virus infection 115
Figure 4.41: Measurements of continuous influenza virus infection 116
Figure 4.42: Simulation of continuous infection in the absence of DIPs. 117

Figure 4.43: Simulation of continuous infection in the presence of DIPs 119

Figure A.1: Impact of modifying and extending the deterministic model 173
Figure A.2: Difference between the deterministic model and the mean of stochastic simulations that neglect genome segmentation 174
Figure A.3: Comparison between the deterministic model and stochastic simulations that neglect genome segmentation 175

Figure B.1: Bimodal distribution of cellular NP content during multi-cycle infection 179
Figure B.2: Virus titer dynamics in response to DAA treatment 180

List of Tables

Table 4.1: Parameter estimates for virus entry 53
Table 4.2: Parameter estimates for the transition from transcription to genome replication based on a model that considers the stabilization hypothesis 56
Table 4.3: Parameter estimates for viral RNA synthesis during late infection . 61
Table 4.4: Parameter estimates for the multiscale model fit in Figure 4.24. . . 93
Table 4.5: Parameters and non-zero initial conditions for the simulation of continuous influenza virus infection 118

Table A.1: List of parameters for the deterministic intracellular model 163
Table A.2: Initial conditions and parameter changes used to simulate the stabilization model 165
Table A.3: Initial conditions and parameter changes used to simulate the switching model 165
Table A.4: Parameter estimates for the transition from transcription to genome replication based on a model that accounts for the switching hypothesis 166
Table A.5: Parameter estimates for the switching model considering data in Figure 4.6. 166
Table A.6: Parameters corresponding to the mechanisms listed in Figure 4.8. . 167
Table A.7: List of parameters for the stochastic intracellular model 168

Table B.1: List of parameters for the intracellular level of the multiscale model. 176
Table B.2: List of parameters for the extracellular level of the multiscale model. 177
Table B.3: List of non-zero initial conditions for the multiscale model 177

Table B.4: Parameters corresponding to the drug targets in Figure 4.28 and 4.30. 178

Table C.1: List of parameters for the intracellular model of DI RNA replication. 181
Table C.2: Initial conditions and parameter changes for the model of intracellular DI RNA replication 182
Table C.3: Initial conditions and parameter changes for the model of DIP growth during continuous virus production 182

List of Publications

Results from the following publications and supervised theses were included in this work.

Publications

Heldt FS, Frensing T, Pflugmacher A, Gröpler R, Peschel B, Reichl U (2013) Multiscale modeling of influenza A virus infection supports the development of direct-acting antivirals. PLoS Comput Biol 9: e1003372.

Frensing T*, **Heldt FS***, Pflugmacher A, Behrendt I, Jordan I, Flockerzi D, Genzel Y, Reichl U (2013) Continuous influenza virus production in cell culture shows a periodic accumulation of defective interfering particles. PLoS One 8: e72288.

Heldt FS, Frensing T, Reichl U (2012) Modeling the intracellular dynamics of influenza virus replication to understand the control of viral RNA synthesis. J Virol 86: 7806–7817.

*authors contributed equally

Supervised theses

Dorl S (2013) Stochastic modelling of the intracellular replication of influenza virus during vaccine production. Bachelor thesis, Faculty for Process and Systems Engineering, Otto von Guericke University, Magdeburg

Kaffka H (2013) Model-based analysis of the influence of defective interfering particles on influenza virus replication. Bachelor thesis, Faculty for Process and Systems Engineering, Otto von Guericke University, Magdeburg.

Talks

Heldt FS, Frensing T, Reichl U (2014) The multiscale nature of influenza A virus infection and its implications for modeling antiviral therapy. The Joint Meeting of the Japanese Society of Mathematical Biology and the Society for Mathematical Biology, Osaka, Japan.

Heldt FS, Isken B, Frensing T, Reichl U (2013) Multiscale modeling of influenza virus infection supports the development of antiviral drugs. 14th International Conference on Systems Biology, Copenhagen, Denmark.

Heldt FS, Isken B, Pflugmacher A, Frensing T, Reichl U (2013) Multiscale modeling of influenza virus infection elucidates the performance of antivirals. 1st Workshop on Virus Dynamics, Frankfurt, Germany.

Heldt FS, Frensing T, Reichl U (2012) Elucidating bottlenecks in influenza virus replication to optimize vaccine production. International Conference on Systems Biology of Human Disease, Heidelberg, Germany.

Heldt FS, Reichl U (2011) Understanding the dynamics of intracellular virus replication — How does influenza control its RNA and protein synthesis? 4th ESWI Influenza Conference, Malta.

Posters

Heldt FS, Frensing T, Reichl U (2014) A multiscale model of influenza A virus infection that elucidates the treatment with direct-acting antivirals. International Conference on Systems Biology of Human Disease, Boston, United States of America.

Heldt FS, Isken B, Pflugmacher A, Frensing T, Reichl U (2013) A multiscale model of influenza virus infection elucidates the performance of antivirals. 23rd Annual Meeting of the German Society for Virology, Kiel, Germany.

Heldt FS, Isken B, Frensing T, Reichl U (2012) Elucidating bottlenecks in influenza virus replication to optimize vaccine production. International Conference on Systems Biology of Human Disease, Heidelberg, Germany.

Heldt FS, Frensing T, Reichl U (2012) Elucidating the dynamics of influenza virus replication by mathematical modeling. 22nd Annual Meeting of the German Society for Virology, Essen, Germany.

Heldt FS, Frensing T, Reichl U (2011) Mechanistic model of influenza virus replication elucidates the intracellular dynamics and control of viral RNA synthesis. 12th International Conference on Systems Biology, Mannheim, Germany.

Heldt FS, Reichl U (2010) Modeling influenza virus infection dynamics in cell culture-based vaccine production. 11th International Conference on Systems Biology, Edinburgh, United Kingdom.

Heldt FS, Reichl U (2010) Multiscale modeling of influenza virus infection dynamics in cell culture-based vaccine production. International Conference on Systems Biology of Human Disease, Boston, United States of America.

Bibliography

1. Potter CW (2001) A history of influenza. J Appl Microbiol 91: 572–579.

2. Taubenberger JK, Morens DM (2006) 1918 influenza: the mother of all pandemics. Emerg Infect Dis 12: 15–22.

3. Morens DM, Taubenberger JK, Fauci AS (2009) The persistent legacy of the 1918 influenza virus. N Engl J Med 361: 225–229.

4. World Health Organization (2014). Influenza (seasonal) - fact sheet no 211. URL `http://www.who.int/mediacentre/factsheets/fs211/en/`. accessed August 12, 2014.

5. Wright PF, Neumann G, Kawaoka Y (2013) Orthomyxoviruses, In: Bernard N. Fields and David M. Knipe (ed.), Fields virology 6th edition. Philadelphia, Pa. [u.a.]: Wolters Kluwer Lippincott Williams & Wilkins, chapter 41. pp. 1186–1243.

6. Noh JY, Kim WJ (2013) Influenza vaccines: Unmet needs and recent developments. Infect Chemother 45: 375–386.

7. Rumschlag-Booms E, Rong L (2013) Influenza A virus entry: implications in virulence and future therapeutics. Adv Virol 2013: 121924.

8. Simonsen L, Spreeuwenberg P, Lustig R, Taylor RJ, Fleming DM, et al. (2013) Global mortality estimates for the 2009 influenza pandemic from the glamor project: a modeling study. PLoS Med 10: e1001558.

9. Wathen MW, Barro M, Bright RA (2013) Antivirals in seasonal and pandemic influenza–future perspectives. Influenza Other Respir Viruses 7 Suppl 1: 76–80.

10. Cvijovic M, Almquist J, Hagmar J, Hohmann S, Kaltenbach HM, et al. (2014) Bridging the gaps in systems biology. Mol Genet Genomics 289: 727–734.

11. Nowak MA, May RM (2004) Virus Dynamics: Mathematical Principles of Immunology and Virology. Oxford, UK: Oxford University Press.

12. Dorjee S, Poljak Z, Revie CW, Bridgland J, McNab B, et al. (2013) A review of simulation modelling approaches used for the spread of zoonotic influenza viruses in animal and human populations. Zoonoses Public Health 60: 383–411.

13. Lee BY, Haidari LA, Lee MS (2013) Modelling during an emergency: the 2009 H1N1 influenza pandemic. Clin Microbiol Infect 19: 1014–1022.

14. Smith AM, Perelson AS (2011) Influenza A virus infection kinetics: quantitative data and models. Wiley Interdiscip Rev Syst Biol Med 3: 429–445.

15. Beauchemin CAA, Handel A (2011) A review of mathematical models of influenza A infections within a host or cell culture: lessons learned and challenges ahead. BMC Public Health 11 Suppl 1: S7.

16. Sidorenko Y, Reichl U (2004) Structured model of influenza virus replication in MDCK cells. Biotechnol Bioeng 88: 1–14.

17. Madrahimov A, Helikar T, Kowal B, Lu G, Rogers J (2013) Dynamics of influenza virus and human host interactions during infection and replication cycle. Bull Math Biol 75: 988–1011.

18. Josset L, Tisoncik-Go J, Katze MG (2013) Moving H5N1 studies into the era of systems biology. Virus Res 178: 151–167.

19. Shaw ML, Palese P (2013) Orthomyxoviridae, In: Bernard N. Fields and David M. Knipe (ed.), Fields virology 6th edition. Philadelphia, Pa. [u.a.]: Wolters Kluwer Lippincott Williams & Wilkins, volume I, chapter 40. pp. 1151–1185.

20. Harris A, Cardone G, Winkler DC, Heymann JB, Brecher M, et al. (2006) Influenza virus pleiomorphy characterized by cryoelectron tomography. Proc Natl Acad Sci U S A 103: 19123–19127.

21. Calder LJ, Wasilewski S, Berriman JA, Rosenthal PB (2010) Structural organization of a filamentous influenza A virus. Proc Natl Acad Sci U S A 107: 10685–10690.

22. Compans RW, Content J, Duesberg PH (1972) Structure of the ribonucleoprotein of influenza virus. J Virol 10: 795–800.

23. Moeller A, Kirchdoerfer RN, Potter CS, Carragher B, Wilson IA (2012) Organization of the influenza virus replication machinery. Science 338: 1631–1634.

24. Shaw ML, Stone KL, Colangelo CM, Gulcicek EE, Palese P (2008) Cellular proteins in influenza virus particles. PLoS Pathog 4: e1000085.

25. Lamb RA, Krug RM (2001) *Orthomyxoviridae*: the viruses and their replication, In: D. M. Knipe and P. M. Howley (ed.), Fields virology 4th edition. Philadelphia, Pa: Lippincott Williams & Wilkins. pp. 1487–1531.

26. Huang TS, Palese P, Krystal M (1990) Determination of influenza virus proteins required for genome replication. J Virol 64: 5669–5673.

27. Vasin AV, Temkina OA, Egorov VV, Klotchenko SA, Plotnikova MA, et al. (2014) Molecular mechanisms enhancing the proteome of influenza A viruses: an overview of recently discovered proteins. Virus Res 185: 53–63.

28. Noda T, Kawaoka Y (2010) Structure of influenza virus ribonucleoprotein complexes and their packaging into virions. Rev Med Virol 20: 380–391.

29. Zheng W, Tao YJ (2013) Structure and assembly of the influenza A virus ribonucleoprotein complex. FEBS Lett 587: 1206–1214.

30. Arranz R, Coloma R, Chichón FJ, Conesa JJ, Carrascosa JL, et al. (2012) The structure of native influenza virion ribonucleoproteins. Science 338: 1634–1637.

31. Fodor E (2013) The RNA polymerase of influenza A virus: mechanisms of viral transcription and replication. Acta Virol 57: 113–122.

32. Desselberger U, Racaniello VR, Zazra JJ, Palese P (1980) The 3' and 5'-terminal sequences of influenza A, B and C virus RNA segments are highly conserved and show partial inverted complementarity. Gene 8: 315–328.

33. Noda T, Sagara H, Yen A, Takada A, Kida H, et al. (2006) Architecture of ribonucleoprotein complexes in influenza A virus particles. Nature 439: 490–492.

34. Fournier E, Moules V, Essere B, Paillart JC, Sirbat JD, et al. (2012) A supramolecular assembly formed by influenza A virus genomic RNA segments. Nucleic Acids Res 40: 2197–2209.

35. Skehel JJ, Wiley DC (2000) Receptor binding and membrane fusion in virus entry: the influenza hemagglutinin. Annu Rev Biochem 69: 531–569.

36. Matlin KS, Reggio H, Helenius A, Simons K (1981) Infectious entry pathway of influenza virus in a canine kidney cell line. J Cell Biol 91: 601–613.

37. ying Chou Y, Heaton NS, Gao Q, Palese P, Singer RH, et al. (2013) Colocalization of different influenza viral RNA segments in the cytoplasm before viral budding as shown by single-molecule sensitivity fish analysis. PLoS Pathog 9: e1003358.

38. Cros JF, Palese P (2003) Trafficking of viral genomic RNA into and out of the nucleus: influenza, thogoto and borna disease viruses. Virus Res 95: 3–12.

39. Boulo S, Akarsu H, Ruigrok RWH, Baudin F (2007) Nuclear traffic of influenza virus proteins and ribonucleoprotein complexes. Virus Res 124: 12–21.

40. Hutchinson EC, Fodor E (2012) Nuclear import of the influenza A virus transcriptional machinery. Vaccine 30: 7353–7358.

41. Hutchinson EC, Fodor E (2013) Transport of the influenza virus genome from nucleus to nucleus. Viruses 5: 2424–2446.

42. O'Neill RE, Jaskunas R, Blobel G, Palese P, Moroianu J (1995) Nuclear import of influenza virus RNA can be mediated by viral nucleoprotein and transport factors required for protein import. J Biol Chem 270: 22701–22704.

43. Cros JF, García-Sastre A, Palese P (2005) An unconventional NLS is critical for the nuclear import of the influenza a virus nucleoprotein and ribonucleoprotein. Traffic 6: 205–213.

44. Bui M, Whittaker G, Helenius A (1996) Effect of M1 protein and low pH on nuclear transport of influenza virus ribonucleoproteins. J Virol 70: 8391–8401.

45. Martin K, Helenius A (1991) Nuclear transport of influenza virus ribonucleoproteins: the viral matrix protein (M1) promotes export and inhibits import. Cell 67: 117–130.
46. Whittaker G, Bui M, Helenius A (1996) Nuclear trafficking of influenza virus ribonuleoproteins in heterokaryons. J Virol 70: 2743–2756.
47. Martin K, Helenius A (1991) Transport of incoming influenza virus nucleocapsids into the nucleus. J Virol 65: 232–244.
48. Babcock HP, Chen C, Zhuang X (2004) Using single-particle tracking to study nuclear trafficking of viral genes. Biophys J 87: 2749–2758.
49. Elton D, Digard P, Tiley L, Ortin J (2006) Structure and function of the influenza virus RNP, In: Y. Kawaoka (ed.), Influenza Virology: Current Topics. Hethersett, United Kingdom: Caister Academic Press. pp. 1–36.
50. Jorba N, Coloma R, Ortín J (2009) Genetic trans-complementation establishes a new model for influenza virus RNA transcription and replication. PLoS Pathog 5: e1000462.
51. Engelhardt OG, Smith M, Fodor E (2005) Association of the influenza A virus RNA-dependent RNA polymerase with cellular RNA polymerase II. J Virol 79: 5812–5818.
52. Poon LL, Pritlove DC, Fodor E, Brownlee GG (1999) Direct evidence that the poly(A) tail of influenza A virus mRNA is synthesized by reiterative copying of a u track in the virion RNA template. J Virol 73: 3473–3476.
53. Zheng H, Lee HA, Palese P, García-Sastre A (1999) Influenza A virus RNA polymerase has the ability to stutter at the polyadenylation site of a viral RNA template during RNA replication. J Virol 73: 5240–5243.
54. York A, Fodor E (2013) Biogenesis, assembly, and export of viral messenger ribonucleoproteins in the influenza A virus infected cell. RNA Biol 10: 1274–1282.
55. Yángüez E, Nieto A (2011) So similar, yet so different: selective translation of capped and polyadenylated viral mRNAs in the influenza virus infected cell. Virus Res 156: 1–12.
56. Nayak DP, Hui EKW, Barman S (2004) Assembly and budding of influenza virus. Virus Res 106: 147–165.
57. Resa-Infante P, Jorba N, Coloma R, Ortin J (2011) The influenza virus RNA synthesis machine: Advances in its structure and function. RNA Biol 8: 207-215.
58. Hay AJ, Lomniczi B, Bellamy AR, Skehel JJ (1977) Transcription of the influenza virus genome. Virology 83: 337–355.
59. Portela A, Digard P (2002) The influenza virus nucleoprotein: a multifunctional RNA-binding protein pivotal to virus replication. J Gen Virol 83: 723–734.

60. Vreede FT, Jung TE, Brownlee GG (2004) Model suggesting that replication of influenza virus is regulated by stabilization of replicative intermediates. J Virol 78: 9568–9572.

61. Beaton AR, Krug RM (1986) Transcription antitermination during influenza viral template RNA synthesis requires the nucleocapsid protein and the absence of a 5' capped end. Proc Natl Acad Sci U S A 83: 6282–6286.

62. Honda A, Uéda K, Nagata K, Ishihama A (1988) RNA polymerase of influenza virus: role of NP in RNA chain elongation. J Biochem 104: 1021–1026.

63. Shapiro GI, Krug RM (1988) Influenza virus RNA replication in vitro: synthesis of viral template RNAs and virion RNAs in the absence of an added primer. J Virol 62: 2285–2290.

64. Medcalf L, Poole E, Elton D, Digard P (1999) Temperature-sensitive lesions in two influenza A viruses defective for replicative transcription disrupt RNA binding by the nucleoprotein. J Virol 73: 7349–7356.

65. Mullin AE, Dalton RM, Amorim MJ, Elton D, Digard P (2004) Increased amounts of the influenza virus nucleoprotein do not promote higher levels of viral genome replication. J Gen Virol 85: 3689–3698.

66. Vreede FT, Brownlee GG (2007) Influenza virion-derived viral ribonucleoproteins synthesize both mRNA and cRNA in vitro. J Virol 81: 2196–2204.

67. Kawaguchi A, Nagata K (2007) De novo replication of the influenza virus RNA genome is regulated by DNA replicative helicase, MCM. EMBO J 26: 4566–4575.

68. Kawaguchi A, Momose F, Nagata K (2011) Replication-coupled and host factor-mediated encapsidation of the influenza virus genome by viral nucleoprotein. J Virol 85: 6197-6204.

69. Bullido R, Gómez-Puertas P, Saiz MJ, Portela A (2001) Influenza A virus NEP (NS2 protein) downregulates RNA synthesis of model template RNAs. J Virol 75: 4912–4917.

70. Robb NC, Smith M, Vreede FT, Fodor E (2009) NS2/NEP protein regulates transcription and replication of the influenza virus RNA genome. J Gen Virol 90: 1398–1407.

71. Paterson D, Fodor E (2012) Emerging roles for the influenza A virus nuclear export protein (NEP). PLoS Pathog 8: e1003019.

72. Reuther P, Giese S, Götz V, Kilb N, Mänz B, et al. (2014) Adaptive mutations in the nuclear export protein of human-derived H5N1 strains facilitate a polymerase activity-enhancing conformation. J Virol 88: 263–271.

73. Perez JT, Varble A, Sachidanandam R, Zlatev I, Manoharan M, et al. (2010) Influenza A virus-generated small RNAs regulate the switch from transcription to replication. Proc Natl Acad Sci U S A 107: 11525–11530.

74. Perez JT, Zlatev I, Aggarwal S, Subramanian S, Sachidanandam R, et al. (2012) A small-RNA enhancer of viral polymerase activity. J Virol 86: 13475–13485.

75. Shapiro GI, Gurney T, Krug RM (1987) Influenza virus gene expression: control mechanisms at early and late times of infection and nuclear-cytoplasmic transport of virus-specific RNAs. J Virol 61: 764–773.

76. Bui M, Wills EG, Helenius A, Whittaker GR (2000) Role of the influenza virus M1 protein in nuclear export of viral ribonucleoproteins. J Virol 74: 1781–1786.

77. Wu CY, Jeng KS, Lai MMC (2011) The SUMOylation of matrix M1 protein modulates the assembly and morphogenesis of influenza A virus. J Virol 85: 6618-6628.

78. Baudin F, Petit I, Weissenhorn W, Ruigrok RW (2001) In vitro dissection of the membrane and RNP binding activities of influenza virus M1 protein. Virology 281: 102–108.

79. Wakefield L, Brownlee GG (1989) RNA-binding properties of influenza A virus matrix protein M1. Nucleic Acids Res 17: 8569–8580.

80. Huang X, Liu T, Muller J, Levandowski RA, Ye Z (2001) Effect of influenza virus matrix protein and viral RNA on ribonucleoprotein formation and nuclear export. Virology 287: 405–416.

81. Cao S, Liu X, Yu M, Li J, Jia X, et al. (2012) A nuclear export signal in the matrix protein of influenza A virus is required for efficient virus replication. J Virol 86: 4883–4891.

82. Elton D, Simpson-Holley M, Archer K, Medcalf L, Hallam R, et al. (2001) Interaction of the influenza virus nucleoprotein with the cellular CRM1-mediated nuclear export pathway. J Virol 75: 408–419.

83. Neumann G, Hughes MT, Kawaoka Y (2000) Influenza A virus NS2 protein mediates vRNP nuclear export through NES-independent interaction with hCRM1. EMBO J 19: 6751–6758.

84. Huang S, Chen J, Chen Q, Wang H, Yao Y, et al. (2013) A second CRM1-dependent nuclear export signal in the influenza A virus NS2 protein contributes to the nuclear export of viral ribonucleoproteins. J Virol 87: 767–778.

85. Akarsu H, Burmeister WP, Petosa C, Petit I, Müller CW, et al. (2003) Crystal structure of the M1 protein-binding domain of the influenza a virus nuclear export protein (NEP/NS2). EMBO J 22: 4646–4655.

86. Shimizu T, Takizawa N, Watanabe K, Nagata K, Kobayashi N (2011) Crucial role of the influenza virus NS2 (NEP) c-terminal domain in M1 binding and nuclear export of vRNP. FEBS Lett 585: 41–46.

87. Mänz B, Brunotte L, Reuther P, Schwemmle M (2012) Adaptive mutations in NEP compensate for defective H5N1 RNA replication in cultured human cells. Nat Commun 3: 802.

88. Brunotte L, Flies J, Bolte H, Reuther P, Vreede F, et al. (2014) The nuclear export protein of H5N1 Influenza A viruses recruits matrix 1 (M1) protein to the viral ribonucleoprotein to mediate nuclear export. J Biol Chem 289: 20067–20077.

89. O'Neill RE, Talon J, Palese P (1998) The influenza virus NEP (NS2 protein) mediates the nuclear export of viral ribonucleoproteins. EMBO J 17: 288–296.

90. Chua MA, Schmid S, Perez JT, Langlois RA, Tenoever BR (2013) Influenza A virus utilizes suboptimal splicing to coordinate the timing of infection. Cell Rep 3: 23–29.

91. Neumann G, Castrucci MR, Kawaoka Y (1997) Nuclear import and export of influenza virus nucleoprotein. J Virol 71: 9690–9700.

92. Nayak DP, Hui EKW (2002) Assembly and morphogenesis of influenza viruses. Recent Res Dev Virol 4: 35-54.

93. Zvonarjev AY, Ghendon YZ (1980) Influence of membrane (M) protein on influenza A virus virion transcriptase activity in vitro and its susceptibility to rimantadine. J Virol 33: 583–586.

94. Hankins RW, Nagata K, Kato A, Ishihama A (1990) Mechanism of influenza virus transcription inhibition by matrix (M1) protein. Res Virol 141: 305–314.

95. Watanabe K, Handa H, Mizumoto K, Nagata K (1996) Mechanism for inhibition of influenza virus RNA polymerase activity by matrix protein. J Virol 70: 241–247.

96. Nasser EH, Judd AK, Sanchez A, Anastasiou D, Bucher DJ (1996) Antiviral activity of influenza virus M1 zinc finger peptides. J Virol 70: 8639–8644.

97. Perez DR, Donis RO (1998) The matrix 1 protein of influenza A virus inhibits the transcriptase activity of a model influenza reporter genome in vivo. Virology 249: 52–61.

98. Rossman JS, Lamb RA (2011) Influenza virus assembly and budding. Virology 411: 229–236.

99. Rodriguez Boulan E, Sabatini DD (1978) Asymmetric budding of viruses in epithelial monlayers: a model system for study of epithelial polarity. Proc Natl Acad Sci U S A 75: 5071–5075.

100. Zhang J, Pekosz A, Lamb RA (2000) Influenza virus assembly and lipid raft microdomains: a role for the cytoplasmic tails of the spike glycoproteins. J Virol 74: 4634–4644.

101. Leser GP, Lamb RA (2005) Influenza virus assembly and budding in raft-derived microdomains: a quantitative analysis of the surface distribution of HA, NA and M2 proteins. Virology 342: 215–227.

102. Schroeder C, Heider H, Möncke-Buchner E, Lin TI (2005) The influenza virus ion channel and maturation cofactor M2 is a cholesterol-binding protein. Eur Biophys J 34: 52–66.

103. Eisfeld AJ, Kawakami E, Watanabe T, Neumann G, Kawaoka Y (2011) RAB11A is essential for influenza genome transport to the plasma membrane. J Virol 85: 6117-6126.

104. Amorim MJ, Bruce EA, Read EKC, Foeglein A, Mahen R, et al. (2011) A Rab11 and microtubule dependent mechanism for cytoplasmic transport of influenza A virus vRNA. J Virol 85: 4143-4156.

105. Ali A, Avalos RT, Ponimaskin E, Nayak DP (2000) Influenza virus assembly: effect of influenza virus glycoproteins on the membrane association of M1 protein. J Virol 74: 8709–8719.

106. Chen BJ, Leser GP, Morita E, Lamb RA (2007) Influenza virus hemagglutinin and neuraminidase, but not the matrix protein, are required for assembly and budding of plasmid-derived virus-like particles. J Virol 81: 7111–7123.

107. Rossman JS, Jing X, Leser GP, Lamb RA (2010) Influenza virus M2 protein mediates ESCRT-independent membrane scission. Cell 142: 902–913.

108. Hutchinson EC, von Kirchbach JC, Gog JR, Digard P (2010) Genome packaging in influenza A virus. J Gen Virol 91: 313–328.

109. Lamb RA, Choppin PW (1983) The gene structure and replication of influenza virus. Annu Rev Biochem 52: 467–506.

110. Enami M, Sharma G, Benham C, Palese P (1991) An influenza virus containing nine different RNA segments. Virology 185: 291–298.

111. Fournier E, Moules V, Essere B, Paillart JC, Sirbat JD, et al. (2012) Interaction network linking the human H3N2 influenza A virus genomic RNA segments. Vaccine 30: 7359–7367.

112. Noda T, Sugita Y, Aoyama K, Hirase A, Kawakami E, et al. (2012) Three-dimensional analysis of ribonucleoprotein complexes in influenza a virus. Nat Commun 3: 639.

113. Duhaut SD, McCauley JW (1996) Defective RNAs inhibit the assembly of influenza virus genome segments in a segment-specific manner. Virology 216: 326–337.

114. Odagiri T, Tashiro M (1997) Segment-specific noncoding sequences of the influenza virus genome RNA are involved in the specific competition between defective interfering RNA and its progenitor RNA segment at the virion assembly step. J Virol 71: 2138–2145.

115. Gavazzi C, Yver M, Isel C, Smyth RP, Rosa-Calatrava M, et al. (2013) A functional sequence-specific interaction between influenza A virus genomic RNA segments. Proc Natl Acad Sci U S A 110: 16604–16609.

116. Chou YY, Vafabakhsh R, Doganay S, Gao Q, Ha T, et al. (2012) One influenza virus particle packages eight unique viral RNAs as shown by fish analysis. Proc Natl Acad Sci U S A 109: 9101–9106.

117. Loregian A, Mercorelli B, Nannetti G, Compagnin C, Palù G (2014) Antiviral strategies against influenza virus: towards new therapeutic approaches. Cell Mol Life Sci 71: 3659–3683.

118. Shaw ML (2011) The host interactome of influenza virus presents new potential targets for antiviral drugs. Rev Med Virol 21: 358–369.

119. Müller KH, Kakkola L, Nagaraj AS, Cheltsov AV, Anastasina M, et al. (2012) Emerging cellular targets for influenza antiviral agents. Trends Pharmacol Sci 33: 89–99.

120. Planz O (2013) Development of cellular signaling pathway inhibitors as new antivirals against influenza. Antiviral Res 98: 457–468.

121. Das K (2012) Antivirals targeting influenza A virus. J Med Chem 55: 6263–6277.

122. Vanderlinden E, Naesens L (2014) Emerging antiviral strategies to interfere with influenza virus entry. Med Res Rev 34: 301–339.

123. Pinto LH, Lamb RA (2007) Controlling influenza virus replication by inhibiting its proton channel. Mol Biosyst 3: 18–23.

124. Steinhauer DA, Wharton SA, Skehel JJ, Wiley DC, Hay AJ (1991) Amantadine selection of a mutant influenza virus containing an acid-stable hemagglutinin glycoprotein: evidence for virus-specific regulation of the pH of glycoprotein transport vesicles. Proc Natl Acad Sci U S A 88: 11525–11529.

125. Moss RB, Davey RT, Steigbigel RT, Fang F (2010) Targeting pandemic influenza: a primer on influenza antivirals and drug resistance. J Antimicrob Chemother 65: 1086–1093.

126. Belser JA, Lu X, Szretter KJ, Jin X, Aschenbrenner LM, et al. (2007) DAS181, a novel sialidase fusion protein, protects mice from lethal avian influenza H5N1 virus infection. J Infect Dis 196: 1493–1499.

127. Moss RB, Hansen C, Sanders RL, Hawley S, Li T, et al. (2012) A phase II study of DAS181, a novel host directed antiviral for the treatment of influenza infection. J Infect Dis 206: 1844–1851.

128. Matrosovich MN, Matrosovich TY, Gray T, Roberts NA, Klenk HD (2004) Neuraminidase is important for the initiation of influenza virus infection in human airway epithelium. J Virol 78: 12665–12667.

129. McKimm-Breschkin JL (2013) Influenza neuraminidase inhibitors: antiviral action and mechanisms of resistance. Influenza Other Respi Viruses 7 Suppl 1: 25–36.

130. Samson M, Pizzorno A, Abed Y, Boivin G (2013) Influenza virus resistance to neuraminidase inhibitors. Antiviral Res 98: 174–185.

131. Furuta Y, Gowen BB, Takahashi K, Shiraki K, Smee DF, et al. (2013) Favipiravir (T-705), a novel viral RNA polymerase inhibitor. Antiviral Res 100: 446–454.

132. Furuta Y, Takahashi K, Fukuda Y, Kuno M, Kamiyama T, et al. (2002) In vitro and in vivo activities of anti-influenza virus compound T-705. Antimicrob Agents Chemother 46: 977–981.

133. Furuta Y, Takahashi K, Kuno-Maekawa M, Sangawa H, Uehara S, et al. (2005) Mechanism of action of T-705 against influenza virus. Antimicrob Agents Chemother 49: 981–986.

134. Bauman JD, Patel D, Baker SF, Vijayan RSK, Xiang A, et al. (2013) Crystallographic fragment screening and structure-based optimization yields a new class of influenza endonuclease inhibitors. ACS Chem Biol 8: 2501–2508.

135. Palù G, Loregian A (2013) Inhibition of herpesvirus and influenza virus replication by blocking polymerase subunit interactions. Antiviral Res 99: 318–327.

136. Ghanem A, Mayer D, Chase G, Tegge W, Frank R, et al. (2007) Peptide-mediated interference with influenza A virus polymerase. J Virol 81: 7801–7804.

137. Wunderlich K, Mayer D, Ranadheera C, Holler AS, Mänz B, et al. (2009) Identification of a PA-binding peptide with inhibitory activity against influenza A and B virus replication. PLoS One 4: e7517.

138. Carter MJ, Mahy BW (1982) Incomplete avian influenza virus contains a defective non-interfering component. Arch Virol 71: 13–25.

139. Marcus PI, Ngunjiri JM, Sekellick MJ (2009) Dynamics of biologically active subpopulations of influenza virus: plaque-forming, noninfectious cell-killing, and defective interfering particles. J Virol 83: 8122–8130.

140. von Magnus P (1954) Incomplete forms of influenza virus. Adv Virus Res 2: 59–79.

141. Huang AS, Baltimore D (1970) Defective viral particles and viral disease processes. Nature 226: 325–327.

142. Huang AS (1973) Defective interfering viruses. Annu Rev Microbiol 27: 101–117.

143. Nayak DP, Chambers TM, Akkina RK (1985) Defective-interfering (DI) RNAs of influenza viruses: origin, structure, expression, and interference. Curr Top Microbiol Immunol 114: 103–151.

144. Marriott AC, Dimmock NJ (2010) Defective interfering viruses and their potential as antiviral agents. Rev Med Virol 20: 51–62.

145. Dimmock NJ, Easton AJ (2014) Defective interfering influenza virus RNAs: Time to reevaluate their clinical potential as broad-spectrum antivirals? J Virol 88: 5217–5227.

146. Saira K, Lin X, DePasse JV, Halpin R, Twaddle A, et al. (2013) Sequence analysis of in vivo defective interfering-like RNA of influenza a H1N1 pandemic virus. J Virol 87: 8064–8074.

147. Jennings PA, Finch JT, Winter G, Robertson JS (1983) Does the higher order structure of the influenza virus ribonucleoprotein guide sequence rearrangements in influenza viral RNA? Cell 34: 619–627.

148. Frensing T, Heldt FS, Pflugmacher A, Behrendt I, Jordan I, et al. (2013) Continuous influenza virus production in cell culture shows a periodic accumulation of defective interfering particles. PLoS One 8: e72288.

149. Davis AR, Nayak DP (1979) Sequence relationships among defective interfering influenza viral RNAs. Proc Natl Acad Sci U S A 76: 3092–3096.

150. Akkina RK, Chambers TM, Nayak DP (1984) Expression of defective-interfering influenza virus-specific transcripts and polypeptides in infected cells. J Virol 51: 395–403.

151. Odagiri T, Tominaga K, Tobita K, Ohta S (1994) An amino acid change in the non-structural NS2 protein of an influenza a virus mutant is responsible for the generation of defective interfering (DI) particles by amplifying DI RNAs and suppressing complementary RNA synthesis. J Gen Virol 75 (Pt 1): 43–53.

152. Widjaja I, de Vries E, Rottier PJM, de Haan CAM (2012) Competition between Influenza A virus genome segments. PLoS One 7: e47529.

153. Giachetti C, Holland JJ (1989) Vesicular stomatitis virus and its defective interfering particles exhibit in vitro transcriptional and replicative competition for purified L-NS polymerase molecules. Virology 170: 264–267.

154. Chanda PK, Chambers TM, Nayak DP (1983) In vitro transcription of defective interfering particles of influenza virus produces polyadenylic acid-containing complementary RNAs. J Virol 45: 55–61.

155. Duhaut SD, Dimmock NJ (2002) Defective segment 1 RNAs that interfere with production of infectious influenza A virus require at least 150 nucleotides of 5' sequence: evidence from a plasmid-driven system. J Gen Virol 83: 403–411.

156. Dimmock NJ, Beck S, McLain L (1986) Protection of mice from lethal influenza: evidence that defective interfering virus modulates the immune response and not virus multiplication. J Gen Virol 67 (Pt 5): 839–850.

157. Noble S, McLain L, Dimmock NJ (2004) Interfering vaccine: a novel antiviral that converts a potentially virulent infection into one that is subclinical and immunizing. Vaccine 22: 3018–3025.

158. Dimmock NJ, Dove BK, Scott PD, Meng B, Taylor I, et al. (2012) Cloned defective interfering influenza virus protects ferrets from pandemic 2009 influenza A virus and allows protective immunity to be established. PLoS One 7: e49394.

159. Dimmock NJ, Dove BK, Meng B, Scott PD, Taylor I, et al. (2012) Comparison of the protection of ferrets against pandemic 2009 influenza A virus (H1N1) by 244 DI influenza virus and oseltamivir. Antiviral Res 96: 376–385.

160. Shaw A (2012) New technologies for new influenza vaccines. Vaccine 30: 4927–4933.

161. Hannoun C (2013) The evolving history of influenza viruses and influenza vaccines. Expert Rev Vaccines 12: 1085–1094.

162. Perdue ML, Arnold F, Li S, Donabedian A, Cioce V, et al. (2011) The future of cell culture-based influenza vaccine production. Expert Rev Vaccines 10: 1183–1194.

163. WHO (1995) Cell culture as a substrate for the production of influenza vaccines: memorandum from a WHO meeting. Bull World Health Organ 73: 431–435.

164. Partridge J, Kieny MP, World Health Organization H1N1 influenza vaccine Task Force (2010) Global production of seasonal and pandemic (H1N1) influenza vaccines in 2009-2010 and comparison with previous estimates and global action plan targets. Vaccine 28: 4709–4712.

165. Genzel Y, Reichl U (2009) Continuous cell lines as a production system for influenza vaccines. Expert Rev Vaccines 8: 1681–1692.

166. Feng SZ, Jiao PR, Qi WB, Fan HY, Liao M (2011) Development and strategies of cell-culture technology for influenza vaccine. Appl Microbiol Biotechnol 89: 893–902.

167. Lohr V, Genzel Y, Behrendt I, Scharfenberg K, Reichl U (2010) A new MDCK suspension line cultivated in a fully defined medium in stirred-tank and wave bioreactor. Vaccine 28: 6256–6264.

168. Lohr V, Genzel Y, Jordan I, Katinger D, Mahr S, et al. (2012) Live attenuated influenza viruses produced in a suspension process with avian AGE1.CR.pIX cells. BMC Biotechnol 12: 79.

169. Genzel Y, Vogel T, Buck J, Behrendt I, Ramirez DV, et al. (2014) High cell density cultivations by alternating tangential flow (ATF) perfusion for influenza A virus production using suspension cells. Vaccine 32: 2770–2781.

170. Genzel Y, Rödig J, Rapp E, Reichl U (2014) Vaccine production: upstream processing with adherent or suspension cell lines. Methods Mol Biol 1104: 371–393.

171. Burleson FG, Chambers TM, Wiedebrauk DL, editors (1992) Virology – A Laboratory Manual. San Diego, CA: Academic Press Inc.

172. Hierholzer JC, Killington RA (1996) Virus Isolation and Quantitation, In: Brian W. J. Mahy and Hillar O. Kangro (ed.), Virology Methods Manual. San Diego, CA: Academic Press Inc., chapter 2. pp. 25–46.

173. Burleson FG, Chambers TM, Wiedebrauk DL (1992) Hemagglutination assay, In: Virology – A Laboratory Manual. San Diego, CA: Academic Press, chapter 18. pp. 86–92.

174. Hatada E, Hasegawa M, Mukaigawa J, Shimizu K, Fukuda R (1989) Control of influenza virus gene expression: quantitative analysis of each viral RNA species in infected cells. J Biochem 105: 537–546.

175. Kawakami E, Watanabe T, Fujii K, Goto H, Watanabe S, et al. (2011) Strand-specific real-time RT-PCR for distinguishing influenza vRNA, cRNA, and mRNA. J Virol Methods 173: 1–6.

176. Schulze-Horsel J, Genzel Y, Reichl U (2008) Flow cytometric monitoring of influenza A virus infection in MDCK cells during vaccine production. BMC Biotechnol 8: 45.

177. Schulze-Horsel J, Schulze M, Agalaridis G, Genzel Y, Reichl U (2009) Infection dynamics and virus-induced apoptosis in cell culture-based influenza vaccine production-Flow cytometry and mathematical modeling. Vaccine 27: 2712-22.

178. Perelson AS (2002) Modelling viral and immune system dynamics. Nat Rev Immunol 2: 28–36.

179. Beauchemin C, Samuel J, Tuszynski J (2005) A simple cellular automaton model for influenza A viral infections. J Theor Biol 232: 223–234.

180. Beauchemin C (2006) Probing the effects of the well-mixed assumption on viral infection dynamics. J Theor Biol 242: 464–477.

181. Lin H, Shuai JW (2010) A stochastic spatial model of HIV dynamics with an asymmetric battle between the virus and the immune system. New Journal of Physics 12: 043051.

182. Mitchell H, Levin D, Forrest S, Beauchemin CAA, Tipper J, et al. (2011) Higher level of replication efficiency of 2009 (H1N1) pandemic influenza virus than those of seasonal and avian strains: kinetics from epithelial cell culture and computational modeling. J Virol 85: 1125–1135.

183. Bauer AL, Beauchemin CAA, Perelson AS (2009) Agent-based modeling of host-pathogen systems: The successes and challenges. Inf Sci (Ny) 179: 1379–1389.

184. Narang V, Decraene J, Wong SY, Aiswarya BS, Wasem AR, et al. (2012) Systems immunology: a survey of modeling formalisms, applications and simulation tools. Immunol Res 53: 251–265.

185. Iwami S, Koizumi Y, Ikeda H, Kakizoe Y (2013) Quantification of viral infection dynamics in animal experiments. Front Microbiol 4: 264.

186. Rong L, Perelson AS (2009) Modeling HIV persistence, the latent reservoir, and viral blips. J Theor Biol 260: 308–331.

187. Alizon S, Magnus C (2012) Modelling the course of an HIV infection: Insights from ecology and evolution. Viruses 4: 1984–2013.

188. Perelson AS, Ribeiro RM (2013) Modeling the within-host dynamics of HIV infection. BMC Biol 11: 96.

189. Perelson AS, Neumann AU, Markowitz M, Leonard JM, Ho DD (1996) HIV-1 dynamics in vivo: virion clearance rate, infected cell life-span, and viral generation time. Science 271: 1582–1586.

190. Perelson A, Nelson P (1999) Mathematical analysis of HIV-1 dynamics in vivo. SIAM Review 41: 3-44.

191. De Boer RJ, Perelson AS (1998) Target cell limited and immune control models of HIV infection: a comparison. J Theor Biol 190: 201–214.

192. Kirschner D, Webb GF, Cloyd M (2000) Model of HIV-1 disease progression based on virus-induced lymph node homing and homing-induced apoptosis of CD4+ lymphocytes. J Acquir Immune Defic Syndr 24: 352–362.

193. Fraser C, Ferguson NM, de Wolf F, Anderson RM (2001) The role of antigenic stimulation and cytotoxic T cell activity in regulating the long-term immunopathogenesis of HIV: mechanisms and clinical implications. Proc Biol Sci 268: 2085–2095.

194. Rosenbloom DIS, Hill AL, Rabi SA, Siliciano RF, Nowak MA (2012) Antiretroviral dynamics determines HIV evolution and predicts therapy outcome. Nat Med 18: 1378–1385.

195. Murray JM, Emery S, Kelleher AD, Law M, Chen J, et al. (2007) Antiretroviral therapy with the integrase inhibitor raltegravir alters decay kinetics of HIV, significantly reducing the second phase. AIDS 21: 2315–2321.

196. Wang S, Rong L (2014) Stochastic population switch may explain the latent reservoir stability and intermittent viral blips in HIV patients on suppressive therapy. J Theor Biol 360C: 137–148.

197. Chatterjee A, Guedj J, Perelson AS (2012) Mathematical modelling of HCV infection: what can it teach us in the era of direct-acting antiviral agents? Antivir Ther 17: 1171–1182.

198. Chatterjee A, Smith PF, Perelson AS (2013) Hepatitis C viral kinetics: the past, present, and future. Clin Liver Dis 17: 13–26.

199. Snoeck E, Chanu P, Lavielle M, Jacqmin P, Jonsson EN, et al. (2010) A comprehensive hepatitis C viral kinetic model explaining cure. Clin Pharmacol Ther 87: 706–713.

200. Guedj J, Perelson AS (2011) Second-phase hepatitis C virus RNA decline during telaprevir-based therapy increases with drug effectiveness: implications for treatment duration. Hepatology 53: 1801–1808.

201. Adiwijaya BS, Kieffer TL, Henshaw J, Eisenhauer K, Kimko H, et al. (2012) A viral dynamic model for treatment regimens with direct-acting antivirals for chronic hepatitis C infection. PLoS Comput Biol 8: e1002339.

202. Guedj J, Neumann AU (2010) Understanding hepatitis C viral dynamics with direct-acting antiviral agents due to the interplay between intracellular replication and cellular infection dynamics. J Theor Biol 267: 330–340.

203. Guedj J, Dahari H, Rong L, Sansone ND, Nettles RE, et al. (2013) Modeling shows that the NS5A inhibitor daclatasvir has two modes of action and yields a shorter estimate of the hepatitis C virus half-life. Proc Natl Acad Sci U S A 110: 3991–3996.

204. Holder BP, Beauchemin CAA (2011) Exploring the effect of biological delays in kinetic models of influenza within a host or cell culture. BMC Public Health 11 Suppl 1: S10.

205. Lloyd AL (2001) The dependence of viral parameter estimates on the assumed viral life cycle: limitations of studies of viral load data. Proc Biol Sci 268: 847–854.

206. Baccam P, Beauchemin C, Macken CA, Hayden FG, Perelson AS (2006) Kinetics of influenza A virus infection in humans. J Virol 80: 7590–7599.

207. Larson EW, Dominik JW, Rowberg AH, Higbee GA (1976) Influenza virus population dynamics in the respiratory tract of experimentally infected mice. Infect Immun 13: 438–447.

208. Bocharov GA, Romanyukha AA (1994) Mathematical model of antiviral immune response. III. influenza a virus infection. J Theor Biol 167: 323–360.

209. Saenz RA, Quinlivan M, Elton D, Macrae S, Blunden AS, et al. (2010) Dynamics of influenza virus infection and pathology. J Virol 84: 3974–3983.

210. Dobrovolny HM, Reddy MB, Kamal MA, Rayner CR, Beauchemin CAA (2013) Assessing mathematical models of influenza infections using features of the immune response. PLoS One 8: e57088.

211. Handel A, Longini IM, Antia R (2010) Towards a quantitative understanding of the within-host dynamics of influenza A infections. J R Soc Interface 7: 35–47.

212. Tridane A, Kuang Y (2010) Modeling the interaction of cytotoxic t lymphocytes and influenza virus infected epithelial cells. Math Biosci Eng 7: 171–185.

213. Wu H, Kumar A, Miao H, Holden-Wiltse J, Mosmann TR, et al. (2011) Modeling of influenza-specific CD4+ T cells during the primary response indicates that the spleen is a major source of effectors. J Immunol 187: 4474–4482.

214. Pawelek KA, Huynh GT, Quinlivan M, Cullinane A, Rong L, et al. (2012) Modeling within-host dynamics of influenza virus infection including immune responses. PLoS Comput Biol 8: e1002588.

215. Hancioglu B, Swigon D, Clermont G (2007) A dynamical model of human immune response to influenza A virus infection. J Theor Biol 246: 70–86.

216. Miao H, Hollenbaugh JA, Zand MS, Holden-Wiltse J, Mosmann TR, et al. (2010) Quantifying the early immune response and adaptive immune response kinetics in mice infected with influenza A virus. J Virol 84: 6687–6698.

217. Beauchemin CAA, McSharry JJ, Drusano GL, Nguyen JT, Went GT, et al. (2008) Modeling amantadine treatment of influenza A virus in vitro. J Theor Biol 254: 439–451.

218. Handel A, Longini IM, Antia R (2007) Neuraminidase inhibitor resistance in influenza: assessing the danger of its generation and spread. PLoS Comput Biol 3: e240.

219. Dobrovolny HM, Gieschke R, Davies BE, Jumbe NL, Beauchemin CAA (2011) Neuraminidase inhibitors for treatment of human and avian strain influenza: A comparative modeling study. J Theor Biol 269: 234–244.

220. Perelson AS, Rong L, Hayden FG (2012) Combination antiviral therapy for influenza: predictions from modeling of human infections. J Infect Dis 205: 1642–1645.

221. Holder BP, Simon P, Liao LE, Abed Y, Bouhy X, et al. (2011) Assessing the in vitro fitness of an oseltamivir-resistant seasonal A/H1N1 influenza strain using a mathematical model. PLoS One 6: e14767.

222. Möhler L, Flockerzi D, Sann H, Reichl U (2005) Mathematical model of influenza A virus production in large-scale microcarrier culture. Biotechnol Bioeng 90: 46–58.

223. Sidorenko Y, Schulze-Horsel J, Voigt A, Reichl U, Kienle A (2008) Stochastic population balance modeling of influenza virus replication in vaccine production processes. Chemical Engineering Science 63: 157-169.

224. Sidorenko Y, Voigt A, Schulze-Horsel J, Reichl U, Kienle A (2008) Stochastic population balance modeling of influenza virus replication in vaccine production processes. II. detailed description of the replication mechanism. Chemical Engineering Science 63: 2299-2304.

225. Müller T, Dürr R, Isken B, Schulze-Horsel J, Reichl U, et al. (2013) Distributed modeling of human influenza A virus-host cell interactions during vaccine production. Biotechnol Bioeng 110: 2252–2266.

226. Pinilla LT, Holder BP, Abed Y, Boivin G, Beauchemin CAA (2012) The H275Y neuraminidase mutation of the pandemic A/H1N1 influenza virus lengthens the eclipse phase and reduces viral output of infected cells, potentially compromising fitness in ferrets. J Virol 86: 10651–10660.

227. Dee KU, Hammer DA, Shuler ML (1995) A model of the binding, entry, uncoating, and RNA synthesis of semliki forest virus in baby hamster kidney (BHK-21) cells. Biotechnol Bioeng 46: 485–496.

228. Dee KU, Shuler ML (1997) A mathematical model of the trafficking of acid-dependent enveloped viruses: application to the binding, uptake, and nuclear accumulation of baculovirus. Biotechnol Bioeng 54: 468–490.

229. Endy D, Kong D, Yin J (1997) Intracellular kinetics of a growing virus: A genetically structured simulation for bacteriophage T7. Biotechnol Bioeng 55: 375–389.

230. Lim KI, Lang T, Lam V, Yin J (2006) Model-based design of growth-attenuated viruses. PLoS Comput Biol 2: e116.

231. Hensel SC, Rawlings JB, Yin J (2009) Stochastic kinetic modeling of vesicular stomatitis virus intracellular growth. Bull Math Biol 71: 1671–1692.

232. Reddy B, Yin J (1999) Quantitative intracellular kinetics of HIV type 1. AIDS Res Hum Retroviruses 15: 273–283.

233. Nakabayashi J, Sasaki A (2011) A mathematical model of the intracellular replication and within host evolution of hepatitis type B virus: Understanding the long time course of chronic hepatitis. J Theor Biol 269: 318–329.

234. Dahari H, Ribeiro RM, Rice CM, Perelson AS (2007) Mathematical modeling of subgenomic hepatitis C virus replication in Huh-7 cells. J Virol 81: 750–760.

235. McLean AK, Luciani F, Tanaka MM (2010) Trade-offs in resource allocation in the intracellular life-cycle of hepatitis C virus. J Theor Biol 267: 565–572.

236. Nakabayashi J (2012) A compartmentalization model of hepatitis C virus replication: an appropriate distribution of HCV RNA for the effective replication. J Theor Biol 300: 110–117.

237. Binder M, Sulaimanov N, Clausznitzer D, Schulze M, Hüber CM, et al. (2013) Replication vesicles are load- and choke-points in the hepatitis C virus lifecycle. PLoS Pathog 9: e1003561.

238. Haseltine E, Rawlings J, Yin J (2005) Dynamics of viral infections: incorporating both the intracellular and extracellular levels. Computers & chemical engineering 29: 675-686.

239. Haseltine EL, Yin J, Rawlings JB (2008) Implications of decoupling the intracellular and extracellular levels in multi-level models of virus growth. Biotechnol Bioeng 101: 811–820.

240. Rong L, Guedj J, Dahari H, Coffield DJ Jr, Levi M, et al. (2013) Analysis of hepatitis C virus decline during treatment with the protease inhibitor danoprevir using a multiscale model. PLoS Comput Biol 9: e1002959.

241. Rong L, Perelson AS (2013) Mathematical analysis of multiscale models for hepatitis C virus dynamics under therapy with direct-acting antiviral agents. Math Biosci 245: 22–30.

242. Murillo LN, Murillo MS, Perelson AS (2013) Towards multiscale modeling of influenza infection. J Theor Biol 332: 267–290.

243. Handel A, Brown J, Stallknecht D, Rohani P (2013) A multi-scale analysis of influenza A virus fitness trade-offs due to temperature-dependent virus persistence. PLoS Comput Biol 9: e1002989.

244. Gillespie DT (2007) Stochastic simulation of chemical kinetics. Annu Rev Phys Chem 58: 35–55.

245. Raue A, Kreutz C, Maiwald T, Bachmann J, Schilling M, et al. (2009) Structural and practical identifiability analysis of partially observed dynamical models by exploiting the profile likelihood. Bioinformatics 25: 1923-9.

246. van Riel NAW (2006) Dynamic modelling and analysis of biochemical networks: mechanism-based models and model-based experiments. Brief Bioinform 7: 364–374.

247. Gutenkunst RN, Waterfall JJ, Casey FP, Brown KS, Myers CR, et al. (2007) Universally sloppy parameter sensitivities in systems biology models. PLoS Comput Biol 3: 1871–1878.

248. Joshi M, Seidel-Morgenstern A, Kremling A (2006) Exploiting the bootstrap method for quantifying parameter confidence intervals in dynamical systems. Metab Eng 8: 447–455.

249. Efron B, Tibshirani R (1986) Bootstrap methods for standard errors, confidence intervals, and other measures of statistical accuracy. Statistical Science 1: pp. 54-75.

250. Heldt FS, Frensing T, Reichl U (2012) Modeling the intracellular dynamics of influenza virus replication to understand the control of viral RNA synthesis. J Virol 86: 7806–7817.

251. Nunes-Correia I, Ramalho-Santos J, Nir S, de Lima MCP (1999) Interactions of influenza virus with cultured cells: detailed kinetic modeling of binding and endocytosis. Biochemistry 38: 1095–1101.

252. Glick GD, Toogood PL, Wiley DC, Skehel JJ, Knowles JR (1991) Ligand recognition by influenza virus. the binding of bivalent sialosides. J Biol Chem 266: 23660–23669.

253. Koff WC, Knight V (1979) Inhibition of influenza virus uncoating by rimantadine hydrochloride. J Virol 31: 261–263.

254. Duesberg PH (1969) Distinct subunits of the ribonucleoprotein of influenza virus. J Mol Biol 42: 485–499.

255. Enami M, Fukuda R, Ishihama A (1985) Transcription and replication of eight RNA segments of influenza virus. Virology 142: 68–77.

256. Inglis SC, Mahy BW (1979) Polypeptides specified by the influenza virus genome. 3. control of synthesis in infected cells. Virology 95: 154–164.

257. Huang IC, Li W, Sui J, Marasco W, Choe H, et al. (2008) Influenza A virus neuraminidase limits viral superinfection. J Virol 82: 4834–4843.

258. York A, Hengrung N, Vreede FT, Huiskonen JT, Fodor E (2013) Isolation and characterization of the positive-sense replicative intermediate of a negative-strand RNA virus. Proc Natl Acad Sci U S A 110: E4238–E4245.

259. Cohen S, Hindmarsh A (1996) CVODE, a stiff/nonstiff ODE solver in C. Computers in Physics 10: 138-43.

260. Schmidt H, Jirstrand M (2006) Systems biology toolbox for matlab: a computational platform for research in systems biology. Bioinformatics 22: 514–515.

261. Egea JA, Rodriguez-Fernandez M, Banga JR, Marti R (2007) Scatter search for chemical and bio-process optimization. J Global Optim 37: 481-503.

262. Dorl S (2013) Stochastic modelling of the intracellular replication of influenza virus during vaccine production. Bachelor thesis, Faculty for Process and Systems Engineering, Otto von Guericke University, Magdeburg.

263. McCollum JM, Peterson GD, Cox CD, Simpson ML, Samatova NF (2006) The sorting direct method for stochastic simulation of biochemical systems with varying reaction execution behavior. Comput Biol Chem 30: 39–49.

264. Cao Y, Gillespie DT, Petzold LR (2006) Efficient step size selection for the tau-leaping simulation method. J Chem Phys 124: 044109.

265. Elowitz MB, Levine AJ, Siggia ED, Swain PS (2002) Stochastic gene expression in a single cell. Science 297: 1183–1186.

266. Heldt FS, Frensing T, Pflugmacher A, Gröpler R, Peschel B, et al. (2013) Multiscale modeling of influenza A virus infection supports the development of direct-acting antivirals. PLoS Comput Biol 9: e1003372.

267. Isken B, Genzel Y, Reichl U (2012) Productivity, apoptosis, and infection dynamics of influenza A/PR/8 strains and /PR/8-based reassortants. Vaccine 30: 5253–5261.

268. Kalbfuss B, Knöchlein A, Kröber T, Reichl U (2008) Monitoring influenza virus content in vaccine production: precise assays for the quantitation of hemagglutination and neuraminidase activity. Biologicals 36: 145–161.

269. Kaffka H (2013) Model-based analysis of the influence of defective interfering particles on influenza virus replication. Bachelor thesis, Faculty for Process and Systems Engineering, Otto von Guericke University, Magdeburg.

270. Dulbecco R, Vogt M (1954) Plaque formation and isolation of pure lines with poliomyelitis viruses. J Exp Med 99: 167–182.

271. Kirkwood TB, Bangham CR (1994) Cycles, chaos, and evolution in virus cultures: a model of defective interfering particles. Proc Natl Acad Sci U S A 91: 8685–8689.

272. Stegmann T, Schoen P, Bron R, Wey J, Bartoldus I, et al. (1993) Evaluation of viral membrane fusion assays. comparison of the octadecylrhodamine dequenching assay with the pyrene excimer assay. Biochemistry 32: 11330–11337.

273. Vreede FT, Ng AKL, Shaw PC, Fodor E (2011) Stabilisation of influenza virus replication intermediates is dependent on the RNA-binding but not the homo-oligomerisation activity of the viral nucleoprotein. J Virol 85: 12073-12078.

274. Kummer S, Flöttmann M, Schwanhäusser B, Sieben C, Veit M, et al. (2014) Alteration of protein levels during influenza virus H1N1 infection in host cells: a proteomic survey of host and virus reveals differential dynamics. PLoS One 9: e94257.

275. Sidorenko Y (2005) Mathematische Modellierung von Influenza Virus Replikation in Säugerzellen. Ph.D. thesis, Faculty of Process and Systems Engineering, Otto von Guericke University Magdeburg.

276. Yoshimura A, Kuroda K, Kawasaki K, Yamashina S, Maeda T, et al. (1982) Infectious cell entry mechanism of influenza virus. J Virol 43: 284–293.

277. Chase GP, Rameix-Welti MA, Zvirbliene A, Zvirblis G, Götz V, et al. (2011) Influenza virus ribonucleoprotein complexes gain preferential access to cellular export machinery through chromatin targeting. PLoS Pathog 7: e1002187.

278. Wu MS, Yen HR, Chang CW, Peng TY, Hsieh CF, et al. (2011) Mechanism of action of the suppression of influenza virus replication by Ko-Ken Tang through inhibition of the phosphatidylinositol 3-kinase/Akt signaling pathway and viral RNP nuclear export. J Ethnopharmacol 134: 614-623.

279. Watanabe T, Watanabe S, Kawaoka Y (2010) Cellular networks involved in the influenza virus life cycle. Cell Host Microbe 7: 427–439.

280. Vreede FT, Chan AY, Sharps J, Fodor E (2010) Mechanisms and functional implications of the degradation of host RNA polymerase II in influenza virus infected cells. Virology 396: 125–134.

281. Srivastava R, You L, Summers J, Yin J (2002) Stochastic vs. deterministic modeling of intracellular viral kinetics. J Theor Biol 218: 309–321.

282. Zhu Y, Yongky A, Yin J (2009) Growth of an RNA virus in single cells reveals a broad fitness distribution. Virology 385: 39–46.

283. Timm A, Yin J (2012) Kinetics of virus production from single cells. Virology 424: 11–17.

284. Schulte MB, Andino R (2014) Single-cell analysis uncovers extensive biological noise in poliovirus replication. J Virol 88: 6205–6212.

285. Delbrück M (1945) The burst size distribution in the growth of bacterial viruses (bacteriophages). J Bacteriol 50: 131–135.

286. Furusawa C, Suzuki T, Kashiwagi A, Yomo T, Kaneko K (2005) Ubiquity of log-normal distributions in intra-cellular reaction dynamics. Biophysics 1: 25-31.

287. Becskei A, Serrano L (2000) Engineering stability in gene networks by autoregulation. Nature 405: 590–593.

288. Lestas I, Vinnicombe G, Paulsson J (2010) Fundamental limits on the suppression of molecular fluctuations. Nature 467: 174–178.

289. Delbrück M (1940) Statistical fluctuations in autocatalytic reactions. The Journal of Chemical Physics 8: 120-124.

290. Brooke CB, Ince WL, Wrammert J, Ahmed R, Wilson PC, et al. (2013) Most influenza A virions fail to express at least one essential viral protein. J Virol 87: 3155–3162.

291. Brooke CB (2014) Biological activities of 'noninfectious' influenza A virus particles. Future Virol 9: 41–51.

292. Pahle J (2009) Biochemical simulations: stochastic, approximate stochastic and hybrid approaches. Brief Bioinform 10: 53–64.

293. Skehel JJ, Hay AJ, Armstrong JA (1978) On the mechanism of inhibition of influenza virus replication by amantadine hydrochloride. J Gen Virol 38: 97–110.

294. Hastings JC, Selnick H, Wolanski B, Tomassini JE (1996) Anti-influenza virus activities of 4-substituted 2,4-dioxobutanoic acid inhibitors. Antimicrob Agents Chemother 40: 1304–1307.

295. Kiso M, Takahashi K, Sakai-Tagawa Y, Shinya K, Sakabe S, et al. (2010) T-705 (favipiravir) activity against lethal H5N1 influenza A viruses. Proc Natl Acad Sci U S A 107: 882–887.

296. Muratore G, Goracci L, Mercorelli B, Ágnes Foeglein, Digard P, et al. (2012) Small molecule inhibitors of influenza A and b viruses that act by disrupting subunit interactions of the viral polymerase. Proc Natl Acad Sci U S A 109: 6247–6252.

297. Smith AM, Ribeiro RM (2010) Modeling the viral dynamics of influenza A virus infection. Crit Rev Immunol 30: 291–298.

298. Smith AM, Adler FR, McAuley JL, Gutenkunst RN, Ribeiro RM, et al. (2011) Effect of 1918 PB1-F2 expression on influenza A virus infection kinetics. PLoS Comput Biol 7: e1001081.

299. Akkina RK, Chambers TM, Nayak DP (1984) Mechanism of interference by defective-interfering particles of influenza virus: Differential reduction of intracellular synthesis of specific polymerase proteins. Virus Research 1: 687 - 702.

300. Nayak DP, Tobita K, Janda JM, Davis AR, De BK (1978) Homologous interference mediated by defective interfering influenza virus derived from a temperature-sensitive mutant of influenza virus. J Virol 28: 375–386.

301. Harrison DEF, Topiwala HH (1974) Transient and oscillatory states of continuous culture. In: Advances in Biochemical Engineering, Volume 3, Springer Berlin Heidelberg. pp. 167-219. doi:10.1007/3-540-06546-6_6.

302. Agrawal P, Lee C, Lim H, Ramkrishna D (1982) Theoretical investigations of dynamic behavior of isothermal continuous stirred tank biological reactors. Chemical Engineering Science 37: 453-462.

303. Bangham CR, Kirkwood TB (1990) Defective interfering particles: effects in modulating virus growth and persistence. Virology 179: 821–826.

304. Zwart MP, Pijlman GP, Sardanyés J, Duarte J, Januário C, et al. (2013) Complex dynamics of defective interfering baculoviruses during serial passage in insect cells. J Biol Phys 39: 327–342.

305. von Magnus P (1965) The in ovo production of incomplete virus by B-Lee and A-PR8 influenza viruses. Arch Gesamte Virusforsch 17: 414–423.

306. Gooijer CDD, Koken RH, Lier FLV, Kool M, Vlak JM, et al. (1992) A structured dynamic model for the baculovirus infection process in insect-cell reactor configurations. Biotechnol Bioeng 40: 537–548.

307. Stauffer-Thompson KA, Rempala GA, Yin J (2009) Multiple-hit inhibition of infection by defective interfering particles. J Gen Virol 90: 888–899.

308. Palma EL, Huang A (1974) Cyclic production of vesicular stomatitis virus caused by defective interfering particles. J Infect Dis 129: 402–410.

309. Stauffer-Thompson KA, Yin J (2010) Population dynamics of an RNA virus and its defective interfering particles in passage cultures. Virol J 7: 257.

310. Kompier R, Tramper J, Vlak J (1988) A continuous process for the production of baculovirus using insect-cell cultures. Biotechnology Letters 10: 849-854.

311. van Lier F, van der Meijs W, Grobben N, Olie R, Vlak J, et al. (1992) Continuous beta-galactosidase production with a recombinant baculovirus insect-cell system in bioreactors. Journal of Biotechnology 22: 291 - 298.

312. Kool M, Voncken J, Lier FV, Tramper J, Vlak J (1991) Detection and analysis of autographa californica nuclear polyhedrosis virus mutants with defective interfering properties. Virology 183: 739 - 746.

313. Arava Y, Wang Y, Storey JD, Liu CL, Brown PO, et al. (2003) Genome-wide analysis of mRNA translation profiles in Saccharomyces cerevisiae. Proc Natl Acad Sci U S A 100: 3889–3894.

314. Robb NC, Jackson D, Vreede FT, Fodor E (2010) Splicing of influenza A virus NS1 mRNA is independent of the viral NS1 protein. J Gen Virol 91: 2331–2340.

315. Spirin AS (1986) Ribosome structure and protein biosynthesis. Benjamin/Cummings Pub. Co., Advanced Book Program, Menlo Park, CA.

Appendix A

Intracellular virus replication

This chapter provides additional information on the intracellular model of influenza A virus replication. It covers the deterministic implementation first and then presents supplements to the stochastic model.

A.1. Deterministic model

Here, we summarize all parameter values and initial conditions used to simulate the deterministic model of influenza A virus replication at the intracellular level.

Table A.1.: List of parameters for the deterministic intracellular model.

Parameter		**Value**	**Source, Reference, Comment**
$B_{\mathrm{hi}}^{\mathrm{tot}}$	(sites)	150	[251]
$B_{\mathrm{lo}}^{\mathrm{tot}}$	(sites)	1 000	[251]
D_{Rib}	(nucleotides)	160	[313]
F_{Fus}	(–)	0.51	Figure 4.2A
F_{Spl_7}	(–)	0.02	Ratio of M2 to M1 in virion
F_{Spl_8}	(–)	0.125	[314]
K_{swt}	(molecules/cell)	5.89×10^{11}	Figure 4.6
K_{VRel}	(virions)	10	Adjusted
$k_{\mathrm{hi}}^{\mathrm{Att}}$	$(\mathrm{site} \cdot \mathrm{h})^{-1}$	8.09×10^{-2}	Adjusted to data in [251]
$k_{\mathrm{lo}}^{\mathrm{Att}}$	$(\mathrm{site} \cdot \mathrm{h})^{-1}$	4.55×10^{-4}	Adjusted to data in [251]
$k_{\mathrm{M1}}^{\mathrm{Bind}}$	$(\mathrm{molecule} \cdot \mathrm{h})^{-1}$	1.39×10^{-6}	Figure 4.5A and B
$k_{\mathrm{NP}}^{\mathrm{Bind}}$	$(\mathrm{molecule} \cdot \mathrm{h})^{-1}$	3.01×10^{-4}	Figure 4.3B–D
$k_{\mathrm{RdRp}}^{\mathrm{Bind}}$	$(\mathrm{molecule} \cdot \mathrm{h})^{-1}$	1	Figure 4.3B–D
$k_{\mathrm{M}}^{\mathrm{Deg}}$	(h^{-1})	0.33	Figure 4.3B–D
$k_{\mathrm{R}}^{\mathrm{Deg}}$	(h^{-1})	36.36	Figure 4.3B–D
$k_{\mathrm{Rnp}}^{\mathrm{Deg}}$	(h^{-1})	0.09	Figure 4.5A and B

Parameter		**Value**	**Source**
$k^{\text{Deg}}_{\text{RRdRp}}$	(h^{-1})	4.25	Figure 4.3B–D
k^{En}	(h^{-1})	4.8	Figure 4.2A
$k^{\text{Eq}}_{\text{hi}}$	(site^{-1})	1.13×10^{-2}	[251]
$k^{\text{Eq}}_{\text{lo}}$	(site^{-1})	8.33×10^{-5}	[251]
k^{Exp}	$(\text{molecule} \cdot \text{h})^{-1}$	1×10^{-6}	Adjusted to data in [104]
k^{Fus}	(h^{-1})	3.21	Figure 4.2A
k^{Imp}	(h^{-1})	6	[48]
k^{RdRp}	($\text{molecule}^{-2} \cdot \text{h}^{-1}$)	1	Rapid complex formation assumed
k^{Rel}	($\text{virions}/(\text{molecule} \cdot \text{h})$)	3.7×10^{-3}	Cell releases 10^4 virions in 12 h
$k^{\text{Res}}_{\text{C}}$	(h^{-1})	0.03	Figure 4.4A
$k^{\text{Syn}}_{\text{C}}$	(h^{-1})	1.38	Figure 4.5A and B
$k^{\text{Syn}}_{\text{M}}$	(nucleotides/h)	2.5×10^5	Figure 4.5A and B
$k^{\text{Syn}}_{\text{P}}$	(nucleotides/h)	64 800	[315]
$k^{\text{Syn}}_{\text{V}}$	(h^{-1})	13.86	Figure 4.5A and B
L_1	(nucleotides)	2 320	[25]
L_2	(nucleotides)	2 320	[25]
L_3	(nucleotides)	2 211	[25]
L_4	(nucleotides)	1 757	[25]
L_5	(nucleotides)	1 540	[25]
L_6	(nucleotides)	1 392	[25]
L_7	(nucleotides)	1 005	[25]
L_8	(nucleotides)	868	[25]
L^{V}	(nucleotides)	1 700	Based on [25]
$N_{\text{P}_{\text{HA}}}$	(molecules/virion)	500	[25]
$N_{\text{P}_{\text{M1}}}$	(molecules/virion)	3 000	[25]
$N_{\text{P}_{\text{M2}}}$	(molecules/virion)	40	[25]
$N_{\text{P}_{\text{NA}}}$	(molecules/virion)	100	[25]
$N_{\text{P}_{\text{NP}}}$	(molecules/virion)	1 000	[25]
$N_{\text{P}_{\text{NEP}}}$	(molecules/virion)	165	[25]
$N_{\text{P}_{\text{RdRp}}}$	(molecules/virion)	45	[25]
$N^{\text{Nuc}}_{\text{M1}}$	(nucleotides)	200	[79]
$N^{\text{Nuc}}_{\text{NEP}}$	(nucleotides)	1 700	Adjusted to [59]
$N^{\text{Nuc}}_{\text{NP}}$	(nucleotides)	24	[59]

Table A.2.: Initial conditions and parameter changes (compared to Table A.1) used to simulate the stabilization model.

Figure	Non-zero initial conditions	Parameter changes
Figure 4.1A	$V^{\mathrm{Ex}} = 2460$	$k^{\mathrm{En}} = 0$
Figure 4.1B	$V^{\mathrm{Ex}} = 0 - 1.5 \times 10^4$	$k^{\mathrm{En}} = 0$
Figure 4.2A	$V^{\mathrm{Att}}_{\mathrm{hi}} = 100$	
Figure 4.2B	$V^{\mathrm{Ex}} = 10$	$k^{\mathrm{Deg}}_{\mathrm{Rnp}} = 0$, $k^{\mathrm{Syn}}_{\mathrm{P}} = 0$
Figure 4.3A	$Vp^{\mathrm{nuc}} = 8$	$k^{\mathrm{Deg}}_{\mathrm{M}} = 0.37$, $k^{\mathrm{Deg}}_{\mathrm{R}} = 0.06$, $k^{\mathrm{Deg}}_{\mathrm{Rnp}} = 0$, $k^{\mathrm{Syn}}_{\mathrm{C}} = 0.03$, $k^{\mathrm{Syn}}_{\mathrm{M}} = 350$, $k^{\mathrm{Syn}}_{\mathrm{P}} = 0$
Figure 4.3B	$V^{\mathrm{Att}}_{\mathrm{hi}} = 5$, $P_{\mathrm{PA}} = 10^4$, $P_{\mathrm{PB2}} = 10^4$, $P_{\mathrm{NP}} = 10^4$	$F_{\mathrm{Fus}} = 1$, $k^{\mathrm{Deg}}_{\mathrm{Rnp}} = 0$, $k^{\mathrm{Eq}}_{\mathrm{hi}} = 10^8$, $k^{\mathrm{Syn}}_{\mathrm{C}} = 0.76$, $k^{\mathrm{Syn}}_{\mathrm{M}} = 1630$, $k^{\mathrm{Syn}}_{\mathrm{P}} = 0$, $k^{\mathrm{Syn}}_{\mathrm{V}} = 0$
Figure 4.3C	$V^{\mathrm{Att}}_{\mathrm{hi}} = 5$, $P_{\mathrm{RdRp}} = 10^4$, $P_{\mathrm{NP}} = 10^4$	Same as for Figure 4.3B
Figure 4.3D	$V^{\mathrm{Att}}_{\mathrm{hi}} = 5$, $P_{\mathrm{RdRp}} = b \cdot 10^4$, $P_{\mathrm{NP}} = b \cdot 10^4$, $b = [0, 1, 2, 4] \widehat{=} [-, +, ++, ++++]$	Same as for Figure 4.3B
Figure 4.5	$V^{\mathrm{Att}}_{\mathrm{hi}} = 10$	$k^{\mathrm{Eq}}_{\mathrm{hi}} = 10^8$
Figure 4.7	$V^{\mathrm{Att}}_{\mathrm{hi}} = 10$	$k^{\mathrm{Eq}}_{\mathrm{hi}} = 10^8$
Figure 4.8	$V^{\mathrm{Ex}} = 10$	Perturbation by 15%

Table A.3.: Initial conditions and parameter changes (compared to Table A.1) used to simulate the switching model.

Figure	Non-zero initial conditions	Parameter changes
Figure 4.4A	$Vp^{\mathrm{nuc}} = 8$	$k^{\mathrm{Deg}}_{\mathrm{M}} = 0.37$, $k^{\mathrm{Deg}}_{\mathrm{R}} = 0.06$, $k^{\mathrm{Deg}}_{\mathrm{Rnp}} = 0$, $k^{\mathrm{Res}}_{\mathrm{C}} = 0.03$, $k^{\mathrm{Syn}}_{\mathrm{M}} = 350$, $k^{\mathrm{Syn}}_{\mathrm{P}} = 0$
Figure 4.4B	$V^{\mathrm{Att}}_{\mathrm{hi}} = 5$, $P_{\mathrm{PA}} = 10^4$, $P_{\mathrm{PB2}} = 10^4$, $P_{\mathrm{NP}} = 10^4$	$F_{\mathrm{Fus}} = 1$, $K_{\mathrm{swt}} = 8.85 \times 10^6$, $k^{\mathrm{Deg}}_{\mathrm{M}} = 0.34$, $k^{\mathrm{Deg}}_{\mathrm{R}} = 0.92$, $k^{\mathrm{Deg}}_{\mathrm{Rnp}} = 0$, $k^{\mathrm{Eq}}_{\mathrm{hi}} = 10^8$, $k^{\mathrm{Res}}_{\mathrm{C}} = 0.35$, $k^{\mathrm{Syn}}_{\mathrm{M}} = 1.63 \times 10^3$, $k^{\mathrm{Syn}}_{\mathrm{C}} = 152$, $k^{\mathrm{Syn}}_{\mathrm{P}} = 0$, $k^{\mathrm{Syn}}_{\mathrm{V}} = 0$
Figure 4.4C	$V^{\mathrm{Att}}_{\mathrm{hi}} = 5$, $P_{\mathrm{RdRp}} = 10^4$, $P_{\mathrm{NP}} = 10^4$	Same as for Figure 4.4B
Figure 4.4D	$V^{\mathrm{Att}}_{\mathrm{hi}} = 5$, $P_{\mathrm{RdRp}} = b \cdot 10^4$, $P_{\mathrm{NP}} = b \cdot 10^4$, $b = [0, 1, 2, 4] \widehat{=} [-, +, ++, ++++]$	Same as for Figure 4.4B
Figure 4.6	$V^{\mathrm{Att}}_{\mathrm{hi}} = 10$	$k^{\mathrm{Eq}}_{\mathrm{hi}} = 10^8$, $k^{\mathrm{Syn}}_{\mathrm{M}} = 1.79 \times 10^5$, $k^{\mathrm{Deg}}_{\mathrm{R}} = 0.28$, $k^{\mathrm{Syn}}_{\mathrm{C}} = 727$, $k^{\mathrm{Syn}}_{\mathrm{V}} = 603$, $k^{\mathrm{Bind}}_{\mathrm{M1}} = 1.48 \times 10^{-6}$

Table A.4.: Parameter estimates for the transition from transcription to genome replication based on a model that accounts for the switching hypothesis.

Parameter		**Value**		**Local sensitivity**	
		in vitro[a]	**cell culture**[b]	***in vitro***[a]	**cell culture**[b]
K_{swt}	(molecules/cell)	–	8.85×10^{6}	–	3.06×10^{-2}
$k_{\mathrm{NP}}^{\mathrm{Bind}}$	$(\mathrm{molecule} \cdot \mathrm{h})^{-1}$	–	3.01×10^{-4}[c]	–	1.62×10^{-5}
$k_{\mathrm{RdRp}}^{\mathrm{Bind}}$	$(\mathrm{molecule} \cdot \mathrm{h})^{-1}$	–	1[c]	–	5.23×10^{-12}
$k_{\mathrm{M}}^{\mathrm{Deg}}$	(h^{-1})	0.37	0.34	0.13	1.44×10^{-2}
$k_{\mathrm{R}}^{\mathrm{Deg}}$	(h^{-1})	0.06	0.92	1.76×10^{-2}	4.54×10^{-2}
$k_{\mathrm{C}}^{\mathrm{Res}}$	(h^{-1})	0.03	0.35	8.78×10^{-2}	3.93×10^{-2}
$k_{\mathrm{C}}^{\mathrm{Syn}}$	(h^{-1})	–	152	–	3.14×10^{-2}
$k_{\mathrm{M}}^{\mathrm{Syn}}$	(h^{-1})	0.21[d]	0.96[d]	0.18	8.12×10^{-2}

[a] Model fit presented in Figure 4.4A.

[b] Model fit presented in Figure 4.4B–D.

[c] Parameter was fixed to the value from the stabilization model.

[d] For better comparison, the synthesis rate of an mRNA of average length is shown. In the model, transcription is proportional to the actual length of each segment's mRNA and a length specific synthesis rate (here 350 and 1635 nucleotides $\cdot \mathrm{h}^{-1}$, respectively).

Table A.5.: Parameter estimates for the switching model considering data in Figure 4.6.

Parameter		**Value**
K_{swt}	(molecules/cell)	5.89×10^{11}
$k_{\mathrm{M1}}^{\mathrm{Bind}}$	$(\mathrm{molecule} \cdot \mathrm{h})^{-1}$	1.48×10^{-6}
$k_{\mathrm{R}}^{\mathrm{Deg}}$	(h^{-1})	0.28
$k_{\mathrm{C}}^{\mathrm{Syn}}$	(h^{-1})	727
$k_{\mathrm{M}}^{\mathrm{Syn}}$	(h^{-1})	105[a]
$k_{\mathrm{V}}^{\mathrm{Syn}}$	(h^{-1})	603

[a] Synthesis rate of an mRNA of average length using a length specific rate of $1.79 \cdot 10^{5}$ nucleotides $\cdot \mathrm{h}^{-1}$.

Table A.6.: Parameters corresponding to the mechanisms listed in Figure 4.8.

Mechanism	**Parameter**
Binding of M1 to nuclear vRNPs	$k_{\mathrm{M1}}^{\mathrm{Bind}}$
cRNA synthesis	$k_{\mathrm{C}}^{\mathrm{Syn}}$
Degradation of RdRp-RNA complexes	$k_{\mathrm{RRdRp}}^{\mathrm{Deg}}$
Degradation of RNPs	$k_{\mathrm{Rnp}}^{\mathrm{Deg}}$
Degradation of viral mRNAs	$k_{\mathrm{M}}^{\mathrm{Deg}}$
Encapsidation of viral RNAs by NP	$k_{\mathrm{NP}}^{\mathrm{Bind}}$
Endocytosis of virions	k^{En}
Viral mRNA synthesis	$k_{\mathrm{M}}^{\mathrm{Syn}}$
Viral protein synthesis	$k_{\mathrm{P}}^{\mathrm{Syn}}$
Virus assembly / release	k^{Rel}
vRNA synthesis	$k_{\mathrm{V}}^{\mathrm{Syn}}$

A.2. Stochastic model

This section provides parameter values and initial conditions used to simulate the stochastic model of intracellular influenza A virus replication. In addition, it summarizes the equations of three model variants including a model that neglects genome segmentation, an improved version that considers the vRNAs (and cRNAs) of different genome segments, and a stochastic model for segment-specific regulation of viral RNA synthesis.

Table A.7.: List of parameters for the stochastic intracellular model.[a]

Parameter		Value	Source, Reference, Comment
ϵ	(–)	0.03	[264]
$k_{\mathrm{M1}}^{\mathrm{Bind}}$	$(\mathrm{molecule} \cdot \mathrm{h})^{-1}$	1[b]	Rapid binding assumed
k^{In}	$(\mathrm{molecule} \cdot \mathrm{h})^{-1}$	0.87	Fit to the deterministic model
$k_{\mathrm{S}}^{\mathrm{Syn}}$	(h^{-1})	0.1	Adjusted
L_1^{V}	(nucleotides)	2 341	[25]
L_2^{V}	(nucleotides)	2 341	[25]
L_3^{V}	(nucleotides)	2 233	[25]
L_4^{V}	(nucleotides)	1 778	[25]
L_5^{V}	(nucleotides)	1 565	[25]
L_6^{V}	(nucleotides)	1 413	[25]
L_7^{V}	(nucleotides)	1 027	[25]
L_8^{V}	(nucleotides)	890	[25]
n_c	(–)	10	[264]

[a] In addition to the parameters shown here, the model uses the values from Table A.1.

[b] Only used for the model that considers segment-specific regulation (otherwise $k_{\mathrm{M1}}^{\mathrm{Bind}} = 1.39 \times 10^{-6}$) since svRNAs govern the shutdown of RNA(+) synthesis in this model variant.

Initial conditions In terms of initial conditions, the number of extracellular virions, $V^{\mathrm{Ex}}\,(t = 0)$, in the stochastic simulations was set to the NIVC indicated in each figure. For the simulation in Figure 4.9 the initial condition was $V^{\mathrm{Ex}}\,(t = 0) = 30\,\mathrm{virions/cell}$.

A.2.1. Model that neglects genome segmentation

For stochastic simulations it was more convenient to rewrite our model of intracellular influenza A virus replication into chemical equations. Based on Equations (3.1.1)–(3.1.4), we obtained the corresponding formulas for virus entry.

$$V^{\mathrm{Ex}} + B_{\mathrm{n}} \underset{k_{\mathrm{n}}^{\mathrm{Dis}}}{\overset{k_{\mathrm{n}}^{\mathrm{Att}}}{\rightleftharpoons}} V_{\mathrm{n}}^{\mathrm{Att}}, \quad n \in \{\mathrm{hi}, \mathrm{lo}\},$$

$$V_{\mathrm{n}}^{\mathrm{Att}} \xrightarrow{k^{\mathrm{En}}} V^{\mathrm{En}} + B_{\mathrm{n}},$$

$$
\begin{aligned}
V^{\mathrm{En}} &\xrightarrow{k_{\mathrm{En}}^{\mathrm{Deg}}} \emptyset,\\
V^{\mathrm{En}} &\xrightarrow{k^{\mathrm{Fus}}} 8\,Vp^{\mathrm{cyt}},\\
Vp^{\mathrm{cyt}} &\xrightarrow{k^{\mathrm{Imp}}} Vp^{\mathrm{nuc}}.
\end{aligned}
$$

If not otherwise indicated, we assumed that all reaction rates follow from mass action kinetics and that a reaction only occurs if all its substrates are available. For viral RNA replication Equations (3.1.5)–(3.1.13) translate to:

$$
\begin{aligned}
Vp^{\mathrm{nuc}} &\xrightarrow{k_{\mathrm{C}}^{\mathrm{Syn}}} Vp^{\mathrm{nuc}} + R^{\mathrm{C}}, & Cp &\xrightarrow{k_{\mathrm{V}}^{\mathrm{Syn}}} Cp + R^{\mathrm{V}},\\
R^{\mathrm{V}} + P_{\mathrm{RdRp}} &\xrightarrow{k_{\mathrm{RdRp}}^{\mathrm{Bind}}} R_{\mathrm{RdRp}}^{\mathrm{V}}, & R^{\mathrm{C}} + P_{\mathrm{RdRp}} &\xrightarrow{k_{\mathrm{RdRp}}^{\mathrm{Bind}}} R_{\mathrm{RdRp}}^{\mathrm{C}},\\
R_{\mathrm{RdRp}}^{\mathrm{V}} + \lfloor L^{\mathrm{V}}/N_{\mathrm{NP}}^{\mathrm{Nuc}} \rfloor P_{\mathrm{NP}} &\xrightarrow{k_{\mathrm{NP}}^{\mathrm{Bind}}} Vp^{\mathrm{nuc}}, & R_{\mathrm{RdRp}}^{\mathrm{C}} + \lfloor L^{\mathrm{V}}/N_{\mathrm{NP}}^{\mathrm{Nuc}} \rfloor P_{\mathrm{NP}} &\xrightarrow{k_{\mathrm{NP}}^{\mathrm{Bind}}} Cp,\\
Vp^{\mathrm{nuc}} + \lfloor L^{\mathrm{V}}/N_{\mathrm{M1}}^{\mathrm{Nuc}} \rfloor P_{\mathrm{M1}} &\xrightarrow{k_{\mathrm{M1}}^{\mathrm{Bind}}} Vp_{\mathrm{M1}}^{\mathrm{nuc}}, & Vp_{\mathrm{M1}}^{\mathrm{nuc}} + P_{\mathrm{NEP}} &\xrightarrow{k^{\mathrm{Exp}}} Vp_{\mathrm{M1}}^{\mathrm{cyt}}.
\end{aligned}
$$

Note that the binding rates for viral proteins to RNAs and RNPs were calculate from first order mass action kinetics neglecting the exponents that would typically follow when multiple proteins bind in a single step. Viral mRNA and protein synthesis (Equations (3.1.16)–(3.1.26)) can be described by the following equations.

$$
Vp^{\mathrm{nuc}} \xrightarrow{k_{\mathrm{M}}^{\mathrm{Syn}}/(8L_{\mathrm{i}})} Vp^{\mathrm{nuc}} + R_{\mathrm{i}}^{\mathrm{M}}, \quad i = 1,..,8,
$$

$$
\begin{aligned}
R_4^{\mathrm{M}} &\xrightarrow{k_{\mathrm{P}}^{\mathrm{Syn}}/D_{\mathrm{Rib}}} R_4^{\mathrm{M}} + P_{\mathrm{HA}}, & R_7^{\mathrm{M}} &\xrightarrow{k_{\mathrm{P}}^{\mathrm{Syn}}\left(1-F_{\mathrm{Spl7}}\right)/D_{\mathrm{Rib}}} R_7^{\mathrm{M}} + P_{\mathrm{M1}},\\
R_5^{\mathrm{M}} &\xrightarrow{k_{\mathrm{P}}^{\mathrm{Syn}}/D_{\mathrm{Rib}}} R_5^{\mathrm{M}} + P_{\mathrm{NP}}, & R_7^{\mathrm{M}} &\xrightarrow{k_{\mathrm{P}}^{\mathrm{Syn}}F_{\mathrm{Spl7}}/D_{\mathrm{Rib}}} R_7^{\mathrm{M}} + P_{\mathrm{M2}},\\
R_6^{\mathrm{M}} &\xrightarrow{k_{\mathrm{P}}^{\mathrm{Syn}}/D_{\mathrm{Rib}}} R_6^{\mathrm{M}} + P_{\mathrm{NA}}, & R_8^{\mathrm{M}} &\xrightarrow{k_{\mathrm{P}}^{\mathrm{Syn}}F_{\mathrm{Spl8}}/D_{\mathrm{Rib}}} R_8^{\mathrm{M}} + P_{\mathrm{NEP}},
\end{aligned}
$$

$$
R_1^{\mathrm{M}} + R_2^{\mathrm{M}} + R_3^{\mathrm{M}} \xrightarrow{k_{\mathrm{P}}^{\mathrm{Syn}}/D_{\mathrm{Rib}}} R_1^{\mathrm{M}} + R_2^{\mathrm{M}} + R_3^{\mathrm{M}} + P_{\mathrm{RdRp}}.
$$

In the last equation, we calculated the rate of viral polymerase production using $\min\left(R_1^{\mathrm{M}}, R_2^{\mathrm{M}}, R_3^{\mathrm{M}}\right)$ instead of the product of the three viral mRNAs (see Section 3.1.2 for details). For simplicity and agreement with the deterministic model, virus release was assumed to occur in a single reaction step.

$$\begin{aligned}&8\,Vp^{\mathrm{cyt}}_{\mathrm{M1}} + \mathrm{N}_{\mathrm{P}_{\mathrm{HA}}}P_{\mathrm{HA}} + \mathrm{N}_{\mathrm{P}_{\mathrm{NA}}}P_{\mathrm{NA}} + \mathrm{N}_{\mathrm{P}_{\mathrm{M2}}}P_{\mathrm{M2}} + (\mathrm{N}_{\mathrm{P}_{\mathrm{RdRp}}}-8)P_{\mathrm{RdRp}}\\ &+ (\mathrm{N}_{\mathrm{P}_{\mathrm{NP}}}-\lfloor L^{\mathrm{V}}/N^{\mathrm{Nuc}}_{\mathrm{NP}}\rfloor)P_{\mathrm{NP}} + (\mathrm{N}_{\mathrm{P}_{\mathrm{M1}}}-\lfloor L^{\mathrm{V}}/N^{\mathrm{Nuc}}_{\mathrm{M1}}\rfloor)P_{\mathrm{M1}} + (\mathrm{N}_{\mathrm{P}_{\mathrm{NEP}}}-8)P_{\mathrm{NEP}} \xrightarrow{r^{\mathrm{Rel}}} V^{\mathrm{Rel}},\end{aligned}$$

where the release rate (r^{Rel}) is given by Equation (3.1.27). Finally, the equations for degradation processes are the following.

$$\begin{array}{ccc} R^{\mathrm{V}} \xrightarrow{k^{\mathrm{Deg}}_{\mathrm{R}}} \emptyset, & R^{\mathrm{C}} \xrightarrow{k^{\mathrm{Deg}}_{\mathrm{R}}} \emptyset, & R^{\mathrm{M}}_{\mathrm{i}} \xrightarrow{k^{\mathrm{Deg}}_{\mathrm{M}}} \emptyset,\\ R^{\mathrm{V}}_{\mathrm{RdRp}} \xrightarrow{k^{\mathrm{Deg}}_{\mathrm{RRdRp}}} \emptyset, & R^{\mathrm{C}}_{\mathrm{RdRp}} \xrightarrow{k^{\mathrm{Deg}}_{\mathrm{RRdRp}}} \emptyset, & Vp^{\mathrm{nuc}} \xrightarrow{k^{\mathrm{Deg}}_{\mathrm{Rnp}}} \emptyset,\\ Cp \xrightarrow{k^{\mathrm{Deg}}_{\mathrm{Rnp}}} \emptyset, & Vp^{\mathrm{nuc}}_{\mathrm{M1}} \xrightarrow{k^{\mathrm{Deg}}_{\mathrm{Rnp}}} \emptyset, & Vp^{\mathrm{cyt}}_{\mathrm{M1}} \xrightarrow{k^{\mathrm{Deg}}_{\mathrm{Rnp}}} \emptyset. \end{array}$$

A.2.2. Model that considers genome segmentation

The model shown above does not consider the vRNAs (and cRNAs) of individual genome segments explicitly but rather accounts for their total number. Hence, it assumes that these RNA species exist in equimolar concentrations throughout infection. Here, this assumption is dropped in favor of a more general model. From Equations (3.1.1)–(3.1.4) and the modifications in Section 3.1.2 virus entry followed as:

$$\begin{aligned} V^{\mathrm{Ex}} + B_{\mathrm{n}} &\underset{k^{\mathrm{Dis}}_{\mathrm{n}}}{\overset{k^{\mathrm{Att}}_{\mathrm{n}}}{\rightleftharpoons}} V^{\mathrm{Att}}_{\mathrm{n}}, \quad n \in \{\mathrm{hi}, \mathrm{lo}\},\\ V^{\mathrm{Att}}_{\mathrm{n}} &\xrightarrow{k^{\mathrm{En}}} V^{\mathrm{En}} + B_{\mathrm{n}},\\ V^{\mathrm{En}} &\xrightarrow{k^{\mathrm{Deg}}_{\mathrm{En}}} \emptyset,\\ V^{\mathrm{En}} &\xrightarrow{k^{\mathrm{Fus}}} V^{\mathrm{cyt}},\\ V^{\mathrm{cyt}} &\xrightarrow{k^{\mathrm{Imp}}} Vp^{\mathrm{nuc}}_{1} + Vp^{\mathrm{nuc}}_{2} + \ldots + Vp^{\mathrm{nuc}}_{8}, \end{aligned}$$

where V^{cyt} denotes a cytoplasmic complex that comprises the eight genome segments and $Vp^{\mathrm{nuc}}_{\mathrm{i}}$ is the number of vRNPs of segment i in the nucleus. We assumed that the reaction rates follow mass action kinetics if not otherwise stated and that for a reaction to occur all its substrates must be available. For viral RNA replication, the deterministic model was extended by accounting for each segment $i = 1, \ldots, 8$ individually.

$$Vp_{\mathrm{i}}^{\mathrm{nuc}} \xrightarrow{k_{\mathrm{C}}^{\mathrm{Syn}}} Vp_{\mathrm{i}}^{\mathrm{nuc}} + R_{\mathrm{i}}^{\mathrm{C}}, \qquad Cp_{\mathrm{i}} \xrightarrow{k_{\mathrm{V}}^{\mathrm{Syn}}} Cp_{\mathrm{i}} + R_{\mathrm{i}}^{\mathrm{V}},$$

$$R_{\mathrm{i}}^{\mathrm{V}} + P_{\mathrm{RdRp}} \xrightarrow{k_{\mathrm{RdRp}}^{\mathrm{Bind}}} R_{\mathrm{RdRp,i}}^{\mathrm{V}}, \qquad R_{\mathrm{i}}^{\mathrm{C}} + P_{\mathrm{RdRp}} \xrightarrow{k_{\mathrm{RdRp}}^{\mathrm{Bind}}} R_{\mathrm{RdRp,i}}^{\mathrm{C}},$$

$$R_{\mathrm{RdRp,i}}^{\mathrm{V}} + \lfloor L_{\mathrm{i}}^{\mathrm{V}}/N_{\mathrm{NP}}^{\mathrm{Nuc}} \rfloor P_{\mathrm{NP}} \xrightarrow{k_{\mathrm{NP}}^{\mathrm{Bind}}} Vp_{\mathrm{i}}^{\mathrm{nuc}}, \qquad R_{\mathrm{RdRp,i}}^{\mathrm{C}} + \lfloor L_{\mathrm{i}}^{\mathrm{V}}/N_{\mathrm{NP}}^{\mathrm{Nuc}} \rfloor P_{\mathrm{NP}} \xrightarrow{k_{\mathrm{NP}}^{\mathrm{Bind}}} Cp_{\mathrm{i}},$$

$$Vp_{\mathrm{i}}^{\mathrm{nuc}} + \lfloor L_{\mathrm{i}}^{\mathrm{V}}/N_{\mathrm{M1}}^{\mathrm{Nuc}} \rfloor P_{\mathrm{M1}} \xrightarrow{k_{\mathrm{M1}}^{\mathrm{Bind}}} Vp_{\mathrm{M1,i}}^{\mathrm{nuc}}, \qquad Vp_{\mathrm{M1,i}}^{\mathrm{nuc}} + P_{\mathrm{NEP}} \xrightarrow{k^{\mathrm{Exp}}} Vp_{\mathrm{M1,i}}^{\mathrm{cyt}},$$

where $L_{\mathrm{i}}^{\mathrm{V}}$ denotes the length of segment i's vRNA. Note that the binding rates for viral proteins to RNAs and RNPs were calculate from first order mass action kinetics neglecting the exponents that would typically follow when multiple proteins bind in a single step. Viral mRNA and protein synthesis are described by the following equations.

$$Vp_{\mathrm{i}}^{\mathrm{nuc}} \xrightarrow{k_{\mathrm{M}}^{\mathrm{Syn}}/L_{\mathrm{i}}} Vp_{\mathrm{i}}^{\mathrm{nuc}} + R_{\mathrm{i}}^{\mathrm{M}},$$

$$R_4^{\mathrm{M}} \xrightarrow{k_{\mathrm{P}}^{\mathrm{Syn}}/D_{\mathrm{Rib}}} R_4^{\mathrm{M}} + P_{\mathrm{HA}}, \qquad R_7^{\mathrm{M}} \xrightarrow{k_{\mathrm{P}}^{\mathrm{Syn}}\left(1-F_{\mathrm{Spl}_7}\right)/D_{\mathrm{Rib}}} R_7^{\mathrm{M}} + P_{\mathrm{M1}},$$

$$R_5^{\mathrm{M}} \xrightarrow{k_{\mathrm{P}}^{\mathrm{Syn}}/D_{\mathrm{Rib}}} R_5^{\mathrm{M}} + P_{\mathrm{NP}}, \qquad R_7^{\mathrm{M}} \xrightarrow{k_{\mathrm{P}}^{\mathrm{Syn}}F_{\mathrm{Spl}_7}/D_{\mathrm{Rib}}} R_7^{\mathrm{M}} + P_{\mathrm{M2}},$$

$$R_6^{\mathrm{M}} \xrightarrow{k_{\mathrm{P}}^{\mathrm{Syn}}/D_{\mathrm{Rib}}} R_6^{\mathrm{M}} + P_{\mathrm{NA}}, \qquad R_8^{\mathrm{M}} \xrightarrow{k_{\mathrm{P}}^{\mathrm{Syn}}F_{\mathrm{Spl}_8}/D_{\mathrm{Rib}}} R_8^{\mathrm{M}} + P_{\mathrm{NEP}},$$

$$R_1^{\mathrm{M}} + R_2^{\mathrm{M}} + R_3^{\mathrm{M}} \xrightarrow{k_{\mathrm{P}}^{\mathrm{Syn}}/D_{\mathrm{Rib}}} R_1^{\mathrm{M}} + R_2^{\mathrm{M}} + R_3^{\mathrm{M}} + P_{\mathrm{RdRp}},$$

where we calculated the rate of viral polymerase production in the last equation using $\min\left(R_1^{\mathrm{M}}, R_2^{\mathrm{M}}, R_3^{\mathrm{M}}\right)$ instead of the product of the three viral mRNAs (see Section 3.1.2 for details). For simplicity and agreement with the deterministic model, virus release was assumed to occur in a single reaction step.

$$\begin{aligned} &Vp_{\mathrm{M1,1}}^{\mathrm{cyt}} + \ldots + Vp_{\mathrm{M1,8}}^{\mathrm{cyt}} + \mathrm{N}_{\mathrm{P_{HA}}} P_{\mathrm{HA}} + \mathrm{N}_{\mathrm{P_{NA}}} P_{\mathrm{NA}} + \mathrm{N}_{\mathrm{P_{M2}}} P_{\mathrm{M2}} \\ &+ (\mathrm{N}_{\mathrm{P_{RdRp}}} - 8) P_{\mathrm{RdRp}} + (\mathrm{N}_{\mathrm{P_{NP}}} - \textstyle\sum_{\mathrm{i}} \lfloor L_{\mathrm{i}}^{\mathrm{V}}/N_{\mathrm{NP}}^{\mathrm{Nuc}} \rfloor) P_{\mathrm{NP}} \\ &+ (\mathrm{N}_{\mathrm{P_{M1}}} - \textstyle\sum_{\mathrm{i}} \lfloor L_{\mathrm{i}}^{\mathrm{V}}/N_{\mathrm{M1}}^{\mathrm{Nuc}} \rfloor) P_{\mathrm{M1}} + (\mathrm{N}_{\mathrm{P_{NEP}}} - 8) P_{\mathrm{NEP}} \xrightarrow{r^{\mathrm{Rel}}} V^{\mathrm{Rel}}, \end{aligned}$$

with the release rate (r^{Rel}) given by Equation (3.1.32). Finally, the equations for degradation processes are the following.

$$R_{\mathrm{i}}^{\mathrm{V}} \xrightarrow{k_{\mathrm{R}}^{\mathrm{Deg}}} \emptyset, \qquad R_{\mathrm{i}}^{\mathrm{C}} \xrightarrow{k_{\mathrm{R}}^{\mathrm{Deg}}} \emptyset, \qquad R_{\mathrm{i}}^{\mathrm{M}} \xrightarrow{k_{\mathrm{M}}^{\mathrm{Deg}}} \emptyset,$$

$$R^{\mathrm{V}}_{\mathrm{RdRp,i}} \xrightarrow{k^{\mathrm{Deg}}_{\mathrm{RRdRp}}} \emptyset, \qquad R^{\mathrm{C}}_{\mathrm{RdRp,i}} \xrightarrow{k^{\mathrm{Deg}}_{\mathrm{RRdRp}}} \emptyset, \qquad Vp^{\mathrm{nuc}}_{\mathrm{i}} \xrightarrow{k^{\mathrm{Deg}}_{\mathrm{Rnp}}} \emptyset,$$

$$Cp_{\mathrm{i}} \xrightarrow{k^{\mathrm{Deg}}_{\mathrm{Rnp}}} \emptyset, \qquad Vp^{\mathrm{nuc}}_{\mathrm{M1,i}} \xrightarrow{k^{\mathrm{Deg}}_{\mathrm{Rnp}}} \emptyset, \qquad Vp^{\mathrm{cyt}}_{\mathrm{M1,i}} \xrightarrow{k^{\mathrm{Deg}}_{\mathrm{Rnp}}} \emptyset.$$

A.2.3. Model with segment-specific regulation

In Section 4.1.2, we introduced a stochastic model that considers a segment-specific mechanism for the regulation of positive-strand RNA synthesis. This model is similar to the description presented above (Section A.2.2) with the following exceptions. We incorporated the number of svRNAs of segment i ($R^{\mathrm{S}}_{\mathrm{i}}$), which are produced by cRNPs.

$$Cp_{\mathrm{i}} \xrightarrow{k^{\mathrm{Syn}}_{\mathrm{S}}} Cp_{\mathrm{i}} + R^{\mathrm{S}}_{\mathrm{i}},$$

where $k^{\mathrm{Syn}}_{\mathrm{S}}$ denotes the synthesis rate of svRNAs. These svRNAs are assumed to induce an inactive state in nuclear vRNPs (Vp^{In}) that carry the genome segment from which the svRNA originates.

$$Vp^{\mathrm{nuc}}_{\mathrm{i}} \xrightarrow{k^{\mathrm{In}} R^{\mathrm{S}}_{\mathrm{i}}} Vp^{\mathrm{In}}_{\mathrm{i}},$$

where k^{In} is the inactivation rate. The inactivated vRNPs can no longer serve as templates for mRNA and cRNA synthesis but may bind M1 proteins to form M1-vRNP complexes.

$$Vp^{\mathrm{In}}_{\mathrm{i}} + \lfloor L^{\mathrm{V}}_{\mathrm{i}} / N^{\mathrm{Nuc}}_{\mathrm{M1}} \rfloor P_{\mathrm{M1}} \xrightarrow{k^{\mathrm{Bind}}_{\mathrm{M1}}} Vp^{\mathrm{nuc}}_{\mathrm{M1,i}}.$$

In this model, M1 proteins only bind to the inactivated RNPs replacing the corresponding equation in Section A.2.2. The other reactions are as described above.

A.2.4. Comparison between deterministic and stochastic simulations

The following section presents three figures showing that the modifications outlined in Section 3.1.2 do not change model dynamics in a deterministic setting (Figure A.1), that 3 000 stochastic runs are sufficient to obtain a representative sample of the system's dynamics (Figure A.2), and that the stochastic model shows similar results than the deterministic implementation if genome segmentation is neglected (Figure A.3).

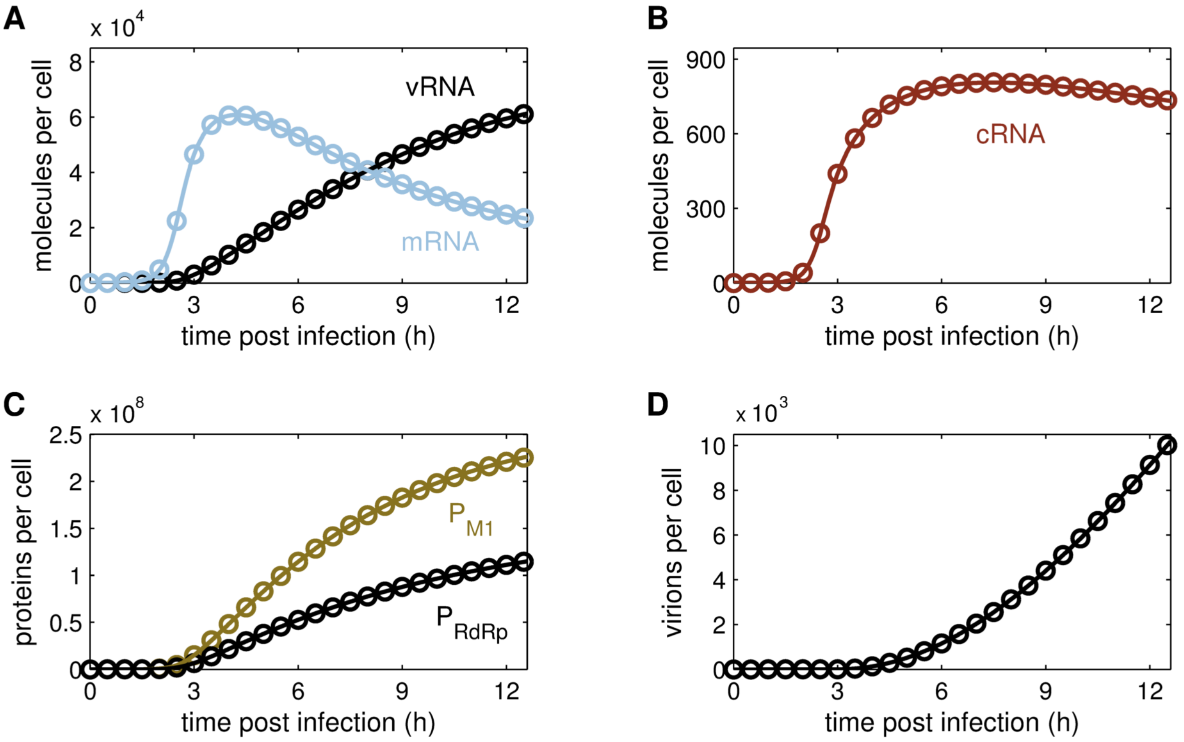

Figure A.1.: Impact of modifying and extending the deterministic model. For an infection at an MOI of 10 the original deterministic model of intracellular virus replication (circles) was compared to a deterministic model that incorporates the modifications and extensions outlined in Section 3.1.2 (lines). These modifications include that vRNAs and cRNAs of individual genome segments are accounted for, segment separation occurs after nuclear import, polymerase subunits were neglected, and discrete numbers of NP, M1 and NEP molecules bind to RNAs. (A) vRNA and mRNA level of segment 5 (encoding NP). (B) cRNA level of segment 5. (C) Abundance of viral polymerases (P_{RdRp}) and M1 proteins (P_{M1}). (D) Cumulative number of released virus particles.

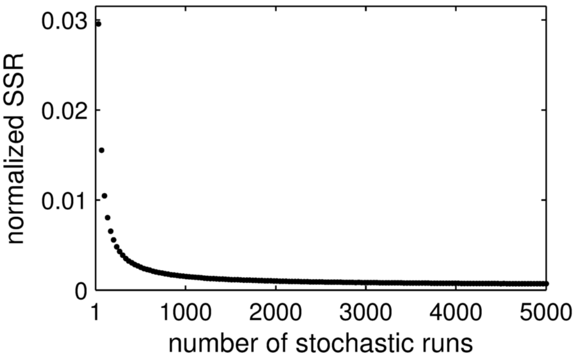

Figure A.2.: Difference between the deterministic model and the mean of stochastic simulations that neglect genome segmentation. The normalized sum of squared residuals (SSR) between both simulation techniques was determined for an infection at an MOI of 10 using a stochastic mean averaged over an increasing number of runs. Each point in the graph corresponds to the mean of 500 SSRs calculated by comparing the deterministic model to the average of the indicated number of stochastic runs, which were randomly drawn from a set of 5 000 runs. The normalized SSRs were calculated over all states present in both models, whereby each state was divided by its maximum in the deterministic model and the number of simulated time points.

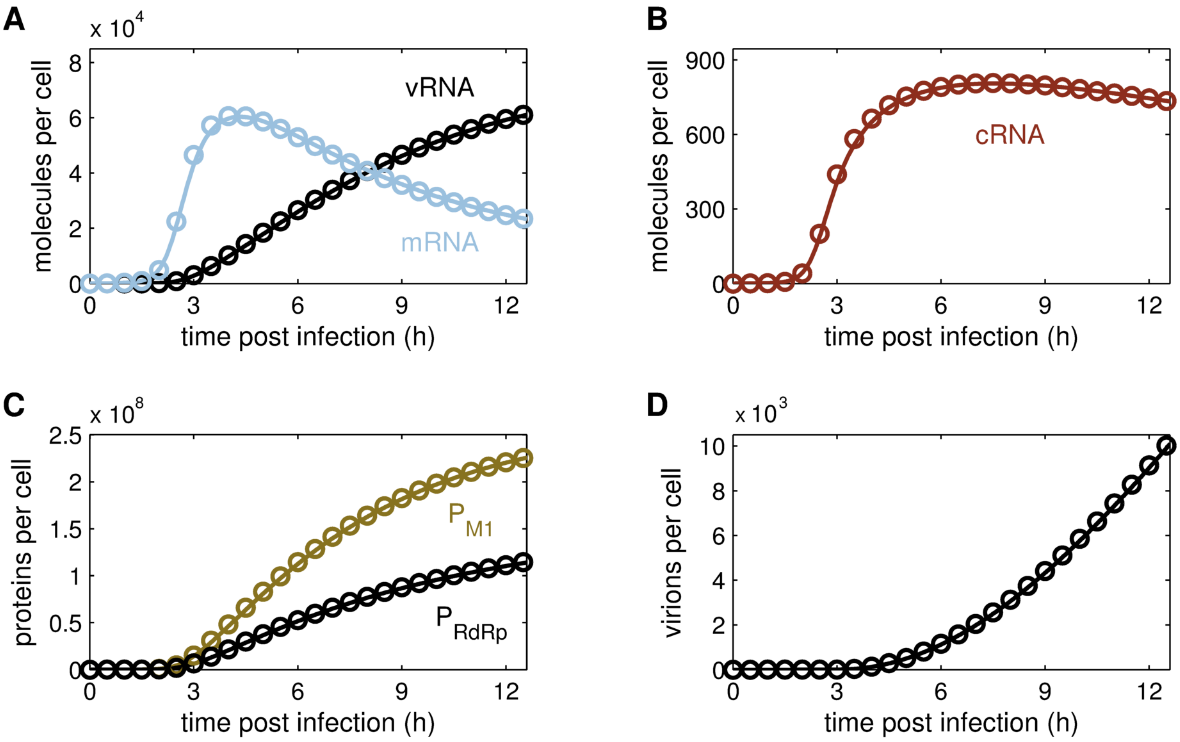

Figure A.3.: Comparison between the deterministic model and stochastic simulations that neglect genome segmentation. The deterministic model of intracellular influenza virus replication (points) was compared to the mean of 3 000 stochastic simulation runs (lines) for an infection at an NIVC of 10. The stochastic model was simulated with the modifications in Section 3.1.2 but without explicit consideration of the vRNAs and cRNAs of individual genome segments (see Section A.2.1). (A) vRNA level of an arbitrary genome segment and mRNA level of segment 5 (encoding NP). (B) cRNA level or an arbitrary segment. (C) Abundance of viral polymerases (P_{RdRp}) and M1 proteins (P_{M1}). (D) Cumulative number of released virus particles.

Appendix B

Multiscale model of infection

Here, supplementary information on the multiscale model of infection are given. These include the parameters and initial conditions used for simulations and two additional figures depicting bimodal NP distributions in infected cell populations (Figure B.1) and virus titer dynamics under drug treatment (Figure B.2).

Table B.1.: List of parameters for the intracellular level of the multiscale model.[a]

Parameter		Value	Source, Reference, Comment
$K_{V^{\mathrm{Rel}}}$	(virions)	300	Adjusted
$k_{\mathrm{M1}}^{\mathrm{Bind}}$	$(\mathrm{molecule} \cdot \mathrm{h})^{-1}$	2.43×10^{-4}	Figure 4.24A
$k_{\mathrm{C}}^{\mathrm{Syn}}$	(h^{-1})	5.29	Figure 4.24A
$k_{\mathrm{M}}^{\mathrm{Syn}}$	(nucleotides/h)	8.53×10^{5}	Figure 4.24A
$k_{\mathrm{V}}^{\mathrm{Syn}}$	(h^{-1})	32.18	Figure 4.24A
$k_{\mathrm{max}}^{\mathrm{Rel}}$	$(\mathrm{virions}/(\mathrm{cell} \cdot \mathrm{h}))$	586	Figure 4.24A

[a] If not explicitly shown here, the parameters from Table A.1 were used.

Table B.2.: List of parameters for the extracellular level of the multiscale model.

Parameter		**Value**	**Source, Reference, Comment**
μ_{max}	(h^{-1})	0.03	[177]
$B_{\mathrm{hi}}^{\mathrm{tot}}$	(sites/cell)	150	[251]
$B_{\mathrm{lo}}^{\mathrm{tot}}$	(sites/cell)	1 000	[251]
F_{Inf}	(cells/virion)	1	Figure 4.24B
$k_{\mathrm{I}}^{\mathrm{Apo}}$	(h^{-1})	3.28×10^{-2}	Figure 4.24B
$k_{\mathrm{T}}^{\mathrm{Apo}}$	(h^{-1})	7.35×10^{-3}	Figure 4.24B
$k_{\mathrm{c,hi}}^{\mathrm{Att}}$	($\mathrm{ml}/(\mathrm{site} \cdot \mathrm{h})$)	3.32×10^{-8}	Adjusted to data in [251]
$k_{\mathrm{c,lo}}^{\mathrm{Att}}$	($\mathrm{ml}/(\mathrm{site} \cdot \mathrm{h})$)	1.85×10^{-10}	Adjusted to data in [251]
$k_{\mathrm{V}}^{\mathrm{Deg}}$	(h^{-1})	0.1	[217]
k^{En}	(h^{-1})	4.8	Figure 4.2A
$k_{\mathrm{c,hi}}^{\mathrm{Eq}}$	(ml/site)	4.48×10^{-9}	[251]
$k_{\mathrm{c,lo}}^{\mathrm{Eq}}$	(ml/site)	3.32×10^{-11}	[251]
k^{Fus}	(h^{-1})	9.56×10^{-3}	Figure 4.24A
k^{Lys}	(h^{-1})	6.39×10^{-2}	Figure 4.24B
T_{max}	(cells/ml)	7×10^{5}	Data not shown

Table B.3.: List of non-zero initial conditions for the multiscale model.

Simulation	**Level**	**Initial condition**
Figure 4.23D, 4.24A	intracellular	$V^{\mathrm{Ex}} = 1.2\,\mathrm{virions/cell}$
Figure 4.24B, 4.26	intracellular	$Vp^{\mathrm{cyt}} = 8\,\mathrm{molecules/cell}$
	extracellular	$T = 4.90 \times 10^{5}\,\mathrm{cells/ml}$, $T_{\mathrm{a}} = 9.49 \times 10^{3}\,\mathrm{cells/ml}$, $V = 6.90 \times 10^{4}\,\mathrm{virions/ml}$
Figure 4.25	intracellular	$Vp^{\mathrm{cyt}} = 8\,\mathrm{molecules/cell}$
	extracellular (MOI $= 10^{-4}$)	$T = 5.10 \times 10^{5}\,\mathrm{cells/ml}$, $T_{\mathrm{a}} = 8.90 \times 10^{3}\,\mathrm{cells/ml}$, $V = 51\,\mathrm{virions/ml}$
	extracellular (MOI $= 0.1$)	same as in Figure 4.24B
	extracellular (MOI $= 3$)	$T = 5.24 \times 10^{5}\,\mathrm{cells/ml}$, $T_{\mathrm{a}} = 8.06 \times 10^{3}\,\mathrm{cells/ml}$, $V = 1.57 \times 10^{6}\,\mathrm{virions/ml}$
Figure 4.27, 4.28, 4.29	intracellular	$Vp^{\mathrm{cyt}} = 8\,\mathrm{molecules/cell}$
Figure 4.30	intracellular	$Vp^{\mathrm{cyt}} = 8\,\mathrm{molecules/cell}$,
	extracellular	$T = 5.29 \times 10^{5}\,\mathrm{cells/ml}$, $V = 52.9\,\mathrm{virions/ml}$

Table B.4.: Parameters corresponding to the drug targets in Figure 4.28 and 4.30.

Mechanism	Parameter
Assembly of RdRp-complexes	k^{RdRp}
Binding of M1 to nuclear vRNPs	$k^{\mathrm{Bind}}_{\mathrm{M1}}$
Binding of RdRp to viral RNAs	$k^{\mathrm{Bind}}_{\mathrm{RdRp}}$
cRNA synthesis	$k^{\mathrm{Syn}}_{\mathrm{C}}$
Encapsidation of viral RNAs by NP	$k^{\mathrm{Bind}}_{\mathrm{NP}}$
Endocytosis of virions	k^{En}
Fusion with endosomes	k^{Fus}
Nuclear export of viral genomes	k^{Exp}
Nuclear import of viral genomes	k^{Imp}
Viral mRNA synthesis	$k^{\mathrm{Syn}}_{\mathrm{M}}$
Viral protein synthesis	$k^{\mathrm{Syn}}_{\mathrm{P}}$
Virus binding to high-affinity sites	$k^{\mathrm{Att}}_{\mathrm{c,hi}}$
Virus binding to low-affinity sites	$k^{\mathrm{Att}}_{\mathrm{c,lo}}$
Virus assembly / release	$k^{\mathrm{Rel}}_{\mathrm{max}}$
vRNA synthesis	$k^{\mathrm{Syn}}_{\mathrm{V}}$
Splicing of mRNAs for M2	F_{Spl_7}
Splicing of mRNAs for NEP	F_{Spl_8}

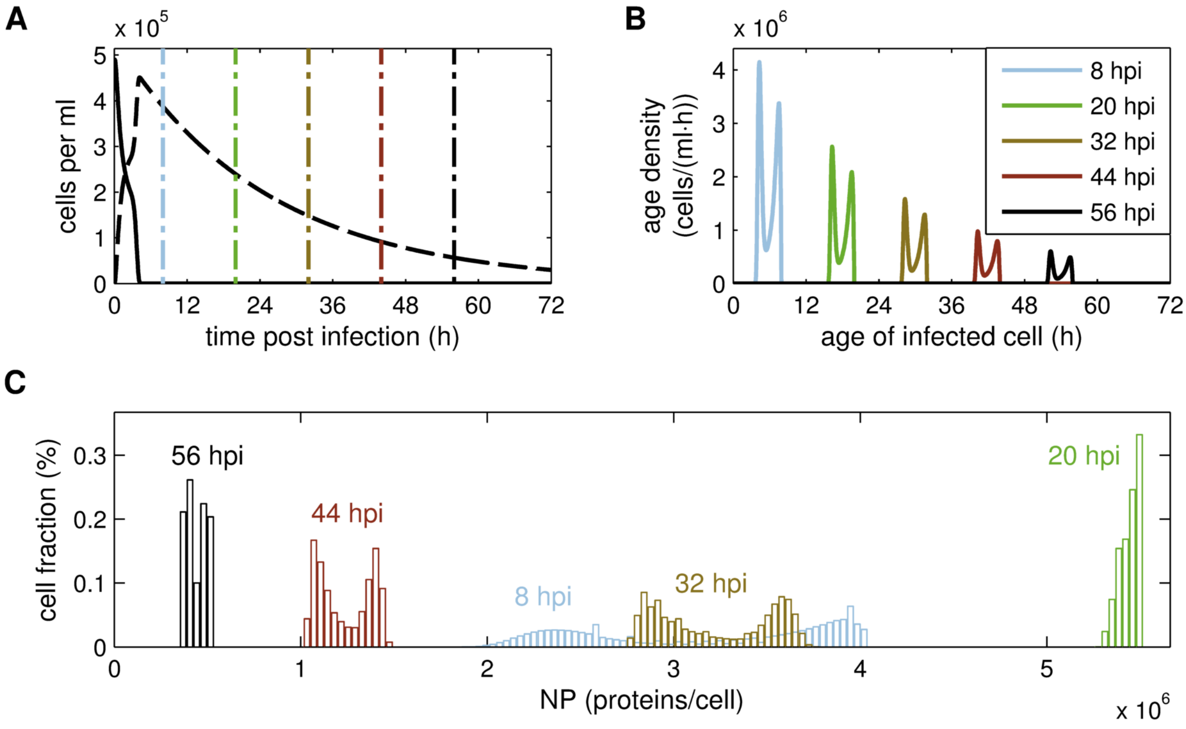

Figure B.1.: Bimodal distribution of cellular NP content during multi-cycle infection. Same as in Figure 4.26 except that an MOI of 1 was simulated and the rate of virus fusion was increased to the value in Table 4.1. (A) Concentration of uninfected (solid) and infected cells (dashed). (B) Infection age density. (C) Distribution of cells that contain the indicated amount of NP proteins at different times post infection.

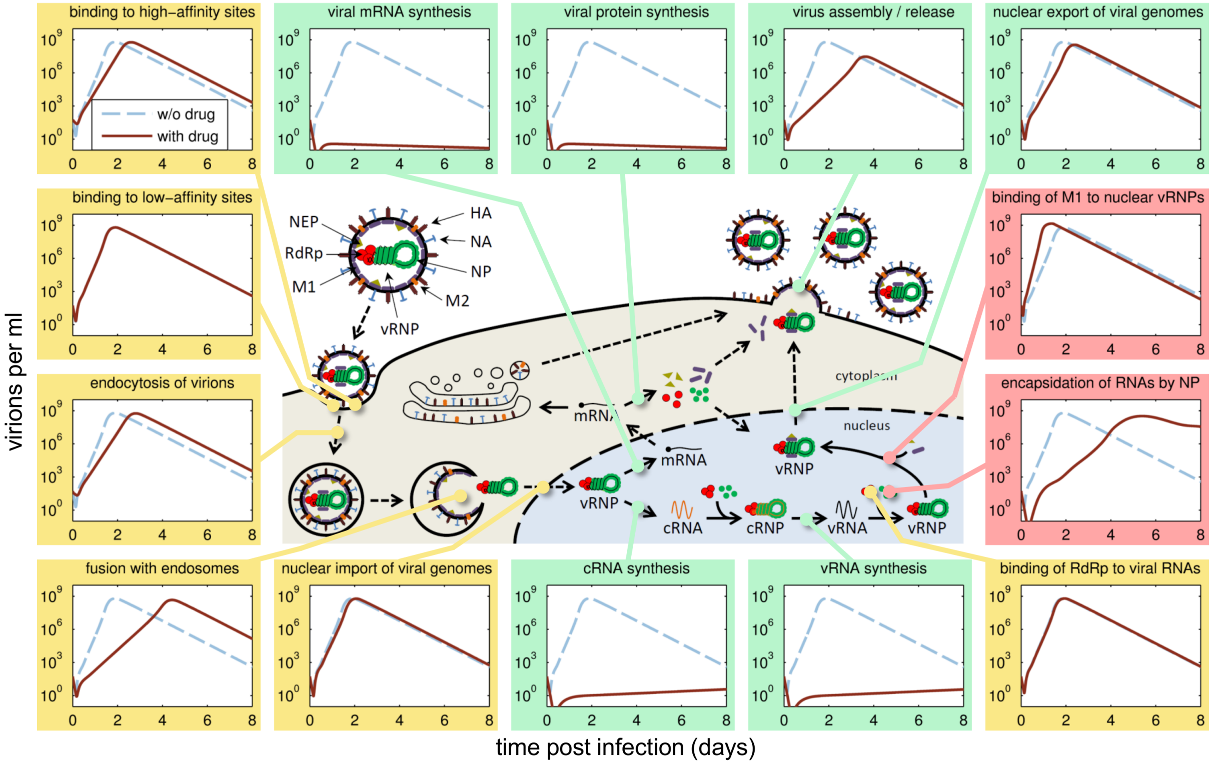

Figure B.2.: Virus titer dynamics in response to DAA treatment. Infectious virus titer in the absence (dashed line) and presence (solid line) of drugs that target the indicated steps of viral replication with an efficacy of 95% during an infection at an MOI of 10^{-4}. Colors indicate whether the drug decreases virus titers (green), primarily delays infection (yellow), or increases virus production (red).

Appendix C

Defective interfering viruses

This chapter provides additional information on the models for DI RNA replication at the intracellular level and DIP growth during continuous virus infection experiments. It lists their parameters and initial conditions and presents model equations for the synthesis of DI RNAs of segment 3 (encoding PA) and 4 (encoding HA), respectively.

Table C.1.: List of parameters for the intracellular model of DI RNA replication.[a]

Parameter		**Value**	**Source, Reference, Comment**
F_{Adv}	(–)	3.65[b]	Assumption (see Figure 4.31)
k^{Cplx}	(molecules$^{-7} \cdot$ h^{-1})	1	Rapid complex formation assumed
L_1^{V}	(nucleotides)	2 341	[25]
L_2^{V}	(nucleotides)	2 341	[25]
L_3^{V}	(nucleotides)	2 233	[25]
L_4^{V}	(nucleotides)	1 778	[25]
L_5^{V}	(nucleotides)	1 565	[25]
L_6^{V}	(nucleotides)	1 413	[25]
L_7^{V}	(nucleotides)	1 027	[25]
L_8^{V}	(nucleotides)	890	[25]
L_9^{V}	(nucleotides)	480[b]	[108]

[a] In addition to the parameters shown, here the model uses the values from Table A.1.

[b] Advantage and length for a model DI RNA of segment 3 (if not otherwise indicated). Simulations of a DI RNA of segment 4 use $F_{\text{Adv}} = 4.39$ and $L_9^{\text{V}} = 330$ nt.

Table C.2.: Initial conditions and parameter changes (compared to Table C.1 and Table A.1) used to simulate the intracellular model of DI RNA replication.

Figure	Non-zero initial conditions	Parameter changes
Figure 4.31C	$Vp_9^{\mathrm{nuc}} = 1$, $P_{\mathrm{RdRp}} = 10^4$, $P_{\mathrm{NP}} = 10^4$, $\mathrm{d}P_j/\mathrm{d}t = 0$	$F_{\mathrm{Adv}} = [0, 1, 3.65]$, $L_9^{\mathrm{V}} = [2233, 1117, 480]$
Figure 4.32, 4.33	$V^{\mathrm{Ex}} = [2, 1]$, $D^{\mathrm{Ex}} = [0, 1]$	
Figure 4.34	$V^{\mathrm{Ex}} = b$, $D^{\mathrm{Ex}} = b$, with $b = [0, 1, 2] \widehat{=} [-, +, ++]$	$F_{\mathrm{Adv}} = 0$ for $\mathrm{DIP_{NA}}$
Figure 4.36	$V^{\mathrm{Ex}} = 0 - 15$, $D^{\mathrm{Ex}} = 0 - 15$	
Figure 4.37	$V^{\mathrm{Ex}} = 1$, $D^{\mathrm{Ex}} = 1$	$F_{\mathrm{Adv}} = 0 - 4.2$, $L_9^{\mathrm{V}} = 2233 - 429$
Figure 4.38A	$V^{\mathrm{Ex}} = 1$, $D^{\mathrm{Ex}} = 0$ (1 after delay)	
Figure 4.38B	$D^{\mathrm{Ex}} = 1$, $V^{\mathrm{Ex}} = 0$ (1 after delay)	
Figure 4.39A	$D^{\mathrm{Ex}} = 1$, $V^{\mathrm{Ex}} = 0$ (1 after delay)	$F_{\mathrm{Adv}} = 0 - 2$, $L_9^{\mathrm{V}} = 2233 - 744$
Figure 4.39B	$D^{\mathrm{Ex}} = 1$, $V^{\mathrm{Ex}} = 0$ (1 after delay)	$F_{\mathrm{Adv}} = 0 - 2$, $L_9^{\mathrm{V}} = 1778 - 593$
Figure 4.39C	$D^{\mathrm{Ex}} = 1$, $V^{\mathrm{Ex}} = 0$	$F_{\mathrm{Adv}} = 0.5$, $L_9^{\mathrm{V}} = 1489$
Figure 4.39D	$D^{\mathrm{Ex}} = 1$, $V^{\mathrm{Ex}} = 0$	$F_{\mathrm{Adv}} = 0.5$, $L_9^{\mathrm{V}} = 1185$

Table C.3.: Initial conditions and parameter changes (compared to Table 4.5) used to simulate the model of DIP growth during continuous influenza A virus production.

Figure	Non-zero initial conditions	Parameter changes
Figure 4.42B	$T = 5.33 \times 10^6$, $V_{\mathrm{s}} = 10^4$	$f = 0$, $D = 10^{-8}$
Figure 4.42C	$T = 5.33 \times 10^6$, $V_{\mathrm{s}} = 10^4$	$f = 0$
Figure 4.43B	$T = 5.33 \times 10^6$, $V_{\mathrm{s}} = 10^4$	
Figure 4.43C	$T = 5.33 \times 10^6$, $V_{\mathrm{s}} = 10^4$, $V_{\mathrm{d}} = 0 - 10^4$	$f = 0$
Figure 4.43D	$T = 5.33 \times 10^6$, $V_{\mathrm{s}} = 10^4$	$f = 0 - 1$

C.1. Model for a DI RNA of segment 3

In the following, we provide a complete list of the equations for our model of intracellular DI RNA replication that considers a defect in segment 3 (encoding PA). Entry of STVs into the cell follows from Equations (3.1.1)–(3.1.4). We assumed that DIPs are taken up in a similar way.

$$\frac{\mathrm{d}D^{\mathrm{Ex}}}{\mathrm{d}t} = k_{\mathrm{hi}}^{\mathrm{Dis}} D_{\mathrm{hi}}^{\mathrm{Att}} + k_{\mathrm{lo}}^{\mathrm{Dis}} D_{\mathrm{lo}}^{\mathrm{Att}} - \left(k_{\mathrm{hi}}^{\mathrm{Att}} B_{\mathrm{hi}} + k_{\mathrm{lo}}^{\mathrm{Att}} B_{\mathrm{lo}} \right) D^{\mathrm{Ex}},$$

$$
\begin{aligned}
&\text{for}\quad B_{\mathrm{n}} = B_{\mathrm{n}}^{\mathrm{tot}} - V_{\mathrm{n}}^{\mathrm{Att}} - D_{\mathrm{n}}^{\mathrm{Att}}, \quad n \in \{\mathrm{hi}, \mathrm{lo}\}, \\
\frac{\mathrm{d}D_{\mathrm{n}}^{\mathrm{Att}}}{\mathrm{d}t} &= k_{\mathrm{n}}^{\mathrm{Att}} B_{\mathrm{n}} D^{\mathrm{Ex}} - \left(k_{\mathrm{n}}^{\mathrm{Dis}} + k^{\mathrm{En}}\right) D_{\mathrm{n}}^{\mathrm{Att}}, \\
\frac{\mathrm{d}D^{\mathrm{En}}}{\mathrm{d}t} &= k^{\mathrm{En}} \left(D_{\mathrm{hi}}^{\mathrm{Att}} + D_{\mathrm{lo}}^{\mathrm{Att}}\right) - \left(k^{\mathrm{Fus}} + k_{\mathrm{En}}^{\mathrm{Deg}}\right) D^{\mathrm{En}},
\end{aligned}
$$

where D denotes the defective virus and the notation of indices follows Equations (3.1.1)–(3.1.4). Upon fusion with late endosomes, both types of viruses release a complex comprising the eight genome segments.

$$
\begin{aligned}
\frac{\mathrm{d}V^{\mathrm{cyt}}}{\mathrm{d}t} &= k^{\mathrm{Fus}} V^{\mathrm{En}} - k^{\mathrm{Imp}} V^{\mathrm{cyt}}, \\
\frac{\mathrm{d}D^{\mathrm{cyt}}}{\mathrm{d}t} &= k^{\mathrm{Fus}} D^{\mathrm{En}} - k^{\mathrm{Imp}} D^{\mathrm{cyt}},
\end{aligned}
$$

where V^{cyt} and D^{cyt} contain a full-length vRNA or a DI vRNA of segment 3, respectively. When these complexes enter the nucleus the genome segments separate into independent replication units.

$$
\begin{aligned}
\frac{\mathrm{d}Vp_{\mathrm{k}}^{\mathrm{nuc}}}{\mathrm{d}t} &= k^{\mathrm{Imp}} V^{\mathrm{cyt}} + k^{\mathrm{Imp}} D^{\mathrm{cyt}} + k_{\mathrm{NP}}^{\mathrm{Bind}} P_{\mathrm{NP}} R_{\mathrm{RdRp,k}}^{\mathrm{V}} - \left(k_{\mathrm{M1}}^{\mathrm{Bind}} P_{\mathrm{M1}} + k_{\mathrm{Rnp}}^{\mathrm{Deg}}\right) Vp_{\mathrm{k}}^{\mathrm{nuc}}, \\
&\text{for}\quad k = 1, 2, 4, \dots, 8 \quad \text{and} \\
\frac{\mathrm{d}Vp_{3}^{\mathrm{nuc}}}{\mathrm{d}t} &= k^{\mathrm{Imp}} V^{\mathrm{cyt}} + k_{\mathrm{NP}}^{\mathrm{Bind}} P_{\mathrm{NP}} R_{\mathrm{RdRp,3}}^{\mathrm{V}} - \left(k_{\mathrm{M1}}^{\mathrm{Bind}} P_{\mathrm{M1}} + k_{\mathrm{Rnp}}^{\mathrm{Deg}}\right) Vp_{3}^{\mathrm{nuc}}, \\
\frac{\mathrm{d}Vp_{9}^{\mathrm{nuc}}}{\mathrm{d}t} &= k^{\mathrm{Imp}} D^{\mathrm{cyt}} + k_{\mathrm{NP}}^{\mathrm{Bind}} P_{\mathrm{NP}} R_{\mathrm{RdRp,9}}^{\mathrm{V}} - \left(k_{\mathrm{M1}}^{\mathrm{Bind}} P_{\mathrm{M1}} + k_{\mathrm{Rnp}}^{\mathrm{Deg}}\right) Vp_{9}^{\mathrm{nuc}},
\end{aligned}
$$

where $k = 1, \dots, 8$ are the full-length segments and $k = 9$ denotes the defective segment 3. We assumed that the DI RNA has a replication advantage over its full-length counterpart at the level of cRNA synthesis.

$$
\begin{aligned}
\frac{\mathrm{d}R_{\mathrm{i}}^{\mathrm{C}}}{\mathrm{d}t} &= k_{\mathrm{C}}^{\mathrm{Syn}} Vp_{\mathrm{i}}^{\mathrm{nuc}} - k_{\mathrm{RdRp}}^{\mathrm{Bind}} P_{\mathrm{RdRp}} R_{\mathrm{i}}^{\mathrm{C}} - k_{\mathrm{R}}^{\mathrm{Deg}} R_{\mathrm{i}}^{\mathrm{C}}, \quad i = 1, \dots, 8, \\
\frac{\mathrm{d}R_{9}^{\mathrm{C}}}{\mathrm{d}t} &= \left(F_{\mathrm{Adv}} + 1\right) k_{\mathrm{C}}^{\mathrm{Syn}} Vp_{9}^{\mathrm{nuc}} - k_{\mathrm{RdRp}}^{\mathrm{Bind}} P_{\mathrm{RdRp}} R_{9}^{\mathrm{C}} - k_{\mathrm{R}}^{\mathrm{Deg}} R_{9}^{\mathrm{C}},
\end{aligned}
$$

where F_{Adv} denotes the factor with which the synthesis of the DI cRNA exceeds the production of its full-length counterpart. We estimated F_{Adv} from the DI RNA length.

$$
F_{\mathrm{Adv}} = \left(\frac{L_{3}^{\mathrm{V}}}{L_{9}^{\mathrm{V}}} - 1\right),
$$

where L_3^{V} denotes the length of segments 3's vRNA and L_9^{V} is the length of the DI vRNA. Apart from cRNA synthesis, RNA replication occurs as described in the original model.

$$\begin{aligned}
\frac{\mathrm{d}R_{\mathrm{m}}^{\mathrm{V}}}{\mathrm{d}t} &= k_{\mathrm{V}}^{\mathrm{Syn}} Cp_{\mathrm{m}} - k_{\mathrm{RdRp}}^{\mathrm{Bind}} P_{\mathrm{RdRp}} R_{\mathrm{m}}^{\mathrm{V}} - k_{\mathrm{R}}^{\mathrm{Deg}} R_{\mathrm{m}}^{\mathrm{V}}, \quad m = 1, \ldots, 9,\\
\frac{\mathrm{d}R_{\mathrm{RdRp,m}}^{\mathrm{C}}}{\mathrm{d}t} &= k_{\mathrm{RdRp}}^{\mathrm{Bind}} P_{\mathrm{RdRp}} R_{\mathrm{m}}^{\mathrm{C}} - k_{\mathrm{NP}}^{\mathrm{Bind}} P_{\mathrm{NP}} R_{\mathrm{RdRp,m}}^{\mathrm{C}} - k_{\mathrm{RRdRp}}^{\mathrm{Deg}} R_{\mathrm{RdRp,m}}^{\mathrm{C}},\\
\frac{\mathrm{d}R_{\mathrm{RdRp,m}}^{\mathrm{V}}}{\mathrm{d}t} &= k_{\mathrm{RdRp}}^{\mathrm{Bind}} P_{\mathrm{RdRp}} R_{\mathrm{m}}^{\mathrm{V}} - k_{\mathrm{NP}}^{\mathrm{Bind}} P_{\mathrm{NP}} R_{\mathrm{RdRp,m}}^{\mathrm{V}} - k_{\mathrm{RRdRp}}^{\mathrm{Deg}} R_{\mathrm{RdRp,m}}^{\mathrm{V}},\\
\frac{\mathrm{d}Cp_{\mathrm{m}}}{\mathrm{d}t} &= k_{\mathrm{NP}}^{\mathrm{Bind}} P_{\mathrm{NP}} R_{\mathrm{RdRp,m}}^{\mathrm{C}} - k_{\mathrm{Rnp}}^{\mathrm{Deg}} Cp_{\mathrm{,m}},\\
\frac{\mathrm{d}Vp_{\mathrm{M1,m}}^{\mathrm{nuc}}}{\mathrm{d}t} &= k_{\mathrm{M1}}^{\mathrm{Bind}} P_{\mathrm{M1}} Vp_{\mathrm{m}}^{\mathrm{nuc}} - \left(k^{\mathrm{Exp}} P_{\mathrm{NEP}} + k_{\mathrm{Rnp}}^{\mathrm{Deg}}\right) Vp_{\mathrm{M1,m}}^{\mathrm{nuc}}.
\end{aligned}$$

Upon binding of NEP, M1-vRNP complexes leave the nucleus.

$$\begin{aligned}
\frac{\mathrm{d}Vp_{\mathrm{M1,k}}^{\mathrm{cyt}}}{\mathrm{d}t} &= k^{\mathrm{Exp}} P_{\mathrm{NEP}} Vp_{\mathrm{M1,k}}^{\mathrm{nuc}} - k^{\mathrm{Cplx}} Vp_{\mathrm{M1,3}}^{\mathrm{cyt}} \prod_k Vp_{\mathrm{M1,k}}^{\mathrm{cyt}}\\
&\quad - k^{\mathrm{Cplx}} Vp_{\mathrm{M1,9}}^{\mathrm{cyt}} \prod_k Vp_{\mathrm{M1,k}}^{\mathrm{cyt}} - k_{\mathrm{Rnp}}^{\mathrm{Deg}} Vp_{\mathrm{M1,k}}^{\mathrm{cyt}},\\
&\text{for} \quad k = 1, 2, 4, \ldots, 8 \quad \text{and}\\
\frac{\mathrm{d}Vp_{\mathrm{M1,3}}^{\mathrm{cyt}}}{\mathrm{d}t} &= k^{\mathrm{Exp}} P_{\mathrm{NEP}} Vp_{\mathrm{M1,3}}^{\mathrm{nuc}} - k^{\mathrm{Cplx}} Vp_{\mathrm{M1,3}}^{\mathrm{cyt}} \prod_k Vp_{\mathrm{M1,k}}^{\mathrm{cyt}} - k_{\mathrm{Rnp}}^{\mathrm{Deg}} Vp_{\mathrm{M1,3}}^{\mathrm{cyt}},\\
\frac{\mathrm{d}Vp_{\mathrm{M1,9}}^{\mathrm{cyt}}}{\mathrm{d}t} &= k^{\mathrm{Exp}} P_{\mathrm{NEP}} Vp_{\mathrm{M1,9}}^{\mathrm{nuc}} - k^{\mathrm{Cplx}} Vp_{\mathrm{M1,9}}^{\mathrm{cyt}} \prod_k Vp_{\mathrm{M1,k}}^{\mathrm{cyt}} - k_{\mathrm{Rnp}}^{\mathrm{Deg}} Vp_{\mathrm{M1,9}}^{\mathrm{cyt}},
\end{aligned}$$

where k^{Cplx} denotes the formation rate of a cytoplasmic complex that comprises the eight vRNPs including either the full-length or DI vRNA of segment 3. Viral mRNA and protein production was described by the following equations.

$$\begin{aligned}
\frac{\mathrm{d}R_{\mathrm{i}}^{\mathrm{M}}}{\mathrm{d}t} &= \frac{k_{\mathrm{M}}^{\mathrm{Syn}}}{L_{\mathrm{i}}} Vp_{\mathrm{i}}^{\mathrm{nuc}} - k_{\mathrm{M}}^{\mathrm{Deg}} R_{\mathrm{i}}^{\mathrm{M}}, \quad i = 1, \ldots, 8,\\
\frac{\mathrm{d}P_{\mathrm{PB1}}}{\mathrm{d}t} &= \frac{k_{\mathrm{P}}^{\mathrm{Syn}}}{D_{\mathrm{Rib}}} R_2^{\mathrm{M}} - k^{\mathrm{RdRp}} P_{\mathrm{PB1}} P_{\mathrm{PB2}} P_{\mathrm{PA}},\\
\frac{\mathrm{d}P_{\mathrm{PB2}}}{\mathrm{d}t} &= \frac{k_{\mathrm{P}}^{\mathrm{Syn}}}{D_{\mathrm{Rib}}} R_1^{\mathrm{M}} - k^{\mathrm{RdRp}} P_{\mathrm{PB1}} P_{\mathrm{PB2}} P_{\mathrm{PA}},\\
\frac{\mathrm{d}P_{\mathrm{PA}}}{\mathrm{d}t} &= \frac{k_{\mathrm{P}}^{\mathrm{Syn}}}{D_{\mathrm{Rib}}} R_3^{\mathrm{M}} - k^{\mathrm{RdRp}} P_{\mathrm{PB1}} P_{\mathrm{PB2}} P_{\mathrm{PA}},
\end{aligned}$$

$$
\begin{aligned}
\frac{\mathrm{d}P_{\mathrm{RdRp}}}{\mathrm{d}t} &= k^{\mathrm{RdRp}} P_{\mathrm{PB1}} P_{\mathrm{PB2}} P_{\mathrm{PA}} - k^{\mathrm{Bind}}_{\mathrm{RdRp}} P_{\mathrm{RdRp}} \sum_{m} \left[R^{\mathrm{V}}_{\mathrm{m}} + R^{\mathrm{C}}_{\mathrm{m}} \right], \quad m = 1, \ldots, 9, \\
\frac{\mathrm{d}P_{\mathrm{NP}}}{\mathrm{d}t} &= \frac{k^{\mathrm{Syn}}_{\mathrm{P}}}{D_{\mathrm{Rib}}} R^{\mathrm{M}}_{5} - k^{\mathrm{Bind}}_{\mathrm{NP}} P_{\mathrm{NP}} \sum_{m} \frac{L^{\mathrm{V}}_{\mathrm{m}}}{N^{\mathrm{Nuc}}_{\mathrm{NP}}} \left(R^{\mathrm{V}}_{\mathrm{RdRp,m}} + R^{\mathrm{C}}_{\mathrm{RdRp,m}} \right), \\
\frac{\mathrm{d}P_{\mathrm{M1}}}{\mathrm{d}t} &= \frac{k^{\mathrm{Syn}}_{\mathrm{P}}}{D_{\mathrm{Rib}}} \left(1 - F_{\mathrm{Spl}_7} \right) R^{\mathrm{M}}_{7} - k^{\mathrm{Bind}}_{\mathrm{M1}} P_{\mathrm{M1}} \sum_{m} \frac{L^{\mathrm{V}}_{\mathrm{m}}}{N^{\mathrm{Nuc}}_{\mathrm{M1}}} V p^{\mathrm{nuc}}_{\mathrm{m}} \\
&\quad - (N_{\mathrm{P_{M1}}} - \sum_{p=1,\ldots,8} \frac{L^{\mathrm{V}}_{\mathrm{p}}}{N^{\mathrm{Nuc}}_{\mathrm{M1}}}) r^{\mathrm{Rel}} - (N_{\mathrm{P_{M1}}} - \sum_{p=1,2,4,\ldots,9} \frac{L^{\mathrm{V}}_{\mathrm{p}}}{N^{\mathrm{Nuc}}_{\mathrm{M1}}}) r^{\mathrm{Rel}}_{\mathrm{D}}, \\
\frac{\mathrm{d}P_{\mathrm{NEP}}}{\mathrm{d}t} &= \frac{k^{\mathrm{Syn}}_{\mathrm{P}}}{D_{\mathrm{Rib}}} F_{\mathrm{Spl}_8} R^{\mathrm{M}}_{8} - k^{\mathrm{Exp}} P_{\mathrm{NEP}} \sum_{m} V p^{\mathrm{nuc}}_{\mathrm{M1,m}}, \\
\frac{\mathrm{d}P_{\mathrm{HA}}}{\mathrm{d}t} &= \frac{k^{\mathrm{Syn}}_{\mathrm{P}}}{D_{\mathrm{Rib}}} R^{\mathrm{M}}_{4} - N_{\mathrm{P_{HA}}} \left(r^{\mathrm{Rel}} + r^{\mathrm{Rel}}_{\mathrm{D}} \right), \\
\frac{\mathrm{d}P_{\mathrm{NA}}}{\mathrm{d}t} &= \frac{k^{\mathrm{Syn}}_{\mathrm{P}}}{D_{\mathrm{Rib}}} R^{\mathrm{M}}_{6} - N_{\mathrm{P_{NA}}} \left(r^{\mathrm{Rel}} + r^{\mathrm{Rel}}_{\mathrm{D}} \right), \\
\frac{\mathrm{d}P_{\mathrm{M2}}}{\mathrm{d}t} &= \frac{k^{\mathrm{Syn}}_{\mathrm{P}}}{D_{\mathrm{Rib}}} F_{\mathrm{Spl}_7} R^{\mathrm{M}}_{7} - N_{\mathrm{P_{M2}}} \left(r^{\mathrm{Rel}} + r^{\mathrm{Rel}}_{\mathrm{D}} \right),
\end{aligned}
$$

where $r^{\mathrm{Rel}}_{\mathrm{D}}$ is the release rate of DIPs. Compared to the original model we neglected the release of free viral polymerases, NP, and NEP with budding virions (see reference [269] for a discussion). We, also, assumed that one NEP protein binds per genome segment to induce nuclear export. In the cytoplasm, the eight full-length RNAs and the defective segment form complexes.

$$
\begin{aligned}
\frac{\mathrm{d}V^{\mathrm{cyt}}_{\mathrm{Cplx}}}{\mathrm{d}t} &= k^{\mathrm{Cplx}} V p^{\mathrm{cyt}}_{\mathrm{M1,3}} \prod_{k} V p^{\mathrm{cyt}}_{\mathrm{M1,k}} - r^{\mathrm{Rel}} - k^{\mathrm{Deg}}_{\mathrm{Rnp}} V^{\mathrm{cyt}}_{\mathrm{Cplx}}, \quad k = 1, 2, 4, \ldots, 8, \\
\frac{\mathrm{d}D^{\mathrm{cyt}}_{\mathrm{Cplx}}}{\mathrm{d}t} &= k^{\mathrm{Cplx}} V p^{\mathrm{cyt}}_{\mathrm{M1,9}} \prod_{k} V p^{\mathrm{cyt}}_{\mathrm{M1,k}} - r^{\mathrm{Rel}}_{\mathrm{D}} - k^{\mathrm{Deg}}_{\mathrm{Rnp}} D^{\mathrm{cyt}}_{\mathrm{Cplx}},
\end{aligned}
$$

where $V^{\mathrm{cyt}}_{\mathrm{Cplx}}$ and $D^{\mathrm{cyt}}_{\mathrm{Cplx}}$ denote a complex containing all eight genome segments including a full-length or defective segment 3, respectively. The equations for virus release are the following.

$$
\frac{\mathrm{d}V^{\mathrm{Rel}}}{\mathrm{d}t} = r^{\mathrm{Rel}} = 8 k^{\mathrm{Rel}} V^{\mathrm{cyt}}_{\mathrm{Cplx}} \prod_{\mathrm{j}} \frac{P_{\mathrm{j}}}{P_{\mathrm{j}} + K_{\mathrm{V^{Rel}}} N_{\mathrm{P_j}}},
$$

$$\frac{\mathrm{d}D^{\mathrm{Rel}}}{\mathrm{d}t} = r_{\mathrm{D}}^{\mathrm{Rel}} = 8k^{\mathrm{Rel}} D_{\mathrm{Cplx}}^{\mathrm{cyt}} \prod_{\mathrm{j}} \frac{P_{\mathrm{j}}}{P_{\mathrm{j}} + K_{V^{\mathrm{Rel}}} N_{P_{\mathrm{j}}}},$$

$$\text{with} \quad j \in \{\mathrm{HA}, \mathrm{NA}, \mathrm{M1}, \mathrm{M2}\},$$

where V^{Rel} and D^{Rel} are the STVs and DIPs, respectively, that are released from the cell.

C.2. Model for a DI RNA of segment 4

We used the same equations as presented in Section C.1 to model the replication of a DI RNA of segment 4 with the following exceptions.

$$\frac{\mathrm{d}Vp_{\mathrm{k}}^{\mathrm{nuc}}}{\mathrm{d}t} = k^{\mathrm{Imp}} V^{\mathrm{cyt}} + k^{\mathrm{Imp}} D^{\mathrm{cyt}} + k_{\mathrm{NP}}^{\mathrm{Bind}} P_{\mathrm{NP}} R_{\mathrm{RdRp,k}}^{\mathrm{V}} - \left(k_{\mathrm{M1}}^{\mathrm{Bind}} P_{\mathrm{M1}} + k_{\mathrm{Rnp}}^{\mathrm{Deg}}\right) Vp_{\mathrm{k}}^{\mathrm{nuc}},$$

$$\text{with} \quad k = 1, 2, 3, 5, \ldots, 8,$$

$$\frac{\mathrm{d}Vp_{4}^{\mathrm{nuc}}}{\mathrm{d}t} = k^{\mathrm{Imp}} V^{\mathrm{cyt}} + k_{\mathrm{NP}}^{\mathrm{Bind}} P_{\mathrm{NP}} R_{\mathrm{RdRp,4}}^{\mathrm{V}} - \left(k_{\mathrm{M1}}^{\mathrm{Bind}} P_{\mathrm{M1}} + k_{\mathrm{Rnp}}^{\mathrm{Deg}}\right) Vp_{4}^{\mathrm{nuc}},$$

$$\frac{\mathrm{d}R_{9}^{\mathrm{C}}}{\mathrm{d}t} = \left(F_{\mathrm{Adv}} + 1\right) k_{\mathrm{C}}^{\mathrm{Syn}} Vp_{9}^{\mathrm{nuc}} - k_{\mathrm{RdRp}}^{\mathrm{Bind}} P_{\mathrm{RdRp}} R_{9}^{\mathrm{C}} - k_{\mathrm{R}}^{\mathrm{Deg}} R_{9}^{\mathrm{C}}, \quad \text{with} \quad F_{\mathrm{Adv}} = \frac{L_{4}^{\mathrm{V}}}{L_{9}^{\mathrm{V}}} - 1,$$

$$\begin{aligned}\frac{\mathrm{d}Vp_{\mathrm{M1,k}}^{\mathrm{cyt}}}{\mathrm{d}t} &= k^{\mathrm{Exp}} P_{\mathrm{NEP}} Vp_{\mathrm{M1,k}}^{\mathrm{nuc}} - k^{\mathrm{Cplx}} Vp_{\mathrm{M1,4}}^{\mathrm{cyt}} \prod_{k} Vp_{\mathrm{M1,k}}^{\mathrm{cyt}} \\ &\quad - k^{\mathrm{Cplx}} Vp_{\mathrm{M1,9}}^{\mathrm{cyt}} \prod_{k} Vp_{\mathrm{M1,k}}^{\mathrm{cyt}} - k_{\mathrm{Rnp}}^{\mathrm{Deg}} Vp_{\mathrm{M1,k}}^{\mathrm{cyt}},\end{aligned}$$

$$\frac{\mathrm{d}Vp_{\mathrm{M1,4}}^{\mathrm{cyt}}}{\mathrm{d}t} = k^{\mathrm{Exp}} P_{\mathrm{NEP}} Vp_{\mathrm{M1,4}}^{\mathrm{nuc}} - k^{\mathrm{Cplx}} Vp_{\mathrm{M1,4}}^{\mathrm{cyt}} \prod_{k} Vp_{\mathrm{M1,k}}^{\mathrm{cyt}} - k_{\mathrm{Rnp}}^{\mathrm{Deg}} Vp_{\mathrm{M1,4}}^{\mathrm{cyt}},$$

$$\begin{aligned}\frac{\mathrm{d}P_{\mathrm{M1}}}{\mathrm{d}t} &= \frac{k_{\mathrm{P}}^{\mathrm{Syn}}}{D_{\mathrm{Rib}}} \left(1 - F_{\mathrm{Spl}_7}\right) R_{7}^{\mathrm{M}} - k_{\mathrm{M1}}^{\mathrm{Bind}} P_{\mathrm{M1}} \sum_{m=1,\ldots,9} \frac{L_{\mathrm{m}}^{\mathrm{V}}}{N_{\mathrm{M1}}^{\mathrm{Nuc}}} Vp_{\mathrm{m}}^{\mathrm{nuc}} \\ &\quad - (N_{P_{\mathrm{M1}}} - \sum_{p=1,\ldots,8} \frac{L_{\mathrm{p}}^{\mathrm{V}}}{N_{\mathrm{M1}}^{\mathrm{Nuc}}}) r^{\mathrm{Rel}} - (N_{P_{\mathrm{M1}}} - \sum_{p=1,2,3,5,\ldots,9} \frac{L_{\mathrm{p}}^{\mathrm{V}}}{N_{\mathrm{M1}}^{\mathrm{Nuc}}}) r_{\mathrm{D}}^{\mathrm{Rel}},\end{aligned}$$

$$\frac{\mathrm{d}V_{\mathrm{Cplx}}^{\mathrm{cyt}}}{\mathrm{d}t} = k^{\mathrm{Cplx}} Vp_{\mathrm{M14}}^{\mathrm{cyt}} \prod_{k} Vp_{\mathrm{M1,k}}^{\mathrm{cyt}} - r^{\mathrm{Rel}} - k_{\mathrm{Rnp}}^{\mathrm{Deg}} V_{\mathrm{Cplx}}^{\mathrm{cyt}},$$

$$\frac{\mathrm{d}D_{\mathrm{Cplx}}^{\mathrm{cyt}}}{\mathrm{d}t} = k^{\mathrm{Cplx}} Vp_{\mathrm{M1,9}}^{\mathrm{cyt}} \prod_{k} Vp_{\mathrm{M1,k}}^{\mathrm{cyt}} - r_{\mathrm{D}}^{\mathrm{Rel}} - k_{\mathrm{Rnp}}^{\mathrm{Deg}} D_{\mathrm{Cplx}}^{\mathrm{cyt}}.$$

Lebenslauf

Persönliche Daten

Name	Frank Stefan Heldt
Geburtsdaten	8. Mai 1985 in Magdeburg
Nationalität	Deutsch
Familienstand	ledig
E-Mail	heldt@mpi-magdeburg.mpg.de
Telefon	(+49) 391 6110 227

Schulbildung

1991 – 1995 **Grundschule am Neustädter Feld**, Magdeburg, Deutschland

1995 – 2001 **Bettina-von-Arnim-Gymnasium**, Magdeburg, Deutschland

2001 – 2004 **Albert-Einstein-Gymnasium**, Magdeburg, Deutschland
- Abschluss mit Abitur (Gesamtnote: 1,3)

Hochschulstudium

Okt. 2004 – Nov. 2009 **Otto-von-Guericke-Universität**, Magdeburg, Deutschland
- Studium der Biosystemtechnik an der Fakultät für Verfahrens- und Systemtechnik
- Abschluss als Diplom-Ingenieur mit Auszeichnung (Gesamtnote: 1,1)

März 2008 – Nov. 2008 **Max-Planck-Institut f. Dyn. Compl. Techn. Syst.**, Magdeburg, Deutschland
- Studienarbeit in der Arbeitsgruppe „Bioprozesstechnik“ betreut von Dr.-Ing. Björn Heynisch
- Thema: „Die Dynamik antiviraler Signalkaskaden in MDCK Zellen während einer Infektion mit Influenzaviren“
- Abschluss mit Note 1,0

März 2009 – Nov. 2009 **University of Aberdeen**, Aberdeen, Schottland
- Diplomarbeit im „Department of Physics“ betreut von Dr. Marco Thiel
- Thema: „A Computational Model of Protein Translation and the Competition for Rare Cellular Resources in Response to Amino Acid Starvation“
- Abschluss mit Note 1,0

Berufserfahrung

Juni 2004 – Sept. 2004 **Öhmi Analytik GmbH**, Magdeburg, Deutschland
- Praktikum im Labor für Umweltanalytik

Okt. 2008 – Febr. 2009 **Solvay Pharmaceuticals**, Weesp, Niederlande
- Praktikum in der Forschungs- und Entwicklungsabteilung

seit Dez. 2009 **Max-Planck-Institut f. Dyn. Compl. Techn. Syst.**, Magdeburg, Deutschland
- Wissenschaftlicher Mitarbeiter (Promotion) in der Arbeitsgruppe „Bioprozesstechnik“unter Leitung von Prof. Dr.–Ing. Udo Reichl
- Thema: „Mathematische Modellierung von Infektionen durch Influenzaviren im Kontext zellkulturbasierter Impfstoffherstellung“

Publikationen (peer-reviewed)

2010 Vester D, Lagoda A, Hoffmann D, Seitz C, **Heldt S**, Bettenbrock K, Genzel Y, Reichl U (2010) Real-time RT-qPCR assay for the analysis of human influenza A virus transcription and replication dynamics. J Virol Methods 168(1-2): 63-71

2012 **Heldt FS**, Frensing T, Reichl U (2012) Modeling the intracellular dynamics of influenza virus replication to understand the control of viral RNA synthesis. J Virol 86: 7806–7817.

2013 Frensing T*, **Heldt FS***, Pflugmacher A, Behrendt I, Jordan I, Flockerzi D, Genzel Y, Reichl U (2013) Continuous influenza virus production in cell culture shows a periodic accumulation of defective interfering particles. PLoS One 8: e72288.

2013 **Heldt FS**, Frensing T, Pflugmacher A, Gröpler R, Peschel B, Reichl U (2013) Multiscale modeling of influenza A virus infection supports the development of direct-acting antivirals. PLoS Comput Biol 9: e1003372.

*gleichberechtigte Autorenschaft

Vorträge

2009 **Quantitative modelling of protein translation: Ribosomal competition for rare resources and its impact on dynamics.** 1st conference on Dynamics in Systems Biology, Aberdeen, Schottland

2011 **Understanding the dynamics of intracellular virus replication - How does influenza control its RNA and protein synthesis?** 4th ESWI Influenza Conference, Malta

2012 **Elucidating bottlenecks in influenza virus replication to optimize vaccine production.** International Conference on Systems Biology of Human Disease, Heidelberg, Deutschland

2013 **Multiscale modeling of influenza virus infection elucidates the performance of antivirals.** 1st Workshop on Virus Dynamics, Frankfurt, Deutschland

2013 **Multiscale modeling of influenza virus infection supports the development of antiviral drugs.** 14th International Conference on Systems Biology, Copenhagen, Dänemark

2014 **The multiscale nature of influenza A virus infection and its implications for modeling antiviral therapy.** Joint Annual Meeting of the JSMB and the SMB, Osaka, Japan

Poster

2009 **Ribosomal competition and traffic jams during protein translation.** 1st conference on Dynamics in Systems Biology, Aberdeen, Schottland

2010 **Multiscale modeling of influenza virus infection dynamics in cell culture-based vaccine production.** International Conference on Systems Biology of Human Disease, Boston, Vereinigte Staaten von Amerkia

2010 **Modeling influenza virus infection dynamics in cell culture-based vaccine production.** 11th International Conference on Systems Biology, Edinburgh, Schottland

2011 **Mechanistic model of influenza virus replication elucidates the intracellular dynamics and control of viral RNA synthesis.** 12th International Conference on Systems Biology, Mannheim, Deutschland

2012 **Elucidating the dynamics of influenza virus replication by mathematical modeling.** 22nd Annual Meeting of the German Society for Virology, Essen, Deutschland

2012 **Elucidating bottlenecks in influenza virus replication to optimize vaccine production.** International Conference on Systems Biology of Human Disease, Heidelberg, Deutschland

2013 **A multiscale model of influenza virus infection elucidates the performance of antivirals.** 23rd Annual Meeting of the German Society for Virology, Kiel, Deutschland

2014 **A multiscale model of influenza A virus infection that elucidates the treatment with direct-acting antivirals.** International Conference on Systems Biology of Human Disease, Boston, Vereinigte Staaten von Amerkia